SLAC-409
UC-414
(E/I)

STRANGE MESON SPECTROSCOPY IN Kω AND Kφ AT 11 GeV/c AND CHERENKOV RING IMAGING AT SLD *

Youngjoon Kwon

Stanford Linear Accelerator Center
Stanford University
Stanford, CA 94309

January 1993

Prepared for the Department of Energy
uncer contract number DE-AC03-76SF00515

Printed in the United States of America. Available from the National Technical Information Service, U.S. Department of Commerce, 5285 Port Royal Road, Springfield, Virginia 22161.

---

* Ph.D. thesis

Abstract

This thesis consists of two independent parts; development of Cherenkov Ring Imaging Detector (CRID) system and analysis of high-statistics data of strange meson reactions from the LASS spectrometer.

Part I: The CRID system is devoted to charged particle identification in the SLAC Large Detector (SLD) to study e^+e^- collisions at $\sqrt{s} = m_{Z^\circ}$. By measuring the angles of emission of the Cherenkov photons inside liquid and gaseous radiators, $\pi/K/p$ separation will be achieved up to ~ 30 GeV/c.

The signals from CRID are read in three coordinates, one of which is measured by charge-division technique. To obtain a $\sim 1\%$ spatial resolution in the charge-division, low-noise CRID preamplifier prototypes were developed and tested resulting in < 1000 electrons noise for an average photoelectron signal with 2×10^5 gain.

To help ensure the long-term stability of CRID operation at high efficiency, a comprehensive monitoring and control system was developed. This system continuously monitors and/or controls various operating quantities such as temperatures, pressures, and flows, mixing and purity of the various fluids.

The results from the engineering run and initial physics run of the CRID in the SLD experiment show that the CRID hardware performs well and produces Cherenkov rings.

Part II: Results from the partial wave analysis of strange meson final states in the reactions $K^-p \to K^-\omega p$ and $K^-p \to \overline{K}^\circ \phi n$ are presented. The analyses are based on data from a 4.1 event/nb exposure of the LASS spectrometer in K^-p interactions at 11 GeV/c.

The data sample of $K^-\omega p$ final state contains $\sim 10^5$ events, which is at least 25 times larger than in any other experiments. From the partial wave analysis,

resonance structures of $J^P = 2^-$, 3^- and 2^+ amplitudes are observed in the $K\omega$ system. The analysis of 2^- amplitudes provides an evidence for two strange meson states in the mass region around 1.75 GeV/c^2. The 3^- signal corresponding to $K_3^*(1780)$ is observed to decay into $K\omega$ for the first time. A clear signal of the $K_2^*(1430) \rightarrow K\omega$ decay is also observed. The appropriate branching fractions are calculated and compared with the SU(3) predictions.

The partial wave analysis of $\overline{K}^0\phi$ system favors $J^P = 1^-$ and 2^+ states in the $1.9 - 2.0$ GeV/c^2 region, but due to low statistics, the interpretation of partial waves in terms of resonance parameters is inconclusive.

Acknowledgments

For all this, I thank God, my Lord; only He has been, is, and will be the true source of my strength and inspiration.

Although this thesis bears my name, it is essentially the work of many people. First and foremost, I would like to thank David Leith, my advisor, for all the helps that he provided me. When I first arrived at Stanford without knowing at all what detectors and accelerators are made of, he was kind enough to give me an opportunity to work in the SLAC Group B. Ever since, he has always been willing to offer me help and advice. He has always encouraged me to transcend the myoptic view of a graduate student and look deeply into and broadly over the fundamental problems of physics in whatever works I might be doing. He is certainly one of the models that I want to follow as a physicist, a teacher and a person.

Blair Ratcliff first introduced me to the strange meson spectorscopy and suggested me to look into the $K\omega$ system regarding the unnatural spin-parity states. Bill Dunwoodie spent countless hours with me providing helps with all his insights on meson spectroscopy and analysis ideas. Dave Aston has always been willing to answer whatever silly questions I asked in computing and programming. Dick Bierce provided precisous help in managing data tapes.

I am greatly indebted to Paschal Coyle and Greg Hallewell who guided me through many stages of my involvement in the SLD CRID project. Considering almost no experience in experimental physics that I had when I first arrived here, it is only an understatement that their helps were tremendously important for me to learn many aspects of R&D in building a detector system. I enjoyed observing all the ideas that Greg Hallewell provided to overcome the technical problems coming through. I learned a lot from Hideaki Kawahara with his expertise in electronics and hardware design. Don McShurley, Gerard Oxoby, Bob Reif and many other people provided me with technical assistances.

I also received a lot of direct and indirect helps from former and current graduate students in SLAC Group B. Tim Bienz and Paul Rensing were very patient

and kind to teach me the basic techniques of programming and helped me overcome the threshold of a beginner. Tom Pavel helped me a lot in the CRID project. Their enthusiasm, energy, and insights were something I can only envy. I feel very fortunate to have worked with them. I am also greatly indebted to Pekka Sinervo and Fred Bird, both former graduate students in Group B. Their experiences in analyzing the humongous data set of E-135, excellently documented in their dissertations, were invaluable assets throughout my analysis. I was lucky to have chances to meet them in person, whenever I had very crucial questions, which only they could answer.

Lillian Vasillian and Eileen Brennan, Group B administrative assistants, have been very kind and very helpful in dealing with administrative materials, especially with the University. Without their helps, I should have had a lot more trouble in finishing this thesis.

I appreciate the Korea Foundation for Advanced Studies (KFAS) as they partially supported my graduate study. Being a KFAS fellow provided me with opportunities to meet many good friends through KFAS fellows' meetings.

If it were not for my parents, it would have been absolutely impossbile for me even to start this thesis, not to mention finish it. I feel very sorry for my father being no longer with us to see this work finished. I hope that now he can feel happier for his son, even in heaven. And, special thanks be to my mother. Her consistent support and prayer are something I can always count on. I am also grateful to my parent-in-laws for their support during the final year of my study.

Although I mention it last, the contribution of Seungmin, my wife, to this thesis is at least as great as mine. She stopped her brilliant career in Korea as a reasearcher in psychology and education to become my wife and gave her heart and soul to support and encourage me to finish this work. Whatever she has done for me is something that I should remember and reward throughout my life. Therefore, it is only appropriate to dedicate this thesis to my mother and my wife.

Contents

Signature

Abstract ii

Acknowledgments iv

1 Introduction 1

2 Principles of Cherenkov Ring Imaging 5

2.1 Cherenkov Radiation 5

2.2 Ring Imaging Devices 8

2.2.1 Mirror Focusing 8

2.2.2 Proximity Focusing 9

3 SLD Cherenkov Ring Imaging Detector 12

3.1 SLD Overview 12

3.2 Motivation for CRID 15

3.3 Components of CRID 17

3.3.1 Cherenkov Radiator 17

3.3.2 Drift Box 20

3.3.3 Mirrors 25

3.3.4 Electron Detector 25

3.3.5 Data Acquisition 26

3.3.6 Monitoring and Control 28

4 Low-noise Preamplifier for CRID **31**
4.1 Low-noise Requirement for CRID Preamplifier 31
4.2 FET amplifier noise model 33
4.2.1 Thermal noise 34
4.2.2 Shot noise 34
4.2.3 $1/f$ noise 35
4.2.4 Total noise 35
4.3 Noise Performance Test 36
4.3.1 Interchannel Crosstalk 36
4.3.2 Test system setup and results 38

5 Monitor and Control Systems for CRID **49**
5.1 Data acquisition for Monitor and control 49
5.2 Monitoring and control of operating temperature 50
5.3 Gas Delivery system and Pressure Control 55
5.3.1 Pressure Control Tests on the Two-Cell Simulator. 62
5.3.2 Pressure Control Tests on the CRID Prototype 68
5.4 Binary Gas Mixture Monitoring using Sonar 73

6 First Results from the SLD CRID **80**
6.1 Commissioning of CRID 80
6.2 Observation of the Cherenkov rings 85

7 Introduction to Part II **90**

8 The LASS Spectrometer **96**
8.1 The Beamline 98
8.2 The Target 101
8.3 The Solenoid Region 102
8.3.1 The Cylindrical Chambers 102
8.3.2 The Planar Chambers 103
8.3.3 The Cherenkov Counter $\check{C}_1$ 104

8.3.4 The Time of Flight System 108
8.4 The Dipole Region 108
8.4.1 The Magnetostrictive Chambers 111
8.4.2 The Proportional Chambers 112
8.4.3 The Scintillator hodoscopes 112
8.4.4 The Cherenkov Counter $\check{C}_2$ 113
8.5 The Event Trigger 113
8.5.1 The Beam Trigger Logic 114
8.5.2 The Cluster Logic 114
8.5.3 Complete Event Trigger 115
8.6 The Data Acquisition 117
8.7 The Spectrometer Alignment and Calibration 118
8.7.1 Alignment 118
8.7.2 Electronics Calibration 119
8.7.3 Momentum Calibration 119
8.7.4 Time of Flight Calibration 120
8.7.5 dE/dx Calibration 121
8.8 The Event Reconstruction 121
8.8.1 Raw Data Unpacking 122
8.8.2 Beam Track Finding 122
8.8.3 Solenoid Track Finding 123
8.8.4 Dipole Track Finding 124
8.8.5 Vertex Finding and Topology Recognition 125
8.9 Monte Carlo simulation of the spectrometer 126
8.9.1 Beam track generation 126
8.9.2 Particle tracking and spectrometer responses 127
8.9.3 Test of MC simulation 127

9 $K\omega$ system analysis **129**
9.1 $K\omega$ event selection 129

9.1.1 Topology selection 130
9.1.2 MVFit 130
9.1.3 Particle Identification 135
9.1.4 The final event selection 138
9.2 General features of the data 139
9.2.1 Invariant mass distribution of $\pi^+\pi^-\pi^0$ 139
9.2.2 Invariant mass distribution of $K\omega$ 144
9.3 The Double moments 149
9.3.1 Definition of double moments 152
9.3.2 Measurements 153
9.4 The Acceptance correction 153
9.4.1 The Monte Carlo events 153
9.4.2 Formalism 161
9.4.3 Acceptance-corrected moments 164

10 $\overline{K}^\circ\phi$ system analysis **177**
10.1 $\overline{K}^\circ\phi$ event selection 177
10.1.1 Meson and Topology strips 178
10.1.2 MVFit strip (1) 179
10.1.3 MVFit strip (2) 180
10.1.4 Resolution cut and final selection 187
10.2 The general features of the $\overline{K}^\circ\phi$ data 190
10.3 The $\overline{K}^\circ\phi$ double moments 193
10.3.1 Angular distribution 193
10.3.2 Acceptance Correction 199
10.3.3 Mass resolution 199

11 Partial Wave Analysis of $K^-\omega$ and $\overline{K}^\circ\phi$ **205**
11.1 The Formalism 205
11.2 Resonance Fitting with Breit-Wigner Model 209
11.3 $K^-\omega$ Partial Wave Amplitudes 211

11.3.1 The Spin-parity Decomposition of the $K\omega$ Spectrum 212
11.3.2 3^- Amplitude 215
11.3.3 2^- Amplitude 215
11.3.4 2^+ Amplitude 220
11.3.5 1^+ Amplitude 221
11.3.6 t'-dependent PWA of $K^-\omega$ 222
11.4 $\overline{K}^\circ\phi$ Partial Wave Amplitudes 228
11.4.1 Moment Combinations 228
11.4.2 Mass-dependent PWA of $\overline{K}^\circ\phi$ 230
11.4.3 t'-dependent PWA of $\overline{K}^\circ\phi$ 235

12 Spectroscopy and Conclusion **238**
12.1 Branching Fractions and SU(3) 238
12.1.1 $K_2^*(1430) \to K\omega$ 238
12.1.2 $K_3^*(1780) \to K\omega$ 243
12.2 $J^P = 2^-$ state 244
12.3 Conclusion 245

A The Partial waves **249**

B The moment-amplitude relations **251**

List of Figures

2.1 A simple ring imaging system 8
2.2 A proximity focusing technique 10

3.1 Isometric view of the SLD detector 13
3.2 Sectional view of the SLD detector 14
3.3 $K\pi\pi$ mass distribution from Monte Carlo Z° decays 16
3.4 Barrel CRID sectional view 18
3.5 Particle separation ability of the CRID 19
3.6 Drift box and detector for barrel CRID 21
3.7 CRID electron detector region 27
3.8 Data acquisition for CRID 28
3.9 CRID UV fiber system 29

4.1 The charge division technique 32
4.2 Schematic diagram of the MOSFET preamplifier prototype 37
4.3 Schematic diagram of the JFET preamplifier prototype 38
4.4 Crosstalk in prototype MOSFET preamplifier 39
4.5 The effect of the crosstalk shielding screen 40
4.6 Block diagram of preamp noise test system 41
4.7 The calibration circuit for the MOSFET preamp 42
4.8 CRID Preamp pulse shape 43
4.9 Preamp output vs. input charge 44
4.10 ENC vs. added input capacitance 46

4.11 ENC vs. added input resistance 47

5.1 CAMAC monitor and control data acquisition system 51
5.2 Temperature sensor multiplexing 53
5.3 Temperature readout using AD590 sensor 54
5.4 CRID heater switching circuit 56
5.5 Barrel CRID gas delivery system 57
5.6 Desired gas system responses to pressure variation 59
5.7 Pressure-valve response matrix 60
5.8 Pressure Control System Simulator 62
5.9 ERN recovery as a function of ERN Flow 66
5.10 S – A Pressure transients (1) 70
5.11 S – A Pressure transients (2) 71
5.12 Cut-away view of the sonar transducer 74
5.13 Schematic of the sonar driver circuit 76
5.14 Schematic of the sonar preamp circuit 76
5.15 Block diagram of the multi-channel sonar CAMAC module 77
5.16 Barrel CRID sonar time-history 78

6.1 Electron lifetime and O_2 level in CRID drift boxes 82
6.2 UV fiber results 83
6.3 Drift velocity measurements 84
6.4 Integrated gas Cherenkov rings 87
6.5 Resolution in Cherenkov angle from gas radiator 88
6.6 Integrated liquid Cherenkov rings 89

8.1 Overview of the LASS spectrometer 97
8.2 Momentum resolution for the LASS spectrometer 99
8.3 The Solenoid Region of the LASS Spectrometer 102
8.4 The optical cells in $\check{C}_1$ 105
8.5 Momentum dependence of the $\check{C}_1$ counter efficiency 107

8.6 The time of flight hodoscope 109
8.7 The dipole region of the LASS spectrometer 110
8.8 The complete trigger logic for E-135 116

9.1 Missing mass squared for topology selected events 131
9.2 $\pi^+\pi^-\pi^0$ invariant mass distribution for topology selected events . . 131
9.3 Typical confidence level distributions of 4-C and 1-C MVfits 133
9.4 A typical $\pi^+\pi^-\pi^0$ invariant mass distribution of the events removed by the 4-C and 1-C MVFits 134
9.5 $\pi^+\pi^-\pi^0$ invariant mass distribution after MVFit selection 135
9.6 dE/dx and TOF plots 137
9.7 t' distribution and cut positions 139
9.8 $\pi^+\pi^-\pi^0$ invariant mass distribution of the final data sample 141
9.9 $\cos\theta_h$ distribution 142
9.10 $\pi^+\pi^-\pi^0$ spectrum weighted by $-Y_{20}$ 144
9.11 The $K^-\pi^+\pi^-\pi^0$ invariant mass distribution 145
9.12 $\pi^+\pi^-\pi^0$ for $m_{K\omega} = 1.58 \pm 0.02$ GeV/c^2 147
9.13 $m_{\pi^+\pi^-\pi^0}$ weighted by $-Y_{20}$ for $m_{K\omega} = 1.58 \pm 0.02$ GeV/c^2 148
9.14 ω fitting in the $K\omega$ threshold region 149
9.15 $K\omega$ Dalitz plot 150
9.16 Invariant mass distributions of pK and $p\omega$ 151
9.17 Uncorrected double moments 154
9.18 $\pi^+\pi^-\pi^0$ mass resolution 160
9.19 $m_{K\omega}$ resolution 161
9.20 $K\omega$ mass resolution as a function of $m_{K\omega}$ 162
9.21 Acceptance as a function of t' 165
9.22 Acceptance as a function of $m_{K\omega}$ 166
9.23 Acceptance effect on the moments 167
9.24 Acceptance-corrected moments 172

10.1 Mass distributions before PID cut and MVFit 181

10.2 The events removed by Time-of-flight and dE/dx. 182
10.3 The events removed by Cherenkov 182
10.4 Invariant mass distributions of $\pi^+\pi^-$ vs. $\overline{K}^\circ$ decay length 183
10.5 scatter plot: m($\pi\pi$) vs. $\cos\theta_h$ 184
10.6 V^0 in the forward θ_h region as $p\pi^-$ 185
10.7 Mass distributions after PID and GEOFIT cuts and before MVFit . 186
10.8 mass plots after MVFit 188
10.9 $mm^2(\overline{K}^\circ K^- K^+)$ distribution 189
10.10$K^- K^+$ mass distribution 191
10.11$\overline{K}^\circ\phi$ mass spectrum from background subtraction 191
10.12Dalitz plot $m^2_{\overline{K}^\circ\phi}$ vs. $m^2_{\overline{K}^\circ n}$ 192
10.13t' distribution of $\overline{K}^\circ\phi$ 194
10.14Momentum distributions of $\overline{K}^\circ\phi$ final state particles 195
10.15The θ_1 distributions of $\overline{K}^\circ\phi$ 197
10.16The θ_2 distributions of $\overline{K}^\circ\phi$ 198
10.17Acceptance-corrected moments of $\overline{K}^\circ\phi$ 200
10.18Comparison of $K^- K^+$ mass spectrum for real and MC data 204
10.19The resolution of $m_{\overline{K}^\circ\phi}$ as a function of $m_{\overline{K}^\circ\phi}$ 204

11.1 The J^P sum of the $K\omega$ partial waves 213
11.2 The 3^- partial wave 214
11.3 The real and imaginary amplitudes of 2^- and 3^- waves 217
11.4 χ^2 vs σ for 2^- B-W fit 219
11.5 Amplitudes of $J^P = 2^+$ waves 221
11.6 The $|2^+1^+D\rangle$ wave 222
11.7 t' dependence of the $|2^+1^+D\rangle$ amplitude 224
11.8 t' dependence of the $|3^-1^+F\rangle$ 226
11.9 Combinations of moments as functions of $m_{K\phi}$ 229
11.10Decomposition of the $\overline{K}^\circ\phi$ mass spectrum into natural J^P 232
11.11Decomposition of the $\overline{K}^\circ\phi$ mass spectrum into unnatural J^P 233

11.12t' dependence of the $\overline{K}^{\circ}\phi$ partial wave sums 236

12.1 $K_2^*(1430)$ in $K\pi$, $K\omega$ channels 239
12.2 $K_3^*(1780)$ in $K\eta, K\pi$ and $K\omega$ channels 243
12.3 The $q\bar{q}$ level scheme of strange mesons 246

List of Tables

3.1 Momentum thresholds for SLD CRID radiators 20
3.2 Comparison of photocathodes TEA and TMAE 23

5.1 Pressure transients 65

7.1 PDG-suggested $q\bar{q}$ quark-model assignments 91

8.1 The cluster logic signals 115
8.2 The variables in the TOF correction formula. 120

9.1 Mass assignment ambiguity after PID 138
9.2 $K\omega$ cut table 140

10.1 The effect of the event selection on the acceptance 203

11.1 Blatt-Weisskopf barrier factors 210
11.2 The waves used in PWA 211
11.3 The B-W fits to the 2^- waves 218
11.4 The t' analysis of the $K\omega$ partial waves 223
11.5 $|2^+1^+D\rangle$ estimates from mass-dependent and t'-dependent PWA's . 225
11.6 $|3^-1^+F\rangle$ estimates 227
11.7 t' slope parameters of the partial wave sums present in the $\overline{K}^\circ\phi$ system 237

12.1 SU(3) prediction of $K_2^*(1430)$ and $K_3^*(1780)$ decay branching ratios 241
12.2 Branching ratios $(K\rho/K\pi)$ 242

12.3 $K_2^*(1430)$ branching ratios of $K\omega$ final state with respect to $K\rho$ and $K^*\pi$ 242
12.4 $K_3^*(1780)$ branching ratios of $K\omega$ final state with respect to $K\rho$ and $K^*\pi$ 244
12.5 Relative amplitudes of the two $J^P = 2^-$ strange states, $K_2(1773)$ and $K_2(1816)$ 247

A.1 The possible waves in $K\omega$, $K\phi$ systems. 250

Chapter 1

Introduction

In experimental particle physics, we study the basic elements of matter which compose the universe and the fundamental interactions among them. To study the elementary particles and their interactions, it is necessary to probe matter at very short distance scales, currently $\sim 10^{-16} cm$. Then, according to Heisenberg's uncertainty principle, to observe such a short distance scale, we need a large amount of momentum. Due to this, particle physics experiments usually demand bigger and bigger machines as the energy scale of experiment increases. To prepare such big machines, usually high-energy particle accelerators and detectors, it is often necessary for hundreds of physicists to collaborate in one experiment for much longer time scale compared to other physics experiments. For example, the SLD experiment at Stanford Linear Accelerator Center (SLAC) was conceived in 1984, but it was not until the summer of 1992 that SLD began to collect a substantial amount of data for physics analysis.

With the time-scale of high-energy physics experiments becoming longer and longer as the energy frontier goes up, it has become more difficult for a graduate student to follow a single experiment from conception, through design and construction, data-taking and analysis within the typical time-scale of graduate studies. Therefore it has become more common for a student to work for one's thesis in multiple experiments that are in different phases – for example, one in the

design and construction phase and another in the analysis phase – so as to have a broader range of experiences in particle physics experiments within a reasonable time-scale of a graduate study.

I chose to work in two experiments for this thesis emphasizing different aspect in each experiment. Consequently, this thesis consists of two independent parts: development of the Cherenkov Ring Imaging Detector (CRID) system for the SLD experiment; and analysis of data from the LASS spectrometer in E135 experiment to study strange meson spectroscopy.

Part I: CRID Development for SLD

Chapters 2 through 6 constitute the first part of this thesis and describe the works in the development of the SLD CRID system.

SLD is a detector system designed for experiments at the SLAC Linear Collider (SLC) to study high-energy physics related to the production and decay of Z° particles and to test the standard model. CRID is a subsystem of SLD dedicated to charged particle identification. To identify the mass of a particle, both its velocity and momentum need to be determined. In SLD, or other detector systems similarly configured, the momentum of a charged particle produced in the collision is determined by its trajectory as it moves through a magnetic field using drift chambers. To measure the velocities, time-of-flight and/or dE/dx measurements have been used conventionally. These methods, however, can be used for identification only at low momentum. On the other hand, the CRID system as implemented in SLD, can measure charged particle velocities over a very large momentum range with almost 4π solid angle coverage by measuring the angle of emission of the Cherenkov radiation. Using two radiator media, a liquid and a gas, it typically provides $\pi/K/p$ separation up to 30 GeV/c and e/π separation up to 6 GeV/c. The excellent particle identification capability of CRID combined with the high-precision vertex detectors close to a small beam pipe makes SLD very well-designed to study heavy quark systems produced in Z° decay.

In Chapter 2, the principles of Cherenkov ring imaging detectors will be presented. The basic theory of Cherenkov radiation is briefly reviewed, and then its application to high-energy physics experiments in the form of a ring imaging device for particle identification is discussed. The SLD detector which utilizes the CRID system for its main particle identification tool will be briefly described in Chapter 3 to give an idea how a Cherenkov ring imaging system can be actually used in high-energy physics experiments.

As the CRID system is relatively new and very complicated, there are several problems to solve before it is successfully designed, constructed, and fully operational. The problems can be categorized into two sorts: problems of principle and problems of practice.[1] Some of the outstanding problems of principle are:

- choice of radiator;
- choice of photocathode;
- optics scheme;
- detection of single photoelectron;
- photon feedback protection;
- resolution problem – third coordinate readout scheme.

In addition, there are many practical choices to make in realization of the CRID system. A partial list of the practical issues are:

- gas mixture;
- gas purification;
- gas seals and flow;
- operating temperature;
- implementation of electrostatics design;
- gating the multiwire proportional chamber;
- wire aging;
- calibration, monitoring and control.

Some of the issues listed above will be discussed in the next two chapters (chapters 4 and 5). The work presented in chapter 4 is related to one of the

problems of principle – optimizing the third coordinate measurement resolution. For this problem, it is essential to minimize the noise in the CRID preamplifiers. The design and performance of the prototype low-noise CRID preamplifiers are discussed. Some problems of practice, related to the CRID gas system and the monitoring and control system, will be discussed in Chapter 5.

The performances of CRID during the engineering and physics runs through September 1992 will be reviewed in Chapter 6 to show how such a complicated device as a CRID performed in the real life.

Part II: Strange Meson Spectroscopy at 11 GeV/c

The results from the LASS work is presented in the second part of the thesis (Part II), in Chapters 7 through 12. The main focus is on the analysis of high-statistics data obtained in the SLAC E-135 experiment. Especially, two reactions from E-135 are analyzed to investigate new spectroscopic structures in the strange meson system:

$$K^- p \rightarrow K^- \pi^+ \pi^- \pi^0 p$$
$$K^- p \rightarrow \overline{K}^0 K^+ K^- n$$

Chapter 7 provides a more detailed introduction to Part II.

Chapter 2

Principles of Cherenkov Ring Imaging

2.1 Cherenkov Radiation

When a charged particle passes through a medium with a speed greater than the phase velocity of light in that medium, there is emission of Cherenkov radiation. This phenomenon was first observed by P. Cherenkov [2] in 1934, and was later theoretically interpreted by Frank and Tamm[3] in 1937. Unlike bremsstrahlung which is emitted by the moving charge itself, the Cherenkov radiation is emitted by the medium under the action of the field of the particle moving in it. The intense electric field set up by the high-speed charged particle polarizes the medium, which relaxes to equilibrium by radiating an electromagnetic wave.

Considering the field components in the far region, the angle θ_c of emission of Cherenkov radiation relative to the velocity of the particle is found

$$\cos\theta_c = \frac{1}{\beta n(\omega)} , \tag{2.1}$$

where $\beta = v/c$, the velocity of the particle in unit of the light speed and $n(\omega)$ is the index of refraction of the medium at frequency ω. Therefore if we know $n(\omega)$ for a given medium, the measurement of θ_c gives the velocity of the particle. Equa-

tion 2.1 with $|\cos\theta| \leq 1$ sets the threshold velocity to emit Cherenkov radiation of frequency ω : $v_{\rm th} = c/n(\omega)$. There are two ways that Cherenkov radiation can be used for particle identification: either as a threshold counter or as a ring imaging detector.

Threshold counter Two particles of the same momentum p but different masses, therefore different velocities, are distinguishable if the velocity of the lighter one is above the threshold and emits Cherenkov radiation while that of the heavier one is below $v_{\rm th}$. This can provide particle identification only over a limited momentum range. For instance, π/K separation is possible only if the momentum is above π threshold but below K threshold.

Ring imaging detector This method was proposed in 1977 by Ypsilantis and Seguinot[4] in a technical realization of an earlier idea of Roberts[5]. The angle of Cherenkov radiation is directly measured, which is converted to velocity by Eq 2.1. In this setup, π/K separation is still possible above K threshold until the Cherenkov angle saturates. Equation 2.1 shows that in a given medium of index n the Cherenkov angle reaches an asymptotic value $\cos^{-1}(\frac{1}{n})$. There are several high-energy physics experiments equipped with ring imaging Cherenkov devices including E605 at FNAL[6], OMEGA spectrometer at CERN[7], DELPHI at LEP[8], and SLD at SLAC[9].

The energy radiated per unit frequency interval per unit path length is given by[10]

$$\frac{d^2E}{dxd\omega} = \frac{e^2\omega}{c^2}\left(1 - \frac{1}{\beta^2 n^2(\omega)}\right) ,$$

where e is the charge of the moving particle. Since the energy carried by each photon is $\hbar\omega$, the number of photons radiated over the radiating path length L is

$$\frac{dN}{d\omega} = \frac{e^2 L}{c^2\hbar}\left(1 - \frac{1}{\beta^2 n^2(\omega)}\right) .$$

Using the fine structure constant $\alpha = e^2/(\hbar c)$ and integrating over the frequency domain, the number of emitted Cherenkov photons is

$$N = \frac{L\alpha}{c} \int_{\beta n(\omega)>1} \left(1 - \frac{1}{\beta^2 n^2(\omega)}\right) d\omega \ .$$

In reality, it is important to know the number of photons that can be actually detected. The expected number can be used to set a scale for the required efficiency of the CRID and the number of emitted photons can be used to assist in particle identification. Since practical photon detectors are not perfectly efficient, the efficiency of the detector must be taken into account to determine the number of photons actually observed. Denoting the efficiency which is usually a function of frequency as $\epsilon(\omega)$, the number of observed photons is:

$$\begin{aligned} N_d &= \frac{L\alpha}{c} \int_{\beta n(\omega)>1} \epsilon(\omega) \left(1 - \frac{1}{\beta^2 n^2(\omega)}\right) d\omega \\ &= 2\pi L\alpha \int_{\beta n(\lambda)>1} \epsilon(\lambda) \left(1 - \frac{1}{\beta^2 n^2(\lambda)}\right) \frac{d\lambda}{\lambda^2} \end{aligned}$$

In the second line, the integrand is expressed as a function of wavelength. The wavelength distribution has a $1/\lambda^2$ dependence and so is peaked towards short wavelengths. In general, the Cherenkov emission region extends to somewhat below the regions of anomalous dispersion. Therefore the majority of Cherenkov photons are emitted in the far UV region, which places many constraints on the materials and construction techniques that are used in the CRID. If the light is emitted in a region where $n(\omega)$ is approximately constant, *i.e.*, away from an absorption band, the expression for the number of photons can be rewritten as

$$N = N_\circ L \sin^2 \theta_c \tag{2.2}$$

where

$$N_\circ = \frac{\alpha}{c} \int \epsilon(\omega) d\omega \ .$$

The factor $N_\circ$ determines the performance of the detector; the larger $N_\circ$, the device is more sensitive and has higher efficiency.

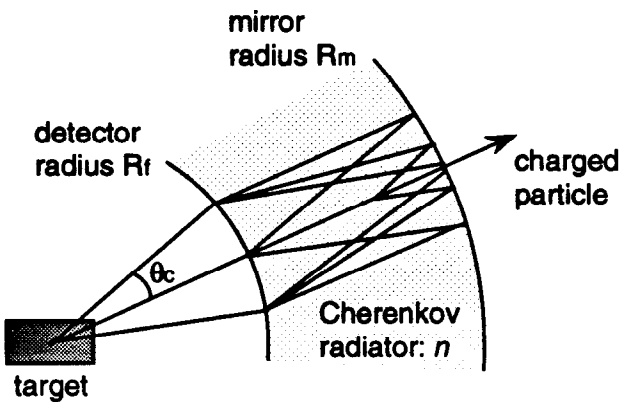

Figure 2.1: A simple ring imaging system.

2.2 Ring Imaging Devices

Once we have Cherenkov radiation inside the radiator volume, we need optical schemes to collect the emitted photons into a ring image in the focal plane so that we can measure the angle of emission. In this section, two types of ring imaging schemes are discussed, which are actually used in the SLD CRID. One is mirror focusing, used in the gas radiator, and the other is proximity focusing used in the liquid radiator.

2.2.1 Mirror Focusing

In a simple ring imaging device, a mirror is used to focus the Cherenkov photons to a ring at its focal plane, where a position sensitive photon detector determines the radius of the ring. Consider a setup shown in Fig 2.1. From the interaction point at the center of the spherical mirror, a relativistic particle is normally incident on a spherical mirror of radius of curvature R_m. The mirror is immersed in a volume of gas or liquid radiator, with index of refraction n, so that when the incident particle has speed larger than the phase velocity of light in that medium, Cherenkov radiation is emitted. The emitted Cherenkov photons are focussed to

a ring-shaped image on the focal plane, a sphere of radius R_f. A photosensitive detector at the focal plane converts the Cherenkov light into signal electrons and then measures the position of conversion in order to reconstruct the ring. If the angle of emission is small, $R_f \approx R_m/2$. The radius r of the ring image gives the Cherenkov angle as

$$r = \frac{R_m}{2} \tan\theta_c \ .$$

In general, incident particles will not be normal to the mirrors. Therefore the 'rings' may not be necessarily circles, but nonetheless form unique shapes in the focal plane. Still they can be analyzed, and so in principle do not affect the power of this method.

In practice, the images do not form smooth curves in the focal plane due to various experimental errors. The Cherenkov angle measurement becomes statistical averaging: it is necessary to fit the few points which comprise the image to a presumed ring shape. Therefore, the larger the number of detected photons, the better the measurement. Since the Cherenkov radiators have finite path lengths, the number of photons emitted is limited (Eq. 2.2). As a result, this method requires a large volume to detect an adequate number of photons per ring. For the SLD CRID, for example, a radiating length of about 50 cm provides approximately 10 detected photons to be used to reconstruct a gas ring to determine the angle θ_c.

Gas phase Cherenkov radiators usually use this imaging system. A typical gas radiator will have an index of refraction of the order of 1.0016, which implies $v_{\rm th} \approx 0.9984\ c$. These radiators work well for separating particles with very high momenta.

2.2.2 Proximity Focusing

Since the threshold velocity for Cherenkov radiation is $v_{\rm th} = 1/n$, to separate particles of low momenta, radiators with higher n are needed. For this purpose, liquid radiators (typically, $n \approx 1.3$ leading to a threshold velocity of $\beta_t \approx 0.7$)

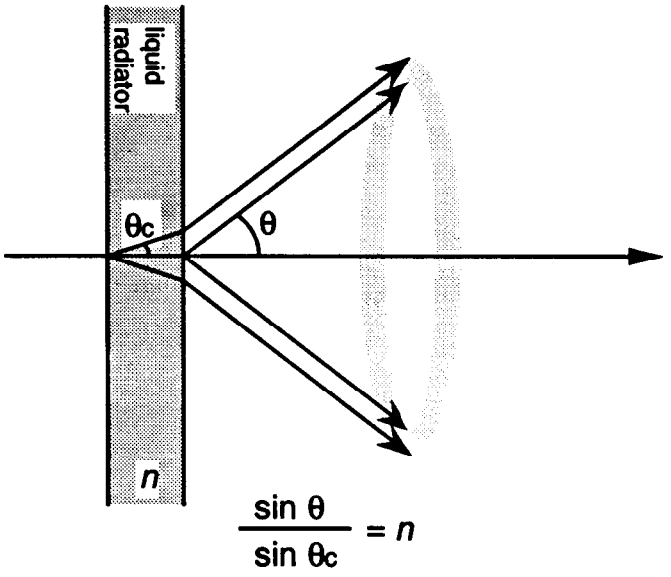

Figure 2.2: A proximity focusing technique.

are used. As n goes higher, the maximum Cherenkov angles become larger and this mirror-focusing method is no longer practical. Instead, a proximity focusing technique is used.

Figure 2.2 shows the basic scheme of a proximity focusing device. The photons emitted at an angle θ_c in a liquid radiator exit the radiator volume at an angle significantly larger than θ_c, because of refraction. The liquid radiator volume is separated by boundary windows from the surrounding low n gas environment. After leaving the radiator volume, the photons are allowed to drift undisturbed until they encounter the detector plane where they are converted to signal electrons as in the gas radiator case. Although there is no active focusing in this method, a ring is approximately formed if the radiator thickness is sufficiently small compared to the spacing between the radiator and the detector plane. The expected number of emitted photons is proportional to the thickness of the radiator. The finite thickness of the radiator, however, contributes a "flat-top" error on the radius of the ring, proportional to that thickness. Thus, the thickness of the radiator

and the spacing from the detector are the important determining elements for the fractional error on the radius of the ring of signal electrons and the expected number of emitted Cherenkov photons.

The angular resolving power of such a device is typically not as good as a gaseous device, but it is very useful nonetheless as it enables good particle identification in a momentum range where gas radiators are not sensitive. It is easily installed into the same detector volume as the gaseous device, so that the two combined, complementary devices provide particle identification covering most of the available phase space in the environment of the SLD experiment.

Chapter 3

SLD Cherenkov Ring Imaging Detector

3.1 SLD Overview

SLD is a detector designed to study e^+e^- collisions at $\sqrt{s} = m_{Z^\circ}$ at the SLAC Linear Collider (SLC). Its main physics goal is to test the standard model and explore new physics in the energy region near m_{Z° through production and decay of Z°'s. More specifically, the physics goals of SLD include:

- studies of electroweak interaction in Z° decay – $\sin^2\theta_W$ measurements primarily through left-right asymmetry measurements;
- QCD studies through hadronic decays of Z°;
- heavy quark physics – b decays, spectroscopy of B mesons, etc.; and
- searches for new particles, new physics.

Figures 3.1 and 3.2 provide isometric and sectional views of the SLD detector. SLD is designed to cover almost 4π solid angle* around the SLC interaction point.

*At the time of this writing, the construction of endcap CRID is not complete. All other components are complete and operational.

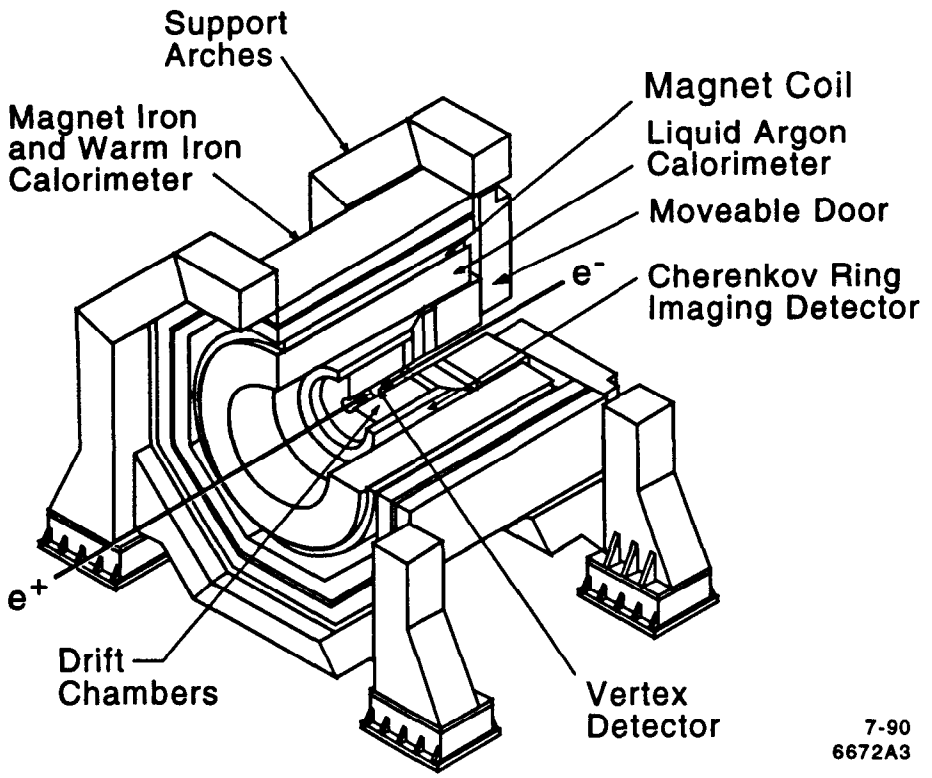

Figure 3.1: Isometric view of the SLD detector

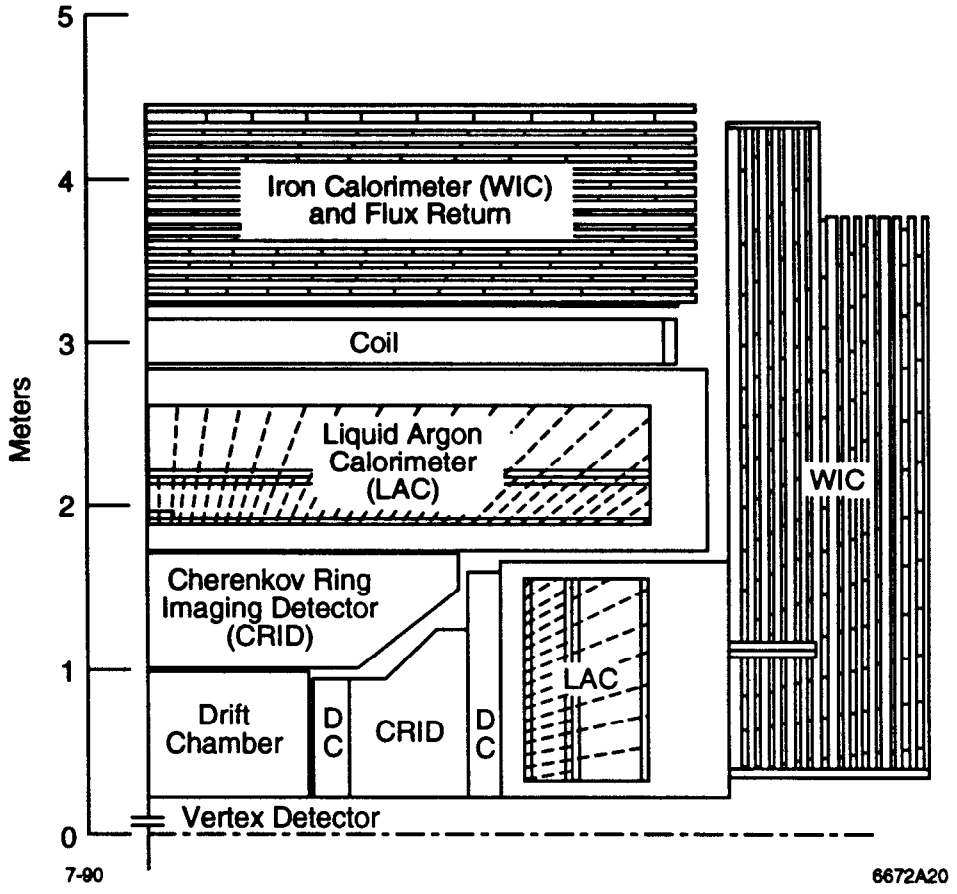

Figure 3.2: Sectional view of the SLD detector

It is composed of subsystems of specialized detectors which include (moving from the beamline and outward) a CCD vertex detector to measure the secondary vertices with high resolution, endcap and central drift chambers for track momentum measurement, barrel and endcap Cherenkov Ring Imaging Detectors (CRID) for particle identification, a liquid argon calorimeter (LAC) for energy measurement using hadronic and EM calorimetry, and a warm iron calorimeter (WIC) for muon detection. All subsystems except the WIC are located inside a 0.6 T solenoidal magnet. The WIC is situated outside the magnet and utilizes the magnet's iron flux return.

3.2 Motivation for CRID

For some of the physics topics that SLD intends to study, it is essential to identify final state particles over a large momentum range. SLD depends on the CRID for this task, especially to identify the long-lived hadrons, $\pi/K/p$, up to 30 GeV/c. The following examples[11] show the use of hadron identification in flavor-tagging of jets and in analysis of heavy quark decays.

Jet flavor-tagging A substantial fraction of Z°'s decay into $q\bar{q}$ pairs. Because of the large m_{Z°, quarks from Z° decays are relativistic and fragment into many mesons and baryons. In the detector these fragment particles will be observed within a space cone around the direction of the initial quark. The collection of many particles in this cone is called a jet. For some of the physics topics that SLD intends to study, it is essential to distinguish the quark flavors of jets in an event. It is sometimes possible to identify a jet of a b quark from event shapes. A clear identification of the other hadronic jets, however, is much harder from event shapes alone. A particle identification device, such as a CRID, can help distinguish different kinds of jets. For instance, if a kaon is identified within a jet with large momentum relative to the jet energy, it is a signature of a primary s-quark production. With jet flavor-tagging, it is possible to examine the angular and energy distributions of $q\bar{q}$ interactions for different quarks and check the QCD-based standard model of strong interactions.

Heavy quark decays A careful study of all possible decay modes of a heavy flavor particle provides a test of the standard model. Hadrons of heavy flavor often decay by weak interaction through the cascade: $(t \rightarrow) b \rightarrow c \rightarrow s$. As a result, a kaon is often produced in the decays of heavy flavor mesons and baryons. Hadron identification is especially useful to study decays of heavy flavors. For instance, the π/K identification is essential to separate B_s events from B_d events. Measuring the mixing of $B_d\bar{B}_d$ and that of $B_s\bar{B}_s$ separately using π/K identification helps determine CKM matrix elements.

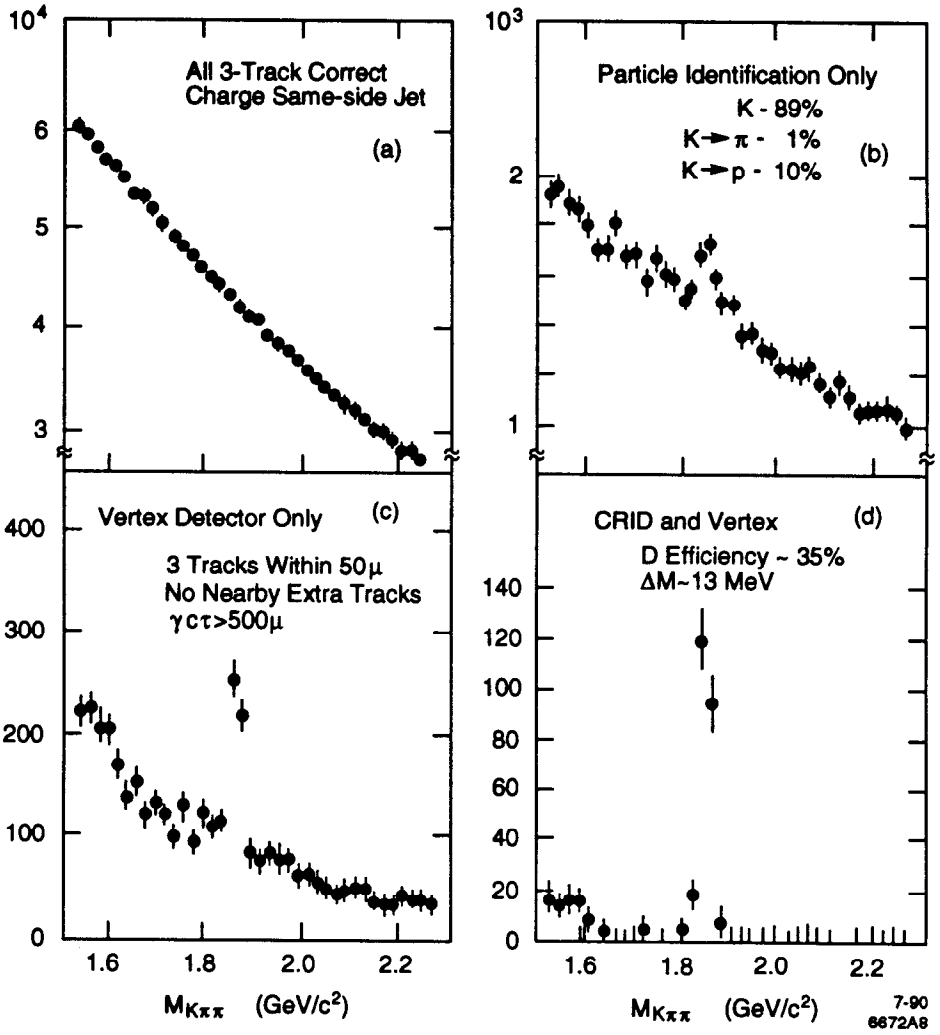

Figure 3.3: Mass distribution for $K\pi\pi$ combinations with total charge ± 1, from Monte Carlo Z° decays: (a) all appropriately charged combinations; (b) π/K separated using CRID; (c) separated secondary vertex using vertex detector without π/K separation; (d) both CRID and vertex detector are used. A very clean D signal is seen.

The vertex detector also plays a very important role for SLD in the heavy flavor physics and complements the CRID extremely well. Figure 3.3 shows how the information from CRID, combined with good vertex information, can provide flavor tagging of heavy quark systems with extremely low backgrounds and quite good efficiency. The plot shows the invariant mass distribution for $K\pi\pi$ combinations from a Monte Carlo study of Z° decays. With both CRID and vertex detector used, a clean signal of $D \rightarrow K\pi\pi$ is seen (Fig 3.3(d)).

3.3 Components of CRID

The SLD CRID system consists of two major parts; a barrel CRID and an endcap CRID. At the time of this writing, the barrel CRID is complete and operational. The endcap CRID is currently being commissioned. Only the barrel CRID will be described in detail and my work to be described in the next two chapters was specific to the barrel CRID. While the endcap CRID is conceptually very similar and uses many of the same components, it differs considerably in details, especially for the effect of magnetic field. Fig 3.4 shows a sectional view of the barrel CRID. The primary components are two radiators, liquid and gas, a drift box which is a time projection chamber (TPC) with a proportional wire chamber detector and readout electronics, and mirrors. Each of these will be discussed below.

3.3.1 Cherenkov Radiator

In the SLD environment where the final state particles can have momenta as high as $\sim$ 45 GeV/c (half of m_{Z°), it is important to provide good particle identification over a wide momentum range. For this purpose, SLD uses a combination of two different radiator materials for CRID; a liquid, Perfluoro-n-hexane (C_6F_{14}), and a gas, Perfluoro-n-pentane (C_5F_{12}). The liquid radiator, with $n = 1.277$ at a wavelength of 190 nm, is used to cover the low momentum range, while the gas radiator, with $n = 1.00173$ at 190 nm, covers higher momenta. Table 3.1 lists the

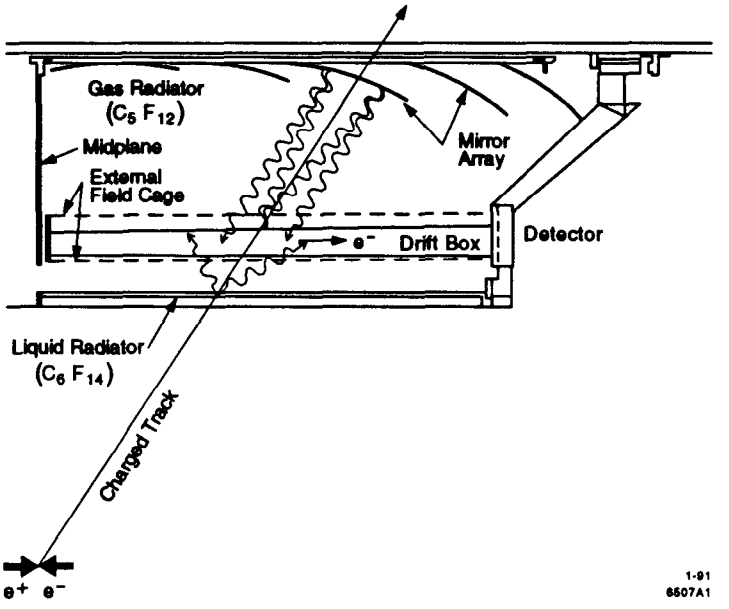

Figure 3.4: Barrel CRID sectional view

momentum thresholds for particles e, μ, π, K and p in both the liquid and gas radiators.

Several criteria were considered in choosing the radiator materials for CRID. The indices of refraction for liquid and gas were chosen so that there is no gap in momentum coverage. Figure 3.5 shows the particle separation ability of the CRID as a function of momentum. The combination of the two radiators provides better than 3σ separation for e/π up to 7 GeV/c, for π/K from 230 MeV/c to 28.8 GeV/c. The K/p separation is expected to be better than 3σ from 800 MeV/c to 46.2 GeV/c except for a region near 7 GeV/c where the separation goes down to $\sim 2\sigma$. In addition, the materials are chosen because they are compatible with other materials in the CRID, transparent for the UV Cherenkov photons, and low in chromatic dispersion. Safety is also considered for the gas radiator. Otherwise, the flammable hydrocarbons would have been as acceptable.

The two radiators use different focusing methods. Since the liquid radiator has

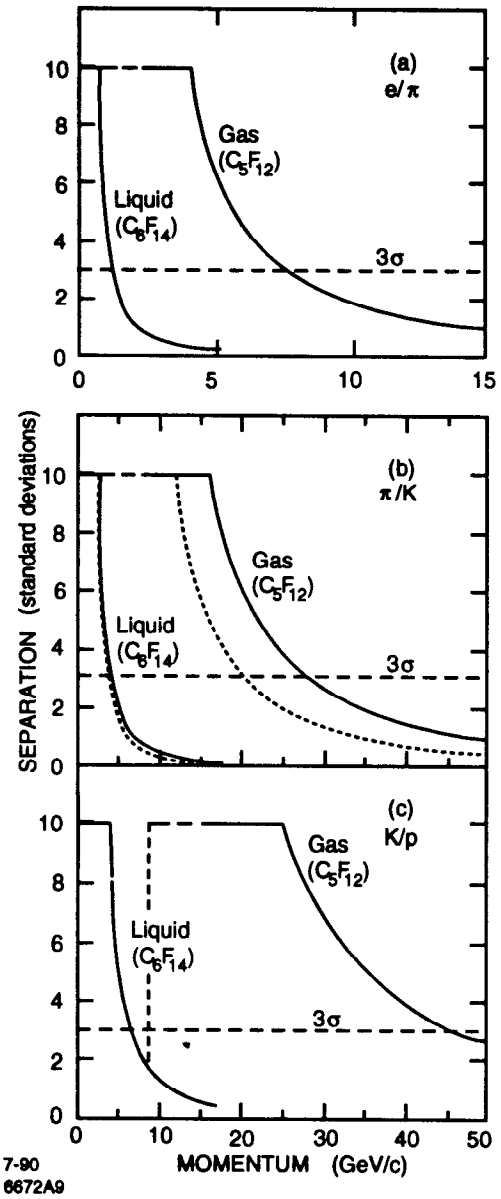

Figure 3.5: Particle separation ability of the CRID as a function of momentum: (a) e/π; (b)π/K; and (c)K/p. Horizontal dashed lines indicate where the heavier particle is below threshold. Dotted line in (b) is for doubled measurement errors.

Table 3.1: Momentum thresholds for SLD CRID liquid and gas radiators for particles e, μ, π, K and p.

Particles	Liquid (C_6F_{14}) $n = 1.277$	Gas (C_5F_{12}) $n = 1.00173$
e	0.64 MeV/c	8.7 MeV/c
μ	0.13 GeV/c	1.8 GeV/c
π	0.18 GeV/c	2.4 GeV/c
K	0.62 GeV/c	8.4 GeV/c
p	1.20 GeV/c	16.0 GeV/c

a fairly large index of refraction, it has a large Cherenkov angle: ($\theta_{\min} = \cos^{-1}\frac{1}{n} \approx 38°$). Since the number of produced photons is proportional to $L \times \sin^2\theta_c$ (eq 2.2), larger Cherenkov angle implies that a desirable number of photons can be obtained with a relatively short pathlength (L). Therefore the liquid radiator can be made thin ($\sim$ 1 cm) and the photons from it make a good ring without further focusing. Only proximity focusing is used. The gas radiator, on the other hand, has a significant pathlength to make up for the small Cherenkov angle. Because of the large pathlength, an optical focusing is needed. The photons from the gas radiator are reflected and focused by the mirrors placed at the outer circumference of the CRID.

3.3.2 Drift Box

The Cherenkov photons are detected in the CRID photon detector system. It has two basic parts: the drift boxes and the electron detectors. Figure 3.6 shows a CRID drift box/detector combination. A CRID drift box is essentially a time-projection-chamber (TPC). The ring of photons from the gas or liquid radiators enter the drift box through the boundary window. The gaseous photocathode

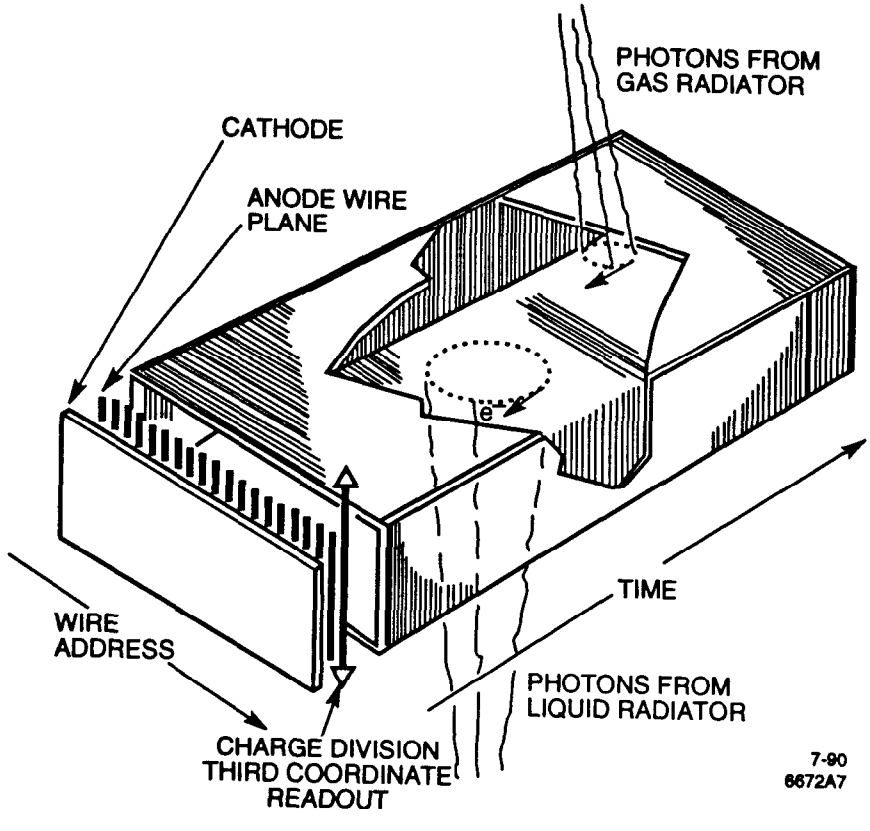

Figure 3.6: Drift box and detector for barrel CRID

absorbs the photons and may release electrons. These photoelectrons drift in a constant electric field ($\approx$ 400 V/cm) to the end region of the box, where they are detected by a multiwire proportional chamber (MWPC). The signal formed by each photoelectron is read out on only one anode sense wire. The point of the photoelectron conversion is measured in three coordinates from the drift time, the wire address, and the charge division along the anode sense wire. These three coordinates are measured to $\sim$ 1 mm accuracy. More on the resolution requirement of CRID will be discussed in chapter 4.

There are 40 drift boxes in the barrel CRID; 20 in the north sector, and 20 in the south. The dimensions of each box is 1.268 m long and 30.7 cm wide. The thickness is tapered from 9.2 cm at the end adjacent to the sense wire plane, to 5.6 cm at the opposite end. This taper helps prevent transverse electron diffusion from causing losses near the faces of the drift box. Metal traces made of etched Cu-Be sheets are placed on the inner and outer surfaces of the quartz faces and sidewalls every 3.175 mm. These traces, whose potential is set by a resistor ladder, shape the field inside the drift box. An additional field cage of wires encloses the box, to further control the field shape inside the box and to control the corona problems at high-voltage end of the box.

The drift boxes are filled with a drift gas mixed with a gaseous photocathode. The photocathode is a very important element of the ring imaging devices. It absorbs a photon and emits a photoelectron with a certain probability, called the quantum efficiency. A high quantum efficiency is critical to have a large fraction of photons convert within the drift box. Since most of the Cherenkov photons are emitted in the far UV, high quantum efficiency in the far UV region is required. In recent years only two photoionizing gases have been widely used: triethylamine (TEA) and tetrakis-dimethylamino-ethylene (TMAE). Table 3.2 lists and contrasts their properties. In SLD, TMAE is chosen because its spectral range is compatible with the readily available quartz (fused silica) windows, and it puts a relatively less stringent demand on the cleanliness of the drift gas. TMAE has a high quantum efficiency; higher than 10 % for wavelengths shorter than 210 nm and reaching

Table 3.2: Comparison of photocathodes TEA and TMAE

	TEA	TMAE
UV Absorption Length	1 mm	$(15-40)$ mm depending on temp.
High edge of wavelength window	~ 150 nm	~ 195 nm
Requirement in O_2, H_2O	≤ 0.2 ppm	≤ 20 ppm
Window material	CaF	Quartz

50 % below 180 nm. While TEA requires maintaining a less than 200 ppb of oxygen and water vapor in the gas, TMAE allows the contamination up to 20 ppm. The disadvantages of TMAE are its low vapor pressure which results in a long Cherenkov photon absorption length, and the highly electronegative contamination (TMO: tetra-methyl-oxamide) that comes with the commercially provided TMAE. Commercially available TMAE must be carefully cleaned before use, in order to remove contaminants which would otherwise ruin the electron lifetime.

For a drift gas to be mixed with TMAE, pure ethane (C_2H_6) has been chosen after the following considerations:

a. UV transparency: The absorption of UV Cherenkov photons before converting to electrons is a direct loss of data.

b. Non-electronegativity: The gas must be non-electronegative so that the photoelectrons can drift from the point of origin to the electron detector with minimal loss. A single electron should be able to travel the full length of the box at least 80 % of the time, corresponding to an electron lifetime in the gas of at least 150 μsec, or approximately 5 times the box length of 1.27 m. In the end, the electron lifetime will be the measure of performance for the CRID.

c. Inertness in the presence of the TMAE photocathode: No compounds which are either UV opaque or electronegative must be produced when the TMAE is mixed with the gas by bubbling.

d. Little photon feedback: An electron produced from a Cherenkov photon initiates an avalanche around a wire in the classic gas amplification process. The chamber gas, left in an excited state by the avalanche, de-excites and emits photons back to the photocathode – the TMAE-doped drift gas volume. It subsequently photoionizes the TMAE and reinitiates secondary avalanches. Some potentially interesting combinations of noble gases fail this condition as they are shown to produce too many avalanches[12].

e. Drift velocity stability: To measure the drift distance with an accuracy of 1 mm, the drift velocity must be known to 0.1 % over the full drift volume. This implies that either the drift velocity needs to be fairly insensitive to samll variations in the electric field (a saturated gas), or very accurate on-line calibration of the drift velocity must be made. The SLD CRID uses unsaturated ethane as the drift gas, operating in the linear region. The drift velocity is continuously monitored by a UV fiber optic system described in a later section.

f. Good gas gain: The drift gas has to maintain a high gas gain for a good pulse-height spectrum. On the other hand, since the light output from the avalanche grows exponentially as the chamber gain increases beyond plateau, the gas gain is limited to $\sim 2 \times 10^5$.

The concentration of TMAE in the drift gas, which is determined by the temperature of the liquid TMAE through which the drift gas is bubbled, is set high (28 °C) to have the absorption length for Cherenkov photons short compared to the thickness of the drift box. This is to assure that a high percentage of photons be converted before they exit the drift box. The concentration should not be too high, however, or most photons would convert very near the walls of the box.

Near the surfaces of the box, the electrostatic effects can alter the trajectories of photoelectrons and cause losses and distortions.

3.3.3 Mirrors

The gas radiator C_5F_{12} is transparent only for light of wavelengths longer than 165 nm, while the photocathode TMAE has a significant quantum efficiency only at wavelengths shorter than 220 nm. In order to detect as many Cherenkov photons from the gas radiator as possible within the constraint of a reasonable cost, it is necessary to require the mirrors to have a reflectivity higher than 80 % in the range of 180 - 220 nm. In addition, they need to have both low distortion and good surface finish. The focal properties and surface quality of mirrors suitable for CRID are not as demanding as those for an astronomical mirror, but are difficult to maintain in large quantities with thin mirrors at reasonable cost.

Each drift box of CRID uses 10 mirrors of 5 different shapes (each pointing to a different position on a drift box) in order to fully cover the solid angle for each box. This requires a total of 400 mirrors for the barrel CRID. Each mirror is produced using a 6 mm thick glass blank and is coated with 80 nm of ultrahigh-purity aluminum and 40 nm of magnesium fluoride (MgF_2). Its focal length is approximately 50 cm to match the available gas radiating path length. Details about the production of the mirrors are reported elsewhere[13].

3.3.4 Electron Detector

The electron detectors consist of anode sense wires, cathodes, a blinding structure, guide wires, and readout electronics. Each drift box of the barrel CRID has 93 sense wires on a 3.175 mm pitch. The single photoelectron drifts to the detector in a constant electric field. At the detector, a strong non-uniform electric field is established within a specialized multiwire proportional chamber, consisting of a plane of anode sense wires separated by the "U-shaped" cathodes, as shown in Fig 3.7.

The "U-shaped" cathode and blinding structure are devised to guide the photoelectron to a sense wire and to prevent photons produced in the avalanche from causing photon feedback. The cathodes are made of a single piece of aluminum machined to specification on a digitally controlled mill. They are nickel-coated to minimize oxidation and to reduce the secondary emission. The cathode-to-anode potential is set at -1.7 kV to establish the correct gas amplification. The blinding structures are made of five layers of etched copper-beryllium sheets, each 254 μm thick. It establishes the fieldlines from the drift box to the anode sense wires (Fig 3.7). The avalanche-induced photons are quickly absorbed by these layers to reduce photon feedback. In the CRID geometry, photon feedback has been measured to be approximately 1 %. On the other hand, an unblinded structure has been measured to produce 6 - 8 times more photon feedback[14].

In front of the first blind, there is a layer of 100μm Cu-Be wires. This wire plane can serve as a gate to prevent background electrons from reaching the anode and avalanche-produced positive ions from entering the drift volume. In typical SLD operation, the gate is opened (-4.2 kV) after each e^+e^- crossing and held open for about 50 μsec to allow electrons drifting the full length of the box to arrive at the detector. It is then closed by applying $\pm$350 V on alternate wires until the next beam crossing.

3.3.5 Data Acquisition

Figure 3.8 shows a block diagram of the data acquisition for one CRID sense wire. To accommodate charge division, both ends of the anode sense wires are read out into separate preamplifiers. Every wire is connected to two waveform digitizer channels, one for each end. Each channel consists of a preamplifier, analog storage, digitizer, and calibration circuitry for channel-to-channel gain and pedestal variations.

The CRID preamplifier is designed as a single-channel hybrid [15] using a low-noise JFET, followed by an analog semicustom integrated circuit. More on the CRID preamplifier will be discussed in chapter 4.

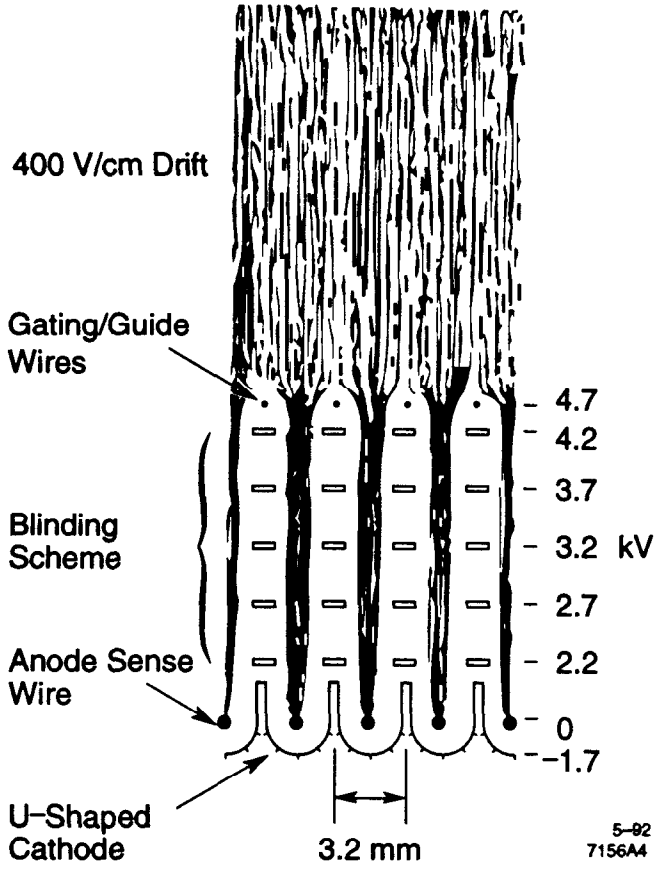

Figure 3.7: A schematic of the CRID single electron detector region.

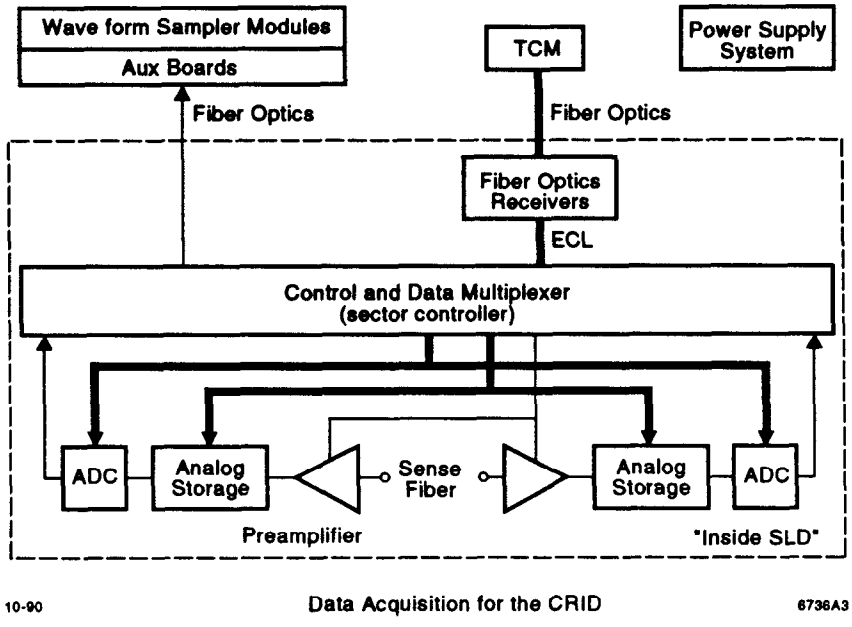

Figure 3.8: Data acquisition for CRID

On each beam crossing, the output of each preamplifier is sent to a storage unit containing two analog sample-and-hold chips, each capable of holding 256 time samples for a total of 512. These chips are called the hybrid analog memory units (HAMU). The HAMU samples are digitized in the 12-bit analog to digital converters (ADC). When an event trigger occurs, the digitized data from ADC's are multiplexed and transmitted via fiber optics to the SLD FASTBUS system for analysis.

3.3.6 Monitoring and Control

There are two kinds of monitoring in SLD; data monitoring and slow monitoring. The former is based on the normal data stream from the detector, and the latter obtained from other sources (e.g. CAMAC).

The data monitoring in CRID includes monitoring the electron drift velocity and drift path distortions, and calibrating the charge division. A UV fiber optic

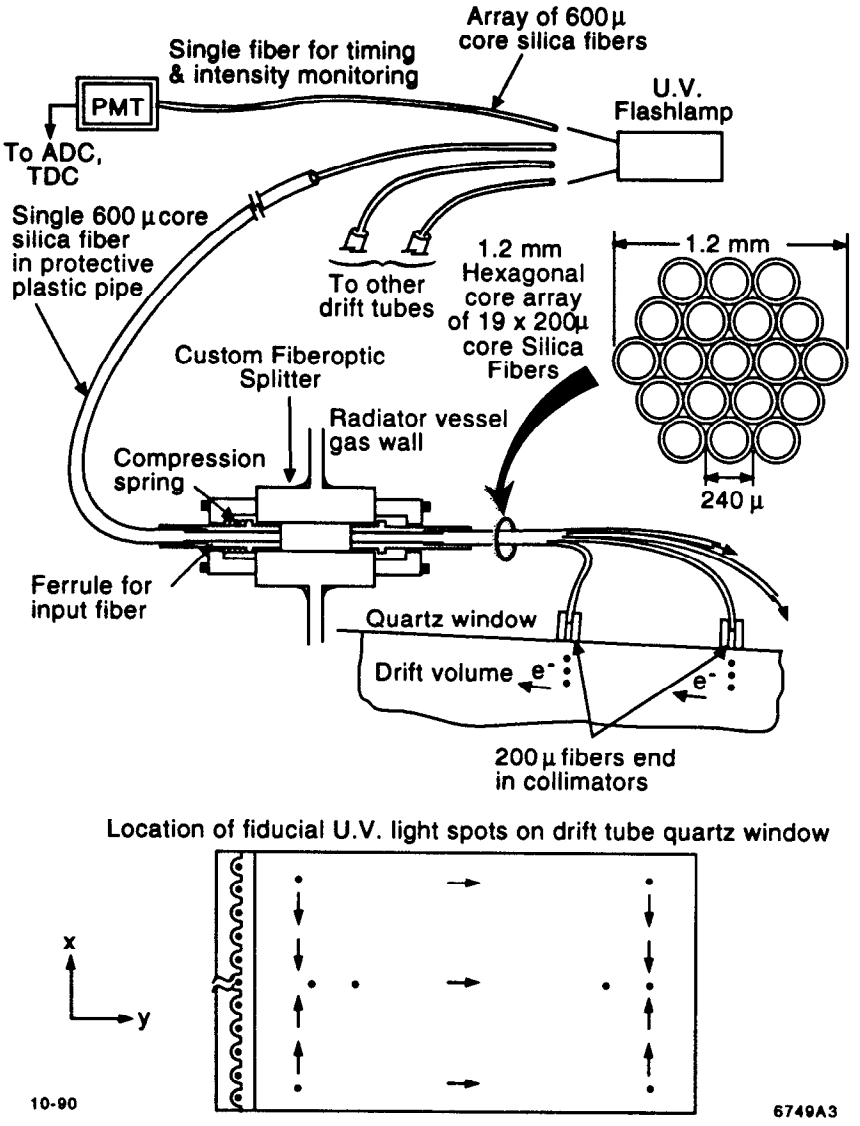

Figure 3.9: CRID UV fiber system: (a) The UV source and fiber-optic light distribution system for the injection of fiducial light in each drift box; and (b) the location of the fiducial UV light spots on the drift box

system[16] is used for this purpose. In this system, a UV flashlamp illuminates a set of optical fiber bundles which transmit the UV light signal to the drift boxes. The fiber pulses provide fiducial markings in the data. Nineteen fibers are connected to each drift box. Figure 3.9 shows the UV source and fiber distribution system, and the location of the UV light spots on the drift box.

Slow monitoring with an appropriate control system is crucial for a long-term, stable CRID operation. For the barrel CRID, slow monitoring includes monitoring temperature, heater status (ON/OFF), gas mixture, oxygen and water concentration, pressure, flow rates, UV transparency, electron lifetime, and high voltages[17]. Control is provided for valve positions, UV monochromator, electron lifetime monitor, heaters, and high voltage. All critical controls, e.g. valve positions, do not depend on software to protect from disaster states caused by computer failures. Instead, hardware has been built to ensure the safety of critical control parts. More details on slow monitoring and control related to the CRID gas system will be described in chapter 5.

Chapter 4

Low-noise Preamplifier for CRID

This chapter will describe the low-noise preamplifier used for single electron detection in the SLD CRID. The requirement for low-noise in CRID is presented in section 4.1. A preamplifier using an FET was developed and tested. Section 4.2 describes a model for the noise in the FET circuit. This model is compared with the actual noise measurements in section 4.3. The measurement shows good noise ($\sim$ 500 electrons rms) and linearity performance for the preamps.

4.1 Low-noise Requirement for CRID Preamplifier

For optimum performance of the CRID, it must reconstruct the position of the photolelectron conversion in all three dimensions with good spatial resolutions. Although many of the errors inherent to the Cherenkov angle measurement have already been reduced by careful choice of geometry and detector segmentation, there are other sources of error such as diffusion, chromatic aberration, and momentum smearing which contribute an irreducible total error of approximately 1 mm to the spatial resolution. Thus, there is little to be gained by reducing other sources of error significantly below this value.

Two coordinates of the point of origin of the photoelectron are measured by the

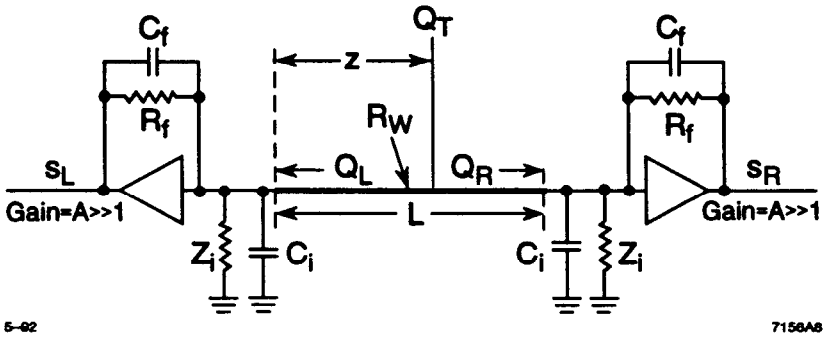

Figure 4.1: The charge division technique.

wire address at which the electron is detected and its associated drift time. The CRID proportional chamber has a wire spacing of 3.175 mm, corresponding to a resolution $\sigma_x = 3.175/\sqrt{12} = 0.92$ (mm). The maximum drift distance of barrel CRID is 1268 mm. The use of two AMU chips per channel gives a total of 512 segmentation in the drift time measurement equivalent to $\sim$ 2.5 mm segmentation in the drift distance, thus resulting in a tophat error of $\sim$ 0.7 mm. This gives essentially the same resolution as the one due to wire spacing.

We also need a similar dimension of resolution ($\sim$ 1 mm) in the third coordinate measurements, which correspond to the conversion depth of the photon within the drift box. The third coordinate is measured using the charge division along the anode sense wire of the proportional chamber. The wires are resistive carbon filaments of 7 μm in diameter, 10 cm long. Figure 4.1 illustrates the charge division technique. Each end of the anode sense wires is connected to the input of a separate operational amplifier. Each amplifier will see a different amount of charge depending on the point of avalanche generation. If we define

$$A_Q = \frac{Q_R - Q_L}{Q_R + Q_L}$$

as the charge asymmetry for a charge division, the hit position z on the sense wire can be measured by

$$z = \frac{L}{2}(1 + A_Q) \ ,$$

where L is the length of the wire.

In general, the spatial resolution in charge division due to a noise current i_n is given by:

$$\begin{aligned} \frac{\Delta z}{L} &= \frac{i_n}{i_0}\sqrt{(\frac{L-z}{L})^2+(\frac{z}{L})^2} \\ &= \frac{i_n}{i_0}\sqrt{1-\frac{2z}{L}+2(\frac{z}{L})^2} \\ &\leq \frac{i_n}{i_0} \end{aligned}$$

where z is the position along the wire ($0 \leq z \leq L$), and i_0 is the signal current. As can be seen, the resolution is best at the center and worst by a factor of $\sqrt{2}$ at the ends of the wire. Since the wires are 10 cm long, we need to achieve a 1 % charge-division resolution for a 1 mm spatial resolution. The gas gain in the proportional chamber was determined such that an average photoelectron signal will produce 2×10^5 electrons. Therefore, to obtain a 1 % resolution, which requires a signal-to-noise ratio of at least 100:1, implies that the maximum acceptable noise level is below 2000 electrons (rms). In practice, a substantial fraction of the signals will be smaller than the average and it is important to keep the noise below the nominal 2000 electrons.

4.2 FET amplifier noise model

Because of the progressive amplification by the successive stages of amplifiers, most of the noise in the output comes from the first stage and it is essential to choose a low-noise front-end for the CRID preamp system. Field Effect Transistors (FET) are commonly used for low noise input stages. The front-end of the CRID preamp input stage is also based on an FET.

There are several sources of noise in the FET amplifier circuit*; (1) thermal noise in the gate resistor and in the FET channel, (2) shot noise from the gate current, (3) $1/f$ noise in the FET channel. The details of each are discussed below.

*In this section, we follow the model described in Delaney[18]

4.2.1 Thermal noise

Thermal noise, also called Johnson noise, comes from the random Brownian motion of electrons in a resistor. It results in the small fluctuating voltages across the resistor. Such fluctuations can make no steady voltage in any direction, but the mean square voltage need not be zero, and, in fact, is found[19] to be

$$\overline{v^2} = 4kTRdf$$

where T is the absolute temperature, k is the Boltzman's constant, R is the resistance, and df is the frequency range of the system of interest.

Both the gate resistor (R_g) and the FET channel equivalent resistance (R_{eq}) contribute to the thermal noise in the FET circuit. Since the gate resistance R_g is large, the noise current will flow through C_{in}, the input capacitance of the FET and detector so that the gate thermal noise can be considered as being generated by a current source of size $\overline{i^2} = 4kTdf/R_g$ in parallel with a noiseless resistor R_g. Then the mean square noise voltage at the FET input stage is

$$\overline{v_R^2} = \frac{4kTdf}{R_g}(\frac{1}{2\pi f C_{\text{in}}})^2.$$

The thermal noise at the FET channel is given by the equivalent channel noise resistance R_{eq} such that

$$\overline{v_C^2} = 4kTR_{eq}df.$$

4.2.2 Shot noise

Since an electric current is not a continuous fluidlike flow but a flow of discrete electric charges, this results in statistical fluctuations of the current. For an average gate current I_g, the mean-squared fluctuation is

$$\overline{I^2} = 2eI_gdf.$$

If the gate resistance is chosen to be large, most of the noise current flows through C_{in}. Then the mean square voltage at the FET input due to this source is

$$\overline{v_S^2} = \frac{2eI_gdf}{(2\pi f C_{\text{in}})^2}.$$

4.2.3 $1/f$ noise

In addition to the thermal and shot noise, which have flat frequency responses, there is another noise source present in vacuum tubes or transistors. The origin of this noise is not very well understood but it has a frequency spectrum proportional to $1/f$, thus the name of '$1/f$ noise'. The mean square noise voltage is given by

$$\overline{v_f^2} = \frac{A_f df}{f}.$$

4.2.4 Total noise

The total noise at the output of the amplifier is calculated by summing each of the noise sources and integrating over the frequency range. The noise from different noise sources are uncorrelated and are added in quadrature. The frequency response of the preamplifier must be counted in the integration. If the risetime of the amplifier is set equal to its falltime, the noise is minimized[18] and the frequency response function $g(f)$ is given by

$$g(f) = A_0^2 \left(\frac{2\pi f\tau}{1+(2\pi f\tau)^2} \right)^2 ,$$

where τ is the risetime (or falltime) of the amplifier. The CRID preamplifier approximates equal rise and fall time with $te^{-t/\tau}$ pulse shape.

Using the integrations

$$\begin{aligned} \int_0^\infty \frac{1}{(1+x^2)^2}\,dx &= \frac{\pi}{4} \\ \int_0^\infty \frac{x}{(1+x^2)^2}\,dx &= \frac{1}{2} \\ \int_0^\infty \frac{x^2}{(1+x^2)^2}\,dx &= \frac{\pi}{4} \end{aligned}$$

the total noise at the output is

$$\overline{v^2}_{\text{total}} = A_0^2\left(\frac{kT}{2R_g}\frac{\tau}{C_{\text{in}}^2} + \frac{eI_g}{4}\frac{\tau}{C_{\text{in}}^2} + \frac{kTR_{\text{eq}}}{2}\frac{1}{\tau} + \frac{A_f}{2}\right). \tag{4.1}$$

This can be minimized with respect to τ. In the real CRID, the preamplifer tolerance and the sampling interval of data acquisition are also considered and τ is chosen to be 67 nsec.

4.3 Noise Performance Test

The low-noise performance test of the CRID preamplifier prototypes is described in this section. The circuits and specifications used in the test described in this section were at the prototype stage, prior to the production of the final electronics. The changes made after the test can be found in references [15] and [20].

Two different kinds of CRID preamplifier prototypes using (1) BF992 MOSFET and (2) J309 JFET were tested for gain, linearity, crosstalk and noise levels. Figure 4.2 is a schematic diagram of the MOSFET preamplifier prototype which was measured to have a noise figure of $\sim$ 500 electrons (rms). The main factor for the low-noise performance is the choice of the front end BF992 MOSFET, the RC-CR shaping time of the circuit, τ, of 65 nsec, and an intrinsic capacitance of 10 pF. In the CRID, an amplifier is attached at each end of the resistive anode wire so that an additional parallel noise source (*i.e.* the thermal noise of the resistive wire) must be added in quadrature to the amplifier noise. At a τ of 65 nsec the 40 kΩ wire has approximately 980 electrons (rms) noise for a total noise figure of about 1100 electrons (rms). The other prototype tested is based on a J309 JFET. Figure 4.3 is a schematic diagram of JFET preamplifier prototype. The maximum shaping time of the JFET circuit is 50 nsec.

4.3.1 Interchannel Crosstalk

The CRID preamplifiers are subject to a very wide range of input charge, over almost four orders of magnitude. To minimize the neighboring channel crosstalk over this wide dynamic range, the production amplifiers are individually packaged as a single channel hybrid. When a large input charge is injected, significant interchannel crosstalk is measured in the MOSFET prototype amplifier. Figure 4.4 shows

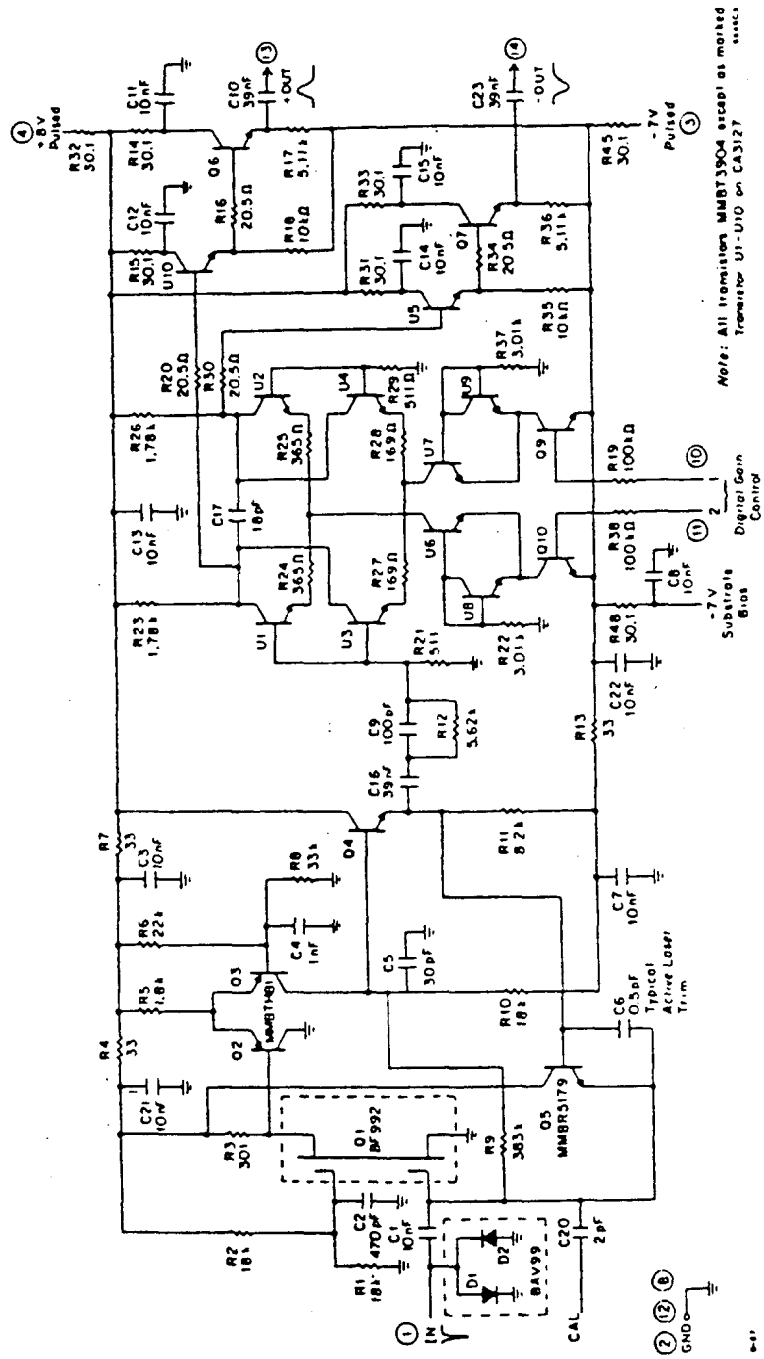

Figure 4.2: Schematic diagram of the MOSFET preamplifier prototype.

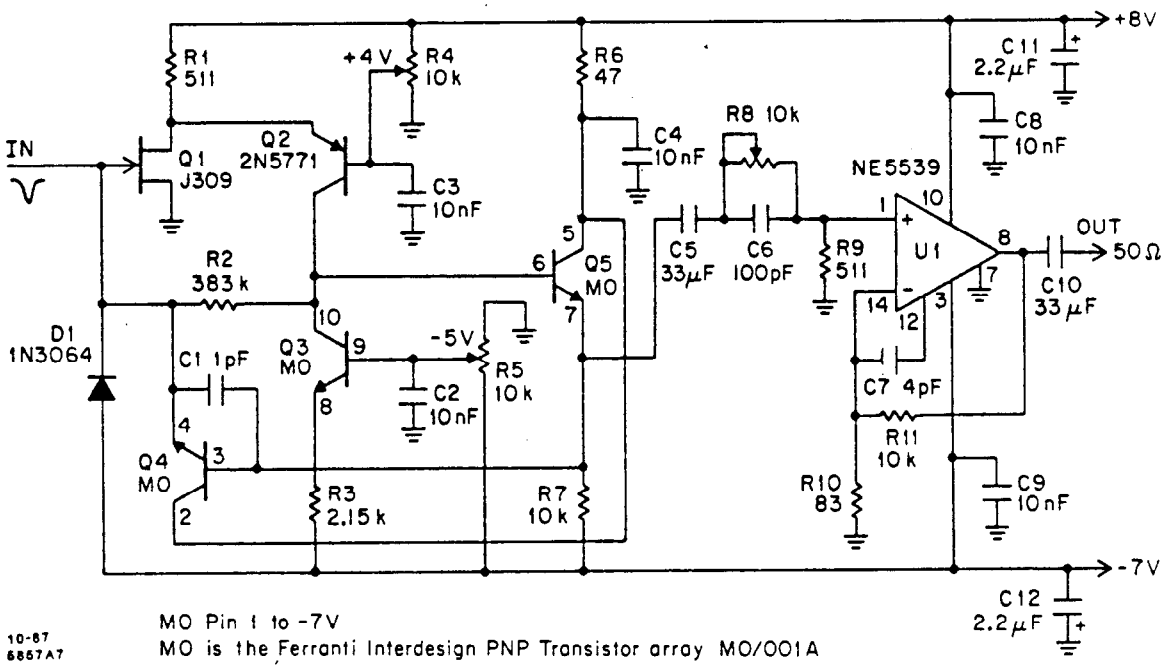

Figure 4.3: Schematic diagram of the JFET preamplifier prototype.

that a large input signal of about 10^8 electrons gives rise to a crosstalk equivalent to a signal of about 1.6×10^6 electrons on its nearest neighboring channel. The measured crosstalk is nonlinear; it is negligible for signals less than 10^7 electrons.

The crosstalk is reduced by a factor of 15 by interposing a grounded metallic screen between adjacent channel hybrids for a total crosstalk rejection ratio of about 60 dB. Figure 4.5 shows the effect of the crosstalk reduction by the shielding screens on the MOSFET prototype amplifiers. The crosstalk shielding is applied also to the production hybrid preamplifier packages. The back of the each hybrid is made conductive and grounded (screen 1), and the motherboard has 5 mm-high metal guards (screen 2) between pin rows.

4.3.2 Test system setup and results

A largely automated preamplifier test system has been constructed for measurements of amplifier charge gain and noise levels. A LeCroy 2261 Image Chamber

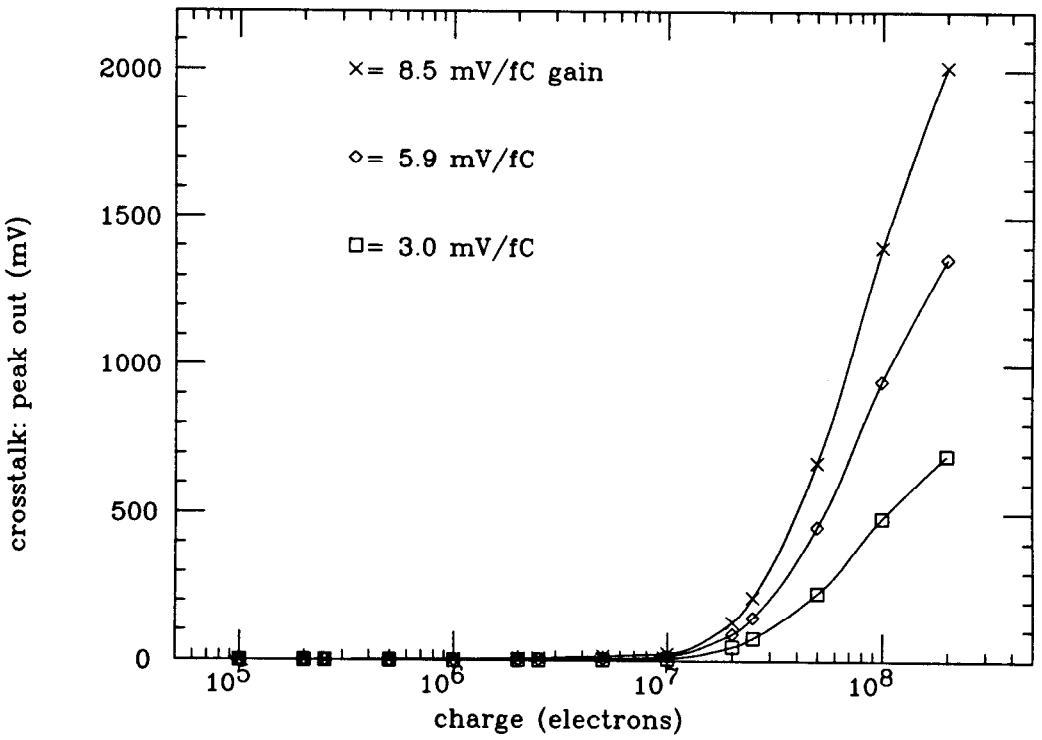

Figure 4.4: A crosstalk measured on the nearest neighboring channel in the prototype MOSFET preamplifier packages. Three gain settings are used.

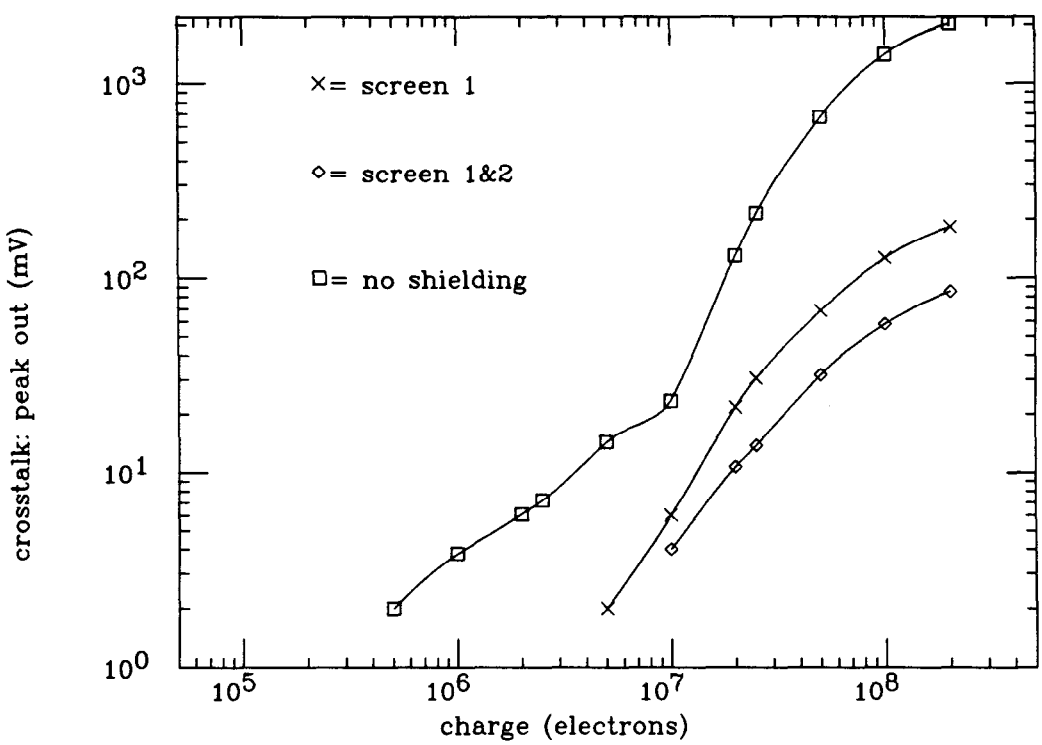

Figure 4.5: The effect of the crosstalk shielding by the shielding screen interposed between the PC board prototype channels. The measured values are using 8.5 mV/fC gain setting.

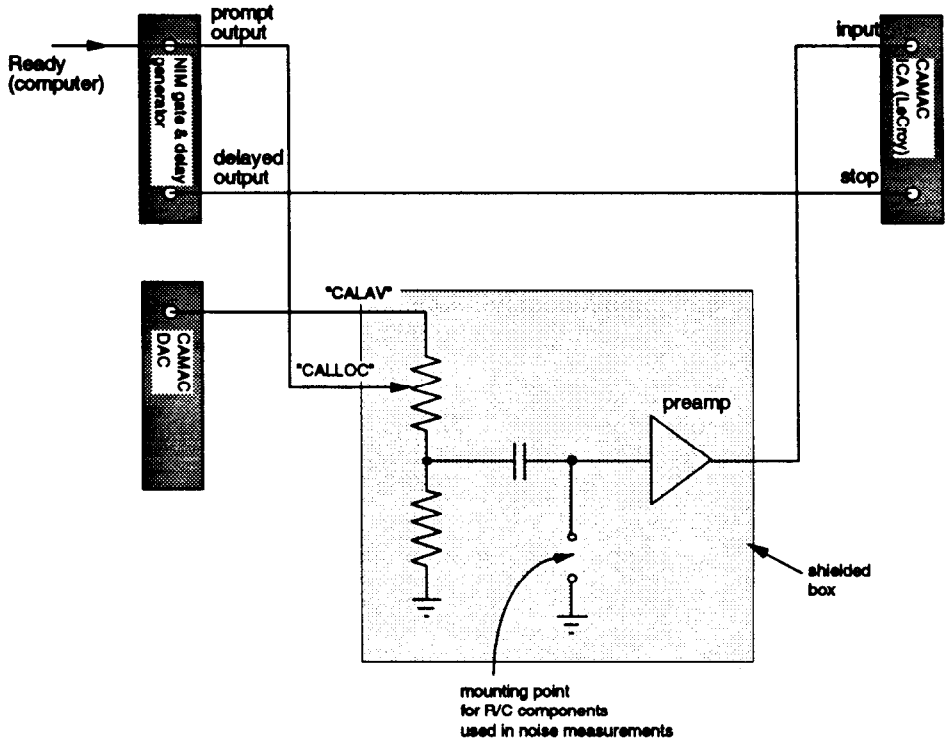

Figure 4.6: The block diagram of the preamp noise performance test system setup.

Analyzer (ICA), operating at 50 MHz, with unity gain, 11 bit resolution and 320 time slices, provides high-speed sampling of the preamplifier output pulses, while the CAMAC packaged DAC and a charge injection circuit allow the preamplifier to be studied over the full range of input charge expected in operation. A block diagram representation of the test system setup is shown in Figure 4.6.

A digitally pulsed voltage step created by a DAC is presented to the amplifier input for the calibration. The circuitry for the calibration is shown schematically in Figure 4.7. The circuit resides on each of the preamplifier hybrids. During the fabrication process an active laser trim of R43 provides an accurate trim of the charge injected.

In the tests, the outputs of the preamplifiers have been approximately matched,

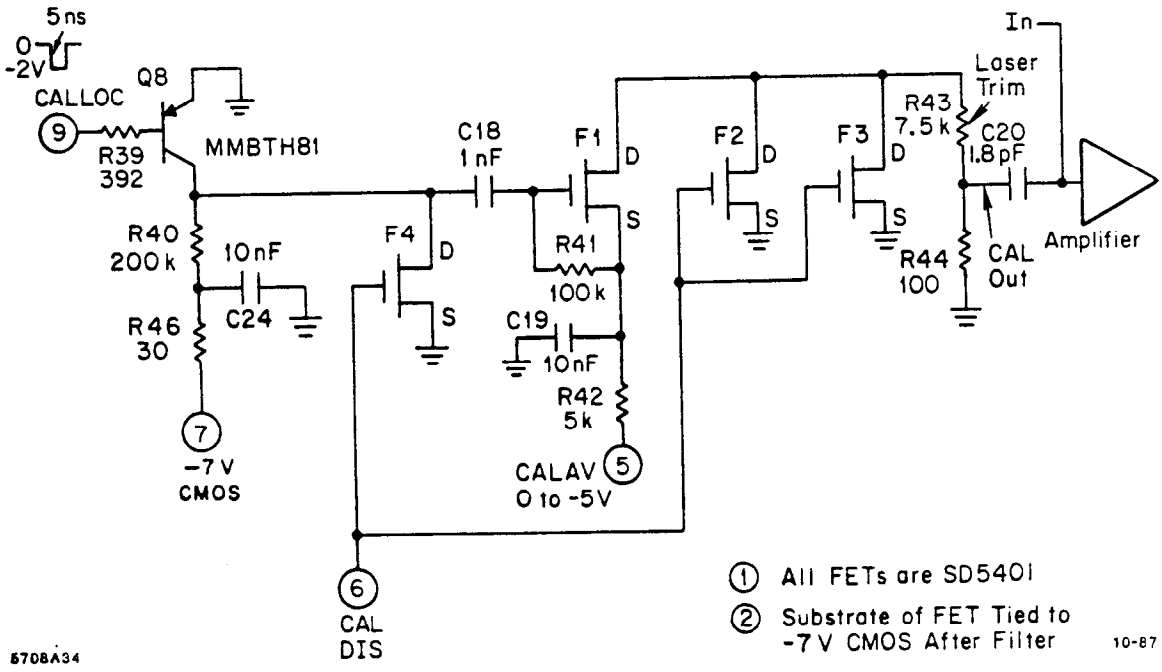

Figure 4.7: The calibration circuit for the MOSFET preamp.

using a 50Ω driver, to the 2 V dynamic range of the ICA. Figures 4.8(a) and 4.8(b) show ICA digitizings of MOSFET preamplifier output pulse corresponding to 2×10^5 and 8×10^5 electrons respectively. Figure 4.8(c) shows the fit of the output pulse to the form $Ate^{-t/\tau}$. A more complicated model using 4 time constants[21] gave a better fit in the tail region. The fit is shown in Figure 4.8(d).

Figure 4.9 shows histograms of preamplifier output voltage as a function of input charge for the three selectable gain settings of the MOSFET preamplifier prototype. These characteristics were obtained automatically by applying the CAMAC DAC voltage to the charge injection capacitor in series with the input. The slope of each line gives the charge to voltage conversion gain. The saturation of preamplifier output occurs only for charges in excess of 10^7 electrons, even with the highest gain.

To measure the noise characteristics of the MOSFET and JFET preamplifiers under various input loadings, the charge injection capacitor is removed, and parallel

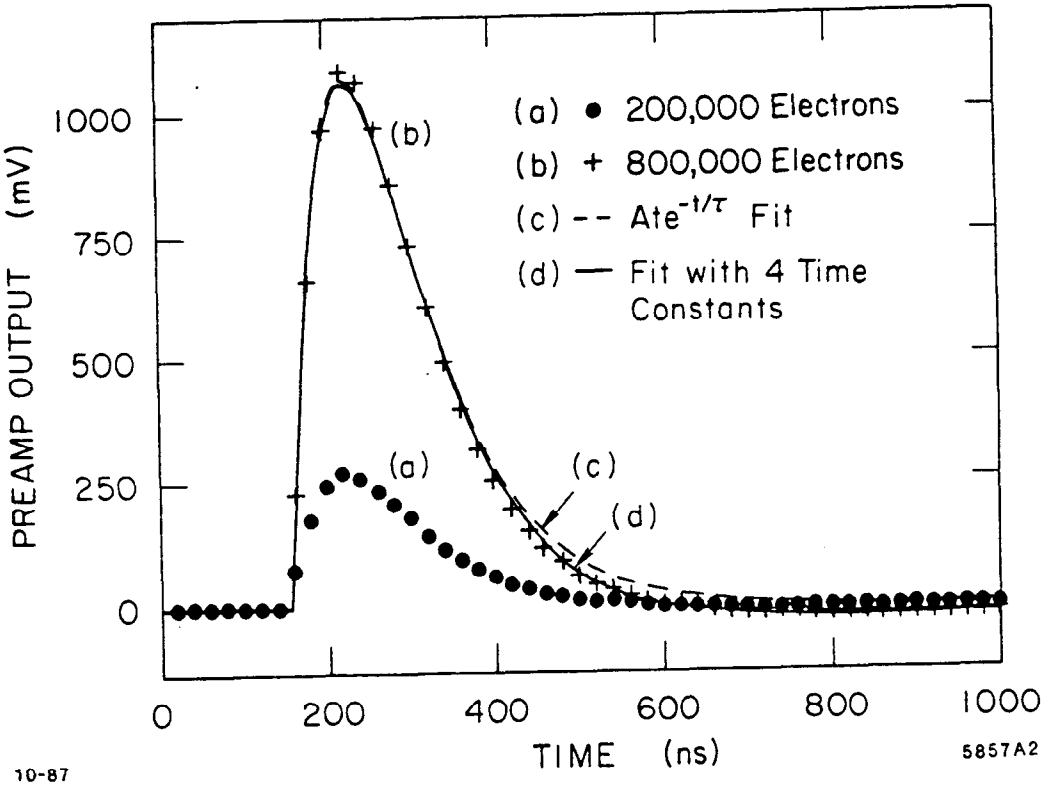

Figure 4.8: CRID Preamp pulse shape: (a) MOSFET preamp pulse shape for 2×10^5 electrons; (b) For 2×10^5 electrons; (c) Fit of the data to the form $Ate^{-t/\tau}$; and (d) Fit of the data to a four time constant expression.

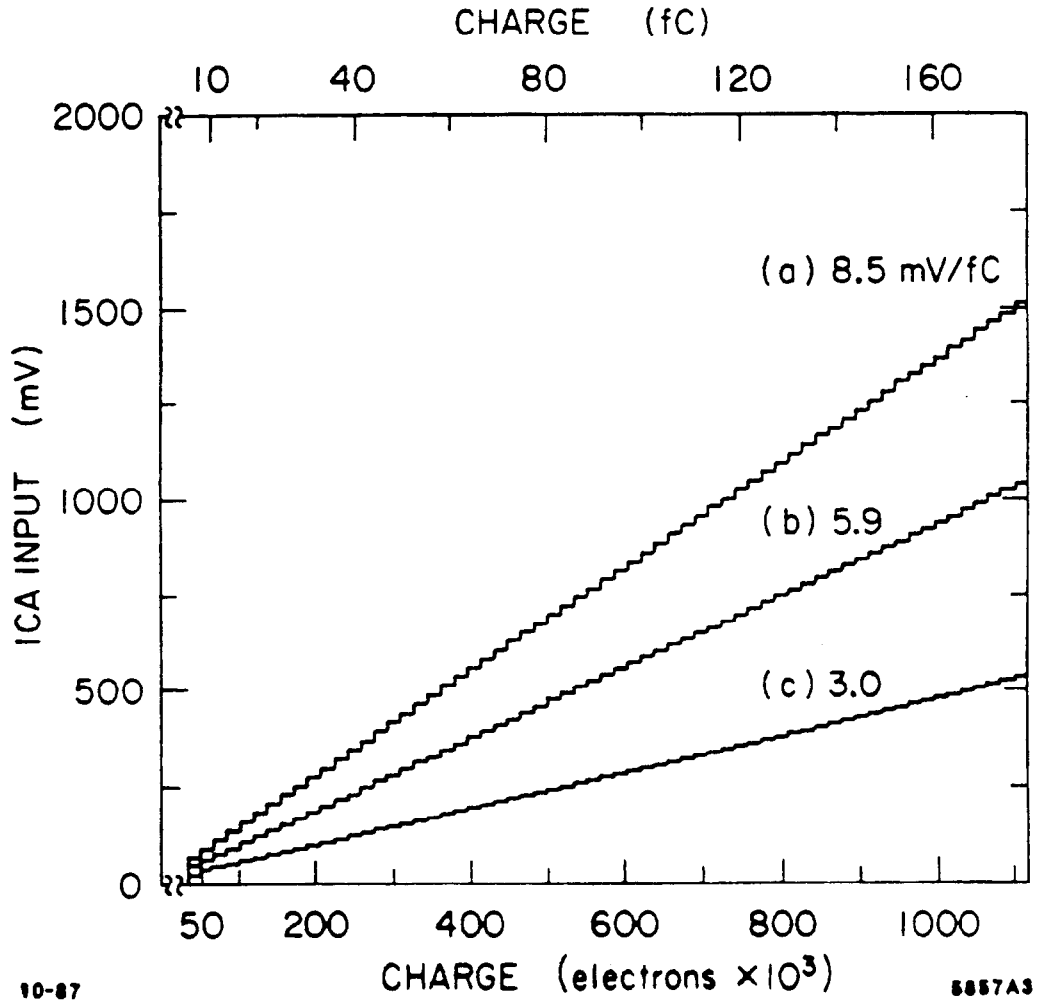

Figure 4.9: Histogram of preamplifier output voltage vs. input charge for the three gain settings of the MOSFET preamplifier prototype.

capacitance, resistance or CR combinations are added between the amplifier input and ground. The amplified input noise is measured with the ICA, using a software-defined "gate width". The gate width is chosen to be six times the amplifier shaping time, as measured from an independent fit to the output pulse shape using a single time constant. The interval contains approximately 98 % of the pulse output charge. (Equation 4.2)

$$\int_0^{6\tau} te^{-t/\tau}\,dt = 0.98 \times \int_0^{\infty} te^{-t/\tau}\,dt \tag{4.2}$$

The gatewidths are set to 390 nsec for MOSFET and to 300 nsec for JFET prototypes. The equivalent noise charge (ENC) in number of electrons is given by

$$\mathrm{ENC} = \frac{\sqrt{\sigma_V^2(\mathrm{amp}) - \sigma_V^2(\mathrm{ica})}}{\mathrm{G} \cdot \mathrm{e}}$$

where σ_V(amp) and σ_V(ica) are the standard deviations (in mV) of the pedestal distributions seen in the ICA with and without the amplifier connected, based on comparable sample of at least 1,000 measurements; G is the charge gain of the amplifier (in mV/fC under the appropriate input loading conditions) and e is the electron charge in femtocoulombs.

Figures 4.10 and 4.11 show the variation of ENC with added capacitance and/or resistance for the MOSFET and JFET preamplifier prototypes. The measurements confirm that either amplifier circuit would give acceptable noise performance for CRID. Both circuits have about 500 electrons (rms) noise with no resistance or capacitance added. When a capacitance of 10 pF, which is similar to the intrinsic chamber capacitance, and a resistance of 40 kΩ, which is characteristic of a 10 cm long 7 μm diameter carbon sense wire, are added, the rms noise figures are 1100 electrons for MOSFET and 950 electrons for JFET amplifiers.

The measurements of Figures 4.10 and 4.11 have been fit using the MINUIT program to a general FET amplifier noise model derived from Eq. 4.1:

$$\mathrm{ENC} = \frac{2.718}{e}\left(\frac{kT\tau}{2(R_{\mathrm{int}} \parallel R_{\mathrm{ch}})} + \frac{eI_G\tau}{a} + \frac{a}{a} + \frac{a}{a}\right)^{1/2}.$$

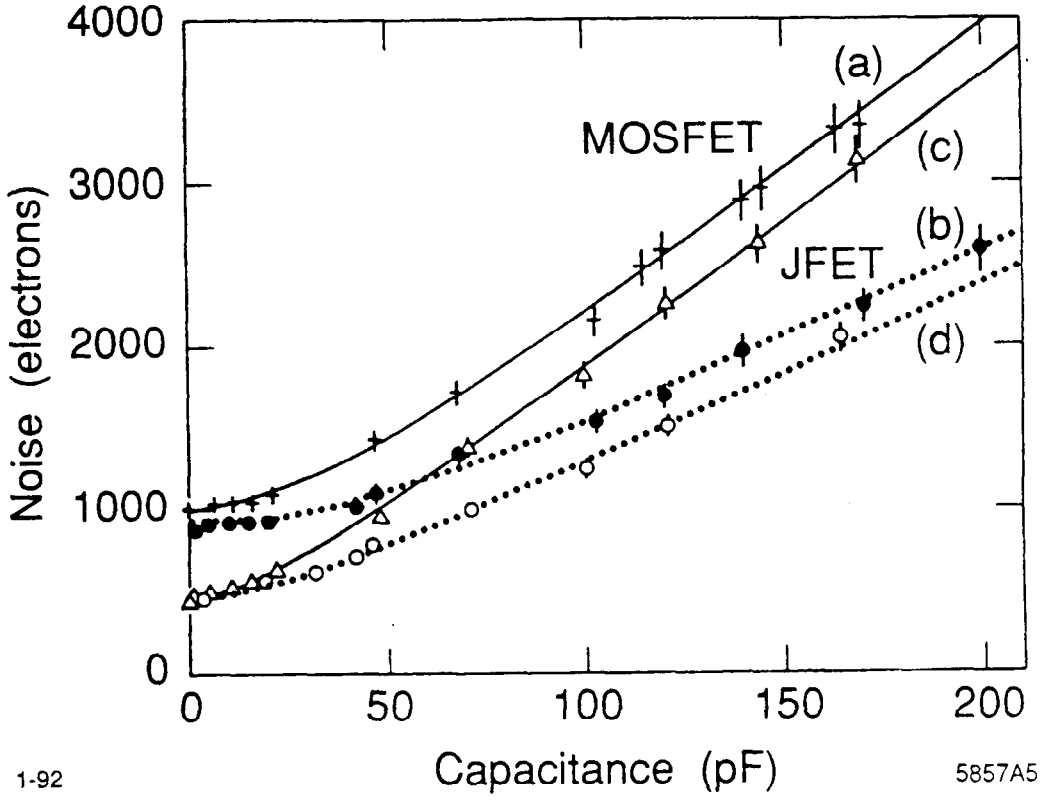

Figure 4.10: Variation of ENC with added input capacitance for: (a) The MOSFET preamp with 40 kΩ resistance to ground; (b) The JFET preamp with 40 kΩ resistance to ground; (c) The MOSFET preamp with no resistance added; (d) The JFET preamp with no resistance added.

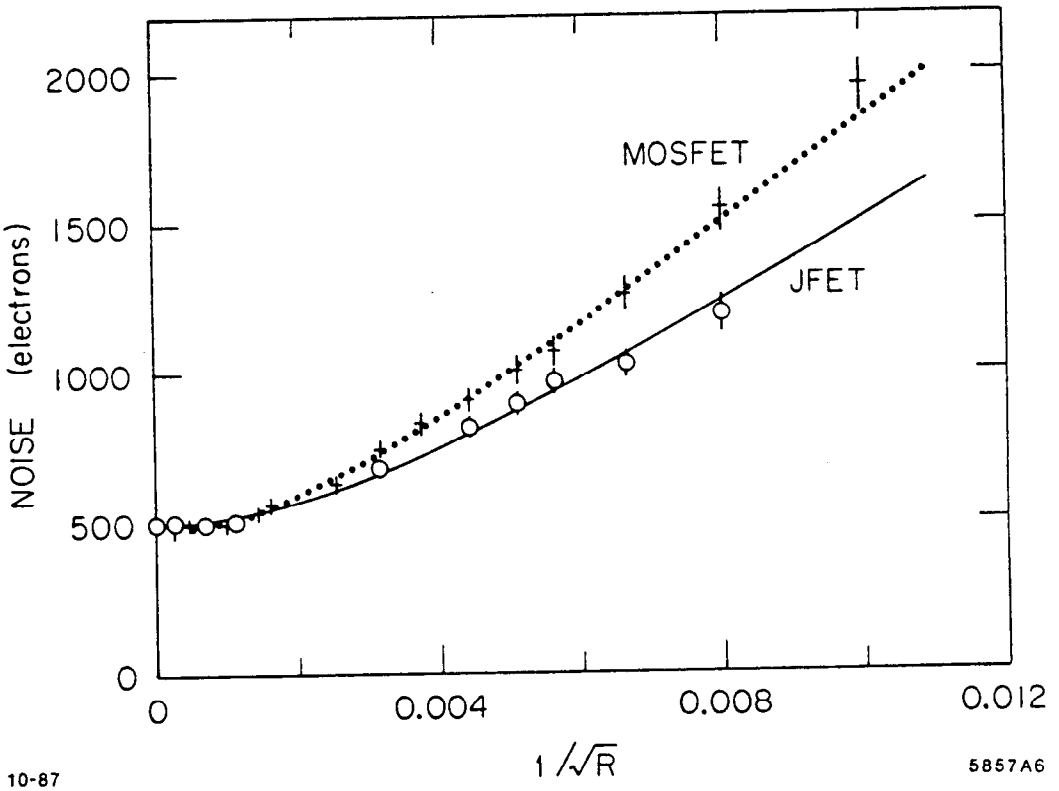

Figure 4.11: Variation of ENC with added input resistance for: (a) The MOSFET preamp; (b) The JFET preamp.

$R_{\rm ch}$ and $C_{\rm ch}$ represent the chamber resistance and capacitance respectively; these are simulated by added resistance and capacitance in the tests. The free parameters in the fit are $C_{\rm int}$ and $R_{\rm int}$, which represent the intrinsic capacitance and resistance of the amplifier, I_G and R_{EC}, which are the FET gate current and equivalent noise resistance, and A_f, the coefficient of the $1/f$ noise. $R_{\rm int} \parallel R_{\rm ch}$ is $R_{\rm int}$ in parallel sum with its input resistance: the latter is the 40 kΩ sense wire in real operation.

$$R_{\rm int} \parallel R_{\rm ch} = \frac{R_{\rm int} R_{\rm ch}}{R_{\rm int} + R_{\rm ch}}$$

For each curve, a good fit (χ^2 per degree of freedom ≈ 1) was obtained with final parameter values within the ranges expected. $C_{\rm int}$ was fit to be between 5 and 10 pF. The fit values for A_f and I_G were found to be in the ranges $10^{-13} \sim 10^{-12}$ (Volt^2) and $2 \times 10^{-11} \sim 10^{-9}$ (A) respectively.

Chapter 5

Monitor and Control Systems for CRID

To help ensure the stable and long-term operation of a Cherenkov Ring Imaging Detector at high efficiency, a comprehensive monitor and control system has been developed[17]. The system continuously monitors and maintains the correct operating temperatures, pressures, and provides an on-line monitor of the flows, mixing and purity of the various fluids. In addition, the velocities and trajectories of the Cherenkov photoelectrons drifting inside the imaging chambers are measured using a pulsed UV lamp and a fiber-optic light injection system. This chapter will describe some features of the monitor and control system in such areas as operating temperature (section 5.2), gas delivery system and pressure control (section 5.3), and binary gas mixture monitoring (section 5.4) along with the brief introduction to the monitor and control data acquisition and other aspects of the system.

5.1 Data acquisition for Monitor and control

The CRID monitor and control system has many features in common with the monitor and control systems of the other major SLD subsystems. It is based on

a parallel CAMAC* branch (Fig 5.1) supported by a DEC VAXstation 3200. The workstation is one of several in the SLD cluster located in various positions around the SLD and is connected to the main processor (SLD VAX 8800) via Ethernet.

The various SLD monitor and control systems operate and take data independently of one another on separate CAMAC branches. In all cases, however, a standard user interface - the SLAC "Solo Control Program (SCP)" - is used. The SCP is based on a program of the same name first developed and used by the SLAC Linear Collider (SLC) group for the monitor and control of the SLC. Although the main functions of the VAX 8800 are the acquisition and processing of experimental data through fastbus, it also supports monitoring and control activities in the VAXstations by running batch processes, recording data in a central database, and writing the various monitor-system data to tape.

In the CRID monitor and control system, the action of the computer and CAMAC is limited mainly to monitoring, rather than direct-control of the processes. For example, the pressure control in the CRID drift boxes and the radiator gas volumes - on which the integrity of the quartz window depends - is accomplished by the combination of an analog feedback system and second-level protective circuits using programmable logic devices, thus running free of any software-based processors. The main reason of operating control processes without computers is to protect the system in case of computer breakdowns. The only exception is in the temperature control, where the computer can play a more active role because of the large thermal inertia of the CRID that prevents rapid temperature fluctuations.

5.2 Monitoring and control of operating temperature

The need for controlling the operating temperature of CRID is obvious considering the following consequences that might happen in case of temperature failure:

*Model 2922 Q-Bus-CAMAC interface with DMA and model 3922 parallel-branch crate controller: Kinetic Systems Corp., Lockport, IL 60441, USA.

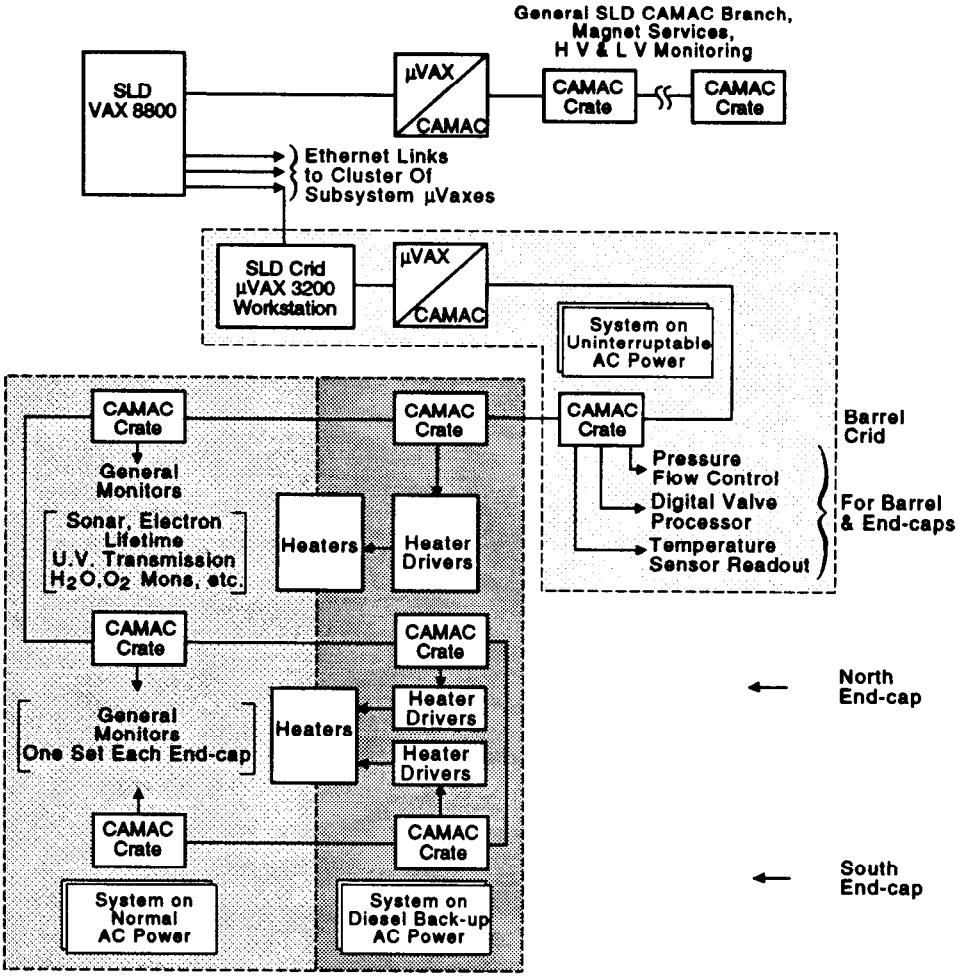

Figure 5.1: The CAMAC monitor and control data acquisition system of the SLD CRID.

- If the temperature of the radiator gas, C_5F_{12}, drops below its condensation point, which is 30 °C at 1 atm, a potentially damaging pressure differential might occur across the quartz windows of drift boxes.

- If the temperature drops below the condensation point of TMAE, the photosensitive agent added inside the drift box gas, the normal CRID operation is almost disabled.

- Significant temperature fluctuations cause fluctuations in the index of refraction, such that the CRID data would be distorted.

With these things in mind, the barrel CRID vessel is maintained at 34 ± 1 °C, a safe margin above the C_5F_{12} condensation point. As a matter of fact, the original design for the barrel CRID operation temperature was 40 °C for running with 100 % C_5F_{12}. However, there was a concern about the possible wire breakage in the central drift chamber (CDC) system in case the heat shield cooling water between CDC and CRID fails with CRID running at 40 °C. As a result, it was decided to run the CRID radiator gas in a mixture of C_5F_{12} and N_2 so that the operation temperature could be lowered.

The temperature monitoring is achieved by using 32×32 array of AD590JF[22] sensors. AD590's are chosen for their linear current output and inexpensive cost. They are grouped into 32 addresses where each group has 32 sensors read by 32-channel CAMAC scanning ADC module called a 'SAM'[23]. For each SAM reading, one out of 32 addresses is chosen by a CAMAC output register module called an 'IDOM'[24]. IDOM gives a positive voltage output signal to one of its 32 channels. This signal activates the corresponding group of 32 sensors, each of which generates a current output proportional to the absolute temperature (nominally 1 μA/K). The multiplexing scheme of the temperature readout sensors is illustrated in Fig 5.2. All sensors are calibrated at 40 °C before installation by adjusting the potentiometer that works as a trim resistor on which the current output is converted to the monitor voltage (Fig 5.3). The 32 sensors in the same address shares a common trim resistor so that their calibrations match within ± 1 °C of

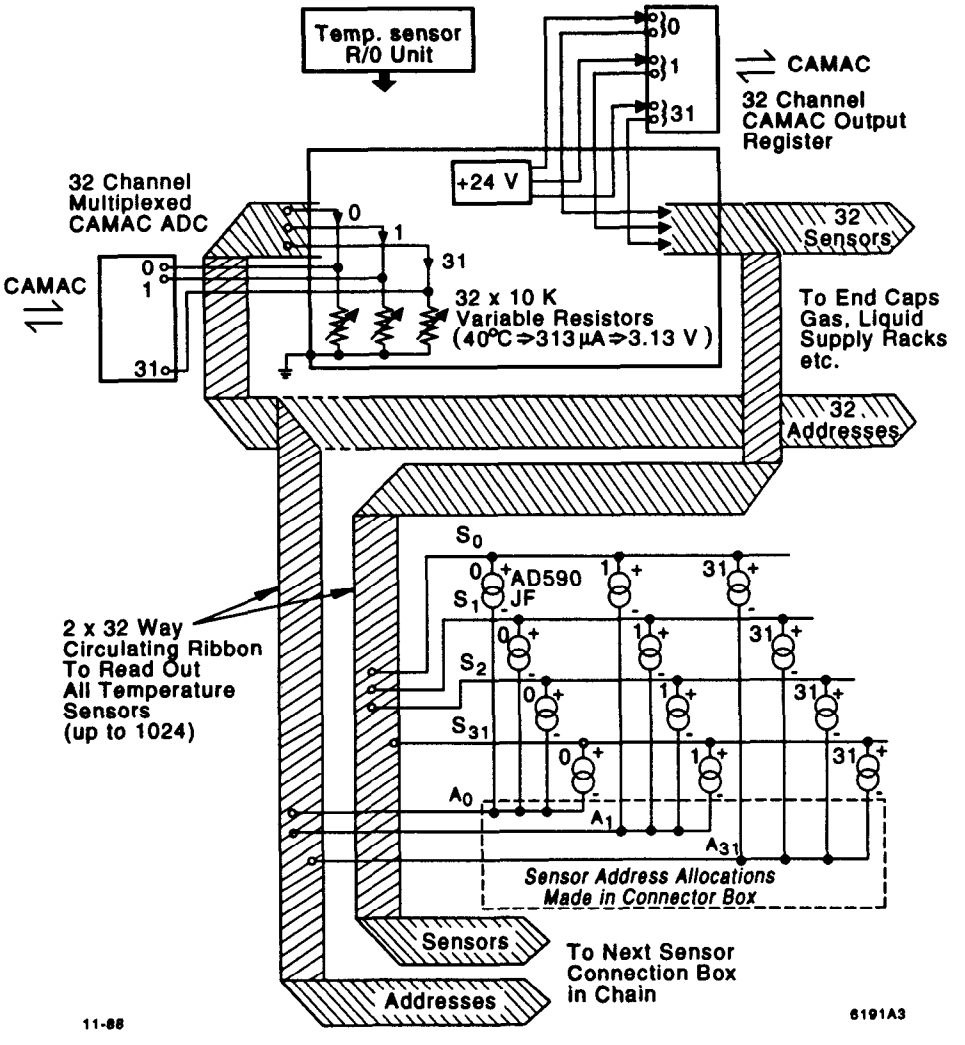

Figure 5.2: The multiplexing scheme of the temperature readout sensors.

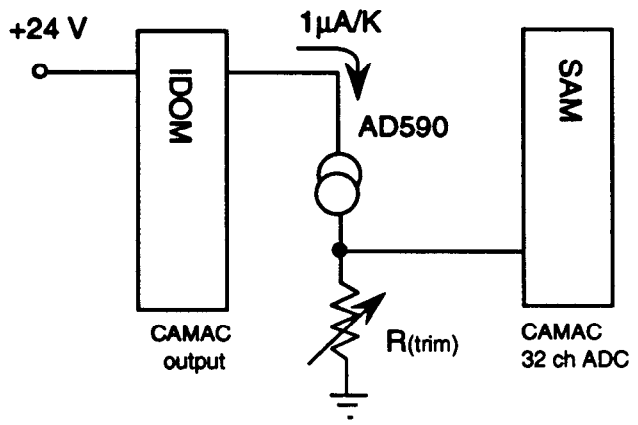

Figure 5.3: The Temperature readout using AD590 sensor.

34 °C. In the more critical applications (usually those surfaces in contact with CRID fluids), sensors with a tighter calibration within ±0.5 °C are used.

An array of heater pads are used to supply necessary heating to CRID. The surfaces of the CRID vessel are populated with an array of Kapton-insulated heater pads as well as temperature sensors. The supply of power from the heaters to the CRID vessel is divided in two categories. First, to provide uniform background heat, there are "distributed" circuits of heaters whose pads are scattered in a regular geometrical pattern over the whole surface of the vessel. Then there are "local" circuits whose pads are grouped together by locality so as to provide local trim. In the barrel CRID, approximately 200 heater circuits will provide the enough heating with a high level of redundancy. Approximately 50 % of the available heater power is provided by a backup diesel generator in the event of failure of the commercial electricity supply.

The CAMAC-based temperature control system activates heater circuits based on the temperature monitored by nearby sensors. The 'on-time' duty cycle of the heater circuits is determined by the computer as a function of monitored temperature. Since the configuration of temperature sensors do not necessarily match with that of heater circuits, a on-line database is used to store the required set points

and the geometric correlation between the sensor positions and heater pads.

The current to each heater circuit is digitally switched using an individual "zero-crossing" solid-state relay (SSR)[25]. Switching operations are requested from software via an IDOM. The SSR is followed by a rectifier and a smoothing capacitor to provide "soft-start" DC current for use inside the SLD magnetic field (Fig 5.4). To check the circuit integrity, the voltage drop across a 3 Ω series resistor is read by a CAMAC input register.[26]

5.3 Gas Delivery system and Pressure Control

The barrel CRID gas supply and pressure control system is shown schematically in Fig 5.5. The base drift gas, ethane (C_2H_6), is delivered through a mass-flow-controller (MFC)[†] at atmospheric pressure and is bubbled through liquid TMAE maintained at a temperature of 28 °C to prevent recondensation of the TMAE vapor. The exhausts of the 40 drift boxes are monitored individually.

The side walls of the drift boxes are constructed in two layers with a purge space between the layers, which is flushed continuously with pure methane (CH_4), supplied by a MFC. Although leak communication between the highly electronegative radiator gas and the TMAE-ladden UV-absorbing drift gas through the two series glue joints is expected to be minimal, the side-wall exhaust gas is monitored for evidence of leakage in either direction.

Due to its expense, the C_5F_{12} radiator gas is continuously recirculated through the radiator vessel and a filter stack via an evaporator-condenser "thermal engine". Prior to filling with C_5F_{12}, the radiator vessel is purged of air by nitrogen (N_2) which is then thermodynamically replaced by C_5F_{12} using a refrigeration system. Due to the lowered temperature of CRID vessel for CDC protection (section 5.2), we are only allowed to run a C_5F_{12}/N_2 mixture instead of 100 % C_5F_{12} to lower the condensation temperature of the radiator gas. The C_5F_{12}/N_2 ratio of the radiator gas is monitored at six points throughout the radiator, using a ultrasonic-based

[†]Model 258B, MKS Inc., Burlington, MA 01803, USA.

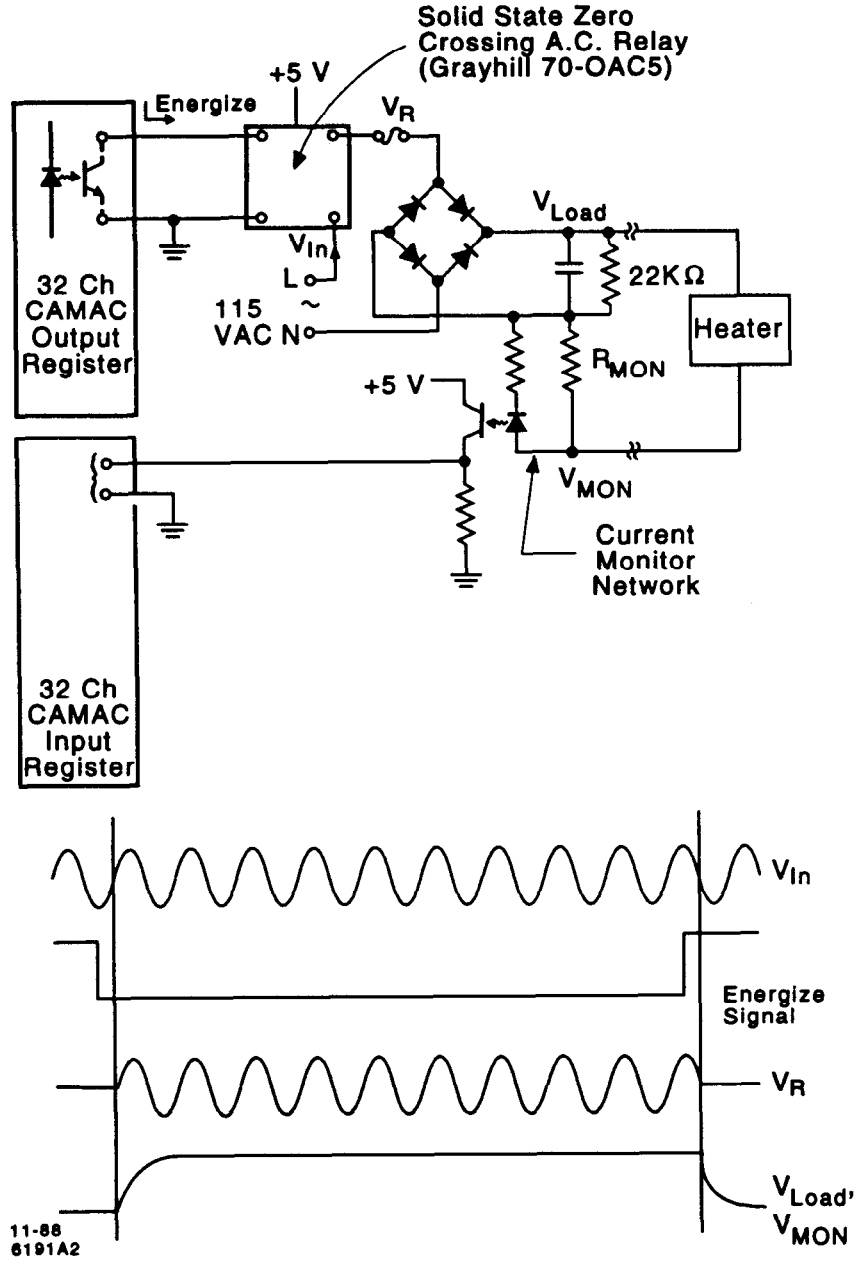

Figure 5.4: The circuit for switching CRID heaters.

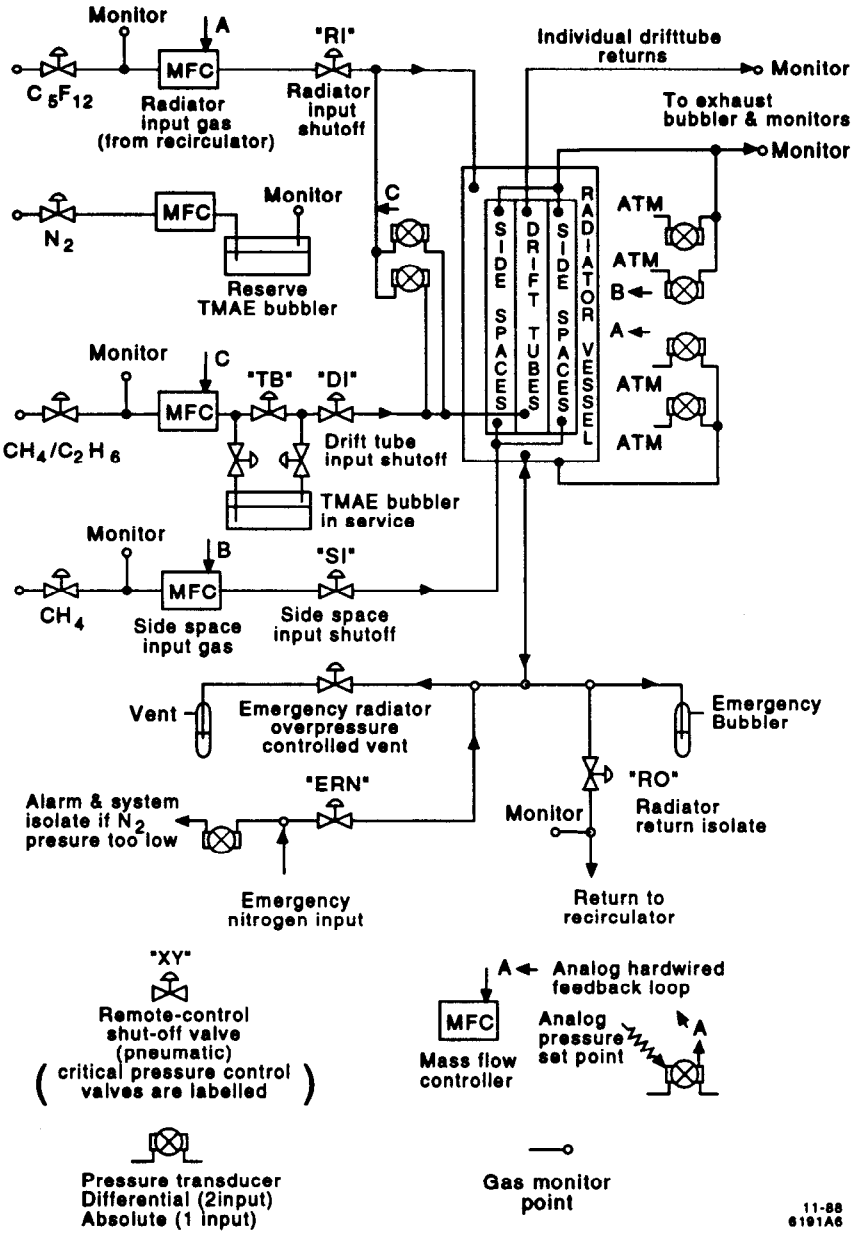

Figure 5.5: Schematic of the barrel CRID gas delivery system, showing some of the components of the pressure control system.

technique (section 5.4) to determine the residual N_2.

To minimize the mechanical stress on the fragile CRID drift boxes, the differential pressure across the quartz window is controlled with a triple-layered safety system:

(i) In the normal operation, analog feedback from sensitive pressure transducers to the delivery MFCs maintains the correct differential pressures by regulating the flow of the input gases. Two pressure sensors are mounted in parallel; thus the control can be transferred to the survivor in case of a single sensor failure.

(ii) Once the pressure goes outside the normal operating ranges, as a result of a failure of the analog feedback system, signals from the pressure sensors are used in a custom processor to sequentially open or close a series of input flow and overpressure or underpressure relief valves.

(iii) In the event of failure of both electronic systems, a bi-directional passive pressure relief bubbler (auto vent/auto add) allows excess gas to leave the radiator vessel in the event of an overpressure condition, or admits air in the event of underpressure.

A custom digital processor system[27] responsible for the step (ii) of pressure control was constructed and tested. It monitors the outputs of all the pressure sensors, and responds to pressure variations outside the allowed limits by opening and closing the various input, output, overpressure, and underpressure relief valves (See Fig 5.5). This is a stand-alone system, composed of custom-built VME circuit boards and an uninterruptible power supply. Listed below are the basic elements of the system.

Comparator Cards(CC): These compare the sensed pressure with operating range set points, and pass a 4-bit comparator output word for each sensor to the pressure control card. The four operating range set points for each pressure sensor

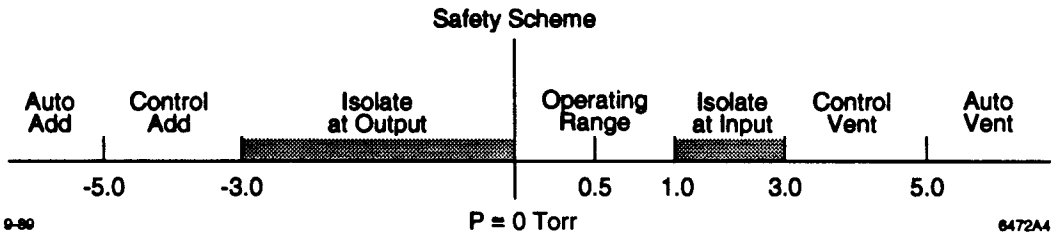

Figure 5.6: The desired gas system responses to variation in gas pressure.

and the desired gas system responses to variation in gas pressure are shown in Fig 5.6. There are 5 control cards for the full barrel CRID. A comparator card has 2×4 channels since there are two pressure sensors each with four set points. There is voting between the two pressure sensors, detecting disagreement of more than 1 bit. There is built-in electronic hysteresis of approximately 0.1 Torr, to reduce oscillations between states on opposite sides of the pressure range set points.

Pressure Control Card (PCC): This card consists of 3 parts.

- Main processor: This contains programmable logic ICs [‡] in which the sequenced valve response to the current pressure status of the system is programmed as a finite state machine.[28] Figure 5.7 shows the 25-element response matrix for correlated variations in differential pressure between drift and radiator (D – R) gas circuits, and between the CRID radiator vessel and atmospheric pressure (R – A). More about the response matrix will be discussed in section 5.3.1

[‡]EP1800, EP900:Altera Inc, Santa Clara 95051, USA.

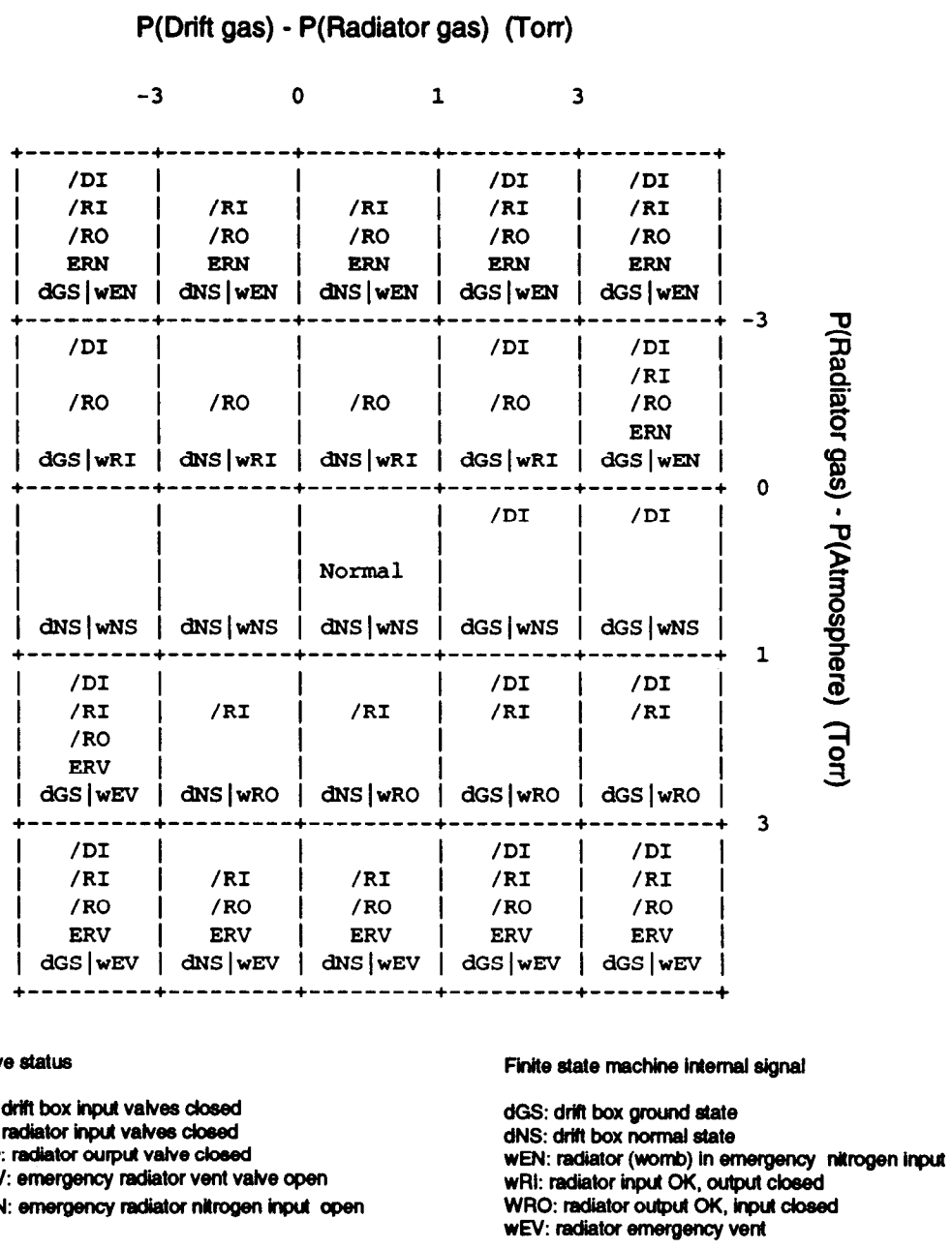

Figure 5.7: Response matrix to correlated variations in pressure between the drift gas and radiator gas circuits, and between the pressure of the CRID radiator vessel and the atmospheric pressure.

- Valve error handling: A programmable logic chip [§] is used to take care of the valve errors. If any one valve fails (detected by a disagreement between the status of the signal to the valve actuator and its microswitch: see (3) below), the system is programmed to close all the valves.

- Interface to the override unit: A manual override unit is interfaced to the system through this card. A selection switch in the override unit can enable/disable the outputs from the main processor. This unit is used only during system start-up or for specialized testing.

Valves and Valve Driver Cards: The valves used are actuated pneumatically with compressed air switched by miniature solenoid valves[¶] which operate with 5 V dc TTL logic with a power dissipation of 0.5 W per valve. Each shut-off valve has a stem microswitch that senses stem position. The valve driver cards actuate the valves as selected by the PCC, and compare the current valve state with the microswitches. Any discrepancies are reported back to the PCC, which closes all the valves in the pressure control system and warns the operator.

Uninterruptible Power Supply (UPS): The UPS under design includes a $24V$ battery system. It is used for the VME crate, including valve and pressure control. It also powers the gas supply MFC's and the pressure sensors.

The pressure control system using the custom digital processor was extensively tested both in a two-cell simulator system and in the barrel CRID prototype before it was installed into the barrel CRID. The results of the tests will be discussed in the following subsections.

[§]EP600:Altera.

[¶]K3P02LO, Honeywell, Skinner Valve Division, New Britain, CT 06051, USA.

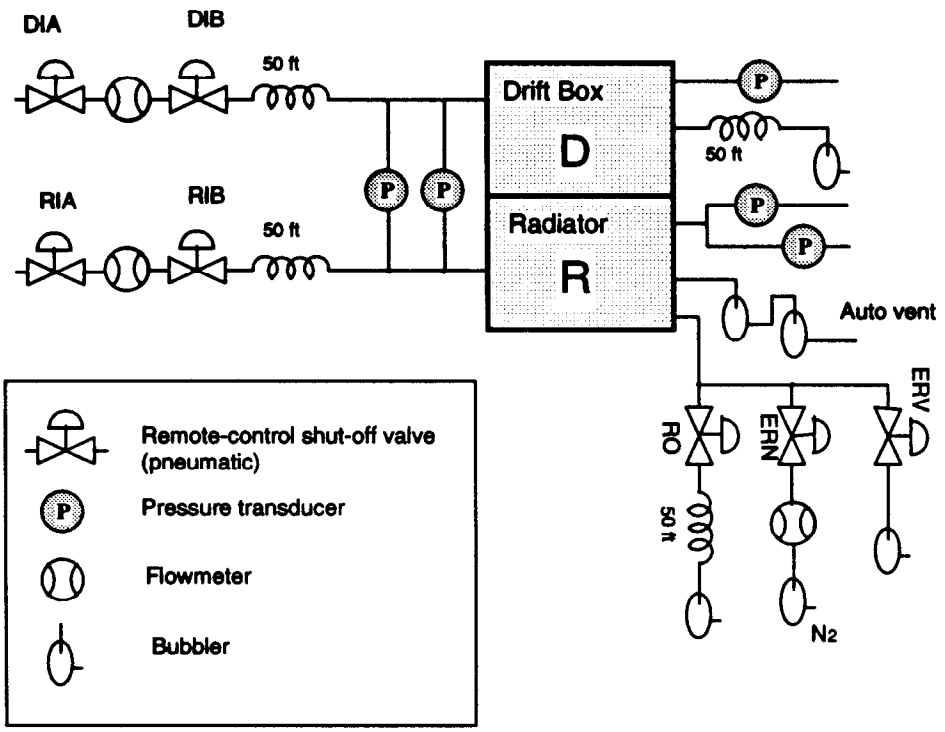

Figure 5.8: Pressure Control System Simulator.

5.3.1 Pressure Control Tests on the Two-Cell Simulator.

The simulator used for the pressure control processor tests consists of two cells of an equal volume of approximately 28.2 l. Sensitive electronic pressure sensors monitor the pressure of the D-cell (simulating the drift box) relative to atmosphere (D – A), D-cell relative to R-cell (simulating the radiator volume: D – R), and R-cell relative to atmosphere (R – A), as shown in Fig 5.8. The flowmeters used in the simulator are simple needle valve flowmeters, whereas the real CRID and CRID prototype flowmeters are MFC electronic controllers. Without MFCs in the simulator tests, input flow rates were controlled and kept constant by manually setting the needle valve flowmeters regardless of the system pressures; D – R, R – A and S – A. Then the system pressures were determined by the dynamic pressures

corresponding to the input flow rates.

In normal operating conditions, both cells have a flow-to-volume ratio approximately equivalent to that of the real CRID system. For both cells, a volume ratio of $f/v = 1/120$ min^{-1} is desired, corresponding to a normal operating input flow of 235 cc/min. In addition, we attempted to establish the correct relative input conductance by using 50 ft coiled input pipes of 1/8 inch diameter to represent the piping between the CRID vessel and the gas rack on the platform. The simulator only uses 1/4 inch remote-controlled shut-off valves, which are pneumatically actuated with compressed air switched by miniature solenoid valves. In the CRID system, the radiator input and output valves are 1.5 inch valves. The effect of a difference in valve size was later tested in the barrel CRID prototype and is discussed in section 5.3.2.

The desired sequence of opening and closing of the various input, output, overpressure, and underpressure relief valves is dependent on the correlated variations in pressure between D – R and R – A, as shown in Fig 5.7. The normal operating state is at the center of the response matrix, where the drift gas pressure is between 0 and 1 Torr higher than the radiator gas, which is between 0 and 1 Torr higher than atmosphere. A manual override box that allowed the selection of all valve states (ie. open or closed), flowmeter-controlled input flows, and a vacuum pump were all used to force the state of the simulator into conditions outside the normal operating state. All 25 states of the response matrix were tested, and the correct valve actions were taken in all cases. In states listed as A $\sim$ D in Fig 5.7, the system oscillated between the indicated state and normal. For instance, in state A the radiator was overpressured using a high radiator input flow (335 cc/min) while the drift was in the normal state (250 cc/min); thus the radiator input valve was closed (\RI). When the radiator pressure lowered as a result, the system reached the normal state and re-opened the radiator input. But the radiator pressure once again increased due to the high radiator input flow, and RI was shut again. The result was oscillation between the two states. In all other states, recovery towards the normal operating state resulted. The system frequently ended up in one of

the above oscillation states between A $\sim$ D and normal. The full response matrix (Fig 5.7) was tested using the electronics for both the north- and south- barrel independently. In addition, the desired uncorrelated valve responses for the sidewall purge spaces were tested using the D-cell with the D $-$ A pressure sensor.

When the simulator system was forced to oscillate between a state A $\sim$ D and the normal operating state, the pressure periodically peaked. Due to high input flow the pressure gradually increased until the comparator card set point of 1 Torr was crossed, at which point the radiator input flow valve was commanded to shut off. Once the valve had actually shut (a few seconds later), the pressure began to decrease, returning to the normal operating range at which point the valve was commanded to open again. The maximum peak-to-peak change in pressure (mainly due to mechanical lag time in the valves) was defined as the pressure transient across the particular set point. The rate of pressure change $\frac{\delta p}{\delta t}$ was defined as; δp was taken as the maximum peak-to-peak pressure change and δt was taken as the fall time from the peak to the minimum.

The pressure tests were performed under three different conditions; two with the prototype version of comparator cards, and one with the production version. The prototype comparator cards were tested with two different gases for the R-cell: nitrogen and isobutane. The production comparator cards were tested using nitrogen for the R-cell. In all three cases, nitrogen was used for the D-cell. The only difference between the prototype and the production comparator cards was the RC response time; 10 msec for the prototype cards and 5.0 sec for the production cards. The normally long RC time constant of the production comparator cards results from the use of a low pass filter to remove electronic noise on the signal line from the pressure sensor. The pressure tests using isobutane as the radiator gas were made because we wanted to test the effect of a heavier gas since the actual radiator gas C_5F_{12} is 12 times heavier than nitrogen, and the readily-available isobutane is 5 times heavier than nitrogen. In Table 5.1, the results show that the pressure changes with isobutane were basically identical to those with nitrogen as the radiator gas. The pressure tests using the production comparator cards showed

Table 5.1: **Pressure transients when oscillating between the radiator overpressure state and normal state with (i) prototype cards with N_2, (ii) prototype cards with C_4H_{10}, and (iii) production cards with N_2. The time constant of the prototype card is 10 msec, while that of the production card is 5.0 sec.**

gas	response time (sec)	Δp:(R-A) (Torr)	$\frac{\delta p}{\delta t}$:(R-A) (Torr/sec)
(i) N_2	0.01	0.32	0.07
(ii) C_4H_{10}	0.01	0.32	0.07
(iii) N_2	5.0	0.75	0.083

larger peak-to-peak pressure changes because of the larger response time of 5.0 sec. However, the rates of pressure change were equivalent to the tests made with the prototype cards with a response time of 10 msec as shown in Table 5.1.

When the CRID radiator is in an underpressure situation, which might be caused by a power loss in the C_5F_{12} heaters, the gas immediately begins to cool. We want to avoid condensation of the gas which occurs at $30°C$. The emergency-radiator-nitrogen valve (ERN) is used to add nitrogen automatically if the differential pressure R – A drops to −3.0 Torr, relative to atmosphere. In this test, the underpressure situation was created by using a vacuum pump on the R-cell. The manual override box was used to temporarily inhibit corrective valve action, and the system was brought to a constant pressure of approximately −5 Torr. When the system was placed in automatic mode (ie. the VME Pressure Control system was turned on) and the ERN flowmeter was opened to a set flow, the system recovered back to −3 Torr where the normal corrective valve actions took over. Figure 5.9 shows the rate of change of pressure as a function of the ERN flow. Both the D-cell and the R-cell were tested independently. It has been cal-

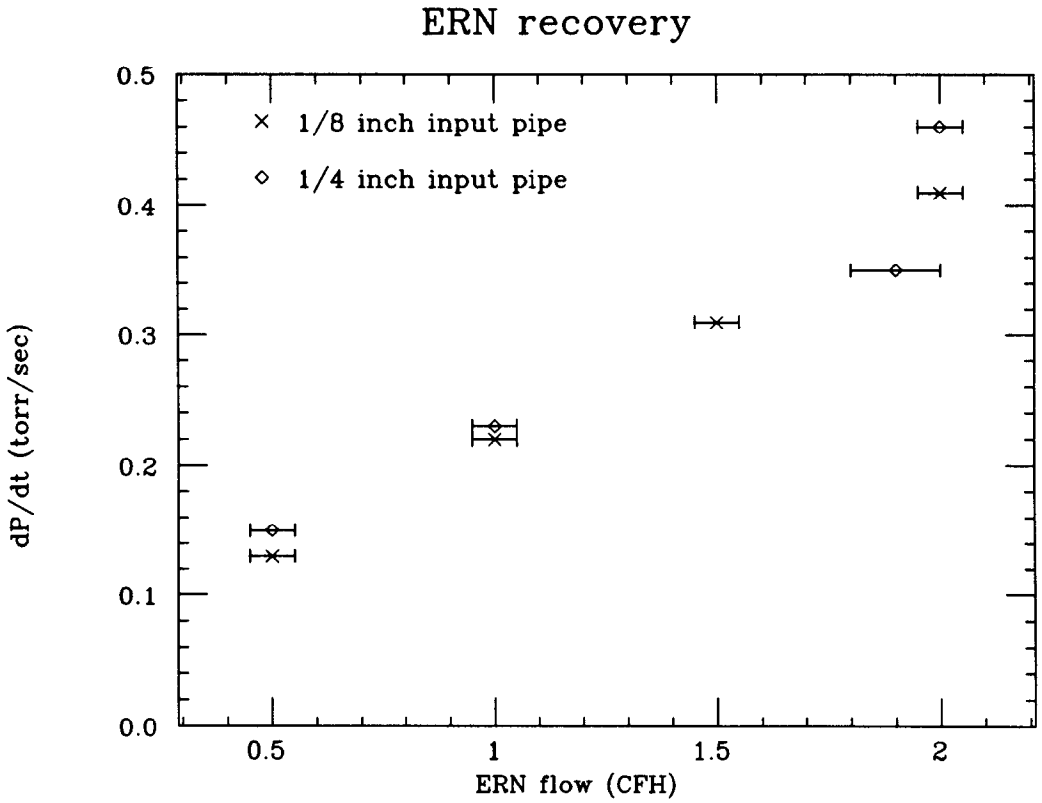

Figure 5.9: ERN recovery as a function of ERN Flow.

culated the necessary ERN input flow to avoid condensation of the C_5F_{12} [29] in the 18000 l vessel. After approximately one hour, the rate of pressure decrease due to condensation is given by $\frac{dp}{dt} = 1.3 \times 10^{-3}$ Torr/sec and an ERN flow of 1.89 l/min (or 4 ft^3/h) is required to maintain the vessel atmospheric pressure. So the simulator equivalent of the required ERN flow is 6.3×10^{-3} ft^3/h, which corresponds to $\frac{dp}{dt} = 1.3 \times 10^{-3}$ Torr/sec in the much smaller simulator volume. Thus we have tested well beyond any possible ERN recovery flows.

Extensive testing was done with the pressure control simulator to ensure that there were no surprises. The safety condition is for all valves to shut. Our testing had just begun when we had a complete failure (including power and compressed air) due to an earthquake[‖]. All were valves shut as desired. We later did more controlled and selected testing, as summarized below:

- Complete power failure/power blips;
- Compressed air failure and sudden return;
- Failure of both ±15V supplies to one or both pressure sensors of a voting pair;
- Asymmetric failure of +15V or -15V to : (a)one or both pressure sensors of a voting pair or (b) one comparator card;
- Asymmetric voltage drop of +/−15V to one or both pressure sensors of a voting pair;
- Failure of +5V supply to a comparator card, pressure control card, or valve driver;
- Voltage drop in the +5V supply to a comparator card, PCC, or valve driver;
- Cable separation during a run to a valve driver, comparator card, or PCC.

In general, the end result was that all the valves shut as desired.

[‖]Loma-Prieta earthquake, Oct. 17, 1989

5.3.2 Pressure Control Tests on the CRID Prototype

Since the 2-cell simulator does not completely simulate all the features of the gas system of real CRID, a separate test of the pressure control system on the CRID prototype was performed in addition to the two-cell simulator test. One of the outstanding differences is the use of the Mass Flow Controllers (MFC) in the CRID (and CRID prototype) to regulate the input gas flows. In the CRID gas system, MFCs are used in conjunction with pressure sensors to regulate the gas flows to the CRID radiator vessel, drift boxes, and sidewall purge spaces. Another major difference is the size of the pneumatic valves used for gas flow control. On the other hand, the prototype gas system is almost identical to the real CRID system described in Fig 5.5 except that there is no upstream radiator input valve and no MFC is used for the radiator gas flow.

In the prototype tests and in the real CRID, the system pressures were controlled by MKS Baratron** pressure sensors which send signals back to the MFC electronic controllers. For the drift box and side-space pressure control, the pressure readout was compared to the Baratron setpoint. For example, D – R pressure was compared with its MFC set point and an analog control signal was fed-back to adjust its analog valve position to set a new drift box input flow rate to bring the system towards the pressure setpoint. The operating setpoints are to be in the normal pressure range for safe CRID operation. In the prototype tests, however, we deliberately set the MFC setpoints in underpressure or overpressure conditions to simulate the abnormal pressure states in D – R and S – A. Since the prototype radiator vessel was not equipped with a MFC, the input flow was controlled by a needle valve flowmeter. The abnormal R – A pressure states were prepared by setting the radiator input flowmeter, as in the simulator tests.

The VME pressure control (PCC) system took care of the abnormal pressure states. This system works as a protection for the failure of the MFC-based analog flow regulation system and the two operations are independent. The non-

**MKS Controller (260), Flow Controller (258b) and Pressure Sensor (221b): these are chosen for high accuracy and because they work in a magnetic field.

communication between the two systems initially caused very high pressure transients. For example suppose that due to a simulated problem, which is deliberately prepared, the differential pressure between the side-wall purge space and the atmosphere (S – A) increased until it becomes larger than 1.0 Torr. Then the sidewall input flow valves (SIA in the upstream, and SIB in the downstream) are closed by PCC operation (valve state \SI). With \SI, no input gas is allowed into the sidewall purge spaces causing the differential pressure S – A to drop, possibly below the set point of the MFC pressure regulation. If the MFC is functioning, its analog valve (controlled by the sidewall pressure sensor and located between the two sidewall input flow valves) could open fully in attempt to keep S – A pressure at the set point. If S – A decreases to within the sidewall normal pressure range, $0.0 < S - A < 1.0$ Torr, then the sidewall flow valves are reopened by the PCC while the MFC analog valve stays wide open between them. Then for a short time, the sidewall input flow could be uncontrolled with all 3 valves fully open which can cause a sudden increase of the S – A pressure until the MFC and/or PCC take corrective action again. Figure 5.10 shows the S – A pressure transients under such conditions. To solve this problem, the output command from the pressure control card (PCC) to the upstream sidewall flow valve (SIA: which was opened after the downstream valve, SIB) was tied to the TTL "close" signal of the MFC valve. Then if the PCC closes SIA, the MFC for the sidewall flow is turned off automatically. Figure 5.11 shows the much reduced pressure transients in S – A with the MFC and PCC communicating this way.

In the Simulator test, all the valves used are size 1/4 inch, smaller than in the real CRID valve system. In the real system, 1/2 inch valves are used except the radiator vessel input and output valves; 1 inch for RIA (upstream input), 1.5 inch for RIB(downstream input) and 2 inch for RO (output) valves. The response of a valve to the signal from a valve driver depends on its size. The larger a valve is, the longer it takes to move its position from open to close or from close to open. With the 1.5 inch RO valve used in the prototype, which is comparable to the radiator output valve of the real CRID, the response time was about 5 seconds.

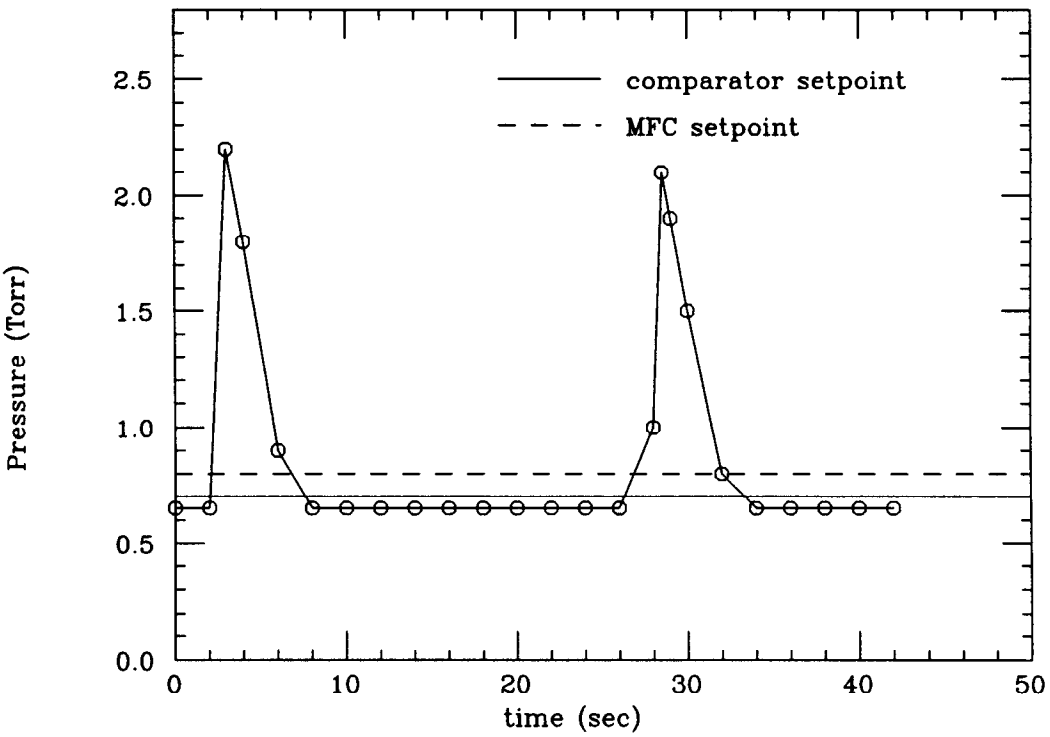

Figure 5.10: Pressure transients between sidespace and atmosphere when MFC and PCC are working independently.

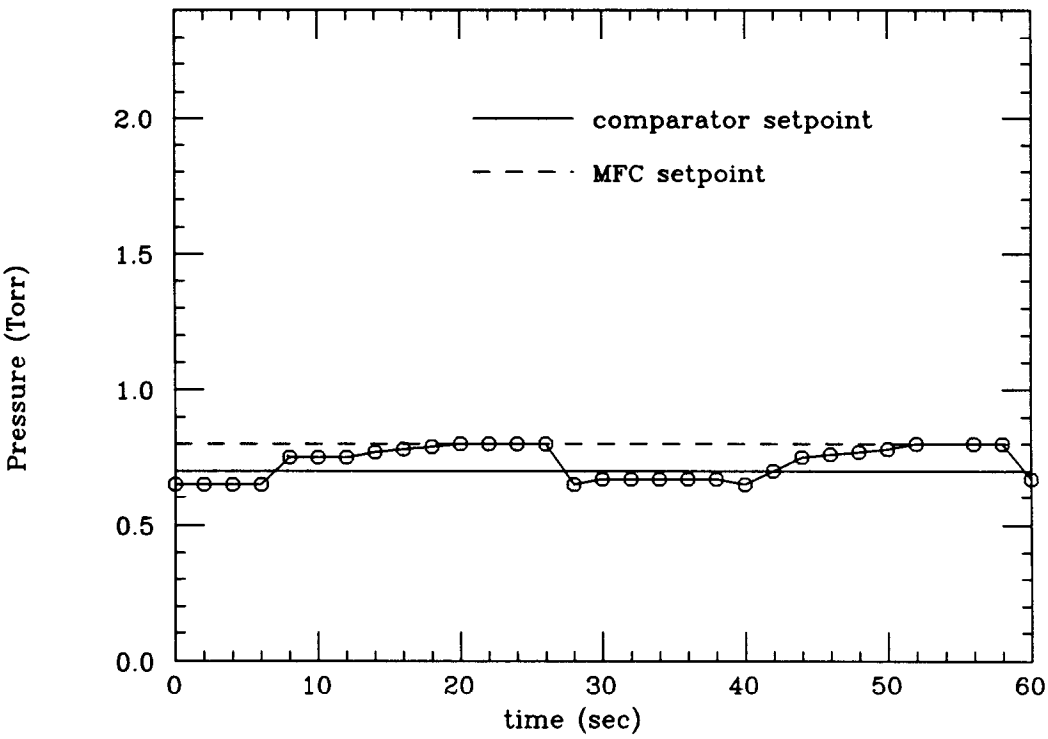

Figure 5.11: Pressure transients between sidespace and atmosphere when MFC and PCC operation are tied together.

That means the valve driver command and the micro-switch response conflicted for 5 seconds, transmitting a "Fault" signal back to the valve driver. If the fault signal lasted longer than a clock cycle, which was about 1 sec, it was latched in the valve driver and an error signal was sent to the PCC. Then the PCC shut all the control valves off attempting to lock the system in a "fail safe" configuration and stopped its operation. To avoid this problem, a circuit to generate a blanking signal was implemented in the PCC. In this circuit, a square wave signal of width about twice the response time ($\sim$ 10 sec) was generated. This square wave was synchronized with the valve action. In our test, the blanking signal was turned on when the RO valve changed its position and the fault signal from RO valve was disabled by the blanking. This way, only fault signals not associated with the slow response valve were sent to the PCC, thus keeping the PCC operation active.

By adjusting the MFC set points, the radiator input flow rate, and the set points in the Comparator Cards (CC) appropriately, we were able to create many abnormal states of the response matrix (Fig 5.7) and test the operation of the VME Pressure Control system. For example, if we set the initial condition to state B, the differential pressures D – R and R – A oscillated between states B and N via state A or D.

$$B \Leftrightarrow \begin{pmatrix} A \\ D \end{pmatrix} \Leftrightarrow N$$

Because of the oscillation, the pressure transient peaks are seen in both R – A and D – R. The pressure transient for R – A is $\sim$ 1.3 Torr and for D – R, it is $\sim$ 1.8 Torr.

Since the radiator vessel has an output valve (RO: Fig 5.5) it can take a corrective action for a R – A underpressure condition; for example RO action occurred when the system was forced into the state U (Fig 5.7). Pressure oscillations between states U and N occurred with the peak-to-peak pressure variation of R – A about 0.3 Torr.

More severe pressure anomaly situations were only simulated by changing the pressure setpoints in the comparator cards (CC). The system took the programmed action every time without failure.

The prototype ERV unit consisted of a single test tube bubbler controlled by a 1/4 inch valve. The flow capacity of this unit is small compared to the 1 qt Mason jar bubblers used for RO and autovent/autoadd. In the real CRID, a much larger bubbler is used for ERV. If the radiator pressure becomes very high, enough to make R − A > 3.0 Torr, the emergency vent valve for the radiator is opened to reduce R−A quickly. In our first test of ERV, the comparator card set point which is usually at 3.0 Torr was lowered to 1.4 Torr. The R − A pressure was forced to 1.6 Torr by keeping RI open and RO closed manually, using the manual switches in the override unit. After the pressure reached 1.6 Torr, we turned the PCC on and it immediately took a corrective action by opening ERV. The $\frac{\delta p}{\delta t}$ due to the ERV action was about $\frac{1}{72}$ Torr/sec.

The ERV test with the real design comparator setpoints and the autovent level at 4.7 Torr was also performed. Using the manual override unit, the pressure was raised to 3.4 Torr and then the PCC was turned on. The pressure drop was about 0.5 Torr for 20 sec giving $\frac{\delta p}{\delta t} \approx \frac{1}{40}$ Torr/sec.

Although many abnormal pressure states were only simulated by changing the operating conditions in anomalous ways as explained above, the VME Pressure Control system was tested on the prototype barrel CRID and proven to work as programmed in all the 25 states in the pressure response matrix (Fig 5.7).

5.4 Binary Gas Mixture Monitoring using Sonar

Since the radiator volume is purged of air by N_2 before being filled with a mixture of N_2 and C_5F_{12}, the index of refraction of the gas radiator varies as a function of the concentration of C_5F_{12} in N_2 in the vessel. To determine the effective Cherenkov thresholds, either a direct measurement of the index of refraction or a measurement of the mixture of C_5F_{12}/N_2 has to be made. To directly measure the index of refraction in the UV requires an expensive optical interferometer and very accurate control of the temperature and pressure of the sample. On the other hand using gas chromatography to determine the mixture is also expensive and needs a

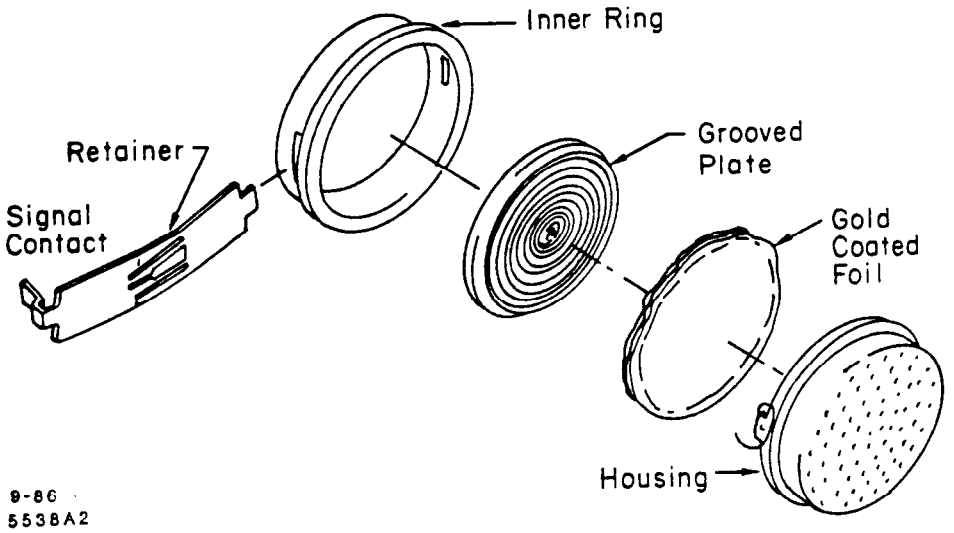

Figure 5.12: The cut-away view of the Polaroid Corporation ultrasonic transducer.

high level of operator supervision. Meanwhile, a new technique using ultrasound velocity measurement (hence it is called the 'sonar' system) was developed[30] for the CRID gas system. Since it requires only the measurement of a time interval between the transmitted and received ultrasound pulses and knowledge of the temperature of the sample gas, neither any expensive equipment nor a high level of operator supervision is demanded.

In general, the sound velocity of a gas depends on the density, pressure, and temperature. If the pressure and temperature are kept constant, the sound velocity is a function of the gas density. Therefore, it is presumed that the sound velocity of a binary gas mixture is a function of the concentration of the mixing ratio. In fact, there are theoretical models that give the sound velocity of binary gas mixtures in terms of the mixing ratio; some of these models are discussed in detail in the original paper on this sonar device[30].

In the CRID sonar system, the sample gas is admitted to an aluminum tube

of an 8 cm diameter that contains two ultrasonic transducers accurately located a known distance apart. A typical length of a sonar tube used in the barrel CRID ranges about $1 \sim 1.5$ m. The major components of the sonar tube are the two ultrasonic transducers from Polaroid Corporation [31]. The device, originally designed for application in the range finder of an autofocus camera, can be operated both as an electrostatic loudspeaker and microphone. Figure 5.12 shows a cut-away view of the transducer. The insulating side of a 3.8 cm gold-coated plastic foil is stretched across a grooved metallic plate to form a capacitor which when charged, exerts an electrostatic force on the foil. In the transmitter mode, in which the unit works as a loudspeaker, the charging effect of the AC pulse train produces the sound oscillations. In the receiver mode, where it works as a microphone, the transducer is generally operated with a bias voltage of between $+50 \sim +150$V DC applied to the grooved electrode, the foil being grounded. The net force acting on the foil is modified by an incoming sound wave train, which alters the transducer capacitance producing an AC output signal. The transducer driving circuit and receiver circuit are designed by H. Kawahara for CRID multichannel application. Figures 5.13 and 5.14 show the schematic diagrams of the driver and receiver circuit, respectively.

Figure 5.15 is a block diagram of a CAMAC module that controls the 8-channel sonar driver and readout electronics used in the barrel CRID sonar system. Eight pulses of a 45 kHz ultrasonic sound wave are passed through the sample gas to be detected at the receiving end of the sonar tube. A 4 MHz readout clock is started on the leading edge of the transmitted pulse envelope and is stopped by the amplified and discriminated output of the receiving transducer. The transit time is recorded in the CRID slow-monitoring workstation through a 24-bit counter. The sound velocity is then calculated easily:

$$v_s = \frac{d}{N \times (4\ \text{MHz})^{-1}}\ \text{m/sec}$$

where d is the known distance (in meters) between the transmitting and receiving transducers, and N is the recorded count of 4 MHz readout clock pulses. The

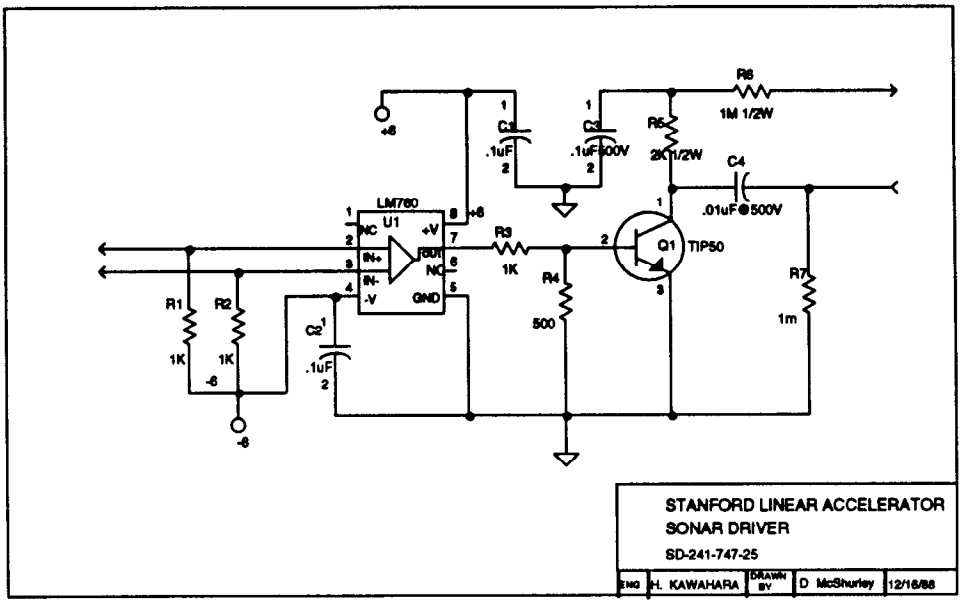

Figure 5.13: The schematic diagram of the sonar driver circuit.

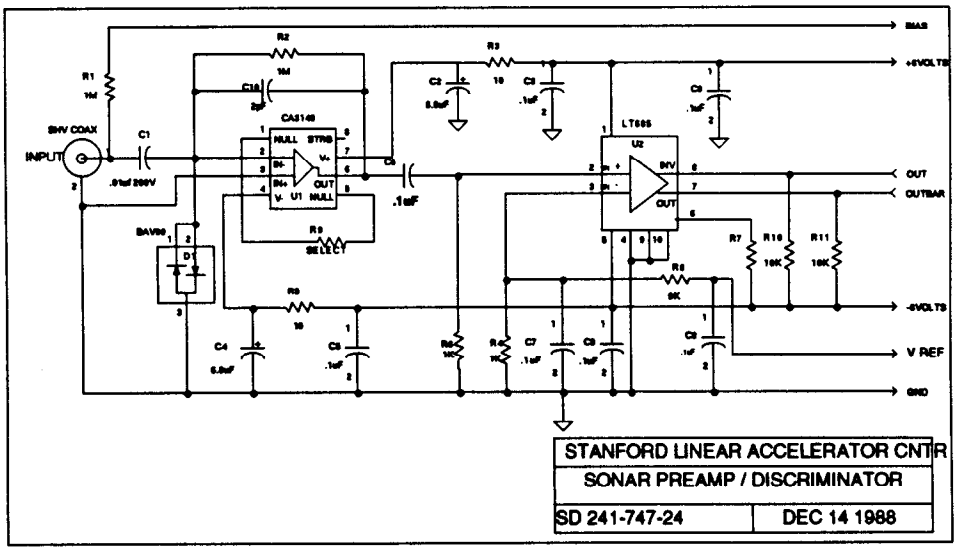

Figure 5.14: The schematic diagram of the sonar preamplifier circuit.

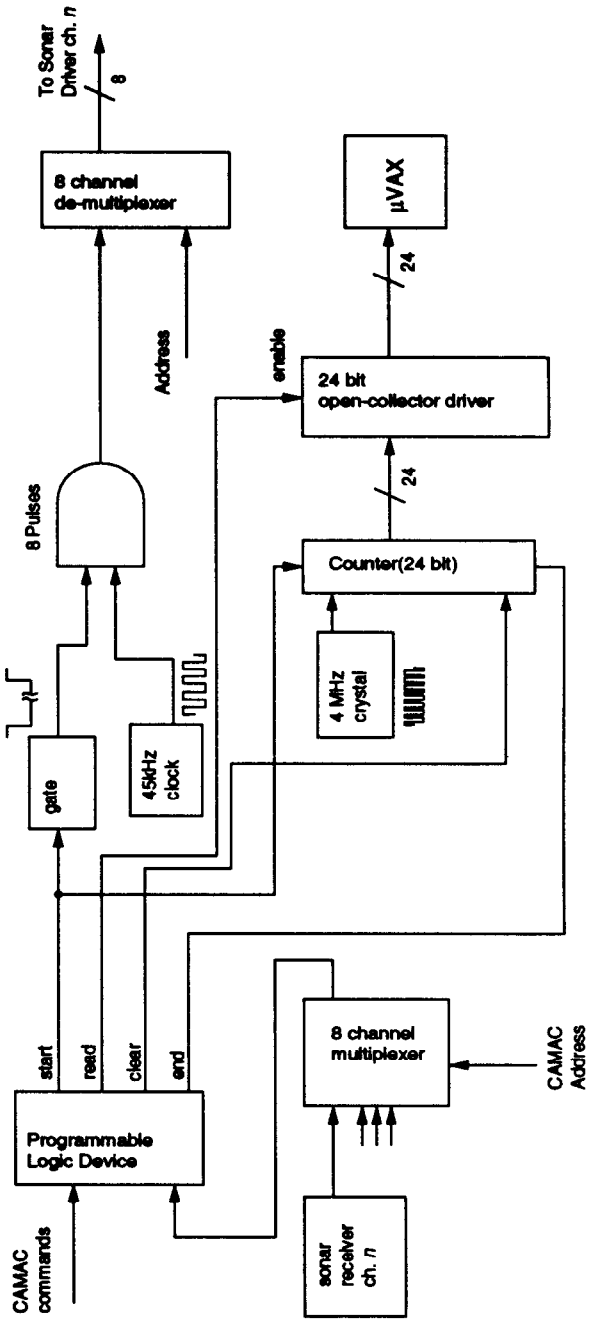

Figure 5.15: The block diagram of the multi-channel sonar CAMAC module.

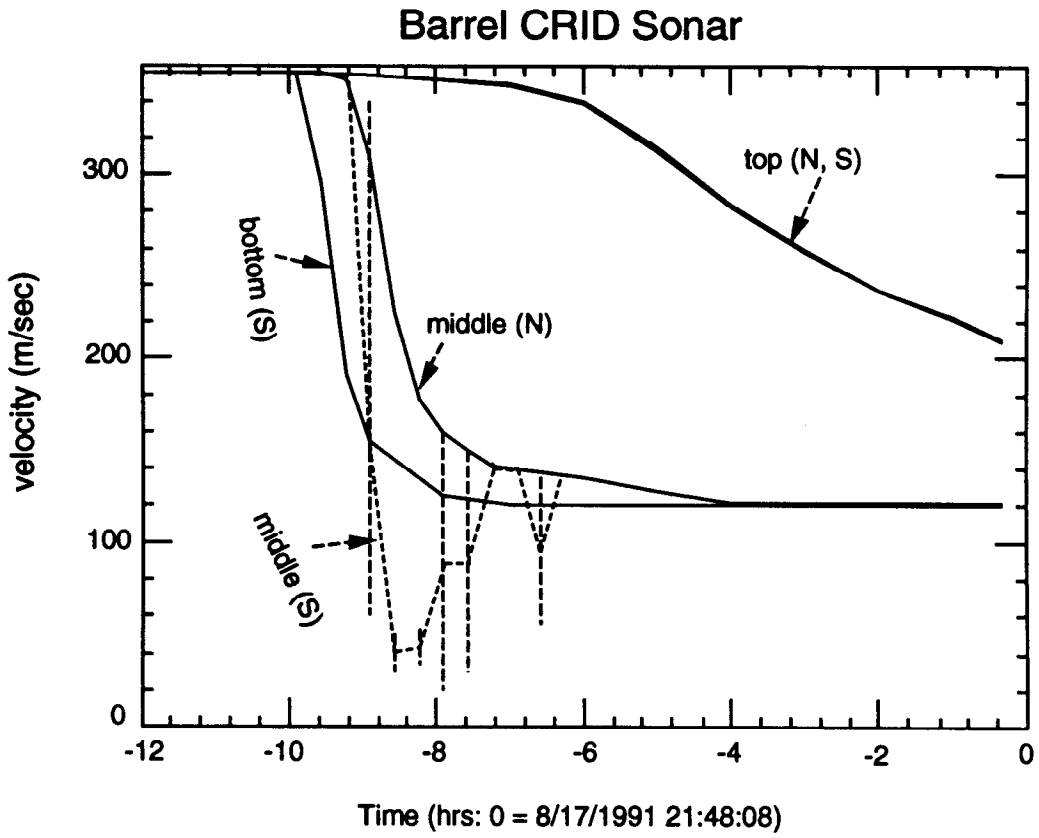

Figure 5.16: The barrel CRID sonar time-history at one point of the SLD engineering run.

8-channel sonar system is installed in the barrel CRID system. Currently, 6 channels are operational; 3 each for north- and south- side of the barrel, covering the top, middle, and bottom parts of each side. Figure 5.16 shows the time-history histogram of the barrel CRID sonar readout at one point of the SLD engineering run, August 1991[32]; it was when the C_5F_{12} gas was first let flow into the CRID filling in the barrel radiator volume by replacing the N_2 purge gas. Although there are 6 sonar tubes installed in the barrel CRID radiator, only 5 channels of data are displayed in the histogram because at that time the radiator-bottom-north channel was not operational due to a connection problem, which was later fixed when the SLD door re-opened after the run. The x-axis of the histogram is the time in hours with respect to 9:48:08 pm, Aug. 17, 1991. The y-axis is the sonar-measured sound velocity in the barrel CRID gas radiator at various locations. Before the C_5F_{12} flowed in, all channels read approximately $\sim$ 355 m/sec, corresponding to pure N_2 at $\sim$ 30°C. As the concentration of C_5F_{12} increased towards 50-50 mixture of C_5F_{12} and N_2, the sound velocity dropped towards 120 m/sec. The sound velocity of pure C_5F_{12} at 30°C is $\sim$ 92 m/sec. The sound velocity in the radiator-bottom dropped fastest while the radiator-top showed the slowest sound velocity drop. This is consistent with the expectation that since C_5F_{12} is much heavier than the N_2 it would fill the bottom part of the barrel first and the top portion last. The south-middle channel showed some erratic behavior (dashed curve in Fig 5.16) for the first few hours of the C_5F_{12} fill-up. The reason for this is not fully understood. It could be either a readout failure - weak receiving signal that did not overcome the discriminator set level - or CO_2 contamination inside the barrel which absorbs ultrasonic waves very strongly[††].

[††]During the initial phase of the engineering run before C_5F_{12} recirculation system was commissioned, the CRID barrel was filled with CO_2 to allow high-voltage operation

Chapter 6

First Results from the SLD CRID

The first results of CRID operation from the 1991 engineering run and the 1992 physics run of the SLD experiment at the SLC are reported in this chapter. Most of the material discussed in this chapter have been presented previously at several conferences[33].

6.1 Commissioning of CRID

The CRID system was commissioned in 1991 during the SLD engineering run. All 400 mirrors, 40 liquid radiator trays, drift boxes, and detectors were installed before the engineering run. The front-end electronics, FASTBUS data acquisition modules, and software systems were debugged during the run. The fiber optics calibration system was in place and was used extensively to monitor the drift box performances. The temperature control system was operated at 30°C rather than the nominal 40°C, because of concerns about protection of the central drift chamber in case of cooling failure. Initially, the barrel vessel was filled with CO_2 to allow high voltage operation while the radiator fluid systems were being commissioned.

For the drift gas, CP-grade C_2H_6 doped with 0.1% (by volume) of TMAE was

used. The ethane gas was passed through filters, a combination of 13X Molecular Sieve[34] and Oxysorb[35] to remove oxygen, water vapor, and other contaminants. The quality of the gas was monitored on return lines from the drift boxes by measuring electron lifetimes, UV transparency, and trace oxygen and water vapor content. The data in Fig. 6.1(a) show that for most of the drift boxes, the O_2 level is about 0.7 ppm. However, there are six boxes with significantly higher O_2 levels, about 1.2 ppm. The effects were found to be caused by leaks in the return lines, as verified by changing the gas flow through those lines. A typical water vapor level was below 5 ppm.

After acceptably low levels of O_2 and H_2O were demonstrated, TMAE was introduced into the drift boxes. The drift gas was bubbled through 15°C liquid TMAE. Once TMAE was introduced, the electron lifetimes were measured using a miniature ionization chamber[36]. The measurements in Fig. 6.1(b) show that a typical lifetime is about 200 μsec, which is above the minimum 150 μsec. There was no degradation of lifetime due to the leaks detected by the O_2 monitor even when a highly electronegative C_5F_{12} gas was later introduced into the gas radiator volume, as indicated by the dark points in Fig 6.1(b).

By the end of the run, a 50-50 mixture of C_5F_{12} and N_2 was introduced into the CRID. It has a condensation point below room temperature and was, therefore, safe to use in the 30°C CRID vessel. The homogeneity of the gas mixture was determined to be better than 1% by sonar monitoring.

The liquid radiator recirculation system was also commissioned at the end of the run. The quality of the liquid was monitored extensively offline by measuring the UV transparency. Six trays were then filled with liquid C_6F_{14}.

A UV fiber-optic system attached to all 40 drift boxes was used to monitor the photoelectron drift and check the charge division. The arrangement of 19 fibers on each drift box is shown in Fig 3.9(b). Eight fibers, indicated by dots in the figure, are directed perpendicular to the quartz window and are used to monitor the electron drift velocity. The remaining fibers (indicated by arrows in the figure) are tilted by 45° with respect to the window. The four fibers closest to the detector

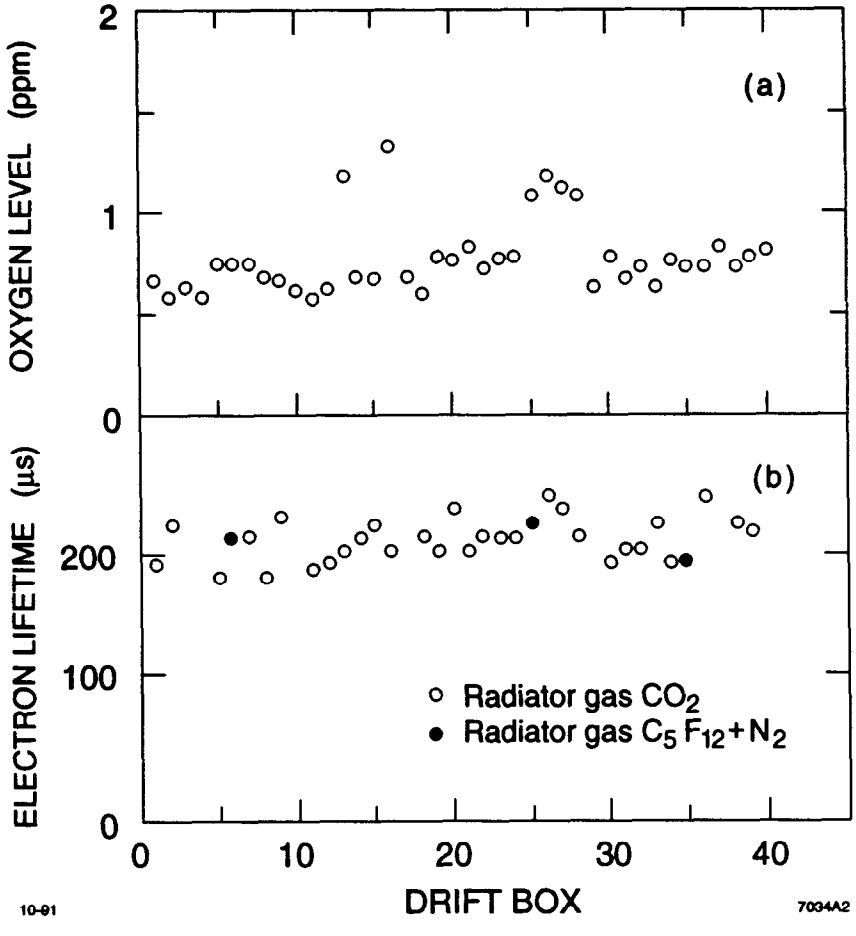

Figure 6.1: (a) Trace oxygen levels before the introduction of TMAE for all 40 drift box return lines. (b) Electron lifetimes as measured by a miniature ionization chamber for the return gas from all the drift boxes.

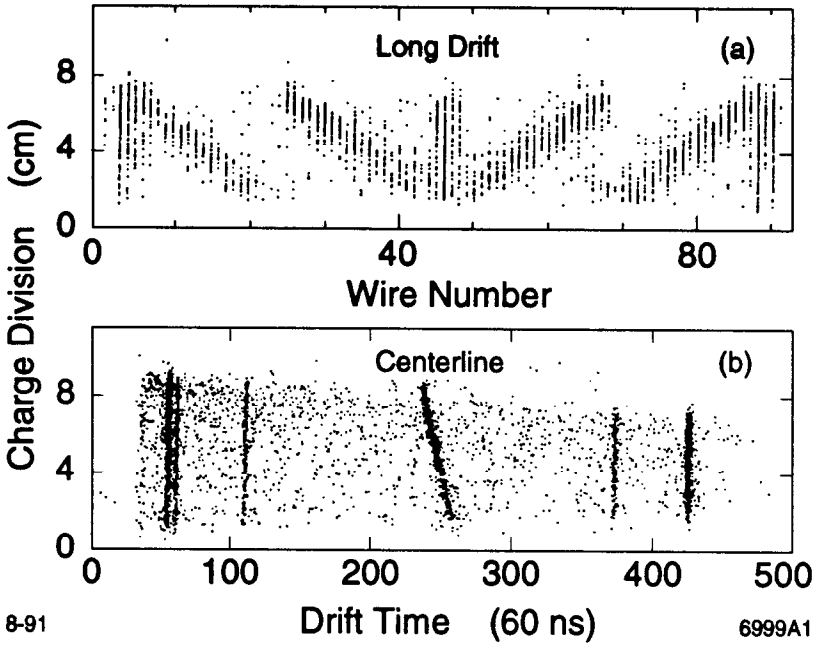

Figure 6.2: Results from UV fiber system: (a) in a plane parallel to the detector wire plane; and (b) in a plane down the middle of the drift box.

are used to check the charge division calibration. The remaining seven are used to measure the drift path distortions in the depth coordinate. All fibers monitor the distortions in the width coordinate.

The patterns of the single electron hits from the fibers, shown in Fig 6.2, were as expected; this demonstrates not only that single electrons are observed, but also that the charge division coordinate is being well reconstructed and there are no serious distortions in the drift paths.

Figure 6.3 shows the UV-measured drift velocity averaged over 17 operational drift boxes as a function of time, over the entire physics run. Large variations ($\sim$2 %) of the drift velocity were observed, which shows that a continuous logging of the fiber data was indeed necessary. If uncorrected, these variations would cause an error of $\sim$2 cm in position measurement, while the design specifications call for an error of 1 mm.

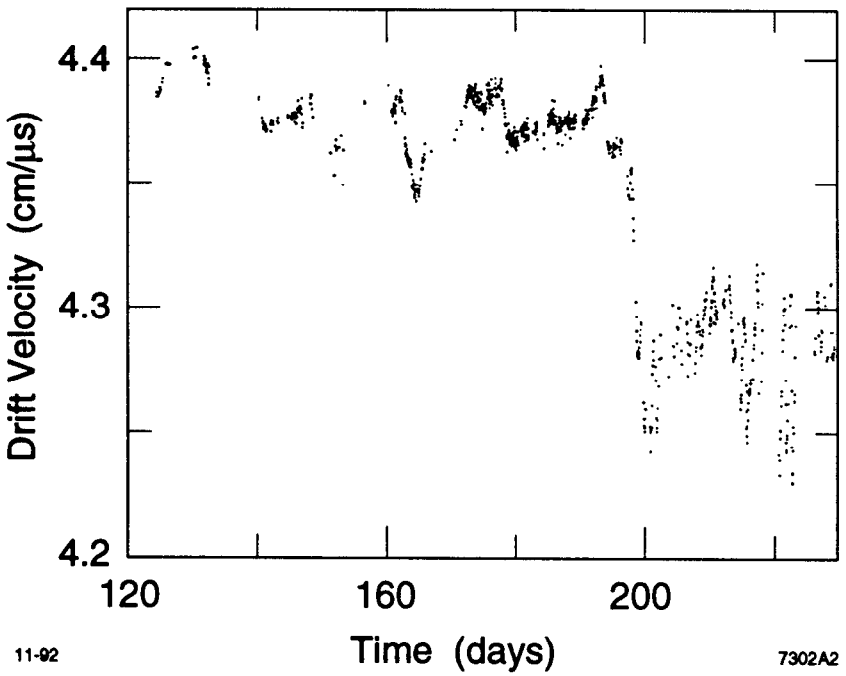

Figure 6.3: Variation of the drift velocity over the entire physics run.

6.2 Observation of the Cherenkov rings

Cherenkov rings have been observed from both radiators in the cosmic ray runs and physics runs during the 1992 SLD physics run. For the cosmic ray runs, the SLD Warm Iron Calorimeter provided the cosmic muon trigger for the CRID and the central drift chamber.

Figures 6.4(a),(b) and (c) show integrated gas rings for cosmic ray muons, Bhabha electrons, and pions from hadronic events, respectively with momenta higher than 7 GeV/c. The radiator gas used for the presented data is 70-30 mixture of C_5F_{12} and N_2. Figures 6.5(a) and (b) show the measured Cherenkov angle resolution and the number of photoelectrons per ring in the case of cosmic ray muons. The results are similar for Bhabha and hadronic events. The measured Cherenkov angle resolution is about 4 mrad, which is close to the expectation. The average number of photoelectrons per ring is typically 10, consistent with the expectation for the particular radiator gas mixture used. The gas rings are well separated from the dE/dx hits by means of the mirror optics design.

Figure 6.6 shows integrated liquid rings for the cosmic ray muons. In Fig 6.6(b), where the events with a partial ring is displayed, also seen are the dE/dx hits and the Cherenkov rings from quartz windows. The average number of photoelectrons per full liquid ring (Fig 6.6(a)) is about 17, consistent with the expectation. The result is similar for the liquid rings observed in Bhabha events. The Cherenkov angle resolution is about factor two larger than expected, mainly because of alignment problems.

The CRID analysis efforts have just begun, and many factors have yet to be fully understood; such as, drift velocity variation, charge division offsets, distortion along the edges of drift boxes, distortions due to the radial component of the magnetic field, mirror alignment, and the drift box alignment with respect to the drift chamber alignment. Nevertheless, the SLD CRID performed very well producing Cherenkov rings from both liquid and gas radiators with good efficiency and resolution. However, it will still take a substantial amount of time and efforts

to align the system and understand other software corrections before the CRID is fully functional as a particle identification device to study the Z° events.

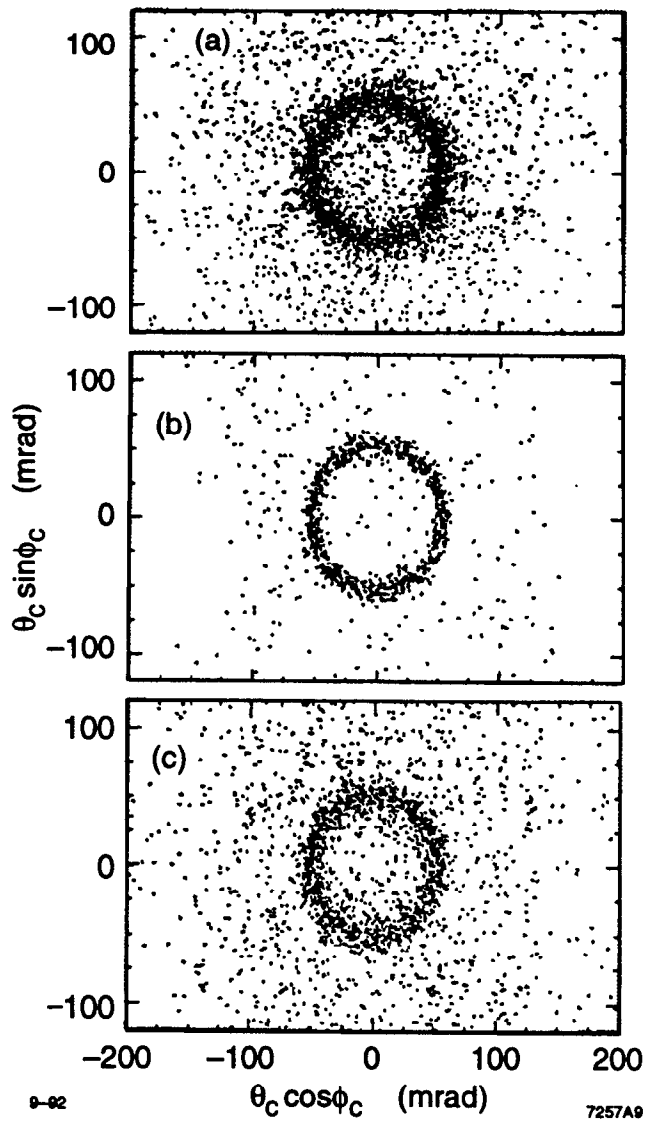

Figure 6.4: Integrated gas Cherenkov rings observed in (a) cosmic ray muons, (b) Bhabha electrons, and (c) pions from hadronic events, for $p > 7$ GeV/c.

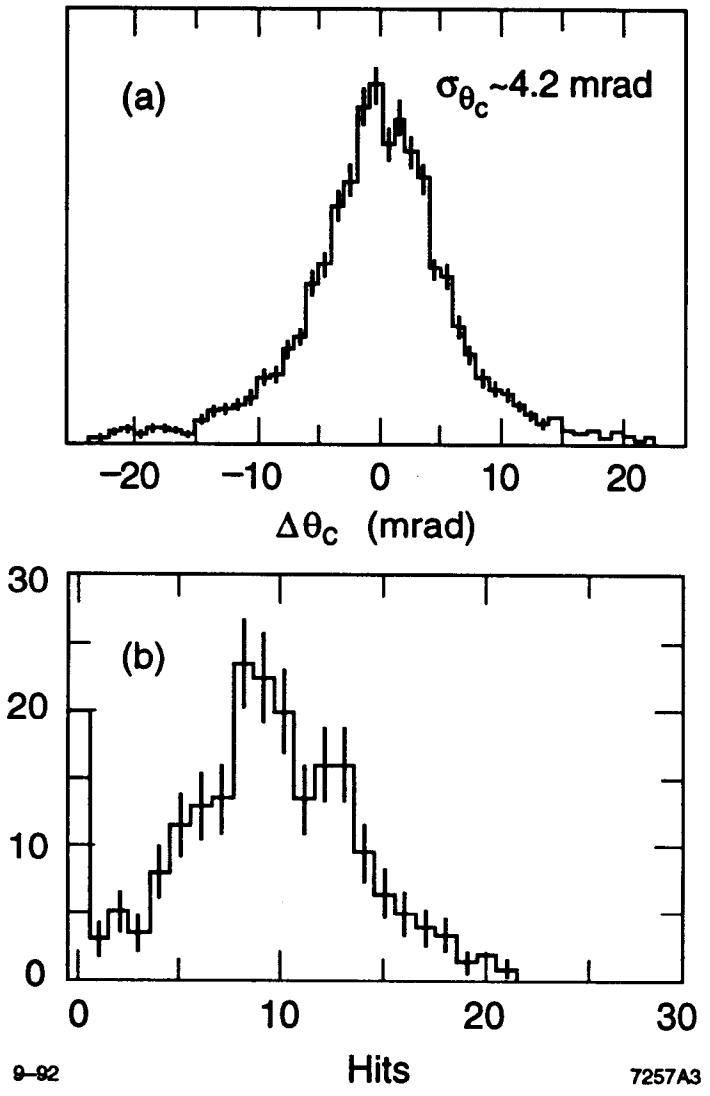

Figure 6.5: (a) Resolution in Cherenkov angle from gas radiator, and (b) number of photoelectrons per gas ring, from cosmic ray muons.

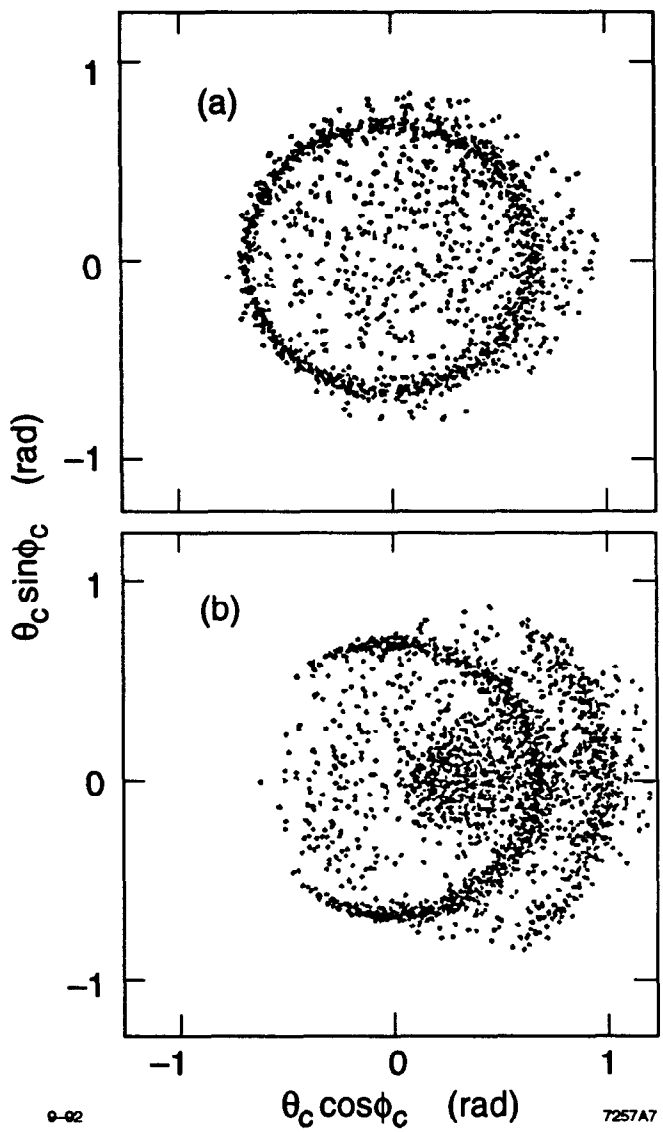

Figure 6.6: Integrated liquid Cherenkov rings observed in cosmic ray muons: (a) for tracks with a full ring; and (b) with a partial ring

Chapter 7

Introduction to Part II

Light-quark meson spectroscopy has been studied for many years, but it remains an interesting field for several reasons. Even with strong evidence for the quark model from many experimental studies, the correct $q\bar{q}$ quark model assignments of all the known mesons are far from clear and complete. There is considerable controversy in the classification of the observed states and experimentally "missing" ones as well. Table 7.1, compiled by the Particle Data Group (PDG), shows the suggested $q\bar{q}$ assignments of the observed mesons. The controversial aspect of the problem is clearly stated in the Review of Particle Properties[37]:

> *Some assignments, especially for the* 0^{++} *multiplet ... are controversial. ... the* $f_1(1420)$, $f_0(1590)$, $f_2(1520)$, $f_2(2300)$, $f_2(2340)$ *and the two peaks in the* $\eta(1440)$ *entry are not in this table. It is especially hard to find a place for the first four of these f mesons or for one of the* $\eta(1440)$ *peaks in the* $q\bar{q}$ *model.*

These controversial states could indicate either our lack of understanding in the strong interactions or evidence for non-$q\bar{q}$ states of mesonic matters. Moreover, there are a number of predicted states that have yet to be experimentally observed. These missing states are indicated as many empty slots in the Table 7.1. Especially, it should be noted that, out of the 11 ground-state ($N = 1$) spin-orbital configurations ($^{2S+1}L_J$) listed in the table, each of which has 9 slots to fill due to

Table 7.1: The $q\bar{q}$ quark-model assignments for most of the known mesons suggested by the Particle Data Group.

$N\,^{2S+1}L_J$	J^{PC}	$u\bar{d}$, $u\bar{u}$, $d\bar{d}$ $I=1$	$u\bar{u}$, $d\bar{d}$, $s\bar{s}$ $I=0$	$c\bar{c}$ $I=0$	$b\bar{b}$ $I=0$	$\bar{s}u$, $\bar{s}d$ $I=1/2$	$c\bar{u}$, $c\bar{d}$ $I=1/2$	$c\bar{s}$ $I=0$	$\bar{b}u$, $\bar{b}d$ $I=1/2$
$1\,^1S_0$	0^{-+}	π	η, η'	η_c		K	D	D_s	B
$1\,^3S_1$	1^{--}	ρ	ω, ϕ	$J/\psi(1S)$	$\Upsilon(1S)$	$K^*(892)$	$D^*(2010)$	$D_s^*(2110)$	$B^*(5330)$
$1\,^1P_1$	1^{+-}	$b_1(1235)$	$h_1(1170)$, $h_1(1380)$			K_{1B}	$D_1(2420)$	$D_{s1}(2563)$	
$1\,^3P_0$	0^{++}	$a_0(980)$	$f_0(1400)$, $f_0(975)$	$\chi_{c0}(1P)$	$\chi_{b0}(1P)$	$K_0^*(1430)$			
$1\,^3P_1$	1^{++}	$a_1(1260)$	$f_1(1285)$, $f_1(1510)$	$\chi_{c1}(1P)$	$\chi_{b1}(1P)$	K_{1A}			
$1\,^3P_2$	2^{++}	$a_2(1320)$	$f_2(1270)$, $f_2'(1525)$	$\chi_{c2}(1P)$	$\chi_{b2}(1P)$	$K_2^*(1430)$	$D_2^*(2460)$		
$1\,^1D_2$	2^{-+}	$\pi_2(1670)$							
$1\,^3D_1$	1^{--}	$\rho(1700)$	$\omega(1600)$	$\psi(3770)$		$K^*(1680)$			
$1\,^3D_2$	2^{--}					$K_2(1770)$			
$1\,^3D_3$	3^{--}	$\rho_3(1690)$	$\omega_3(1670)$, $\phi_3(1850)$			$K_3^*(1780)$			
$1\,^3F_4$	4^{++}	$a_4(2040)$	$f_4(2050)$, $f_4(2220)$			$K_4^*(2045)$			
$2\,^1S_0$	0^{-+}	$\pi(1300)$	$\eta(1295)$	$\eta_c(2S)$		$K(1460)$			
$2\,^3S_1$	1^{--}	$\rho(1450)$	$\omega(1390)$, $\phi(1680)$	$\psi(2S)$	$\Upsilon(2S)$	$K^*(1410)$			
$2\,^3P_2$	2^{++}		$f_2(1810)$, $f_2(2010)$		$\chi_{b2}(2P)$	$K_2^*(1980)$			
$3\,^1S_0$	0^{-+}	$\pi(1770)$	$\eta(1760)$			$K(1830)$			

the variations in flavor and isospin components, only one is completed, namely $1\,^3S_1$.

However, the basic interest in studying the meson spectroscopy goes beyond searching for the missing pieces and filling up the appropriate table. There are cases in the history of science that a thorough empirical study of a specific subject have lead to a big leap in our understanding of the underlying principles of nature: for example, in the days of 'earth-centered cosmology', there were a huge accumulation of observed data on the motion of planets and Keppler found the principles of planetary motions based on this data which eventually lead to the Newton's law of gravitation. The spectroscopy of mesons is expected to play a similar role. We should experimentally measure enough of the spectrum to be reasonably sure that we really understand the origin of the spectrum of states produced in nature: the ordering, the mass splitting, the decay pattern, etc.

Although the standard model describes the strong interaction of matter with a QCD-based gauge theory, it has yet to provide the way to apply this to actually calculate the observed meson spectrums. The non-relativistic potential models, so successful with the heavy-quark systems, cannot be extended to the light-quark systems without introducing substantial uncertainties due to relativistic effects. Even in the charmonium system where a non-relativistic model seems to work well, quarks typically have velocities already about a third of the speed of light; it is difficult to justify applying such a model unaltered in an even more relativistic regime. Because of these problems, the spectroscopy of the light-quark mesons is still confused and it is important to extend our experimental understanding of mesons so that the systematics can be better understood an new directions for theoretical work can be established.

Some of the questions raised above, e.g. the existence of non-$q\bar{q}$ mesonic states could be answered by a direct discovery of a state with exotic quantum numbers which would not be allowed in the $q\bar{q}$ spectrum. On the other hand, to identify the exotic matters calls for an even more thorough understanding of the standard $q\bar{q}$ states, since the standard $q\bar{q}$ states are backgrounds in searches for the exotics. This might better be done with systematic studies of mesons of a specific type, finding all of the candidate states in the $q\bar{q}$ family. If other states are left over – with properties not expected, nor required by the $q\bar{q}$ picture – the production of non-$q\bar{q}$ states could be confirmed. Moreover, the search for missing pieces in the standard $q\bar{q}$ system would be fulfilled much more efficiently in such a systematic, programmatically prepared experiment.

An interesting fact in planning such spectroscopy experiments is that there are many states to be observed, most of which are broad in width and with rather small mass-splittings. This implies that it may not always be possible to find the states as nice clean peaks in a cross-section, but rather we will have to study the details of the scattering amplitudes and measure its interference patterns, in order to piece together a full picture of the meson spectrum. This requires a very large sample of clean undistorted events necessitating a spectrometer of high-efficiency

with the capability of uniformly covering the relevant phase-space.

This is exactly what the series of experiments, performed at SLAC using the LASS spectrometer[38] and culminated by the E-135 experiment, has aimed at. These experiments all used kaon beams (K^+, K^-) on a proton target and analyzed the resulting strange or strangeonium systems depending on the strangeness content of the recoiling baryon. In fact, there are many advantages of this set-up. With a high-intensity incoming beam, the fixed target system can collect a high-statistics sample of events in a much shorter period than the colliding beam set-up. Compared to the non-strange light-quark systems, the expected spectroscopy of strange meson system is simpler because:

- the strange mesons have fewer open decay channels;
- pure glueball states are not possible;
- the neutral states are free from ambiguities inherent in the isoscalar/isovector sectors.

These advantages may apply to any experiment using high-intensity flavored beam on a fixed target. In reality, high-intensity beams of charm- or bottom-flavored particles are not easily made or maintained. A strange particle beam is the only realistic choice.

The LASS experiments have observed many new states and confirmed many other existing states with event samples of unprecedentedly high statistics in the strange meson sector. The number of strange meson states observed by LASS is quite large[39], with orbitally excited states up to 5^- and with a significant number of triplet and radially excited candidates. However, the expected level structure is only complete for the S-wave ($L = 0$) and P-wave ($L = 1$) ground states. In fact it is only for the ground state P-wave sector that both singlet and triplet states are fully understood. Table 7.1 shows that there is an obvious absence of states in the D-wave $J^P = 2^-$ sector. Although a strange meson state of $J^P = 2^-$, $K_2(1770)$, has been observed in several experiments[40], no experiment has been able to resolve the singlet and triplet states. If these states were observed, the D-wave

multiplet would be complete, and this would considerably sharpen comparison of the experimental data with models of the level structure[41], particularly as they concern spin-dependent forces. This sets the main goal of the second part of this thesis: the $J^P = 2^-$ strange meson state is studied along with other states that could be simultaneously studied using a partial wave analysis (PWA).

The 2^- is one of the unnatural spin-parity (J^P) series which also includes $0^-, 1^+, 3^+$, etc. Because of a J^P selection rule, a meson of unnatural J^P cannot have a two-body decay into two pseudoscalars such as $K\pi$. Therefore, to study 2^-, we have to look for the final states that contain pseudoscalar + vector mesons or at least three pseudoscalar particles. For the latter, $K\pi\pi$ system has been studied in the reaction $K^-p \to \overline{K}^\circ\pi^+\pi^-n$ but no 2^- state is observed[42]. This channel has a recoiling neutron in the final state implying that the system is most likely produced by pion exchange where unnatural J^P mesons are not produced.

For the pseudoscalar + vector system, $K\omega$ channel is readily accessible in the reaction $K^-p \to K^-\pi^+\pi^-\pi^0p$. Although this channel has been investigated by several experiments in the past, all those analyses are limited by statistics. However, this system is produced copiously and reconstructed very efficiently in E-135[43] at least 25 times more than in any other experiments. Since it has a proton recoil, most of it is to be produced not from π-exchange but from diffractive processes. Therefore, we expect substantial production of unnatural J^P mesons in this reaction making it possible to study 2^- states in detail. With the narrow resonance of ω in the final state $\pi^+\pi^-\pi^0$, it is possible to use a PWA based on joint-decay moments[44] with a proper background-subtraction. The advantage of this method over the three-body PWA[45] which were used in the E-135 analysis of the reaction $K^-p \to \overline{K}^\circ\pi^+\pi^-n$ is that the background events are more properly treated and the quality of PWA fits is better understood by means of the χ^2 value of the fitted moments.

As a by-product of PWA, strange mesons other than 2^- are also observed in the $K\omega$ system and analyzed with high-statistics. These results, compared with other results from E-135 – being from the same experiments, much of the systematic

uncertainties can be eliminated – can be used to check the flavor SU(3) in the decays of light quark mesons.

In addition to the $K^-\omega$ system, the $\overline{K}^\circ\phi$ system has been studied by analyzing the reaction $K^-p \to \overline{K}^\circ\phi n$. Being similar to the reaction $K^-p \to \overline{K}^\circ\pi^+\pi^-n$, it gives another opportunity to check SU(3) and provides an interesting look of a system whose production is expected to be quite suppressed. In fact, the cross-section of the $\overline{K}^\circ\phi n$ final state in E-135 is small, and the detailed understanding of this channel may not be possible, as PWA requires a very large event sample when the number of amplitudes produced is large.

Although it has not been analyzed in this thesis, the diffractive 3-body process $K^-p \to K^-\pi^+\pi^-p$ is as good a place to study the unnatural J^P mesons as $K^-p \to K^-\pi^+\pi^-\pi^0p$. The cross-section in E-135 is very large. It is hoped that this channel should be studied by someone, either to give a new understanding or to confirm the current understanding of the strange meson spectroscopy.

The second part of this thesis presents new results in the spectroscopy of strange mesons obtained by analyzing the reactions $K^-p \to K^-\pi^+\pi^-\pi^0p$ and $K^-p \to \overline{K}^\circ\phi n$ from E-135. It is organized as follows: The LASS spectrometer is described in Chapter 8 along with the trigger, data acquisition, and the calibration processes. The event selection processes of the reaction $K^-p \to K^-\pi^+\pi^-\pi^0p$ and general features of the $K^-\omega$ data are presented in Chapter 9. The formalism of join-decay moments is reviewed and the measured moments of $K^-\omega$ system is presented. Chapter 10 describes the event selection, data features, and measured moments of the reaction $K^-p \to \overline{K}^\circ\phi n$. Similar formalism of joint-decay moments as in the $K\omega$ analysis is used but with a minor modification in the definition of the frame of reference. The formalism of PWA based on joint-decay moments is reviewed and the results of $K^-\omega$ and $\overline{K}^\circ\phi$ analyses are presented in Chapter 11. The results are discussed in regard to the impacts on the strange meson spectroscopy, and are summarized in Chapter 12.

Chapter 8

The LASS Spectrometer

The Large Aperture Superconducting Solenoid spectrometer (LASS) was built and operated at the Stanford Linear Accelerator through 1982, primarily for the purpose of studying the strong interactions involving strange quarks. An overview of the LASS is shown in Fig. 8.1 and a complete description of the spectrometer is presented elsewhere[38]. The experiment E-135 took data with both K^- and K^+ beams during 1981 and 1982. A total of 1.4×10^8 triggered events are recorded in LASS. K^- beam triggered events are about 4 times as many as K^+ beam triggered events. Event reconstruction was performed at SLAC and Nagoya University in Japan, which required the equivalent of two CPU years on SLAC's two-CPU IBM 3081K. Reconstruction finished in 1985 resulted in $\sim$ 1000 data summary tapes (DST).

The spectrometer consists of two main parts: the dipole region and the solenoid region. The former is a classical forward spectrometer with a large aperture dipole magnet, tracking chambers, and a pressurized gas Cherenkov counter, which measures the fast forward particles. The latter is a target spectrometer which consists of a 1m long liquid hydrogen target surrounded by cylindrical proportional chambers, planar tracking chambers, time-of-flight (TOF) hodoscope and Cherenkov counters all inside a 22.4 kG superconducting solenoid magnet, where the slow and large angle particles produced in the Kp reactions are measured. A good

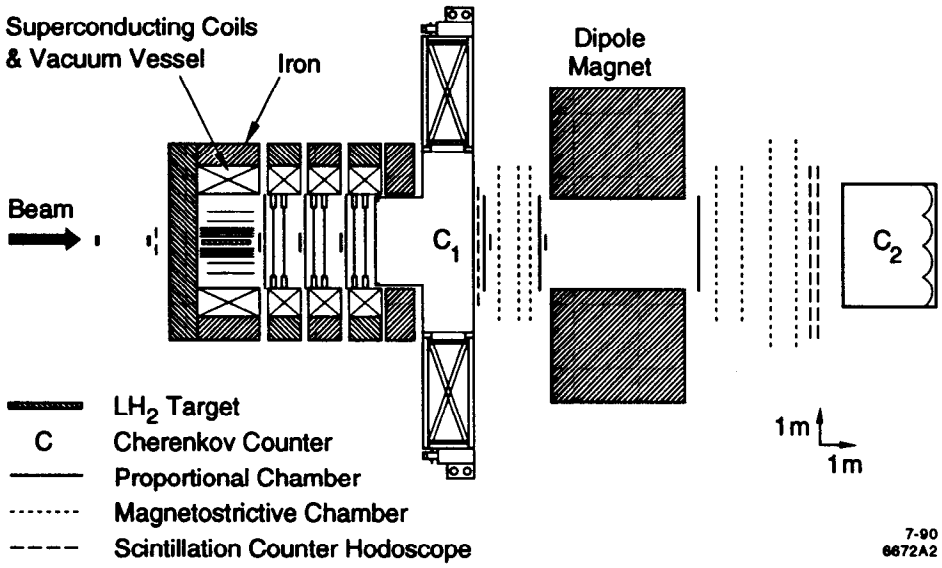

Figure 8.1: Overview of the LASS spectrometer

momentum resolution over a wide range of particle momenta (Fig. 8.2), and an almost complete solid angle coverage is obtained by combining the two sections.

Charged particle tracks are measured with a combination of magnetostrictive spark chambers located in the dipole region, cylindrical proportional wire chambers in the solenoid region surrounding the target, and planar wire chambers in both regions. Particle identification is achieved by two multi-cell Cherenkov counters, a TOF hodoscope, and dE/dx information from the cylindrical chambers. Each of these will be discussed in the following sections along with the beamline, target, data acquisition and reconstruction.

8.1 The Beamline

The beam used for E-135 is an 11 GeV/c RF-separated kaon beam. Initially, electron beams of 21 GeV/c from the SLAC linac are steered onto the production target. The production target is made of a beryllium slab of 1.0 radiation length with a 0.25 radiation length of copper on the upstream face of the slab. Secondary particles produced within 3.85 mrad of 1° from the electron-target scattering are captured by the beamline. The beamline has 4 focusing elements, F1 through F4, and several devices that separate the beam into distinct particle species and measure the momentum and position of the individual beam particles.

Through the use of a collimator, F1 restricts the secondary particle momentum to a range $\delta p/p \leq 2.5\%$. The electron contamination in the beam is then reduced by passing the beam through a 0.56 radiation length thick lead sheet. Following F1, two RF-separators deflect the particles by an amount depending on their mass; different species of particles arrive in the RF-separator at different times and therefore experience different phases of the RF field which determine the deflecting forces. By the time the particles go through F2, an achromatic focus, the different particle species are spatially separated. After F2, a small aperture collimator is used to preferentially select one particle species; kaons, in this experiment.

The momentum of each individual beam particle is measured by its horizontal

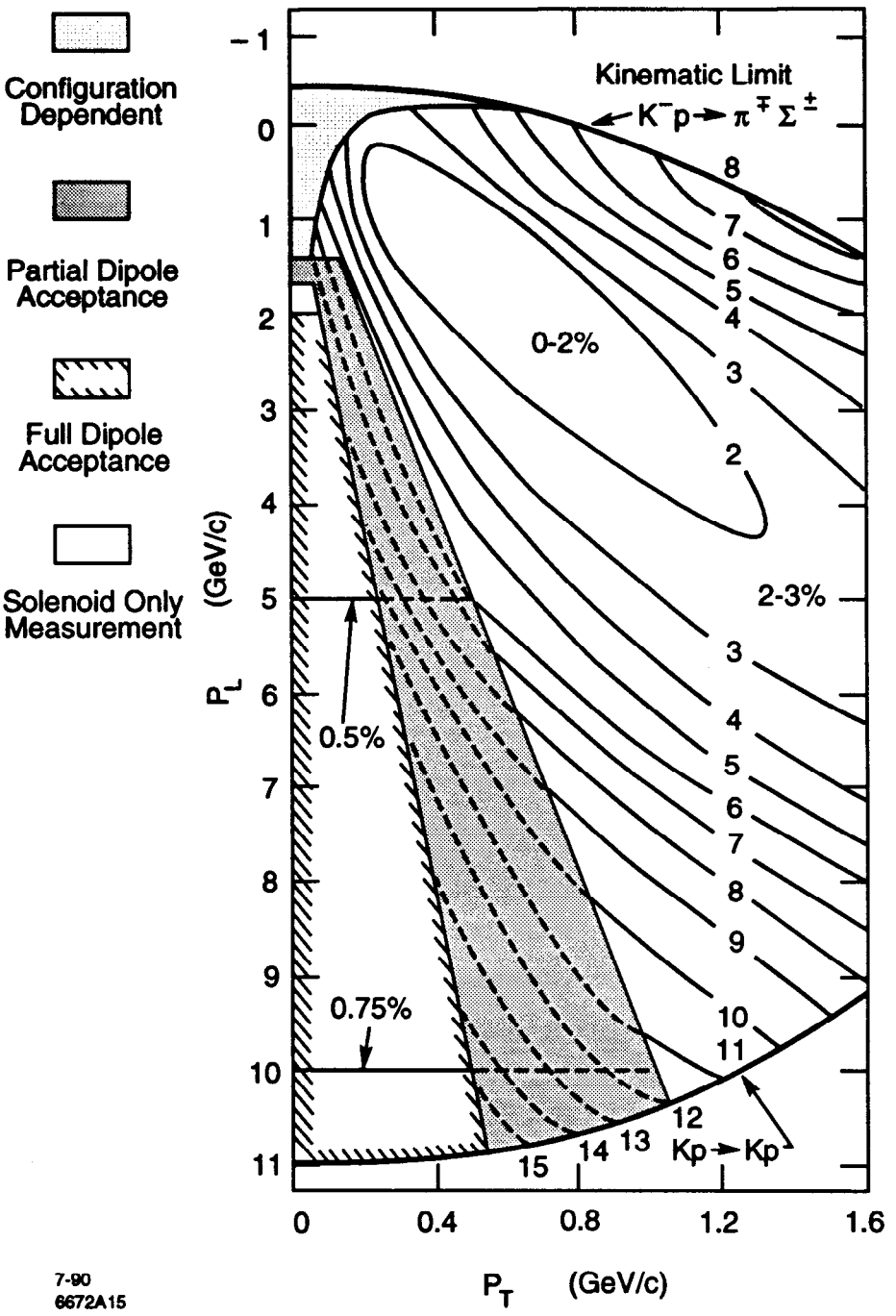

Figure 8.2: Momentum resolution for the LASS spectrometer, as used in experiment E-135. Resolution was determined from Monte Carlo data.

displacement at the momentum-dispersed focus, F3. It is measured by an array of 6 overlapping scintillator paddles located at F3 with a momentum resolution of $\delta p/p = 0.5\%$. The spatial position of the beam is measured in another array of scintillator paddles located further down the beamline at 13.1 m upstream of the LASS. This device known as the $\Theta\Phi$ hodoscope consists of twelve 0.5 inch wide horizontal paddles and twelve 0.5 inch wide vertical paddles. The $\Theta\Phi$ hodoscope is also incorporated in the trigger logic to ensure that the spectrometer triggers on one and only one beam particle.

The beam particle is identified using two threshold Cherenkov counters located downstream of the $\Theta\Phi$ hodoscope. The Cherenkov photons emitted by the beam particle are reflected by an aluminized plane mirror into a parabolic horn that focuses the light onto the photomultiplier tube. The first of the Cherenkov counters, $\check{C}_\pi$, is filled with H_2 at a pressure of 40 psia while the second one, $\check{C}_K$, is filled with CO_2 at 75 psia. The resulting refractive indices due to this gas fill is such that 11 GeV/c π's produce lights in both $\check{C}_\pi$ and $\check{C}_K$ and 11 GeV/c K's radiate only in $\check{C}_K$. A proton produces no photons in either counters. Under normal operating conditions, the K/π ratio in the beam is about $70 - 80$ and the contamination due to other particle species is negligible.

Just upstream of the LASS solenoid, the beam trajectory is measured again using the beam chamber package; a set of 10 planes of proportional wire chambers. Each anode plane contains 64 sense wires of 20 μm gold-plated tungsten at a 1.016 mm pitch. The 10 planes are divided into two groups, approximately 1m apart. The wires in the upstream package of 4 planes are oriented to measure the y, x, p and e coordinates in that order. (x = horizontal, y = vertical, $e = (x - y)/\sqrt{2}$ and $p = (x + y)/\sqrt{2}$). The downstream package of 6 planes have wires oriented to measure the coordinates in the order y, x, y', x', e and p. The coordinate x' is parallel to x but offset by half the wire spacing with respect to x. Similarly, y' is parallel to y but offset by half the wire spacing with respect to y. The beam chamber package measures the beam position and direction to within 300 μm and 0.3 mrad respectively.

The final components of the beamline are three scintillator counters located close to the liquid-H_2 target vessel. The first of these, known as SE, is located $\sim$ 5 m upstream of the target and counts both beam particles and any off-axis "halo" particles. It is used to provide an overall timing signal for the front-end electronics and forms the start pulse for the TOF system which is described in detail in Sec. 8.3.4. Because of this function, it is made particularly thick (0.375 inch) to produce a large signal with little time jitter. The other two counters, SY and RING, are located at the entrance of the spectrometer solenoid and are used to separately identify halo and beam particles. SY is a 2.54 cm diameter $\times$ 0.318 cm thick round counter and RING is a 1.27 cm thick paddle counter with a 2.54 cm diameter hole in the middle. Both counters are aligned on the beam axis.

The final focus in the beamline is F4, located a few cm downstream of the end of the H_2 target. It is an achromatic focus and produces an rms beam size of $\sim$ 0.5 cm in each dimension.

Under normal operations, the beamline provided 3-5 clean beams per linac pulse spread in time over 1.6 μsec spill. The typical linac repetition rate was $\sim$ 90 Hz.

8.2 The Target

The target material for this experiment is liquid H_2 contained inside a cylindrical cell. The target cell is 85.04 cm long and 2.54 cm in radius at room temperature and consists of two concentric mylar cylinders. The operational length shrinks to 84.6 cm due to the contraction of the cell when lowered to the liquid H_2 temperature $\sim$ 20 K. The exterior of the cell is wrapped in several layers of mylar super-insulation and is enclosed in an aluminum vacuum jacket of thickness 0.71 mm. In order to determine H_2 density which is important for later normalization calculation, the temperature and pressure of the H_2 are monitored with four vapor pressure bulbs and three platinum resistors. It takes at least 225 MeV/c of momentum for a proton produced in the reaction to escape the target in the radial direction. The

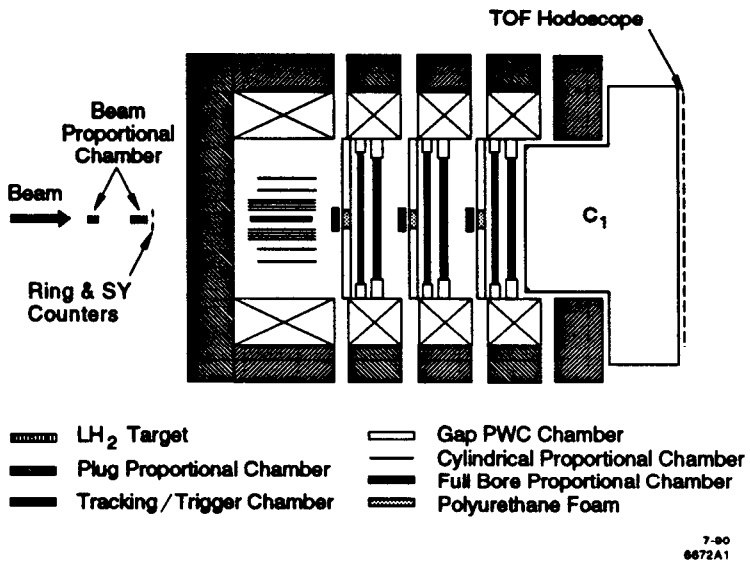

Figure 8.3: The Solenoid Region of the LASS Spectrometer

average density of the H_2 was 0.0716 $\pm$0.0004 over the duration of the E-135 data collection.

8.3 The Solenoid Region

The layout of the solenoid region is shown in Fig. 8.3. The detectors in this region are used to measure the trajectories and momenta of the charged tracks, to locate the primary and any secondary vertices, and to determine the kinematics of the particles at these vertices. The components of the detectors in this region are described in the following subsections.

8.3.1 The Cylindrical Chambers

The target vessel is surrounded by six cylindrical proportional wire chambers (PWC). The six chambers are approximately coaxial with the z axis, with radii of 6.05, 9.55, 12.99, 16.55, 29.41, and 49.02 cm. The chambers consist of an an-

ode wire plane of 20 μm diameter gold-plated tungsten wires, sandwiched between inner and outer layers of cathode strips. The cathode strips are made of metal foil and are supported by a double cylinder of an aluminum-mylar laminate and honeycomb sheet. The strips are oriented at $\pm 10°$ angles to the anode wires for the inner four PWCs and at $\pm 15°$ angles for the outer two cylinders. The anode wires are attached to the fiberglass circuit boards, located at either end of each wire, and are glued to a lucite support ring halfway down the cylinder. As a by-product of the cylindrical chambers, a modest dE/dx measurement is achieved from the pulse height information on the cathode foils of the tracks that pass through several cylinders and have momenta below $\sim$ 0.6 GeV/c. This is used for a particle identification as will be described later.

8.3.2 The Planar Chambers

Each of the three sections of the solenoid magnet downstream of the target is instrumented with a group of chambers; the gap, bore, plug and trigger chambers.

- The Gap Chambers: The gap chambers contained single wire planes spanning the entire inner diameter of the solenoid. Each gap chamber contained 758 anode wires at 2.032 mm intervals. The cathodes for these chambers are made of aluminum-mylar laminate, with 6.86 mm long etched strips spaced 1.27 mm apart and oriented at $\pm 45°$ to the anode wires.

  The cathode and anode are separated by 0.508 cm. A circular region of radius 8.255 cm at the center of each chamber is covered with a styrofoam-supported mylar barrier. This serves to deaden these regions to prevent tracks in the high-intensity beam region from filling the central strips of the chamber with data and complicating the coordinate reconstruction. Tracks in these deadened regions are completely covered by the plug chambers.

- The Plug Chambers: Five identical plug chambers are used in the LASS spectrometer; three are located near the gap chambers in the solenoid region

and the remaining two are installed in the dipole region. A plug chamber consists of three anode planes of 256 sense wires strung at a 1.016 mm pitch. The anode planes are oriented so that they measure y, x, and e coordinates ($e = x\cos(35°) - y\sin(35°)$). The active area that each plug chamber covers is $\sim 26 \times 28cm^2$.

- The Bore Chambers: The three bore chambers provide measurements inside, as opposed to between, the solenoid magnet segments as shown in Fig. 8.3. Each bore chamber is octagonal in shape to maximize coverage, and consists of three planes oriented to read out y, x, and e coordinates ($e = x\cos(45°) - y\sin(45°)$).

- The Trigger Chambers: These are the three planar cathode foil chambers in the solenoid, located between each set of gap and bore chambers. They were intended to be used to provide a high p_t trigger or to measure track multiplicities. In this experiment, they are only used to provide redundancy for tracking. Each trigger chamber consists of an anode and two segmented cathode planes. The anode is not used to provide signals in the chamber, but only to produce a field. Because of this, the anode wires are spaced widely, at 4.064 mm. The upstream cathode in each chamber, known as the tracking foil, is segmented into two concentric rings of 8 and 128 pads each. The downstream cathode, called the trigger foil, is similarly divided into 8 segments in the inner ring and into 16 segments in the outer ring. The tracking foils are read out for all three trigger chambers. The trigger foils are read out only for the two upstream ones.

8.3.3 The Cherenkov Counter $\check{C}_1$

The $\check{C}_1$ Cherenkov Counter occupies a region just downstream of the solenoid and extends beyond the last magnet coil. The device is a segmented, threshold Cherenkov Counter filled with Freon 114 at $\sim$ 1 ATM. With this, the momentum threshold for π's to emit Cherenkov radiation is 2.6 GeV/c^2, while the threshold

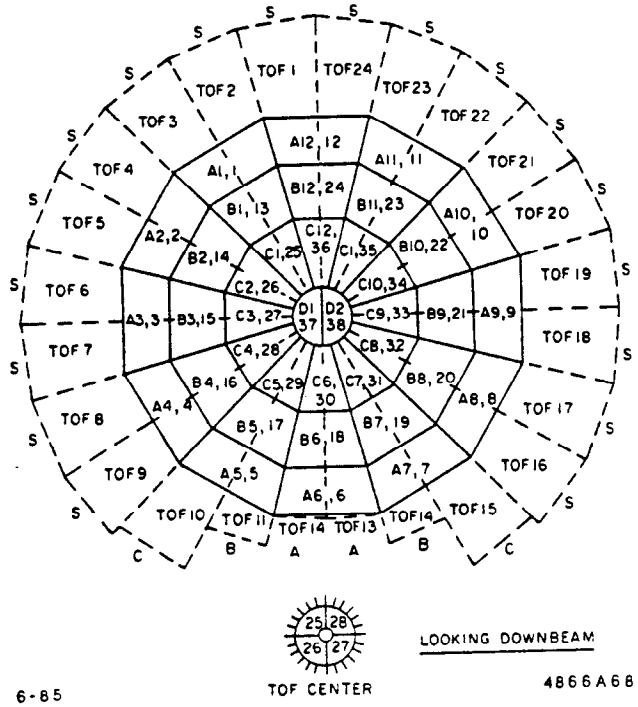

Figure 8.4: The optical cells in $\check{C}_1$

for K's is 9.2 GeV/c^2. The path length of a particle traversing the counter is at least 180 cm.

The counter is segmented into 38 optically isolated cells, organized into four rings. Figure 8.4 shows the segmentation of the $\check{C}_1$ counter. The innermost ring with a radius of 8.5 cm called the D ring is divided into two half-cylindrical volumes. The outer three rings (labelled the C, B and A rings with radii approximately 29.3, 52.0, and 83.0 cm, respectively) are each divided azimuthally into twelve 30° sections. The optical isolation of the cells is achieved with sheets of mylar foils that have been given a double aluminum coating. The counter segmentation begins at $z = 370.2$ cm but the gas volume extends approximately 40 cm more upstream to enhance the Cherenkov photon yield. Because of this, it is possible for a particle to produce a Cherenkov light in more than one cell even if it passed through only one cell. At the downstream of each cell, the light is reflected normal to the beam axis into an optical assembly which consists of a Fresnel lens, a light collection horn, and a photomultiplier tube.

The bottom three cells in the A, B and C rings required a somewhat different geometrical arrangement because of the limited space due to the floor. Their light-collecting channels are shorter than the rest, and the appropriate photomultipliers are at a distance of $\sim$ 1.9 m from the beam axis, in contrast to $\sim$ 4.3 m for the other tubes. Unfortunately, the horns on these bottom cells proved to be somewhat inefficient in collecting light from a particular region of the cell. As a result, the performance of these cells was not as good as that of the other cells.

The readout of the collected light was made using RCA 8850 Quantacon photomultipliers chosen for good single photon response and high quantum efficiency. To protect them from stray magnetic fields, the tubes are shielded in iron and μ-metal pipes.

The $\check{C}_1$ counter's threshold behavior and efficiency as a function of particle trajectory inside the counter is empirically studied using a large sample of π's from K° decays. These π's are used to measure the probability of detecting light in each cell as a function of momentum and the impact position of the particle on the front face of the cell. If the particle momentum is near or above threshold, the impact position and the momentum of the particle determines the combined probability that the particle will radiate Cherenkov light and the light will be detected by the phototube. To take into account cases where the radiated light will pass through more than one cell, if a particle passes within 2 cm of a cell boundary, the adjacent cell is also checked for light. The response of each of the ring is shown in Fig. 8.5. The lower three inefficient counters in the A, B and C rings have been excluded in this measurement. The curves in the Fig. 8.5 correspond to simultaneous fits to the efficiency data for the three rings. The fit takes into account a constant background, an asymptotic efficiency for each counter, and a threshold rise exhibiting a $\sin^2\theta_c$ dependence. The resulting fitted value of the π threshold is 2.61 GeV/c, as expected. The asymptotic efficiencies are 0.971 ± 0.006, 0.987 ± 0.002 and 0.998 ± 0.002 for the A, B and C rings respectively.

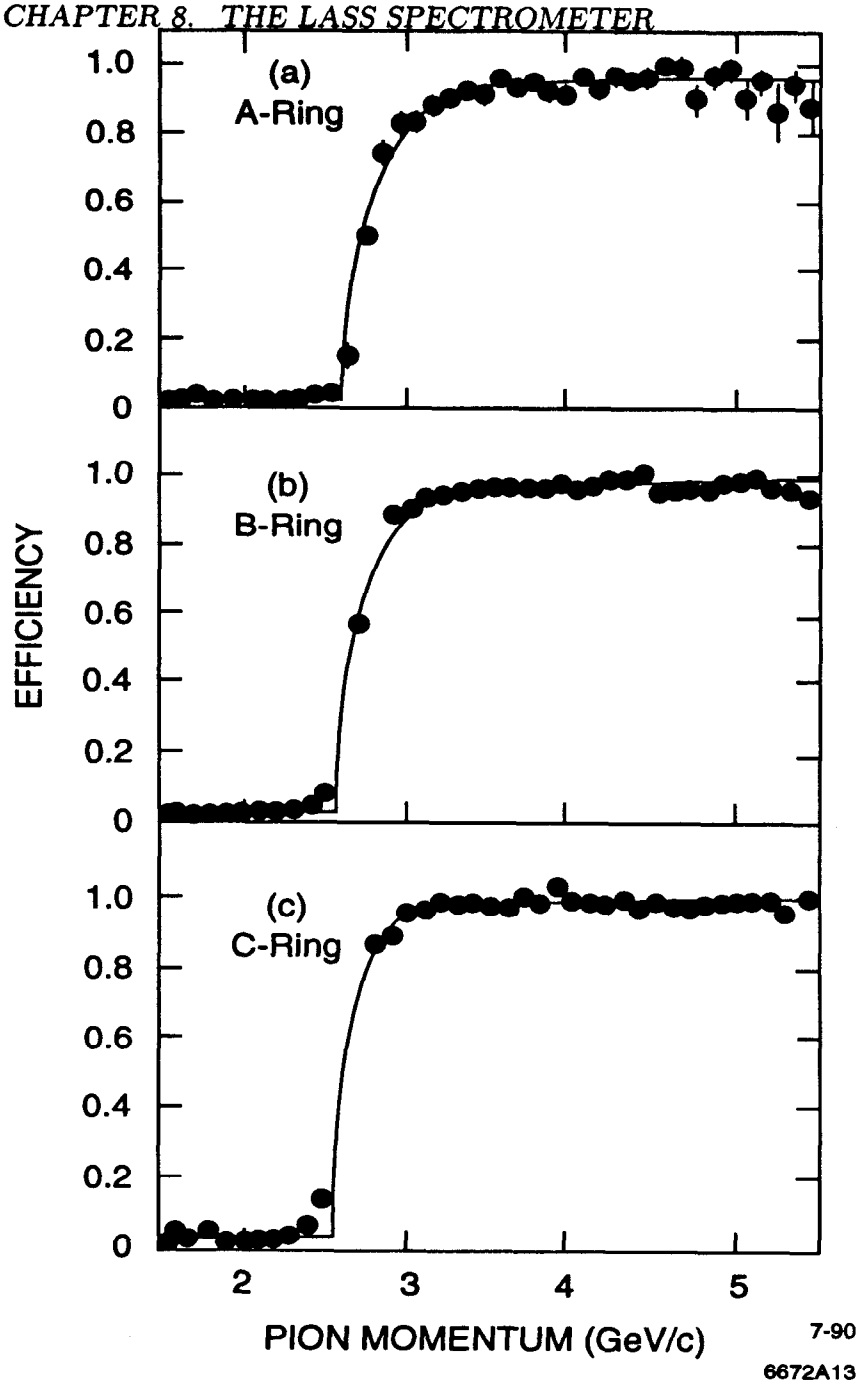

Figure 8.5: The momentum dependence of the efficiency of the $\check{C}_1$ counter. The curves are described in the text.

8.3.4 The Time of Flight System

The time of flight (TOF) system consists of the SE counter located upstream of the target and a segmented scintillator hodoscope located immediately downstream of the $\check{C}_1$ counter. The hodoscope is shown in Fig. 8.6. It is approximately circular in shape and composed of 24 wedge-shaped scintillator paddles. Each paddle is 1 cm thick and 15 ° in angle. Four additional segments (25 - 28 in Fig. 8.6) filled most of the central region of the hodoscope, leaving a 3.8 cm radius hole in the center of the hodoscope. Signals from the wedges (1 - 24) are measured using shielded photomultipliers, which are read into both ADCs and TDCs. The starting signal for the TDCs is provided by the SE counter, mentioned earlier. When the scintillating light from a passing particle is sensed in a phototube, the attached TDC is stopped and the pulse height is recorded by the ADC. The pulse height information is used to correct the measured time for "time walk" of the discriminated light pulse due to the variation in pulse height. The resulting TOF measurement had an average resolution of $\sim$ 0.5 ns. Particle identification is achieved by calculating the expected time of flight for a mass hypotheses of e, π, K, and p for a given track momentum and the point of origin of the track, and comparing the calculated and measured values. A probability reflecting a given hypothesis is determined. Using this method, approximately 3σ separations of e/π up to 350 MeV/c, π/K up to 1.1 GeV/c, and π/p up to 2.5 GeV/c are obtained.

8.4 The Dipole Region

The dipole region of the LASS spectrometer measures the momenta of the particles within 50 - 100 mrad of the beam axis with momenta $p > 1.5$GeV/c. It consists of magnetostrictive chambers, proportional wire chambers, two hodoscope arrays, and a Cherenkov counter. Figure 8.7 shows the layout of the dipole region.

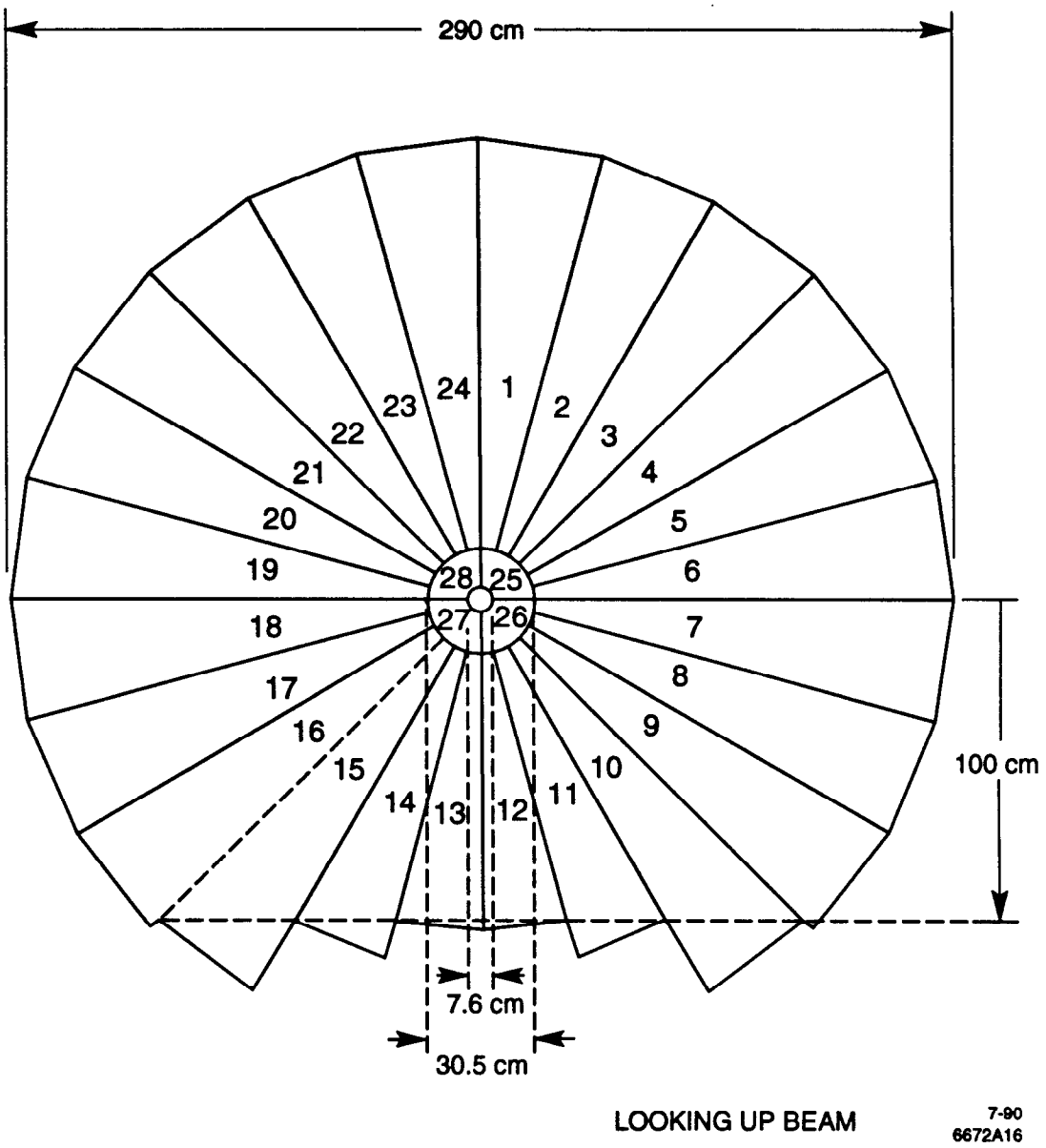

Figure 8.6: The time of flight hodoscope

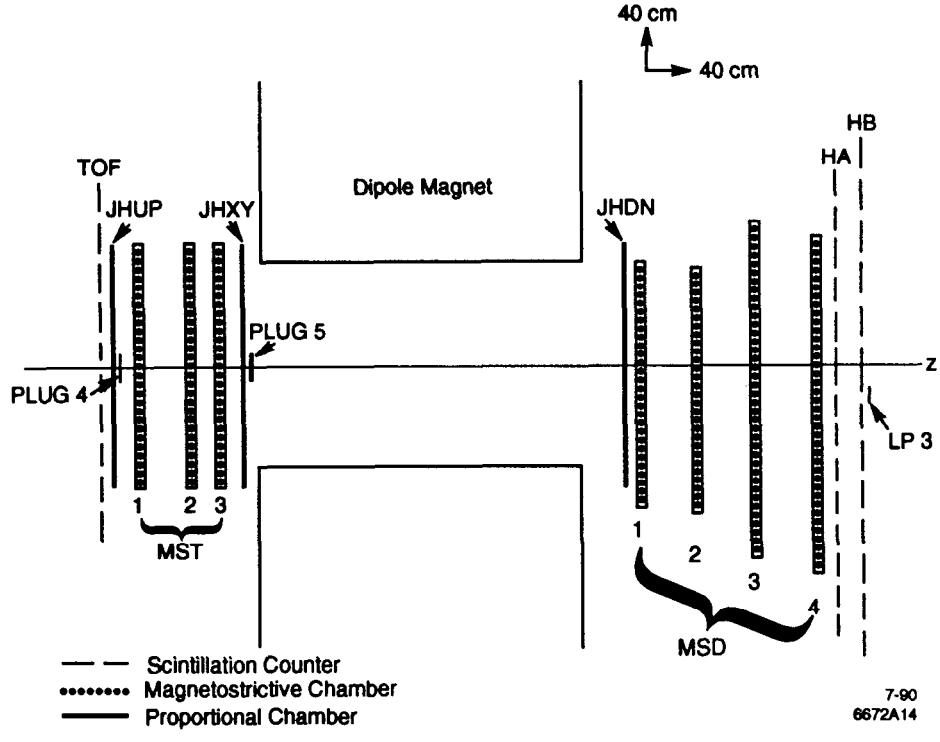

Figure 8.7: The dipole region of the LASS spectrometer

8.4.1 The Magnetostrictive Chambers

The magnetostrictive (MS) chambers are spark chambers that provide most of the coordinates for tracking in the dipole region. (Fig. 8.7) This type of chambers is chosen because it provides accurate coordinate information over a large area with high multiple-hit efficiency at low cost.

The readout is accomplished by means of a magnetostrictive wire which efficiently converts the electrical energy of a spark into a travelling acoustic pulse. The spark chamber consists of two planes of woven wire cloth separated by 1 cm. One plane is kept at high voltage, the other at ground. Whenever an event trigger occurs, a high-voltage pulse is generated by a thyratron amplifier, so that a spark is created across the gap where a particle has left a trail of ionization. The current pulse associated with the spark travels down the wire cloth and induces an acoustic signal on the wand. These acoustic signals travel down to the end of the wand. The wand is connected electrically to a TDC, which records the arrival time of the full set of sparks from the trigger and stores it for subsequent readout.

Seven MS chambers are used; three upstream of the dipole and four downstream. The first five chambers have active areas of 150×300 cm^2, and the two "super-chambers" in the most downstream have 200×400 cm^2. The upstream wire plane in each chamber measures the x and y coordinates of each spark, while the downstream module measures the e and p coordinate defined by $e = x\cos\theta - y\sin\theta$ and $p = x\cos\theta + y\sin\theta$, where $\theta = 30°$ for the five smaller chambers and 25° for the two super-chambers. Polyurethane plugs are installed on axis in order to deaden the spark gaps, otherwise the high beam flux would seriously degrade chamber performance. The downstream chambers are displaced so that the dipole-bent beam would still pass through the plugs.

The y planes of each MS chamber are read out using a single magnetostrictive wand, as are the remaining planes in the first two chambers downstream of the dipole. All the other wire-planes are read out with two wands, located on opposite sides of the chamber. Each wire plane has two "fiducial" wires placed along each side of the plane. A voltage induced on the wires is detected by the wands. The

fiducial wires are also pulsed on the event trigger and are used to calibrate the time scale for each event. The full pulse train for the event is digitized, stored and read out using a CAMAC module. The digitization is done with a 20 MHz clock, resulting in approximately 0.27 mm spatial resolution.

In order to compensate the upstream MS chambers for the large stray magnetic fields, each wand is magnetically biased using a coil of wires wrapped around it.

8.4.2 The Proportional Chambers

The three proportional chambers shown in Fig. 8.7 were built at Johns Hopkins University, and consist of a single plane of 512 wires with a 4.23 mm wire spacing. The aluminum and polyester mesh cathodes of JHUP and JHDN are built with a 1.27 mm gap width while the JHXY chamber uses a segmented aluminum-mylar foil cathode of 128 2.62 mm wide horizontal strips separated by 0.16 cm gaps. These chambers provide in-time corroboration and position information for dipole tracks. The JHXY cathode efficiency was so low, only about 50 %, that it was of limited use.

8.4.3 The Scintillator hodoscopes

Two scintillator arrays, HA and HB, are located immediately downstream of the last magnetostrictive chamber. Each counter consists of two rows of scintillator paddles, with 21 paddles per row in HA and 3 per row in HB. Each paddle is 83.82 cm long. The center paddle in each array is actually a 10.16×10.16 cm^2 hole through which non-interacting beam particles pass and do not generate signals. These hodoscopes trigger the spectrometer on events with dipole particles, and provide in-time corroboration for tracking. A small circular counter, LP3, covers the hole in the beam region and functions as an anti-coincidence counter, to ensure that there were no downstream beam tracks in otherwise good events.

8.4.4 The Cherenkov Counter $\check{C}_2$

The most downstream element of the LASS spectrometer is the Cherenkov Counter $\check{C}_2$. It provides π/K separation for fast particles passing through dipole magnet with $p > 3.5$ GeV/c. The counter is segmented into eight cells and filled with 1 ATM of Freon 12 (CCl_2F_2) that acts as a Cherenkov radiator. Particles enter $\check{C}_2$ through a 2 mm thick aluminum window and traverse at least 1.75 m of gas. Any radiated Cherenkov photons hit one or more of the eight mirrors at the back of the counter; two rows of four mirrors tilted at 10° from the vertical. Light hitting a particular mirror is reflected through one of eight light-collecting horns onto a photomultiplier. Four of the horns and photomultipliers are located at the top of the counter and the remaining four are at the bottom.

The momentum thresholds for π's and K's to produce Cherenkov radiation are 2.9 and 10.3 GeV/c respectively. However, the effective thresholds were approximately 10 % higher because of the geometry and the use of the unshielded photomultipliers.

8.5 The Event Trigger

To obtain the widest variety of physics channels for study, the trigger requirement for E-135 is made minimal. All that is required is that a beam particle interact in the target and at least two charged tracks emerge from the target, which effectively triggers with high efficiency on the full K^-p cross section for charged particle production. In addition to this physics trigger, a few special purpose triggers are used for monitoring the spectrometer performance. The full trigger consists of two parts, the beam trigger and the cluster logic, each of which is discussed in this section.

8.5.1 The Beam Trigger Logic

The purpose of the beam trigger logic is to identify and select acceptable beam particles and to reject events with multiple beam particle candidates. In order to be considered an acceptable beam for an event, the following conditions must be satisfied:

- an incoming beam particle is identified as a K^-;
- the particle enters the target;
- no more than one particle enters the target within 20 ns time window.

The $\check{C}_\pi$ and $\check{C}_K$ counters, discussed in Sec. 8.1, are used to identify the particle as K^-. The SE, SY and RING (R) counters determine if the beam particle enters the target requiring that signals from SE and SY are coincident and at the same time no signal is seen in R. The $\Theta\Phi$ hodoscope is used to ensure that no two beams occur within 20 ns of timing window.

In Boolean notation, the complete beam trigger logic (BT) can be written as:

$$BT = (\Theta\Phi \geq 1) \wedge \overline{(\Theta\Phi \geq 2)} \wedge SE \wedge SY \wedge \overline{R} \wedge \check{C}_K \wedge \overline{\check{C}_\pi}.$$

8.5.2 The Cluster Logic

The purpose of the cluster logic is to determine when two or more charged particles exit the target region. This is done by counting the number of hits in the two innermost cylindrical PWC's and in the first two plug chambers. The number of clusters in each anode plane is used to form the logic signals of Table 8.1. In the formation of these logic signals, the central 32 wires of each plane of plug 1 are omitted in order to protect against multiple beams. The remaining wires are ORed together to generate the cluster multiplicities of Table 8.1. Conversely, in plug 2, only the central wires are included in the count, to include any very forward going tracks in the trigger logic. As seen in Table 8.1, each signal formed from the cylinder cluster logic includes the requirement that cylinder 2 must have at least

Signal	definition
$PLG_1 \geq 1$	at least 2 plug-1 planes have ≥ 1 hit
$PLG_1 \geq 2$	at least 2 plug-1 planes have ≥ 2 hits
$PLG_2 \geq 1$	at least 2 plug-2 planes have ≥ 1 hit
$PLGS \geq 1$	$PLG_1 \geq 1 \wedge PLG_2 \geq 1$
$CYL \geq 2$	$CYL_2 \geq 1 \wedge (CYL_1 \geq 2 \vee CYL_2 \geq 2)$
$CYL \geq 3$	$CYL_2 \geq 1 \wedge (CYL_1 \geq 3 \vee CYL_2 \geq 3)$
$\overline{CYL \geq 3}$	$\overline{CYL_1 \geq 3 \wedge CYL_2 \geq 3}$
$CYL = 2$	$CYL_2 \geq 2 \wedge \overline{CYL \geq 3}$
$CYL = 1$ *or* 2	$CYL_2 \geq 1 \wedge \overline{CYL \geq 3}$

Table 8.1: The cluster logic signals.

one hit, because cylinder 1 has a high accidental hit rate; being located far from the beam axis, cylinder 2 has a substantially low rate of accidental hits.

8.5.3 Complete Event Trigger

The complete event trigger is formed from the logical OR of four physics triggers, labelled $T0_i$ (i = 1 to 4), and four monitoring triggers, labelled Ti (i = 1 to 4). The latter four triggers are "scaled-down", *i.e.* only a fraction of the events that trigger on these types are recorded. They are important for calibration and diagnostic purposes. The complete trigger logic is displayed in Fig. 8.8. Basically, the triggers are defined as follows:

1. $T0_1$: ≥ 3 secondaries and ≥ 2 cylinder tracks
2. $T0_2$: 2 cylinder and 0 dipole tracks
3. $T0_3$: 1 forward and 1 or 2 transverse tracks
4. $T0_4$: ≥ 2 forward tracks

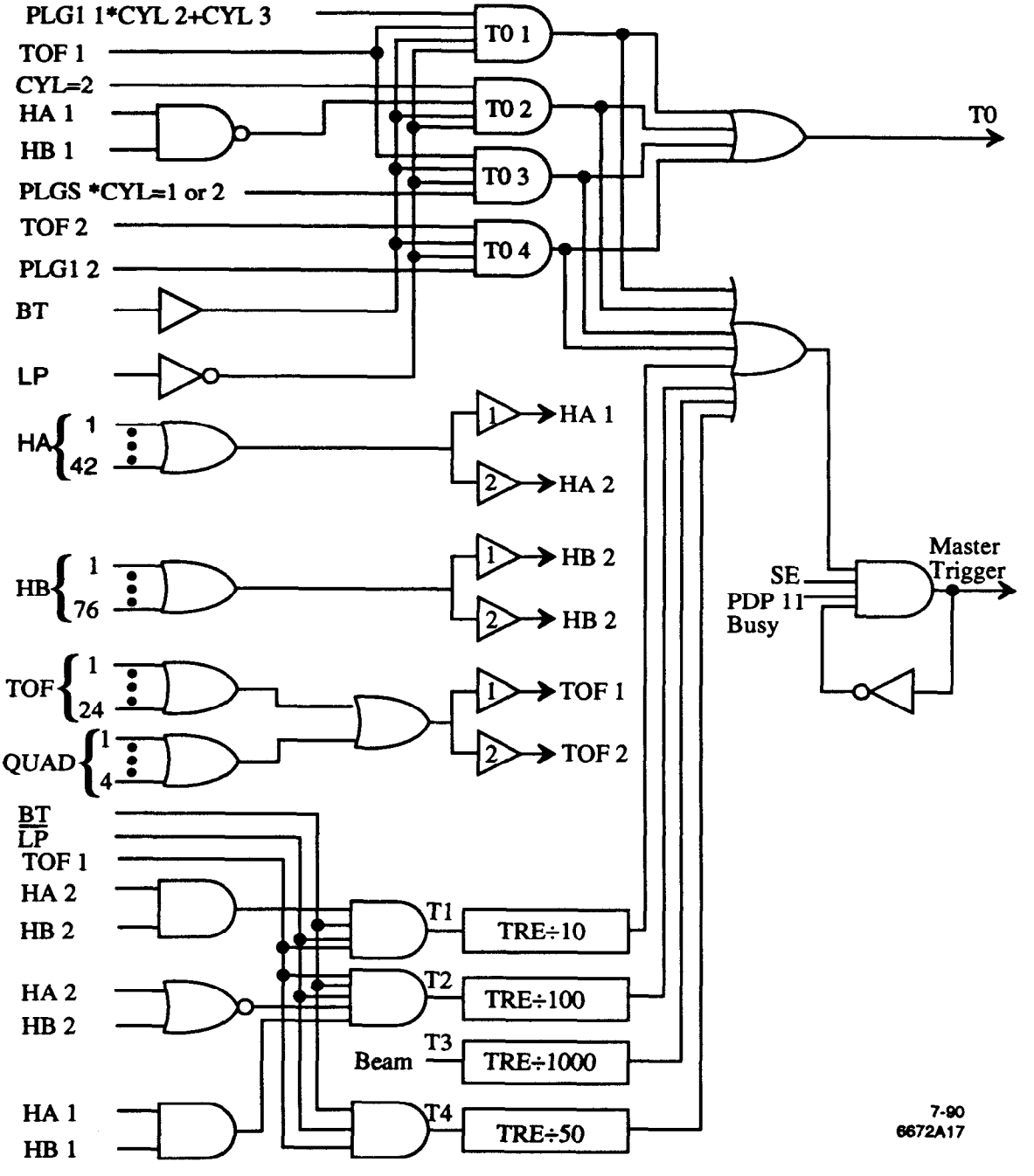

Figure 8.8: The complete trigger logic for E-135

5. $T1$: Beam decay trigger. The 3-prong decays of the beam serve to monitor the relative calibration of the P-hodoscope and the dipole magnet. Scale-down factor = 10.

6. $T2$: Elastic trigger. K^-p elastic scattering events are mainly used to study track-finding and momentum resolution in the dipole region. Scale-down factor = 100.

7. $T3$: Random beam trigger. Designed to provide an unbiased event sample for Monte Carlo trigger efficiency studies. This trigger yields a random sample of beam tracks and thus provides a beam phase space measurement. Scale-down factor = 1000.

8. $T4$: Random interaction trigger. Designed to provide an unbiased event sample for Monte Carlo trigger efficiency studies. Requiring beam particle in and no beam particle in the secondary. Scale-down factor = 50.

The deadtime associated with a trigger is driven by the time needed to clear the track ionization in the spark chamber gaps, which is about 15 ms, but can be larger for very high multiplicity events. Under typical running conditions, the livetime of the detector was $\sim$ 60 %.

8.6 The Data Acquisition

The LASS data acquisition system consists of:

1. Device controllers – Five controllers are used to coordinates the acquisition of data from a separate data branch. Data from the CAMAC data branches of the spectrometer are read into the device controllers for temporary storage until transferred to the PDP-11 using direct memory access (DMA). Only four of the five CAMAC branches are used in data readout; the fifth one is used for online monitoring purposes and to monitor the voltage settings of various devices.

2. DEC PDP-11/04 minicomputer – It reads out the device controllers through DMA. On every event trigger, the contents of the four controllers are copied in parallel to partitions in the PDP memory.

3. IBM system 7 computer – It acts as the communication port between the PDP-11 and the SLAC central computer system. Data are transferred over a 0.5 km coaxial cable to the TRIPLEX.

4. SLAC TRIPLEX computer system* – All the tape logging and online monitoring of the experiment is performed on the TRIPLEX. Tape logging has the highest priority. A background analysis program runs on a sample of the events in the remaining time. Various kinematic quantities could be histogrammed and displayed online, with the aid of an IBM 2250 graphics display terminal.

8.7 The Spectrometer Alignment and Calibration

8.7.1 Alignment

As the gap chambers could be easily surveyed, they are used to define the reference coordinate system for LASS. The wire positions inside the chambers are well-known from bench measurements, and the z positions of the chambers are surveyed. The locations of the other chambers in the LASS are determined relative to the gap chambers by fitting straight tracks, recorded with the magnets turned off. Next, the cylindrical chambers are located by fitting tracks recorded with the magnets on. Tracks found in the planar chambers are projected back as helices. The beam chambers are aligned using events with a T3 trigger. To accomplish this, the plug and full-bore chamber tracks in such events are projected back into the beam

*The SLAC TRIPLEX consisted of a 2Mb IBM 360/91, two 3Mb IBM 370/168, ten 6250bpi tape drives, four IBM 5098 control units and numerous disk drives and I/O devices

chambers. The alignment of the magnetostrictive chambers was found to vary over a few hours. This was traced to instabilities in the wands, and so the wand variations were watched carefully during normal running. A new alignment was taken whenever significant variations were seen, typically once per week.

8.7.2 Electronics Calibration

The ADC electronics used in the experiment was subject to run-to-run variations. In the cases of TOF and Cherenkov , these variations were due to pedestal fluctuations, and in the electronics of cathode readout, they were due to both pedestal and gain fluctuations. To correct for this, the first 100 events in each run were used to define the pedestals for the run. In addition, dedicated calibration electronics were built into the cathode readouts to allow more frequent calibration during runs.

8.7.3 Momentum Calibration

The momentum calibration of the spectrometer was also monitored on a run-by-run basis. By determining the absolute calibration for the dipole spectrometer, the solenoid region and the P-hodoscope were calibrated to agree with the dipole measurement.

The dipole calibration is obtained by reconstructing the K_s decay where at least one of the daughter particles passes through the dipole. The difference between the measured $m_{\pi^+\pi^-}$ and the expected K_s mass is converted into a scale factor which is applied to the dipole magnetic field map. This factor is 1.007 for fu ll-field dipole operation and 1.004 for half-field running. The relative calibration of the dipole and the P-hodoscope is then achieved in two independent ways using: (1) K^-p elastic scattering events in which the final state K^- is reconstructed in the dipole and (2) $K^-(beam) \rightarrow 3\pi$ events where all three π's are measured in the dipole.

Measurements	Definition
l	measured light path in scintillator
TDC	measured TDC of TOF
ADC_{SE}	measured ADC of SE
ADC_{TOF}	measured ADC of TOF
Constant	**Definition**
v	speed of light in scintillator
α_1	conversion from TDC counts to nanoseconds
α_2	timing offset of TOF module and SE counter
α_3	constant for SE time walk correction
α_4	constant for TOF time walk correction
α_5	correlation between light path length in paddle and pulse height due to paddle geometry
α_6, α_7	higher order correction to v due to paddle geometry

Table 8.2: The variables in the TOF correction formula.

8.7.4 Time of Flight Calibration

The TOF system is calibrated offline using processed data. The conversion from the observed TDC counts into particle flight time is determined as

$$t_{meas} = \alpha_1 TDC - \alpha_2 - \frac{\alpha_3}{\sqrt{ADC_{SE}}} - \frac{l}{v} - \frac{\alpha_4 + \alpha_5 l}{\sqrt{ADC_{TOF}}} - \alpha_6 l^2 - \alpha_7 l^3.$$

The variables in this equation are summarized in Table 8.2. The data runs in the experiment are grouped into 13 blocks and the parameters are determined for each TOF channel in every block by fitting the calibration constants to a sample of fast ($p \geq 3$GeV/c) negatively-charged tracks obtained from a subset of runs in the block. The timing offset α_2 is further corrected on a run-by-run basis by using the average raw TDC count for fast particles, since significant run-to-run variations are observed within a block.

8.7.5 dE/dx Calibration

Information on dE/dx is obtained by looking at the pulse height in the cylindrical chambers. The observed pulse height PH is related to the particle's mean ionization per unit gas length I by

$$I = f_\theta(\theta)PH$$

where θ is the angle defined by the particle's trajectory through the cylinder and the vector normal to the cylinder surface and f_θ is the path length correction. If the cylinder package were homogeneous, one would expect that $f_\theta \propto \cos\theta$. However the observed pulse height shows a more complicated dependence on θ. In particular, there is an excess of signal as the tracks are more and more forward. To correct this effect, a quadratic polynomial in $\cos\theta$ is used.

After the path length correction, the β-dependence is measured using the protons from elastic events. It was observed that the distribution of the variable $(f_\theta PH)^{0.3}$ is approximately Gaussian. This feature is used to simplify the description of the pulse-height information. The mean of this distribution as a function of β is determined from the proton sample. The β-dependence of the mean is parametrized by a quadratic function.

With these parametrizations on path length and β-dependence, a likelihood function for the probability that a cylinder track is a π or p is constructed. The likelihoods from the individual cylinders are multiplied to give the overall likelihood.

8.8 The Event Reconstruction

The raw data obtained during the experiment have to be processed prior to physics studies. The processing called "event reconstruction" consists of several stages:

1. raw data unpacking;

2. track finding;

3. vertex finding and topology recognition; and

4. packing of the resulting information into a concise data record for later use in subsequent event selection.

These will be discussed in this section.

8.8.1 Raw Data Unpacking

The raw data record in the data tapes is organized into a fixed header and up to four data blocks, labelled Blocks 2, 3, 4, 7. The first block, Block 2, contains the particle identification information from the Cherenkov ADC's and TOF counter TDC's. It also has information from some strobe signals and some online scaler counts, such as the elapsed time since the last beam track. Block 3 contains the PWC anode information. This consists of a list of the PWC anodes that had hits and the time-slot information for each wire. This time-slot information is used to determine whether the hit on the wire came from the same event or the one before/after the trigger. Block 4 contains the pulse height information from the cathode strips in the gap chambers and the cylindrical chambers. The raw data consist of a list of fired cathode strips and the associated ADC count. The last block holds the raw data from the MS chambers. These data consist of the pulse arrival time at the wands. The counts from the fiducial wires are also recorded here and are used to convert the timing signals into spatial coordinates, with uncertainties depending on the given wand averaging about 0.6 mm.

8.8.2 Beam Track Finding

The beam parameters are measured by the beam chamber package. Since several candidate beam tracks are often found for each trigger, it is necessary to ensure that only the correct beam track is found.

First, anode clusters are formed in the beam chambers and converted to spatial coordinates. Then, lists of possible matchpoints are formed for the upstream and

downstream chambers requiring that the time information for associated clusters be consistent. A beam track candidate is established when a pair of consistent matchpoints, one each from the upstream and downstream chambers, is found. Candidates with the best timing consistency, a satisfactory number of coordinates measured, and good agreement with the allowed beam phase space are kept as legitimate beam tracks in the event. In addition, in-time corroboration with the $\Theta\Phi$ hodoscope and SY counter is required.

Other found beam tracks in an event are usually due to non-interacting beam kaons which can also be seen in the downstream dipole chambers. In this case, the associated matchpoints are not used for any subsequent track finding. Typically, there are 1.5 beam tracks per event trigger in the data.

8.8.3 Solenoid Track Finding

In the solenoid region, the track finding begins with defining precise matchpoints in the PWC devices. An acceptable track candidate should follow a helical path in the solenoid. In this regard, three matchpoints, each from a separate chamber, are initially selected so that they are consistent with forming a helical trajectory. Further corroborating matchpoints are searched over the area determined by the estimated uncertainties in the helix defined by the original matchpoints. Based on the total number of corroborating points found, a χ^2 fit to a helix is performed to the candidate points. The fit allows multiple scattering, assuming that the track particle is a pion and the scattering errors are uncorrelated. The candidate track is accepted if the fit was good, with a confidence level $> 10^{-4}$. If the fit result was not acceptable, coordinates which contribute more than 12 to the χ^2 are dropped and the fit is tried again. This process is repeated until either there are too few points left on the track or the fit converges with an acceptable confidence level. The track-finding efficiency is better than 99% as determined from Monte Carlo studies.

8.8.4 Dipole Track Finding

Track-finding in the dipole region involves the following steps:

1. finding line segments in the region downstream of the dipole magnet;
2. finding lines in the "twixt" region (between the solenoid and the dipole);
3. crossing each dipole line segment through the dipole aperture to the corresponding line segment in the twixt region; and
4. joining the entire dipole track to the corresponding helix exiting the downstream aperture of the solenoid.

First, a pair of x-coordinates, one from each MS chamber plane, is looked for, and the segment is considered a candidate if it is confirmed by the associated pair of e-p coordinates from the corresponding MS chamber. The line segment is extrapolated into the other chambers to look for corroborating points, and a least squares fit is performed if the number of points found is acceptable. The fit result is accepted if it has a confidence level $> 10^{-4}$. Line segments in the twixt region are found in a similar way.

Then, the line segments in the downstream and in the twixt region are crossed through the dipole aperture to form a complete dipole track. Any matching twixt/downstream pair is selected. Those pairs that come close to meeting in the center of the dipole are tentatively matched, and a first order estimate for the track momentum is made based on the bend angle in the dipole. The estimate is used to swim the downstream segment back through the dipole to the upstream piece. The process is iterated until the angles of the swum track and twixt track agree to 0.1 mrad.

Finally, the dipole and solenoid tracks are joined by finding a solenoid track that matches the dipole track, and refitting the solenoid helix using the dipole-measured momentum as a constraint. If the fit is successful, the original helix fit is replaced with the new one. Approximately 95 % of the refits were successful.

Failures were mostly from particle decays in flight of large angle scattering in the dipole.

8.8.5 Vertex Finding and Topology Recognition

A preliminary estimate of the primary vertex position is made by averaging the z coordinates of the closest approach point to the beam for all tracks passing within 1.5 cm of the beam and in the vicinity of the target. A least squares fit is then performed by minimizing the sum-of-squares of perpendicular distances ($\sum d_i^2$) from the common vertex to the associated tracks. The fit is accepted if $\sum d_i^2$ per degree of freedom is less than 1 cm^2. If the fit is not successful, the track with the largest d_i is removed and the fit is repeated.

The secondary vertex of interest in this study is from the K_s decay in the reaction $K^- p \rightarrow \overline{K}^\circ \phi n$. To find the K_s candidates, pairs of oppositely charged tracks that pass within 1 cm of each other are searched. Assuming the track particles to be π's, the invariant mass of the combined track pair is required to be consistent with the $\overline{K}^\circ$ mass: $0.436 < m_{\pi^+\pi^-} < 0.557$ (GeV/c^2).

After vertex finding, the events are classified into various event topologies. There are 8 topologies used in this experiment. An event may have interpretations in more than one topology. In that case, the resolution of the topology ambiguities is left to the subsequent analysis of the data. The eight topologies are:

1. All charged tracks are associated with the primary vertex.
2. A number of tracks and a V°[†] where the V° is consistent with a K_s.
3. A number of tracks and a V° where the V° is consistent with a Λ or $\overline{\Lambda}$.
4. A number of tracks and a V° where the V° is consistent with a γ or e^+e^- pair.

[†]a neutral track that decays subsequently into a pair of charged particles and leaves a 'V'-shaped trajectory

5. A number of tracks from a primary vertex and a V^-, where the V^- decays into a negative and a neutral V°. The V^- must be consistent with a Ξ^- or Ω^-, and the V° with a Λ.

6. A primary vertex and two secondary V°'s.

7. A primary vertex with a V^- and a V°.

8. A primary vertex with 3 V°'s.

The topology recognition program also finds scattered tracks, and slow tracks which may spiral several times within the solenoid.

8.9 Monte Carlo simulation of the spectrometer

Since we only observe a subset of produced events in the spectrometer, it is necessary to have a method of extracting the produced data distribution from the observed one. The Monte Carlo simulation of the spectrometer is essential for this purpose. The algorithms comprising the Monte Carlo procedures are described in the following subsections.

8.9.1 Beam track generation

The generated phase space of the beam is based on the studies of the events satisfying T3 trigger. The generated beam is made to randomly interact in the target, accounting for nuclear absorption in liquid hydrogen. It is then propagated backwards out of the target corrected for the multiple scattering, energy-loss effects, and momentum smearing to define the generated beam track vector in the beam chambers.

The secondary beam tracks in the T3 events are also used in the MC event generation. They are propagated forward through the spectrometer and recorded in the downstream chambers. Smeared by the appropriate chamber resolutions,

these tracks then are used to study the effects of the secondary beam particles on the helix-track reconstruction.

8.9.2 Particle tracking and spectrometer responses

The Monte Carlo generated particle tracks are projected out from the primary interaction vertex and experience the spectrometer effects which include:

- multiple Coulomb scattering;
- energy loss in the spectrometer material;
- nuclear absorption of particles in the spectrometer material;
- weak decays; and
- nonuniformities in the magnetic field strengths.

The traveling of the charged particles in the magnetic field is computed by a Runge-Kutta algorithm with a nominal step size of 30 *cm* to generate track coordinates until the track has interacted, decayed, or exited the spectrometer. Multiple scattering errors are added whenever material would be encountered in the spectrometer. The energy loss is computed at each step from the amount of material traversed by the tracked particle. Nuclear absorption and weak decays are modeled as exponential effects with known characteristic absorption lengths, decay lifetimes, and branching ratios.

The responses of the chambers, scintillators, and Cherenkov counters are modeled as a function of the angle of incidence of the track and the measured efficiencies of each device.

8.9.3 Test of MC simulation

The Monte Carlo simulation is tested using very clean n-prong events, elastic scattering events, and three pion decay of beam particle ($K^- \rightarrow \pi^+\pi^-\pi^-$). The efficiencies and resolutions of the detectors were measured using the tracks of very clean n-prong events. The normalization of the experiment is determined using

the elastic scattering events because the cross section of the elastic scattering $K^-p \rightarrow K^-p$ is very well-known. The three pion decays of K^- beam are studied and found to reproduce the kaon mass very well.

Chapter 9

$K\omega$ system analysis

9.1 $K\omega$ event selection

The $K\omega$ data sample is obtained from the reaction

$$K^- p \rightarrow K^- \pi^+ \pi^- \pi^0 p \tag{9.1}$$

by taking the ω signal region of the 3π system. In the final state of reaction 9.1, there are 4 charged and one neutral tracks with a total net charge zero. Since the LASS spectrometer was not equipped with a photon detector, the π^0 in the final state is not seen. But this reaction can still be reconstructed because of the nearly complete 4π solid angle coverage and the excellent charged particle reconstruction efficiency of LASS. Therefore, by assuming that we reconstruct all charged particle tracks without any missing momentum and there is only one missing neutral track, a kinematic fit can be applied to determine the momentum vector of the missing track, in this case the π^0.

Starting from the Data Summary Tapes (DST), the selection of events corresponding to reaction 9.1 is performed by the following steps in sequence:

1. Topology selection;
2. Kinematic fits (MVFit);
3. Particle identification;

4. Final event selection and background subtraction.

9.1.1 Topology selection

The main goal of the topology selection is to reduce the huge data sample of E135 to a more manageable size by selecting the events whose track topology matches that of the reaction (9.1). The events with four charged tracks associated to the primary vertex with net charge zero are selected as candidates for the reaction (9.1). After that, the following rather loose kinematical requirements are imposed:

(a) for at least one mass assignment combination, the missing mass squared (MM^2) recoiling against $K^-\pi^+\pi^-p$ must satisfy $|MM^2| < 0.3(GeV/c^2)^2$ for the missing neutral particle to be consistent with a π^0;

(b) with the assumption that the missing neutral corresponds to a π^0, the effective mass of the three pion system for at least one of the surviving mass combinations must satisfy $m_{3\pi} \leq 1.10$ (GeV/c^2).

About 3.2×10^6 events* passed these criteria. A typical MM^2 distribution for these events is shown in Fig. 9.1, where up to 4 entries per event are plotted assuming all possibilities of mass assignment combinations of $K^-\pi^+\pi^-p$. The peak around $MM^2 \sim 0$ are consistent with both the reaction (9.1) and the background process $K^-p \rightarrow K^-\pi^+\pi^-p$.

The effective mass distribution of $\pi^+\pi^-\pi^0$ for these events is shown in Fig. 9.2. A clear ω signal is already observed above a large continuous background. Further event selections are, then, to focus on reducing these substantial background events.

9.1.2 MVFit

The next step in the event selection process involves the geometrical and kinematic fitting of the 4-prong events that passed the prior loose kinematic cuts. The

*a direct quote from Hayashii thesis (3177 K)

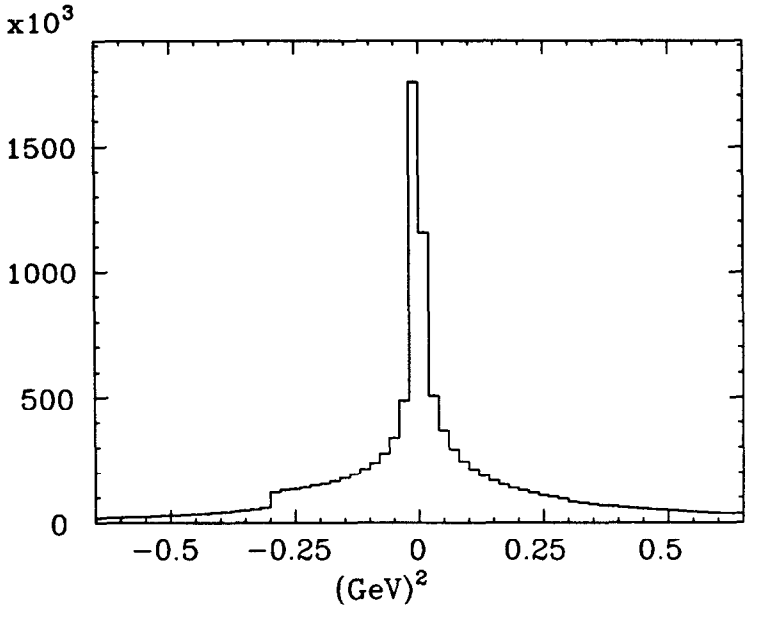

Figure 9.1: Missing mass squared for topology selected events

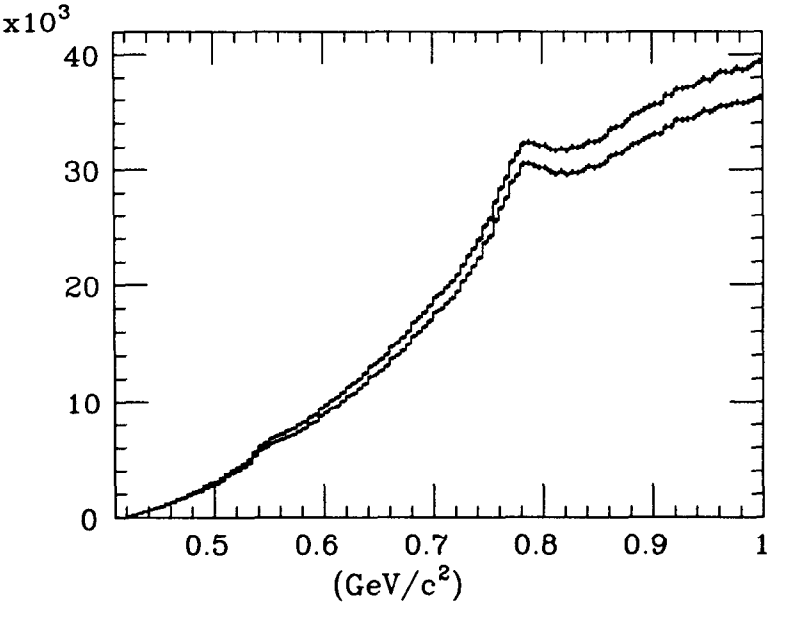

Figure 9.2: $\pi^+\pi^-\pi^0$ invariant mass distribution for topology selected events

fit is performed using the program **MVFIT**, a multi-vertex least-squares fitting program described in detail elsewhere.[46]

First, a fit imposing the constraint that all the reconstructed charged particle tracks originate from one primary vertex (called the "geometry" fit) is performed. The events that do not have a converged geometrical fit are removed. The removed fraction is negligible, $\sim$ 0.6 % , but the geometrical fit is still useful in that it provides an improved initialization of the kinematical fits that follow. After the geometrical fit, each event is kinematically fit with two different hypotheses: first, four-momentum constraint (4-C) fits to the reaction hypothesis

$$K^- p \rightarrow K^- \pi^+ \pi^- p \tag{9.2}$$

are performed to anti-select the events that come from the diffractive background process (9.2); finally, energy constraint (1-C) fits to the reaction (9.1) are performed. Since there are four possible mass assignments for the charged particle tracks – K^- and π^- for the two negative tracks and p and π^+ for the two positively charged tracks – both 1-C and 4-C fits are performed four times according to these different mass assignments.

The event selection criteria from the MVFits are:

1. The event has a converged geometry fit;
2. The event is not consistent with reaction (9.2) in that the 4-C fit confidence level (CL) is less than 10^{-10};
3. The event is consistent with the reaction (9.1) so that the 1-C fit confidence level is bigger than 10^{-10}. Later, a tighter 1-C fit condition is used requiring CL(1-C) $\geq 10^{-2}$.

The confidence level distribution of 4-C fit is shown in Fig. 9.3(a). To show the reliability of this cut, the $\pi^+\pi^-\pi^0$ invariant mass distribution of the events removed by the 4-C fit is shown in Fig. 9.4(a). Approximately 41 % events are removed by this cut but no evidence of the loss of ω signal is seen. The confidence level distribution of 1-C fit is shown in Fig. 9.3(b) and the $\pi^+\pi^-\pi^0$ invariant mass

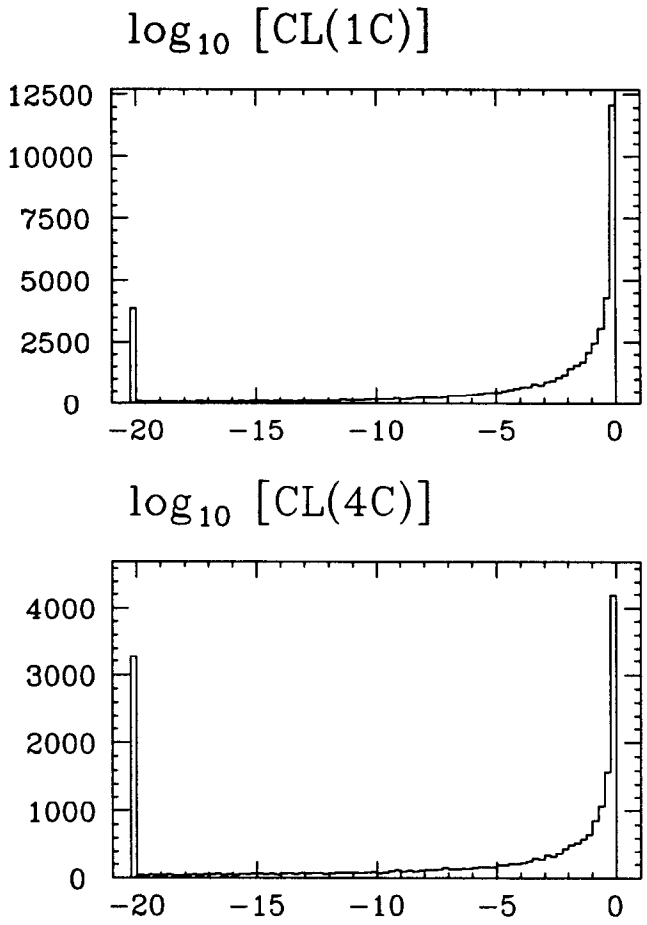

Figure 9.3: Typical confidence level distributions of 4-C and 1-C MVfits. Events with confidence level less than 10^{-20} accumulate in the bin at 10^{-20}.

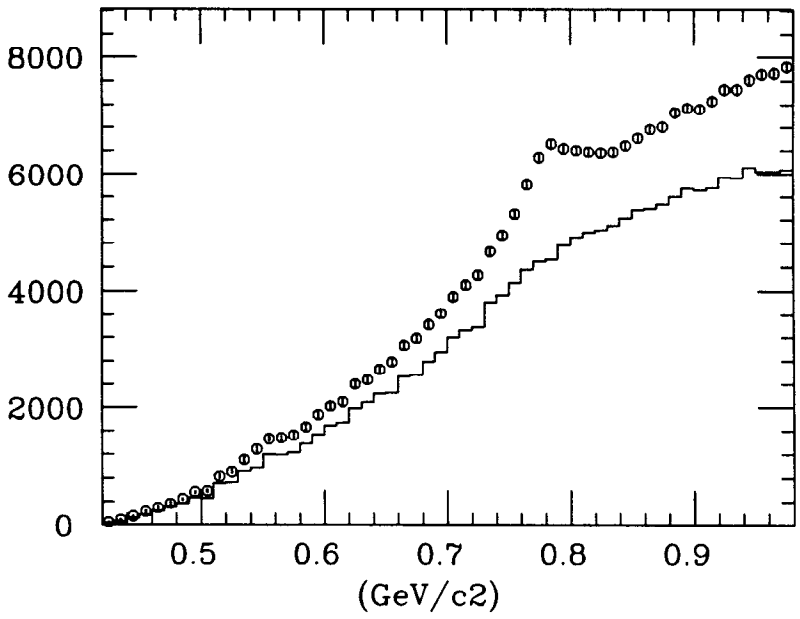

Figure 9.4: The inner histogram shows a typical $\pi^+\pi^-\pi^0$ invariant mass distribution of the events removed by the 4-C and 1-C MVFits. The data points outside the histogram represent the $m_{\pi^+\pi^-\pi^0}$ distribution of the corresponding sample before MVFit.

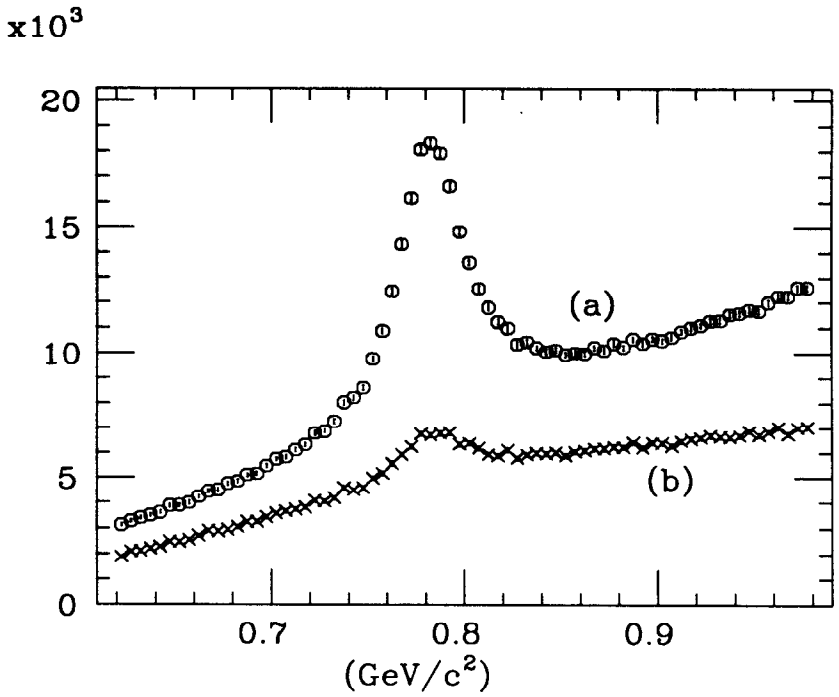

Figure 9.5: (a) $\pi^+\pi^-\pi^0$ invariant mass distribution after MVFit selection (points marked by o); (b) Events removed by PID cut and tighter 1-C cut (points marked by ×)

distribution of the removed events is shown in Fig. 9.4. No evidence of ω signal loss because of this cut is seen. Additional 25 % of events are removed by the 1-C cut. In terms of the efficiency and purity of data selection, the kinematical fits are very effective.

9.1.3 Particle Identification

After the MVFit selection, the $\pi^+\pi^-\pi^0$ invariant mass distribution of the surviving events is shown in Fig. 9.5. Already, the background under ω is significantly reduced. To select the ω events, events with $0.62 \leq m_{\pi^+\pi^-\pi^0} \leq 0.98$ GeV/c^2

only are chosen. To further purify the data sample, the particle identification (PID) information from the dE/dx measurement in the cylindrical proportional chambers, the time-of-flight (TOF) hodoscope, and the two threshold Cherenkov counters ($\check{C}_1$, $\check{C}_2$) are used. The use of PID helps select true $K\omega p$ events with the correct mass assignment in two aspects: a) to remove 4-prong events for which the charged particle set is not $\{K^-\pi^+\pi^-p\}$; b) to anti-select wrong MVFit mass assignments in events which have a correct 4-prong particle set. For each mass assignment of an event, PID information is applied track-by-track such that if the particle hypothesis in any track is proven to be wrong, that mass assignment is dropped but if the PID is inconclusive then it is retained. For example, if an assigned 'π^+' track is consistent with p but not with π from PID, the event is removed, but if that track is consistent with both π and p, it is retained. In general, the main concern is not to select only positively identified events but to remove wrongly identified events (or bad mass assignments). In each PID cut, the $\pi^+\pi^-\pi^0$ invariant mass distribution was used as an indicator of the reliability of the cut.

For example, Fig. 9.6 shows how dE/dx and TOF informations are used to remove pion contamination in the tracks assigned as 'proton'. Figure 9.6(a) shows the gray-scale scatterplot of the 3-momentum vs. TOF-measured mass-squared for 'proton' tracks. In addition to a band at $\sim m_p^2$, there is a very dense population around $m^2 \approx 0 \approx m_\pi^2$, which may be interpreted as a pion contamination. These events are removed and Fig. 9.6(c) shows the $m_{3\pi}$ distribution for the removed events. Only very little ω signal is seen. Similarly, Fig. 9.6(b) shows the gray-scale scatterplot of the 3-momentum vs. p/π log-likelihood for 'proton' tracks. There are many events populated in the region $\log(p/\pi) < 0$, in which case the track is more likely a pion. These events are removed and Fig. 9.6(d) shows the $m_{3\pi}$ distribution for the removed events. There is almost no ω signal in the removed events.

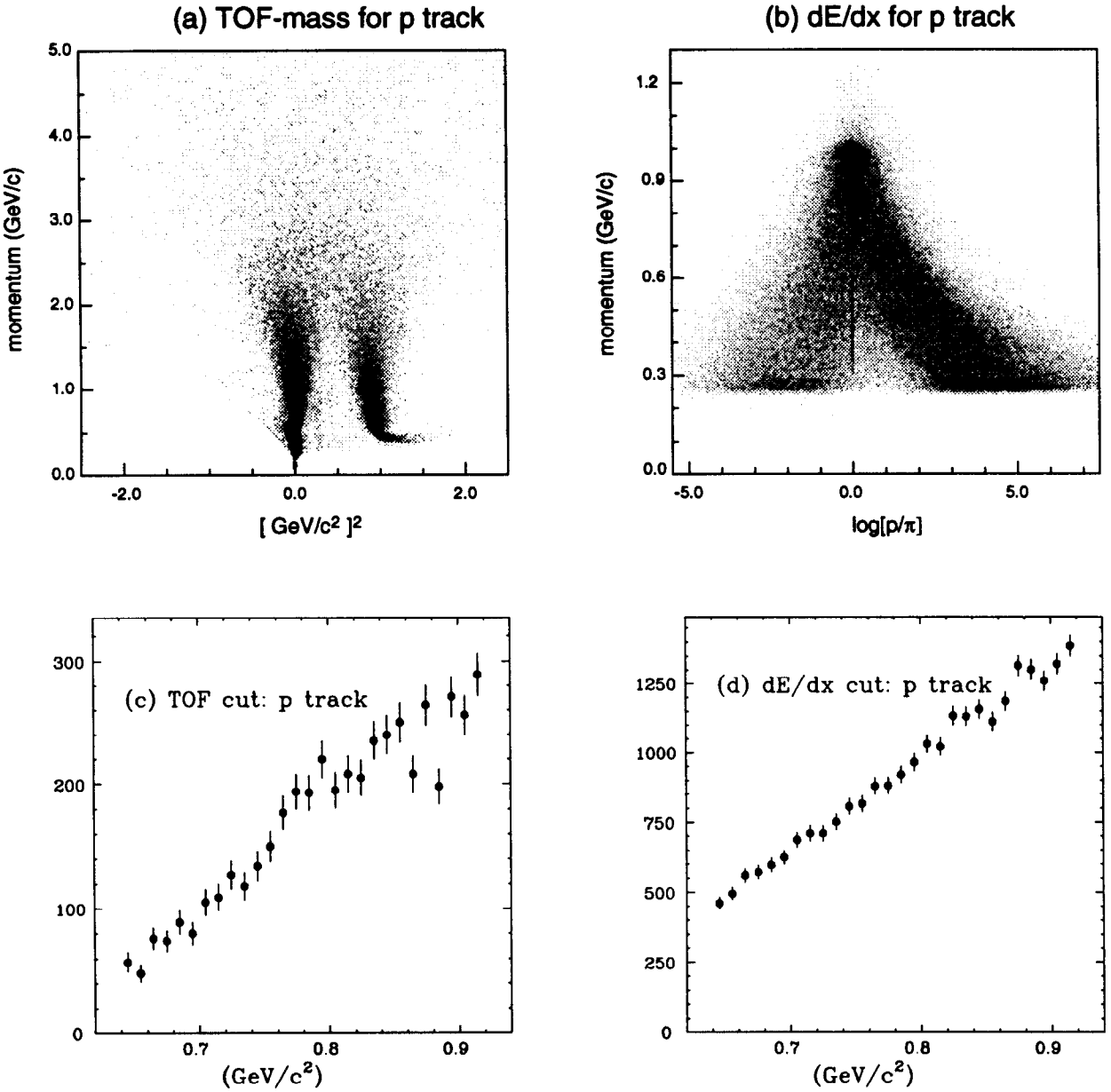

Figure 9.6: dE/dx and TOF plots for PID cut. The cut regions are indicated in the figures: (a) 3-momentum vs. TOF-measured mass-squared for tracks assigned as 'proton'; (b) 3-momentum vs. p/π log-likelihood for 'proton' tracks; (c) $\pi^+\pi^-\pi^0$ invariant mass distribution for events removed by (a); and (d) $\pi^+\pi^-\pi^0$ invariant mass distribution for events removed by (b).

Table 9.1: mass assignment ambiguity after PID

Combinations per event	CL(1-C)$\geq 10^{-10}$	CL(1-C)$\geq 10^{-2}$	CL(1-C)$\geq 10^{-2}$ and PID
1	0.857	0.882	0.922
2	0.142	0.118	0.078
3	0.0002	0.0001	0.0001
4	0.0000	0.0000	0.0000

9.1.4 The final event selection

Since we used PID cuts in a relatively conservative way, there still remains some ambiguities in mass assignment for the 1-C fitted tracks. Table 9.1 shows the mass assignment ambiguity after particle ID cuts. Approximately 86 % of the events have a unique mass assignment but the others have twofold or more ambiguities. This can be reduced, as shown, if we make a tighter cut on the quality of 1-C fits. Therefore, to reduce background and mass assignment ambiguities, the cut criteria on the 1-C fit quality is tightened such that those events with 1-C fit confidence level less than 10^{-2} is removed from the event sample. After a tighter cut on the confidence level of 1-C MVFit, the percentage of events with a unique mass assignment increased to 88 % . The particle identification (PID) requirements are very effective in reducing this ambiguity. As shown in Table 9.1, approximately 92% of events that satisfy the tight 1-C and the PID requirements have a unique mass assignment. The events removed by the PID and the tighter 1-C confidence level requirements are shown in Fig. 9.5(b).

Further event selection, though not necessarily to improve the signal to background ratio, involves the 4-momentum transfer squared between the target proton and the recoil proton, $t' = |t_{p\to p}| - |t_{p\to p}|_{min},$. Since we are mainly interested in the forward production of $K\omega$ system, t' is restricted to $0.1 < t' < 2.0(\mathrm{GeV/c})^2$;

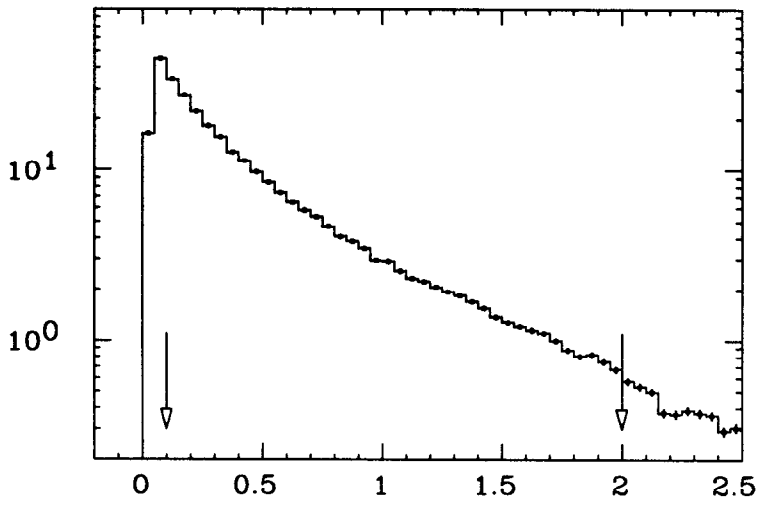

Figure 9.7: the t' distribution and cut positions

the lower cut-off is made since, for $t' \lesssim 0.08(\mathrm{GeV/c})^2$, the resulting slow proton almost always stops in the target. Figure 9.7 shows the t' distribution and cut positions of the remaining events. After all the cuts have been made, the final data set contains 223840 events containing 234644 successful MVFits.

9.2 General features of the data

9.2.1 Invariant mass distribution of $\pi^+\pi^-\pi^0$

The $\pi^+\pi^-\pi^0$ invariant mass distribution of the final data sample is shown in Fig. 9.8. It shows a very clear ω signal. The lineshape of ω is fitted assuming a double-Gaussian mass resolution function together with a second-order polynomial background. The solid curve represents the fit function. The resolution function is well described by double Gaussians with widths of 13 and 32 MeV/c^2 sharing a common center at $\sim$ 783 MeV/c^2.

There are $\sim$ 1.16 $\times$ 10^5 events in the ω signal region 0.72 $<$ $m_{\pi^+\pi^-\pi^0}$ $<$

Selection Criteria	Fraction Cut	Events Survived	Accepted 1-C MVFits
1. Total triggered ervents	1.1×10^8		
2. Topology selection	0.872	1.412×10^7	
3. Loose kinematical selection			
$\lvert mm2 \rvert < 0.3$	0.645	5.013×10^6	
$m(\pi\pi\pi) < 1.1$	0.638	1.817×10^6	
4. Mini DST	0.670	599354	928500
$CL(geo) > 10^{-10}$			
$CL(4C) < 10^{-10}$			
$CL(1C) > 10^{-10}$			
5. ω selection: $0.62 < m(\pi\pi\pi) < 0.98$	0.211	544501	690188
6. Tight 1C: $CL(1C) > 10^{-2}$	0.274	395119	441842
7. PID	0.250	296231	311213
dE/dx			
Time-of-Flight			
Cherenkov			
8. t' cut: $0.1 < t'(K\omega) < 2.0$	0.244	223840	234644

Table 9.2: $K\omega$ cut table

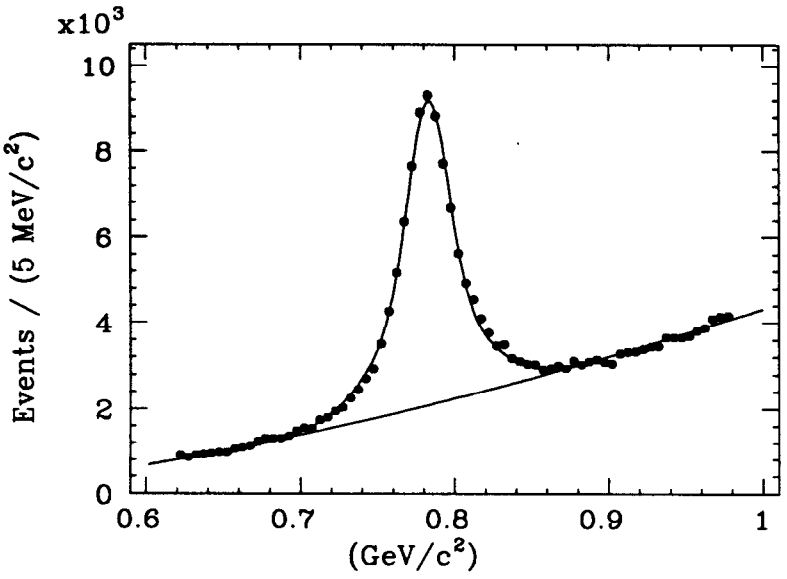

Figure 9.8: The $\pi^+\pi^-\pi^0$ invariant mass distribution of the final data sample

0.84 GeV/c^2. From the fitted lineshape, the ω signal in this region is estimated to be $\sim 6.6 \times 10^4$ events giving a signal to background ratio about 1.3:1. Although it seems that the peak in the ω signal region comes entirely from the decay of the ω meson, in principle it still needs to be checked. It can be done by using the angular distribution characteristic of the $J^P = 1^-$ meson decaying into three pions. The helicity angle θ_h of the ω decay is defined as the angle between the direction of the π^0 3-momentum vector and that of π^+ in the $\pi^+\pi^-$ rest-frame. Then from the quantum mechanics of the $\omega \to \pi^+\pi^-\pi^0$ decay, we expect

$$\frac{dN}{d\cos\theta_h} = (const) \times \sin^2\theta_h \tag{9.3}$$

Figure 9.9 shows that our data is consistent with Eq. (9.3). In Fig. 9.9(a) the events with a combined 3π mass within 0.78 ± 0.06 GeV/c^2 are plotted as a function of $\cos\theta_h$. The distribution (events per 0.05 $\cos\theta_h$ range) is fitted to $1 - \cos^2\theta_h$ plus constant background with χ^2 per degrees of freedom = 1.54. On the other hand, the $\cos\theta_h$ distribution of events in the side-band control region shows at

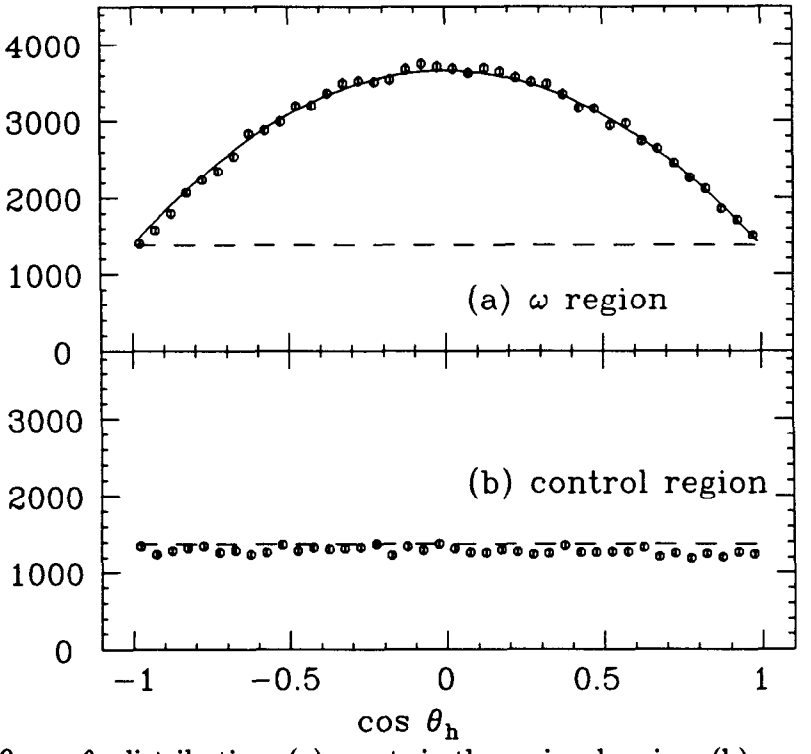

Figure 9.9: $\cos\theta_h$ distribution: (a) events in the ω signal region; (b) events in the control region

most a linear dependence on $\cos\theta_h$; Figure 9.9(b) shows the $\cos\theta_h$ dependence in the control region (0.67 ± 0.03 GeV/c^2 and 0.89 ± 0.03 GeV/c^2). The distribution is consistent with the constant background level determined from the fit in the ω signal region.

Once we accept the $\sin^2\theta_h$ distribution of $\omega \to \pi^+\pi^-\pi^0$ decay, and the independence of other $\pi^+\pi^-\pi^0$ events in the mass range ($0.62 < m_{\pi^+\pi^-\pi^0} < 0.98$ GeV/c^2), we can use the Legendre polynomials (or spherical harmonics) to extract the ω content from the $\pi^+\pi^-\pi^0$ peak. Let us define f_ω as the distribution function of $\omega \to \pi^+\pi^-\pi^0$ decay such that

$$f_\omega(\theta_h) = f_0 \sin^2\theta_h.$$

The coefficient f_0 is related to the total number of ω events N:

$$N = \int_{-1}^{1} f(\theta_h) d\cos\theta_h = \frac{4}{3} f_0$$

In reality, the 3π system is not all from ω but contains significant non-ω background. The θ_h distribution $f_{3\pi}$ of the three pion system can then be written as

$$\begin{aligned} f_{3\pi} &= f_\omega + f_b \\ &= f_0 \sin^2\theta_h + b_0 + b_1 \cos\theta_h, \end{aligned}$$

where $f_b = b_0 + b_1 \cos\theta_h$ is describing the background (non-ω) $\pi^+\pi^-\pi^0$ system angular distribution. Because of the $\sin^2\theta_h$ distribution, f_ω has two spherical harmonics elements, Y_{20} and Y_{00}, while f_b has Y_{00} and Y_{10} under the assumption of linear background in $\cos\theta_h$. Then, using the orthogonality of the spherical harmonic functions, we can extract the ω contents by weighting each event with Y_{20}:

$$\begin{aligned} \sum_{i=\text{events}} [Y_{20}]_i &= \langle Y_{20} | f_{3\pi} \rangle \\ &= \langle Y_{20} | f_\omega \rangle + \langle Y_{20} | f_b \rangle \\ &= f_0 \times \langle Y_{20} | \sin^2\theta_h \rangle \\ &= -1.057 \times f_0 = -0.793 \times N \end{aligned}$$

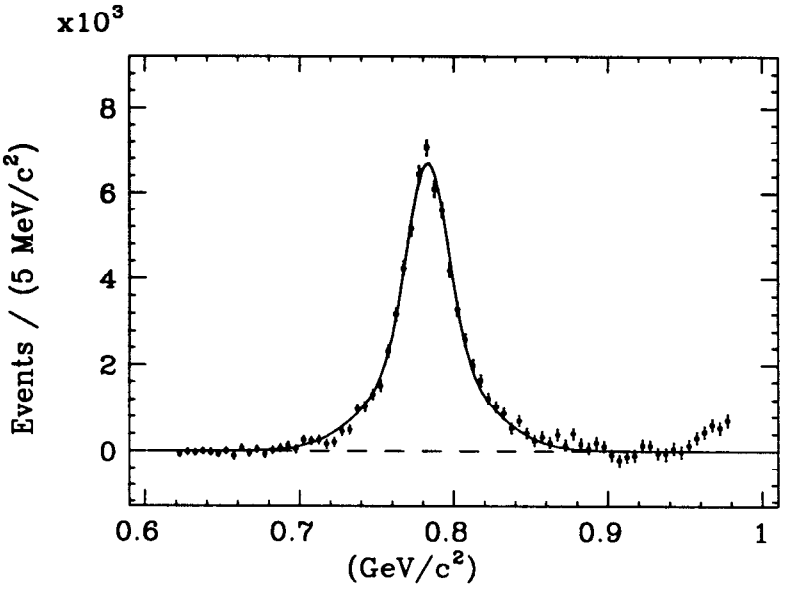

Figure 9.10: $\pi^+\pi^-\pi^0$ spectrum weighted by $-Y_{20}$

Figure 9.10 shows the $-Y_{20}$ weighted mass distribution of the three pion system. The background has almost entirely disappeared and we are left with a clean ω signal. The estimate of ω signal from $-Y_{20}$ weighted spectrum, divided by 0.793 for a proper normalization, is $(63.7 \pm 7.9) \times 10^3$. This is consistent with the estimated ω content of the unweighted $\pi^+\pi^-\pi^0$ mass spectrum. Therefore, we conclude that the events in the peak of $\pi^+\pi^-\pi^0$ mass spectrum centered at ~ 0.78 GeV/c^2 are almost entirely from the decay of $\omega \to \pi^+\pi^-\pi^0$.

9.2.2 Invariant mass distribution of $K\omega$

Selecting the events in the ω mass region ($0.72 < m_{\pi^+\pi^-\pi^0} < 0.84$GeV/c^2), the $K^-\pi^+\pi^-\pi^0$ invariant mass distribution (Fig. 9.11(a)) shows peaks in the $K\omega$ threshold region and in the $1.7 - 1.8$ GeV/c^2 region. Although the underlying states in the peak regions will be determined in the partial wave analysis, we expect that the prominent states might be 1^+ in the threshold region and 2^- in the $1.7 - 1.8$ GeV/c^2 region.

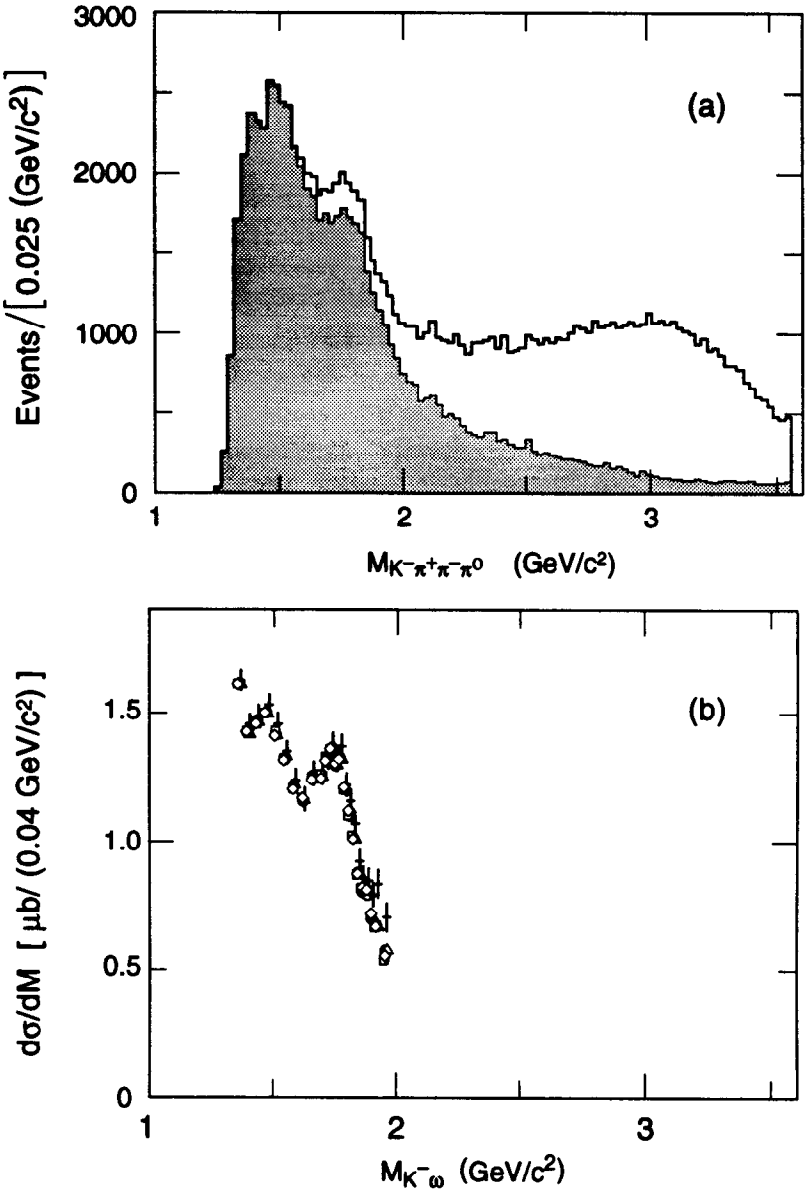

Figure 9.11: The $K^-\pi^+\pi^-\pi^0$ invariant mass distribution for events with $0.1 < t' < 2.0$ (GeV/c)^2: (a) The unshaded curve contains all events that satisfy $0.72 < m_{\pi^+\pi^-\pi^0} < 0.84$ GeV/c^2 while the shaded portion contains only events with $m_{p\omega} > 2.28$ GeV/c^2 and $m_{pK} > 2.0$ GeV/c^2; and (b) The background-subtracted and acceptance-corrected mass distribution; the points with error bars are the measured values and the points displayed by various symbols are the PWA-fitted values shown for comparison.

Since it includes all the events inside the ω mass region which has significant non-ω backgrounds, we cannot accept Fig. 9.11(a) as a true $K\omega$ mass spectrum. To find the mass spectrum of $K\omega$, we have to find a way to separate the ω signal from the background contributions in the $K^-\pi^+\pi^-\pi^0$ mass distribution. Three different methods were tried:

a. Linear background subtraction: This is the simplest method of all. Every event is classified into one of the three regions – signal region, side-band region, and neutral region – and given an appropriate weight w. Those events in the side-band regions ($0.64 < m_{3\pi} < 0.70$ GeV/c^2 and $0.86 < m_{3\pi} < 0.92$ GeV/c^2), are given weight of -1 and the events in the ω signal region are given $+1$. All the other events are given weight of $w = 0$. This method assumes that the background is a linear function of $\pi^+\pi^-\pi^0$ mass, which appears to be a good approximation if we look at the global $\pi^+\pi^-\pi^0$ mass distribution(Fig. 9.8). Unfortunately, if we look at the $\pi^+\pi^-\pi^0$ mass distribution in a specific $K\omega$ mass interval, the background is not always well described by a linear function. Fig. 9.12 shows the $\pi^+\pi^-\pi^0$ mass distribution for the events with $1.56 < m_{K3\pi} < 1.60$ GeV/c^2. The solid curve represents the lineshape fitting with a quadratic background. The quadratic function describes the background better than a linear function. The background becomes more complicated near the $K\omega$ threshold region where the limitation of phase space affects the lineshape of the $\pi^+\pi^-\pi^0$ mass spectrum.

b. Weighting by $-Y_{20}$: As shown in the last section, due to the spin-parity ($J^P = 1^-$) of the ω, weighting by $-Y_{20}$ extracts almost background-free ω signal. Therefore, $-Y_{20}$ weighting is tried to find the $K\omega$ mass spectrum. Figure 9.13 shows the $\pi^+\pi^-\pi^0$ mass distribution weighted by $-Y_{20}$ for events with $1.56 < m_{K3\pi} < 1.60$ GeV/c^2. Although weighting all events by $-Y_{20}$ for the entire kinematic range resulted in a background-free ω signal (Fig. 9.10), if the $K\omega$ mass range is restricted to a narrow region as in Fig. 9.13 a non-zero background appears in the resulting weighted $\pi^+\pi^-\pi^0$ mass distribution.

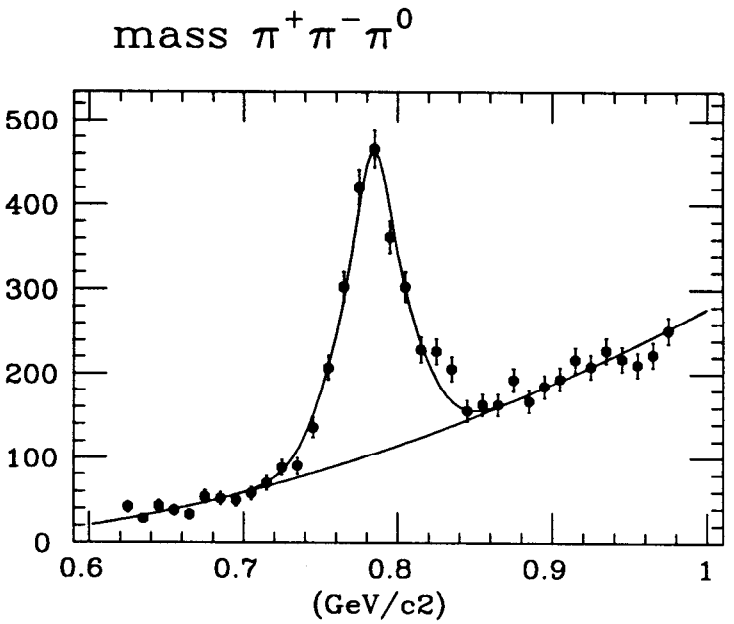

Figure 9.12: $\pi^+\pi^-\pi^0$ for $m_{K\omega} = 1.58 \pm 0.02$ GeV/c^2

The dotted curves in Fig 9.13 represent the fitted signal and background linear in $m_{3\pi}$. It is not understood exactly what causes the distortion of θ_h distribution of the non-ω three pion system when it is restricted to a narrow range of $m_{K3\pi}$.

c. ω lineshape fitting: As either of the methods above do not properly describe the non-ω background in the three pion system, the direct counting of ω contents by fitting its lineshape with a quadratic background is used to find the $K\omega$ invariant mass distribution. Since we have to fit the ω lineshape for every $K^-\pi^+\pi^-\pi^0$ mass bin, it is relatively slow compared to the methods above but it is the most accurate way. Since we are taking $0.72 - 0.84$ GeV/c^2 as the ω signal range, the effect of phase space on the $\pi^+\pi^-\pi^0$ mass distribution is significant for the events with $m_{K3\pi} \lesssim 1.4$GeV/c^2. Therefore, two-body phase space is included in fitting the $\pi^+\pi^-\pi^0$ mass spectrum for $m_{K3\pi} \leq 1.5$ GeV/c^2. Figure 9.14 displays such effects in the $\pi^+\pi^-\pi^0$ mass spectrum in two different $m_{K3\pi}$ bins. The $\pi^+\pi^-\pi^0$ lineshapes of the low $m_{K3\pi}$

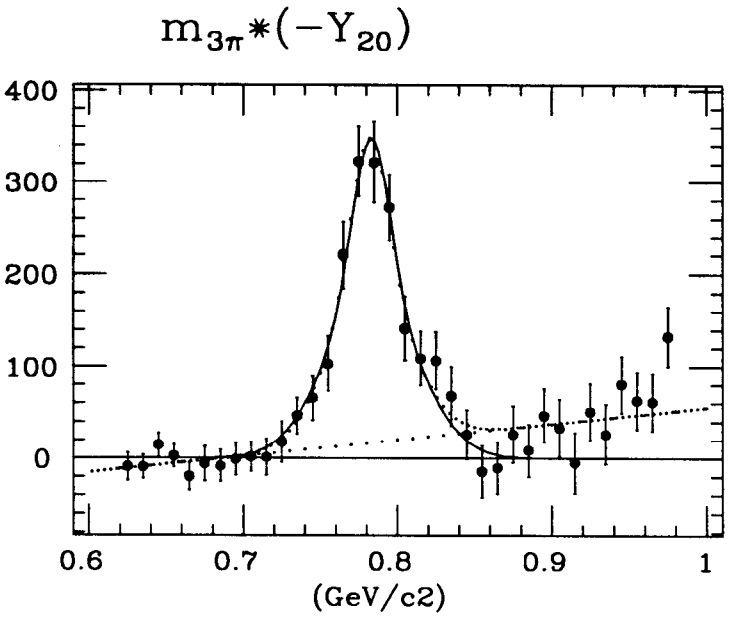

Figure 9.13: $m_{\pi^+\pi^-\pi^0}$ weighted by $-Y_{20}$ for $m_{K\omega} = 1.58 \pm 0.02$ GeV/c^2

events are explained very well by introducing the two-body phase space factor.

Figure 9.11(b) shows the $K\omega$ mass spectrum obtained using the background subtraction method 'c' and corrected for the acceptance loss, which will be discussed in detail in section 9.4. Like the raw $K^-\pi^+\pi^-\pi^0$ mass distribution, significant enhancements are seen at threshold and in the $1.7-1.8$ GeV/c^2 region. The signal in the latter region is much clearer after the background subtraction.

The high mass region of $K\omega$ contains substantial contamination from the production of baryon resonances. These baryons are produced by the processes;

$$K^-p \rightarrow K^-N^*\,,$$
$$K^-p \rightarrow \omega Y^*\,.$$

They are clearly displayed in the Dalitz plot of m^2_{pK} vs. $m^2_{K\omega}$ (Fig. 9.15) which contains only events with $m_{\pi^+\pi^-\pi^0}$ in the ω signal region: most noticeably, a clear production of $\Lambda(1520)$, a broad enhancement in the $m_{pK} \sim 1.8$ GeV/c^2 region, and

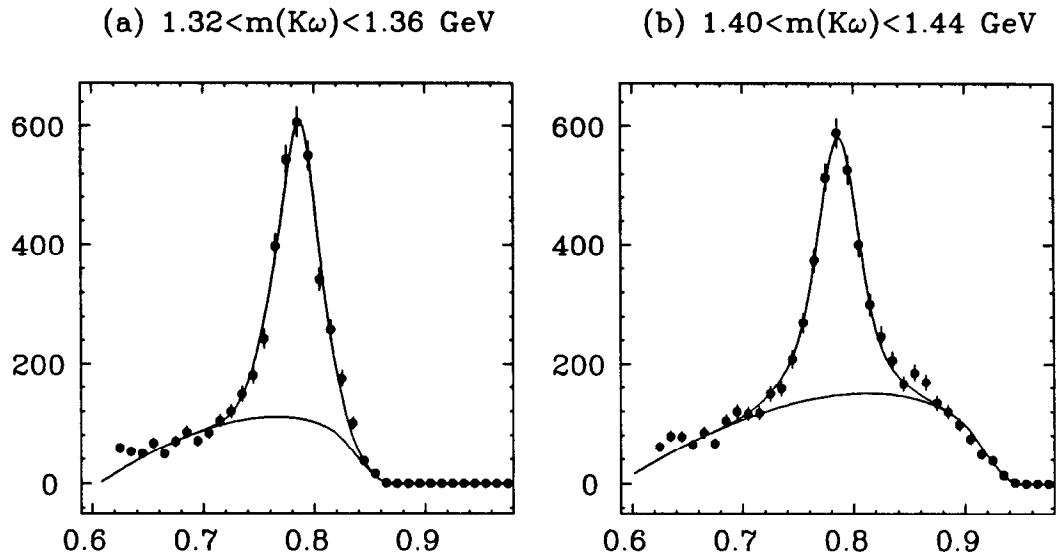

Figure 9.14: ω fitting for two different $m_{K\omega}$ bins in the $K\omega$ threshold region.

a low-mass enhancement in $p\omega$ system. These baryon production backgrounds are removed from the sample used in the partial wave analysis of the $K\omega$ system with the mass cuts $m_{p\omega} < 2.28 GeV/c^2$ and $m_{pK} < 2.0 GeV/c^2$.

The positions of the cuts are shown in the invariant mass distributions of the $p\omega$ and pK (Figs. 9.16(a)-(b)) systems, respectively. The low $m_{K\omega}$ region ($\leq$ 1.8 GeV/c^2) is very little affected by these baryon cuts.

9.3 The Double moments

The $K\omega$ system produced from the two-body decay of a hypothetical strange meson X, the quantum numbers of which are to be determined from partial wave analysis, is specified by $m_{K\omega}$, $t'_{\text{beam}\to K\omega}$, and the angular distributions of the decay of X into $K\omega$ and the subsequent decay of $\omega \to \pi^+\pi^-\pi^0$. The angular distribution is specified by the combined spherical harmonic moments of the two-stage decays ("double moments"). The double moments are defined in section 9.3.1. This is

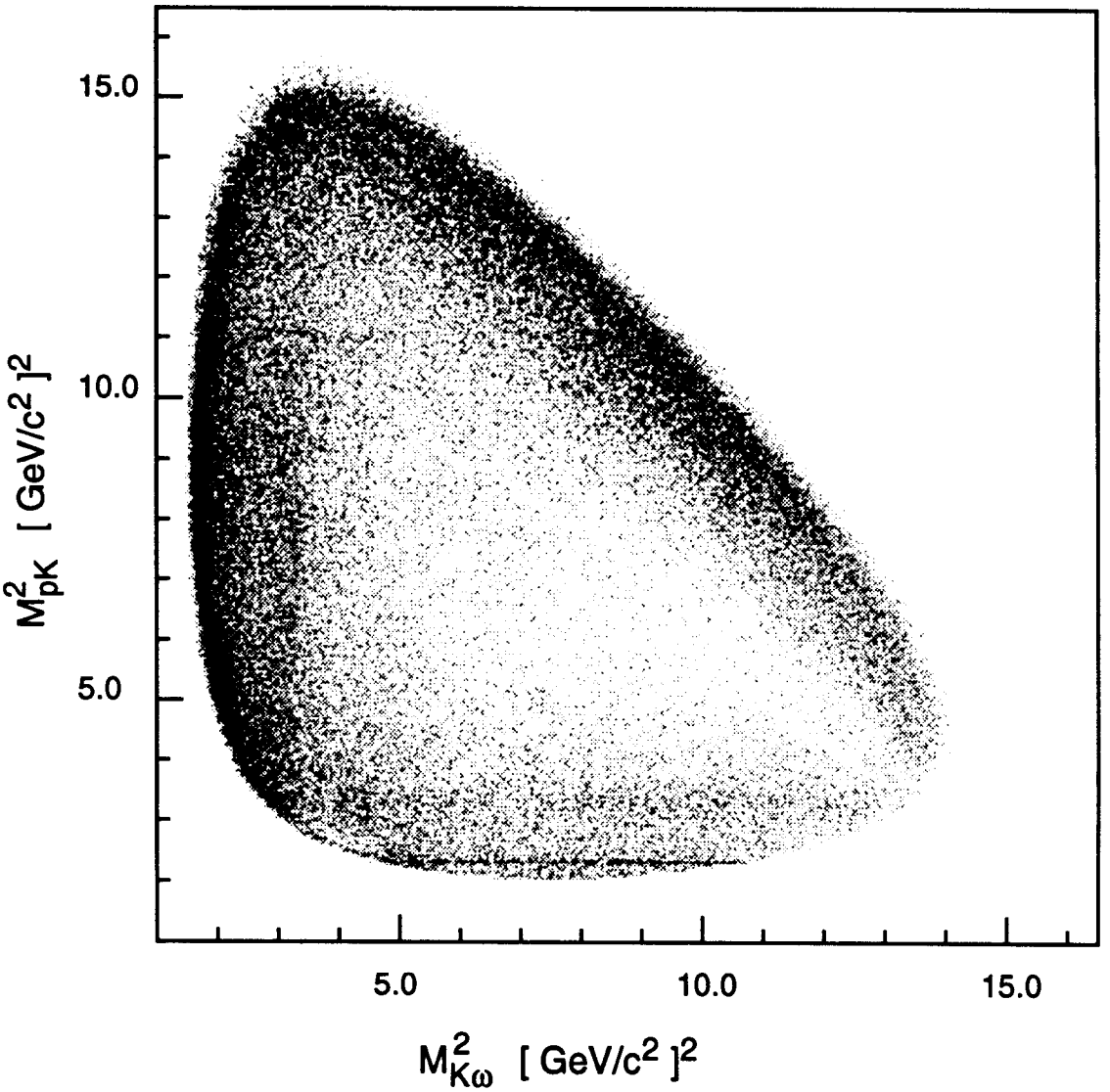

Figure 9.15: $K\omega$ Dalitz plot

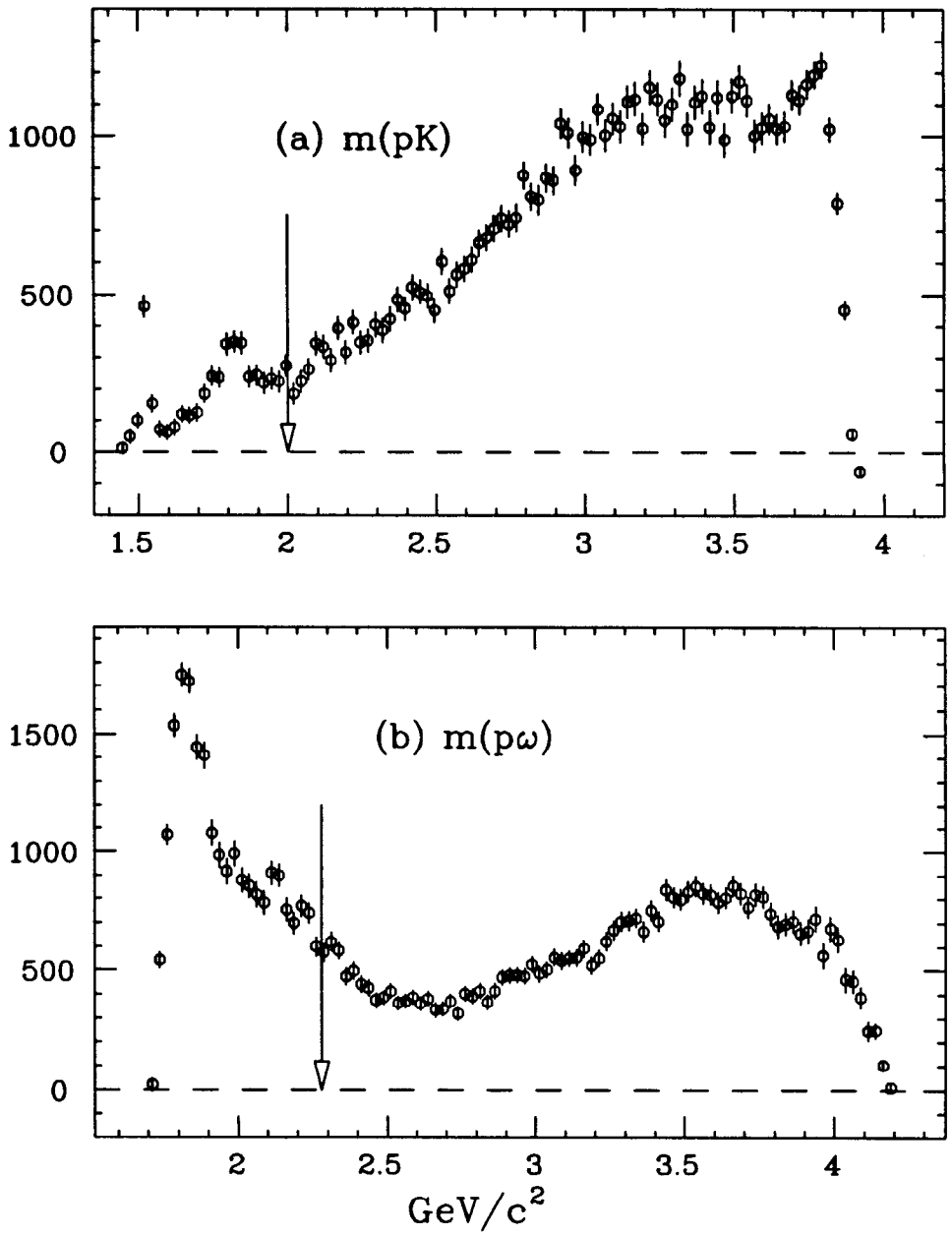

Figure 9.16: The invariant mass distributions of (a) pK and (b) $p\omega$ systems obtained by the $\omega \to \pi^+\pi^-\pi^0$ background-subtraction method.

based on the work by Martin and Nef[44]. The measured moments are presented in 9.3.2.

9.3.1 Definition of double moments

For a given $K\omega$ mass interval and a given range of momentum transfer t' from beam to $K\omega$, the double moments are experimentally measured by

$$\begin{aligned} H(LMlm) &= \int\int I(\Omega_1,\Omega_2) D^L_{Mm}(\Omega_1) D^l_{m0}(\Omega_2)\, d\Omega_1\, d\Omega_2 \\ &= \sum_{i=\text{events}} w_i [D^L_{Mm}(\Omega_1) D^l_{m0}(\Omega_2)]_i, \end{aligned} \tag{9.4}$$

where $I(\Omega_1,\Omega_2)$ is the angular distribution. The normalization is chosen such that

$$\int I\; d\Omega_1\; d\Omega_2 = H(0000) = N,$$

where N is the number of events in a specified $m_{K\omega}$ interval, integrated over a given range of momentum transfer. The solid angle $\Omega_1(\theta_1,\phi_1)$ describes the ω direction in the $K\omega$ rest frame with reference to axes defined such that the $\mathbf{z_1}$ axis is along the K^- beam direction and the $\mathbf{y_1}$ axis is normal to the production plane (Gottfried-Jackson frame), and similarly the solid angle $\Omega_2(\theta_2,\phi_2)$ describes the normal vector to the 3π decay plane in the ω rest frame, with the ω direction in the $K\omega$ rest frame as the $\mathbf{z_2}$ axis, and $\mathbf{y_2} = \mathbf{z_1} \times \mathbf{z_2}$.

For each event, the background subtraction function w_i is defined to separate the ω signal from the non-ω three pion system. The background subtraction for the special case $H(0000)$, which just describes the number of produced events, is detailed in the previous section. For all the other moments, unless $m_{K\pi\pi\pi}$ is near $K\omega$ threshold, the linear background subtraction (method 'a') is used as it gave results consistent with method 'c' (ω signal fitting) within statistical uncertainties. For those events in the $K\omega$ threshold region, the limited phase space affects the shape of the $\pi^+\pi^-\pi^0$ mass spectrum so that the background is not well described by a simple polynomial, and method 'c' is used to measure the signal contents in the double moment calculation.

The index L runs from 0 to $2J$, where J is the highest spin quantum number of the mesons under study. Similarly, l runs from 0 to 2 for ω spin is 1. From the properties of the angular momentum matrix D, M and m should satisfy $-L \leq M \leq L$ and $-l \leq m \leq l$, respectively. Because not all of the moments $H(LMlm)$ are independent, the range of indices can be further reduced to give $l = 0, 2$ and $M \geq 0$. The reasoning is explained in detail in section 9.4 below where the acceptance correction scheme is described.

9.3.2 Measurements

The measured double moments with proper background subtractions are displayed in Fig. 9.17. The moments are displayed as measured; without acceptance correction and baryon mass cuts. The moment set is limited to $L \leq 6$ because the event sample is not large enough to study higher-order moments of the angular distribution reliably and no strange meson state with spin > 3, which requires moments of $L > 6$, is expected in this mass region. All independent moments with $0 \leq L \leq 6$ are presented. The moments with $l = m = 0$ represent the spherical harmonic moments of the two-body decay of $X \rightarrow K\omega$. The acceptance-corrected moments with baryon mass cuts will be shown in section 9.4 below.

9.4 The Acceptance correction

9.4.1 The Monte Carlo events

In a complicated spectrometer, a relativistic particle passing through it can suffer a variety of effects from target materials, various detector components, magnet structures, and other supporting structures so that tracks from real events can be lost or confused by the event reconstruction programs. There are weak decay losses, nuclear absorption losses, losses due to particles being scattered abruptly from their helical orbits, and trigger losses. In addition, the various cuts applied in defining the event sample also affect the distributions in phase space. The

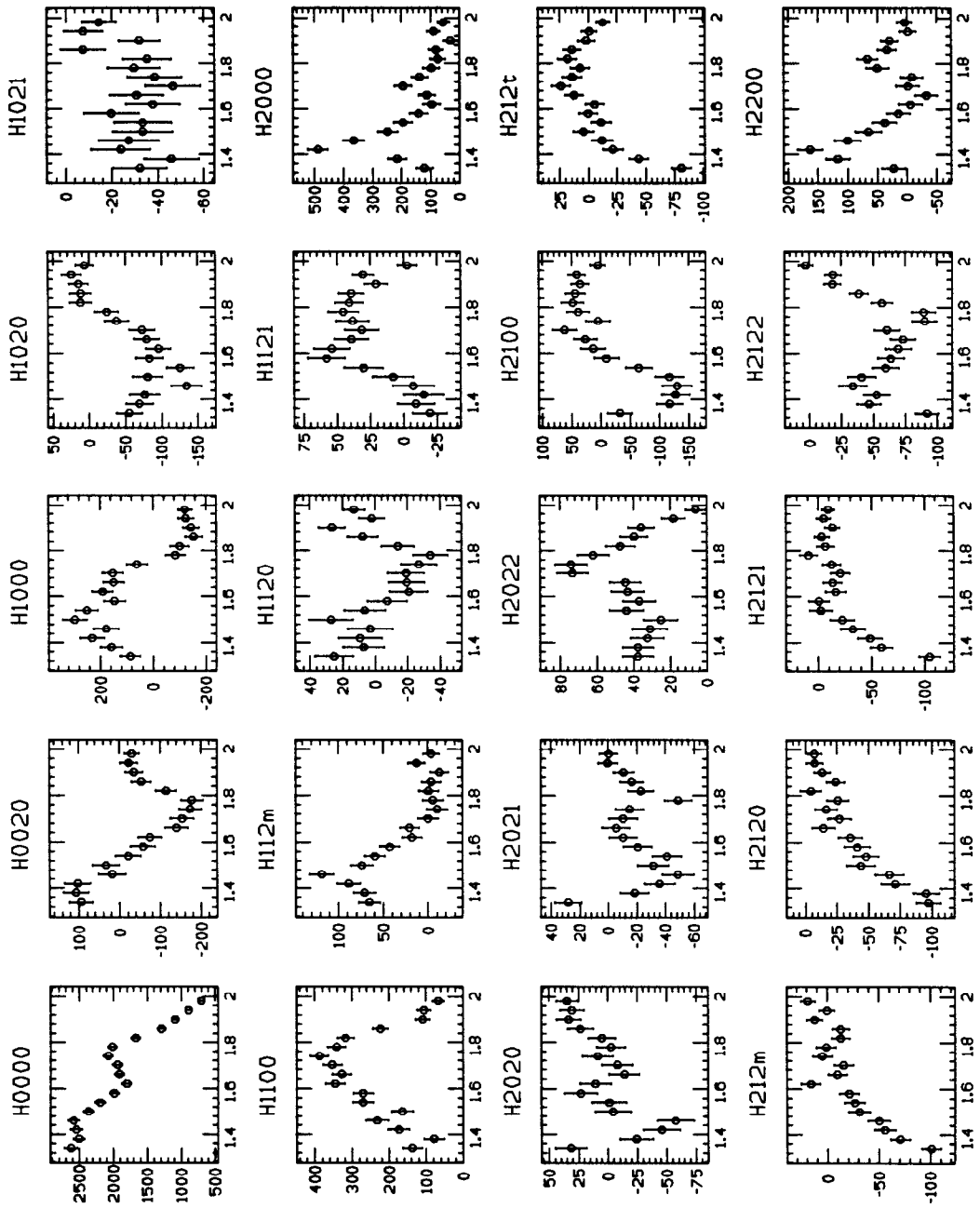

Figure 9.17: Measured double moments without acceptance corrections

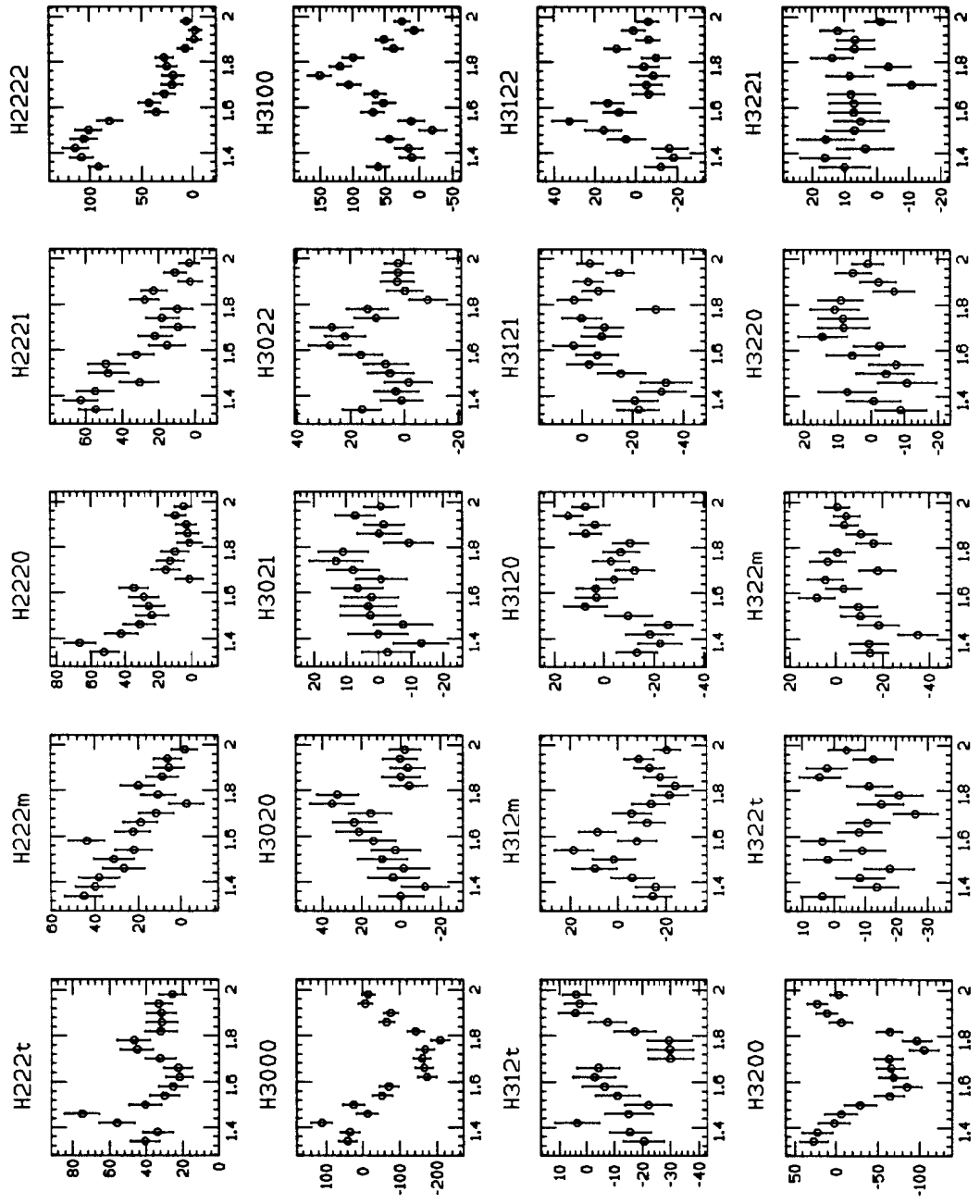

Figure 9.17 continued (2)

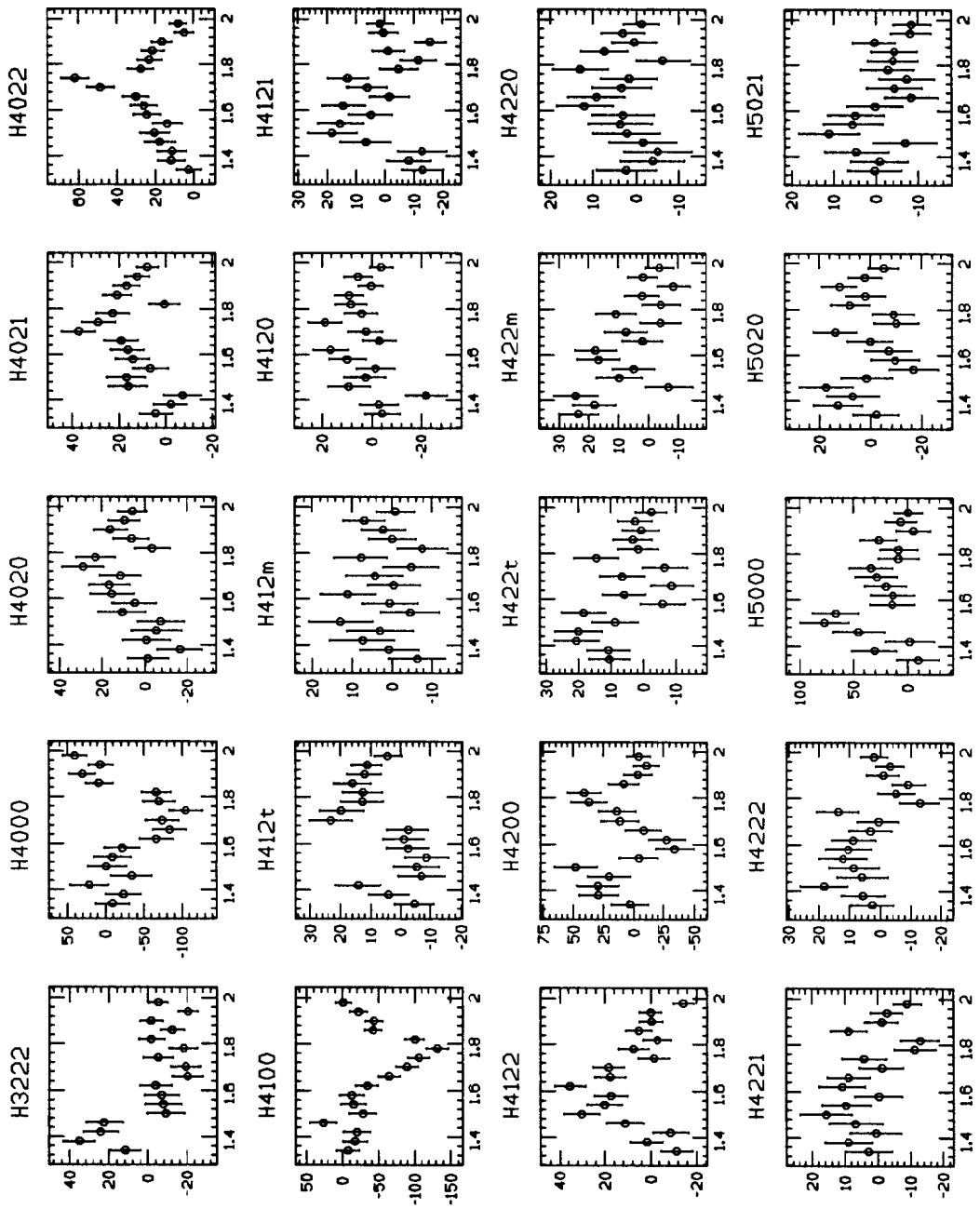

Figure 9.17 continued (3)

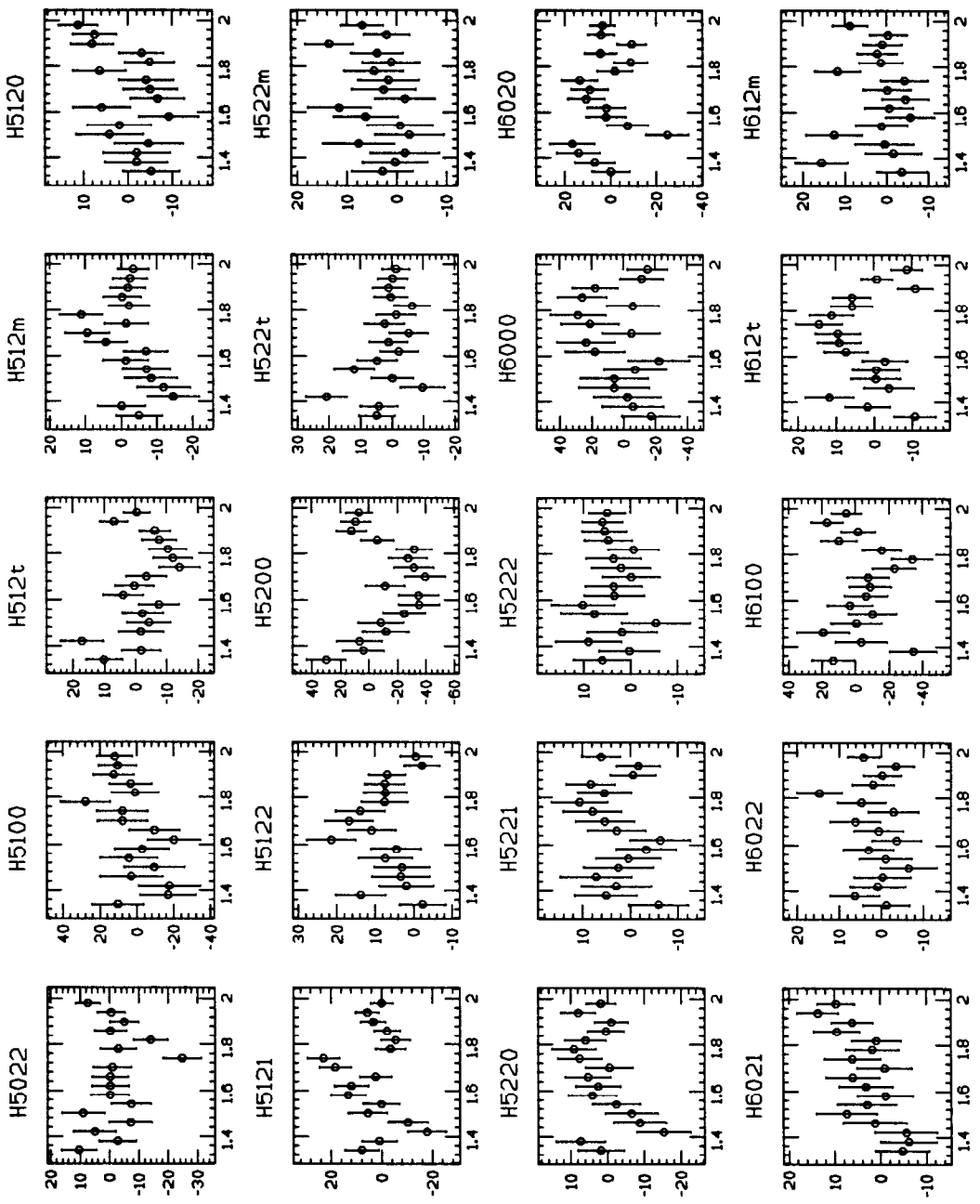

Figure 9.17 continued (4)

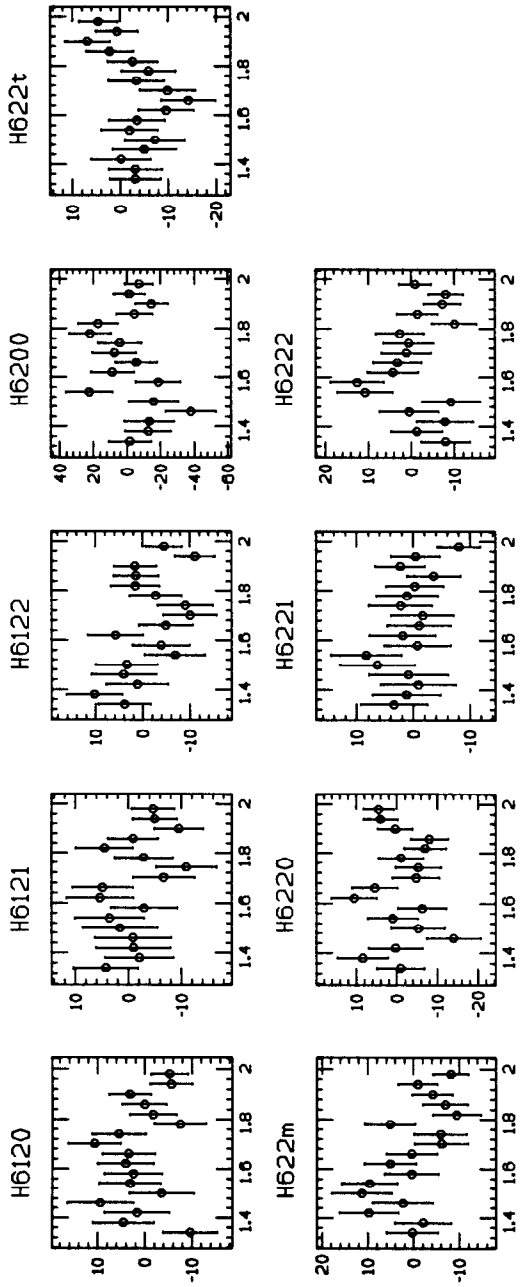

Figure 9.17 continued (5)

magnitude of these problems and their effects on the physics results need to be estimated.

For this purpose, computer programs written by E135 collaborators to model the device and simulate particle tracks interacting with it are used. The tracks are generated by the Monte Carlo method. Particle tracks corresponding to the reaction $K^-p \to K^-\pi^+\pi^-\pi^0 p$ are randomly generated to be uniform in $m_{K\omega}$ and the four angles which are defined in section 9.3.1 and with an exponential dependence on the momentum transfer between the beam and $K\omega$. To simulate the $\sin^2\theta$ distribution of the ω helicity angle θ_h, a portion of the MC events are removed by the rejection method.

Each track of these generated events is processed through the simulation program of LASS spectrometer described in section 8.9. Then, these Monte Carlo events are processed by the same programs of event selection and kinematical fitting so that the acceptance can be mapped as a function of the phase space, by comparing the reconstructed and generated values of kinematical variables. The algebraic scheme of the acceptance correction is described in the next section.

The real and Monte Carlo distributions of $\omega \to \pi^+\pi^-\pi^0$ signal for $1.6 \leq m \leq 1.9$ GeV/c^2 are compared in Fig. 9.18. To account for the different background shapes, both real and MC data are weighted by $-Y_{20}$ so that only the background-free ω signals are extracted. The real and MC data are superimposed on one plot. The resolutions of $m_{\pi^+\pi^-\pi^0}$ agree very well with each other.

Figure 9.19 shows the difference of the produced and the reconstructed masses of the $K^-\pi^+\pi^-\pi^0$ system determined from the Monte Carlo events. This is the distribution of the MC events with $1.5 \leq m_{K\pi\pi\pi} \leq 1.6$ GeV/c^2 and $0.1 \leq t' \leq 2.0$ (GeV/c)^2, but for the events in the other $m_{K\pi\pi\pi}$ regions, the distributions look very similar. The fitted curve in the figure is based on a double-Gaussian resolution function with a background function linear in mass. Taking the full-width at half maximum (FWHM) as the mass resolution, the resolution of the invariant mass of the $K\pi^+\pi^-\pi^0$ system varies from 33 to 38 MeV/c^2 as shown in Fig. 9.20. Considering the mass resolution, the bin size of $m_{K\omega}$ for the partial wave

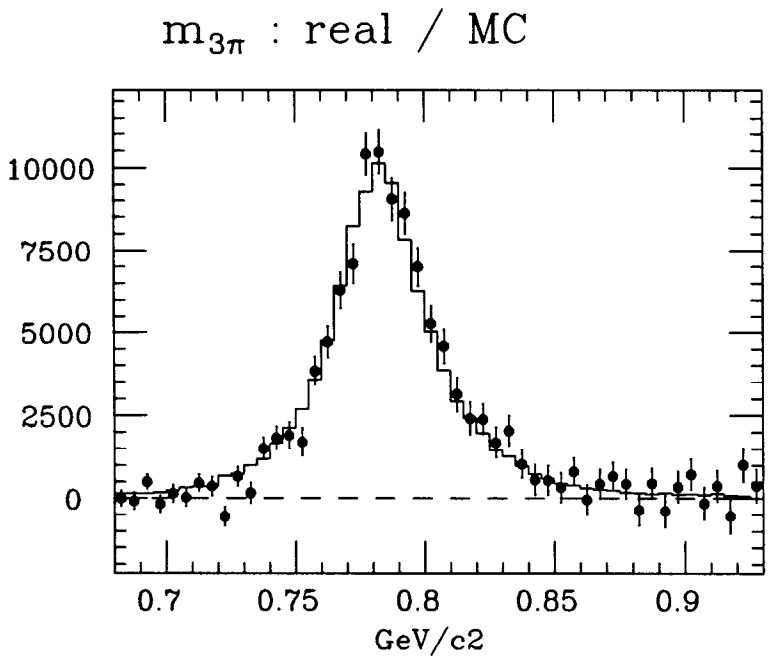

Figure 9.18: $\pi^+\pi^-\pi^0$ mass spectrum weighted by $-Y_{20}$ for real and MC data superposed to compare resolution

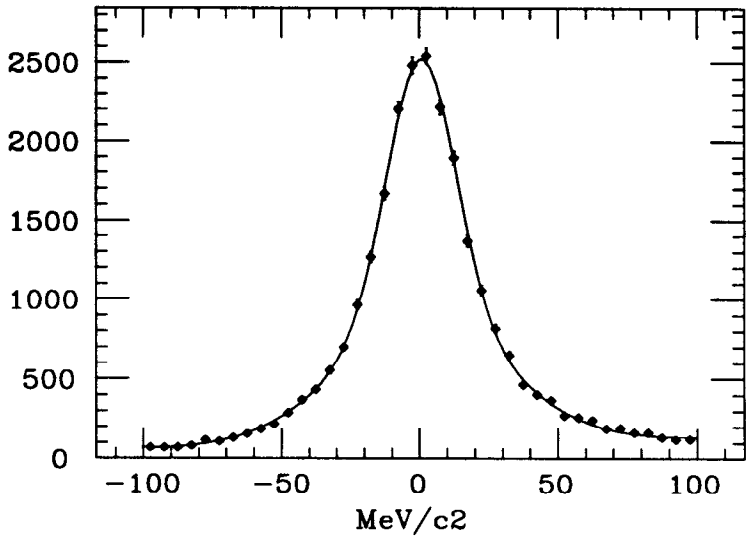

Figure 9.19: The difference of the produced and the reconstructed masses of the $K\pi^+\pi^-\pi^0$ system determined from the Monte Carlo.

fitting is chosen to be 40 MeV/c^2.

9.4.2 Formalism

The angular acceptance $A(\Omega_1, \Omega_2)$ is defined from the equation

$$F(\Omega_1, \Omega_2) = A(\Omega_1, \Omega_2) I(\Omega_1, \Omega_2)$$

where $F(\Omega_1, \Omega_2)$ and $I(\Omega_1, \Omega_2)$ are the angular distributions of the reconstructed and original events, respectively. If we take $M(LMlm)$ to be the measured moments of the data sample,

$$\begin{aligned} M(LMlm) &= \int d\Omega_1 d\Omega_2 F(\Omega_1, \Omega_2) D^L_{Mm}(\Omega_1) D^l_{m0}(\Omega_2) \\ &= \int d\Omega_1 d\Omega_2 A(\Omega_1, \Omega_2) I(\Omega_1, \Omega_2) D^L_{Mm}(\Omega_1) D^l_{m0}(\Omega_2). \end{aligned}$$

By inverting the equation 9.4, we get

$$I(\Omega_1, \Omega_2) = \sum_{L'M'l'm'} \left(\frac{2L'+1}{4\pi}\right)\left(\frac{2l'+1}{4\pi}\right) H(LMlm) D^{L'*}_{M'm'}(\Omega_1) D^{l'*}_{m'0}(\Omega_2). \qquad (9.5)$$

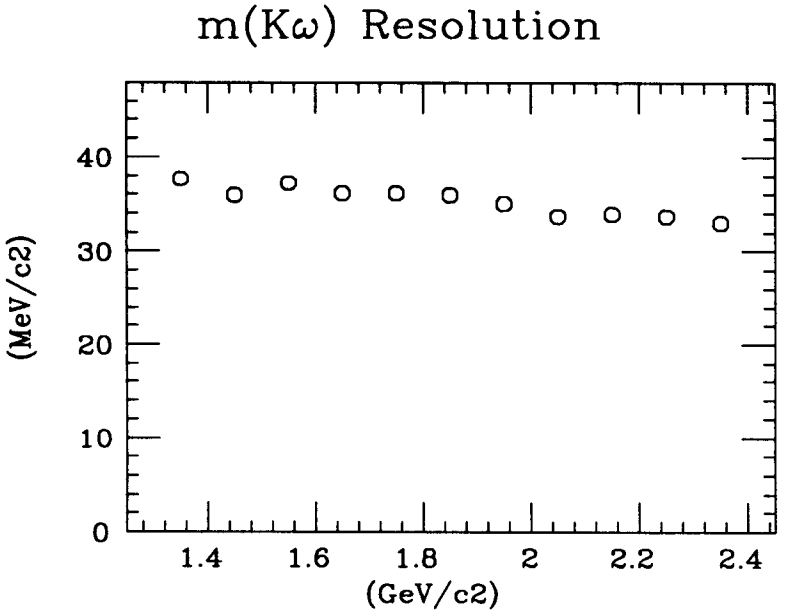

Figure 9.20: The resolution of $m_{K\omega}$ as a function of $m_{K\omega}$

Then we can express the measured moments $M(LMlm)$ in terms of the true moments $H(LMlm)$ and the acceptance matrix A as

$$M(LMlm) = \sum_{L'M'l'm'} A^{L'M'l'm'}_{LMlm} H(L'M'l'm'),$$

where the acceptance matrix A is

$$\begin{aligned} A^{L'M'l'm'}_{LMlm} &= (\frac{2L'+1}{4\pi})(\frac{2l'+1}{4\pi}) \\ &\times \int d\Omega_1 d\Omega_2 D^{L'*}_{M'm'}(\Omega_1) D^{l'*}_{m'0}(\Omega_2) A(\Omega_1,\Omega_2) D^{L}_{Mm}(\Omega_1) D^{l}_{m0}(\Omega_2) \end{aligned}$$

If the original distribution $I(\Omega_1, \Omega_2)$ is uniform over the entire solid angle range, as is the case in this Monte Carlo study, we can replace the integration with a summation as

$$A^{L'M'l'm'}_{LMlm} = \frac{(2L'+1)(2l'+1)}{N_T} \sum_{\text{events}} D^{L'*}_{M'm'}(\Omega_1) D^{l'*}_{m'0}(\Omega_2) D^{L}_{Mm}(\Omega_1) D^{l}_{m0}(\Omega_2) \quad (9.6)$$

where N_T is the total number of the generated MC events.

The summation indices in eq.(9.6) include negative values in M and m. But parity is conserved in the strong interaction and the angular distribution is real so

that not all the $H(LMlm)$'s are independent. This allows us to reduce the number of terms in eq.(9.6).

First, since the angular distribution is real,

$$I(\Omega_1, \Omega_2) = I^*(\Omega_1, \Omega_2) \ ;$$

and using the identity of the D functions,

$$D^{j*}_{m,m'}(\Omega) = (-1)^{m+m'} D^{j}_{-m,-m'}(\Omega) \ ,$$

we get

$$H(LMlm) = (-1)^M H^*(L -Ml -m). \tag{9.7}$$

Parity conservation in the production process $K^-p \rightarrow Xp$ and the subsequent decay $X \rightarrow K^-\omega$ gives a further reduction in the number of independent moments. The double moments can be expressed as a sum of the products of the production and the decay amplitudes as

$$H(LMlm) = \sum_{ij} t^{ij*}_{LM} f^{ij}_{Llm} \langle 10l0|10\rangle \ .$$

Then, from parity conservation in the production, we get

$$t^{ij*}_{LM} = \eta_i \eta_j (-1)^{L+M} t^{ij*}_{L-M} \tag{9.8}$$

and in the decay,

$$f^{ij}_{Llm} = \eta_i \eta_j (-1)^{L+l} f^{ij}_{Ll-m}. \tag{9.9}$$

Equation (9.8) gives

$$H(LMlm) = (-1)^{L+M} H(L -Mlm) \tag{9.10}$$

and eq.(9.9) gives

$$H(LMlm) = (-1)^{L+l} H(LMl -m) \tag{9.11}$$

Then combining eqs. (9.7), (9.10), and (9.11) we get

$$H(LMlm) = (-1)^l H^*(LMlm) \tag{9.12}$$

From eq. (9.12), we see that H is real if l is even and pure imaginary if l is odd. Since parity is also conserved in the subsequent decay $\omega \rightarrow \pi^+\pi^-\pi^0$, l should be even and the moments are real.

Using the relations (9.7), and (9.12), the angular distribution (eq. 9.7) can be rewritten in terms of real quantities only as

$$\begin{aligned} I(\Omega_1,\Omega_2) &= \sum_L \sum_{l=\text{even}} \sum_{M\geq 0} \sum_m \left(\frac{2L+1}{4\pi}\right)\left(\frac{2l+1}{4\pi}\right) \\ &\quad H(LMlm)\mathrm{Re}(D^L_{Mm}(\Omega_1)D^l_{m0}(\Omega_2))(2-\delta_{M0}) \end{aligned} \tag{9.13}$$

If we take the real part of $M(LMlm)$,

$$\begin{aligned} \mathrm{Re}(M(LMlm)) &= \int d\Omega_1 d\Omega_2 F(\Omega_1,\Omega_2)\mathrm{Re}(D^L_{Mm}(\Omega_1)D^l_{m0}(\Omega_2)) \\ &= \int d\Omega_1 d\Omega_2 A(\Omega_1,\Omega_2)I(\Omega_1,\Omega_2)\mathrm{Re}(D^L_{Mm}(\Omega_1)D^l_{m0}(\Omega_2)) \end{aligned}$$

and the acceptance matrix A can be redefined by the relation

$$\mathrm{Re}(M(LMlm)) = \sum_{L'M'l'm'} A^{L'M'l'm'}_{LMlm} H(L'M'l'm')$$

which in turn gives

$$\begin{aligned} A^{L'M'l'm'}_{LMlm} &= \left(\frac{2L'+1}{4\pi}\right)\left(\frac{2l'+1}{4\pi}\right)\int d\Omega_1 d\Omega_2 (2-\delta_{M'0}) \\ &\quad \mathrm{Re}(D^{L'}_{M'm'}(\Omega_1)D^{l'}_{m'0}(\Omega_2))A(\Omega_1,\Omega_2)\mathrm{Re}(D^L_{Mm}(\Omega_1)D^l_{m0}(\Omega_2)) \\ &= \frac{1}{N_T}(2L'+1)(2l'+1)\sum_{\text{events}}(2-\delta_{M'0}) \\ &\quad \mathrm{Re}(D^{L'}_{M'm'}(\Omega_1)D^{l'}_{m'0}(\Omega_2))\mathrm{Re}(D^L_{Mm}(\Omega_1)D^l_{m0}(\Omega_2)) \end{aligned}$$

9.4.3 Acceptance-corrected moments

The most important factor in the overall acceptance is the 4-prong topology requirement; 4 tracks associated with the primary interaction vertex with net charge zero. The overall acceptance is ~40 % as shown in Figs. 9.21 and 9.22. Figure 9.21 shows the acceptance as a function of t'. Because of the difficulty of detecting slow protons, the acceptance drops in the small t' region. On the other hand, Fig. 9.22

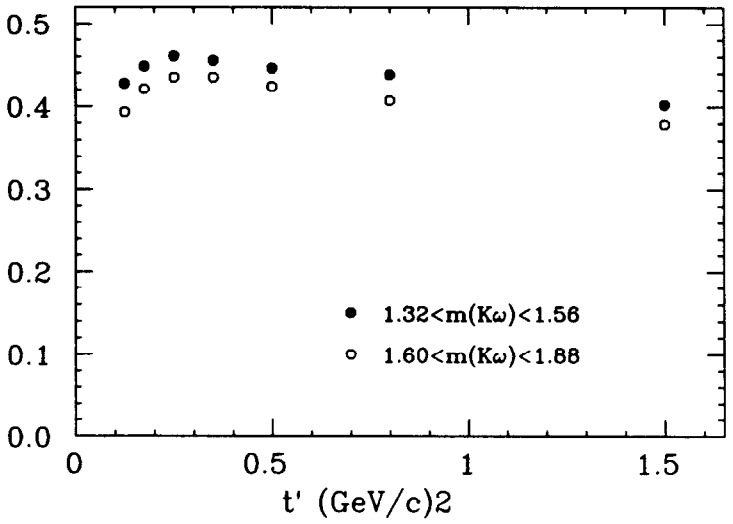

Figure 9.21: The acceptance as a function of t'.

shows the acceptance as a function of $m_{K\omega}$. The acceptance decreases slowly from 0.45 with increasing $m_{K\omega}$. This is mainly due to the baryon cuts. Also, there is acceptance drop near the $m_{K\omega}$ threshold because more events flow out of the threshold region than flow in.

The effect of the acceptance on the measured angular distribution, and the moments, is clearly exhibited in Fig. 9.23. The plots show the thrown and reconstructed moments of the MC sample. Note that the MC events are originally generated uniform over the angles and the acceptance-corrected moments are almost zero everywhere.

The acceptance-corrected moments are shown in the Fig. 9.24. The moment structure is very complicated and we have to extract the partial wave contents by fitting the partial wave amplitudes to the moments, in order to understand the underlying structures.

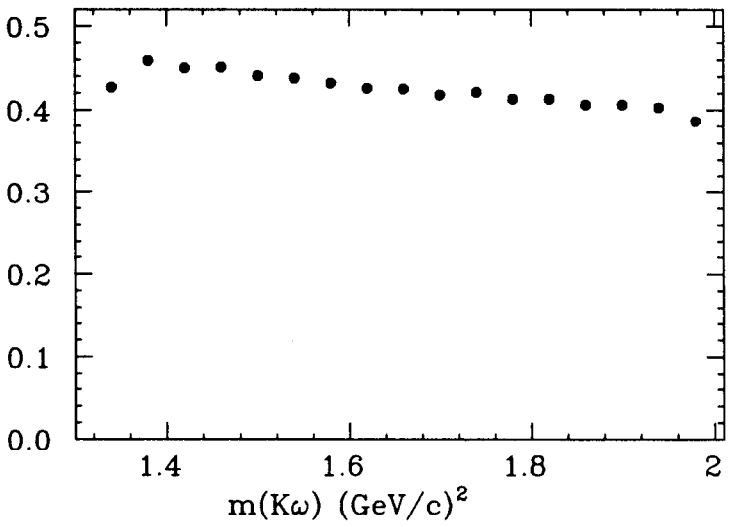

Figure 9.22: The acceptance as a function of $m_{K\omega}$.

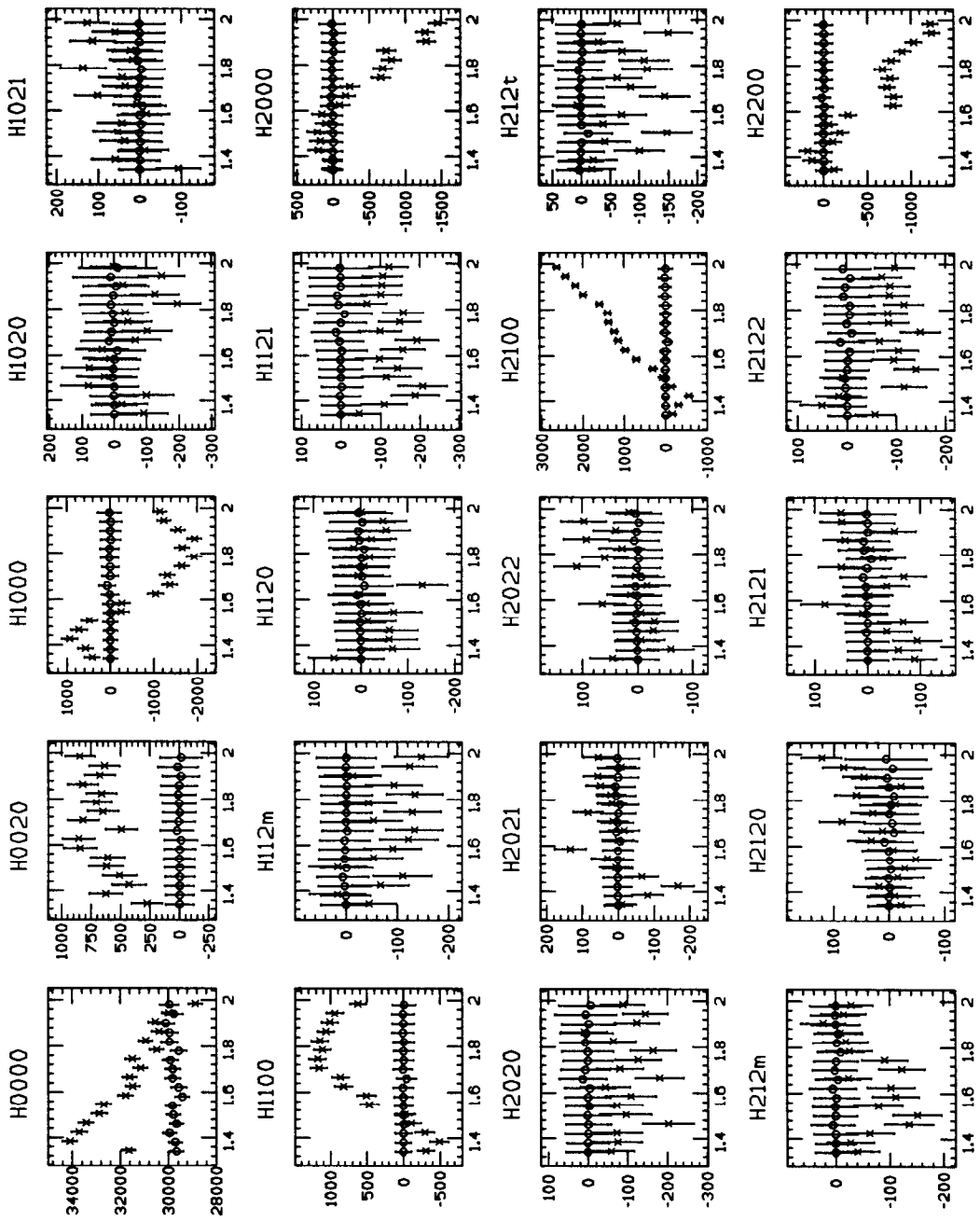

Figure 9.23: The acceptance effect on the moments: o– acceptance corrected moments of MC data; ×– uncorrected moments of MC sample multiplied by 2.5

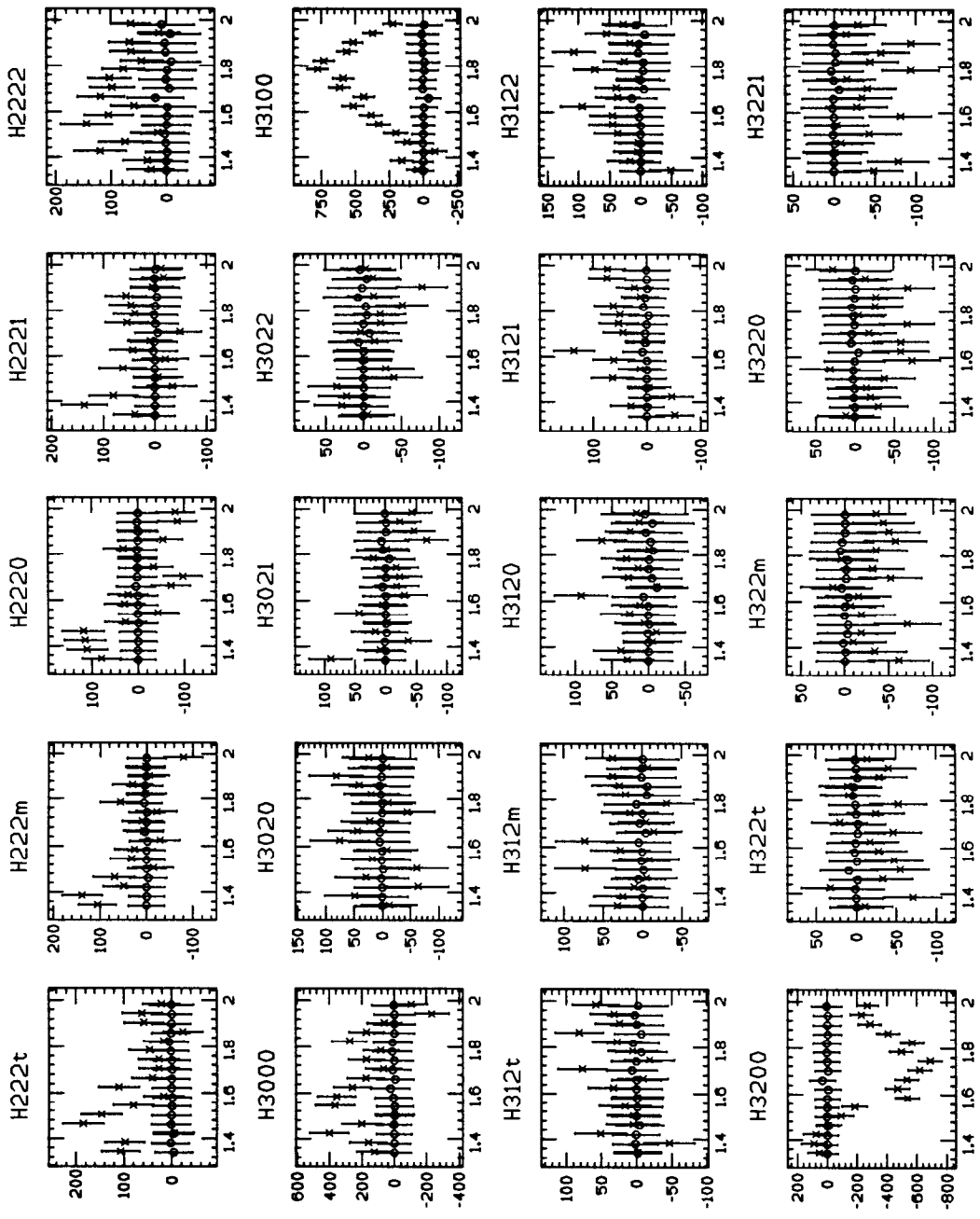

Figure 9.23 continued (2)

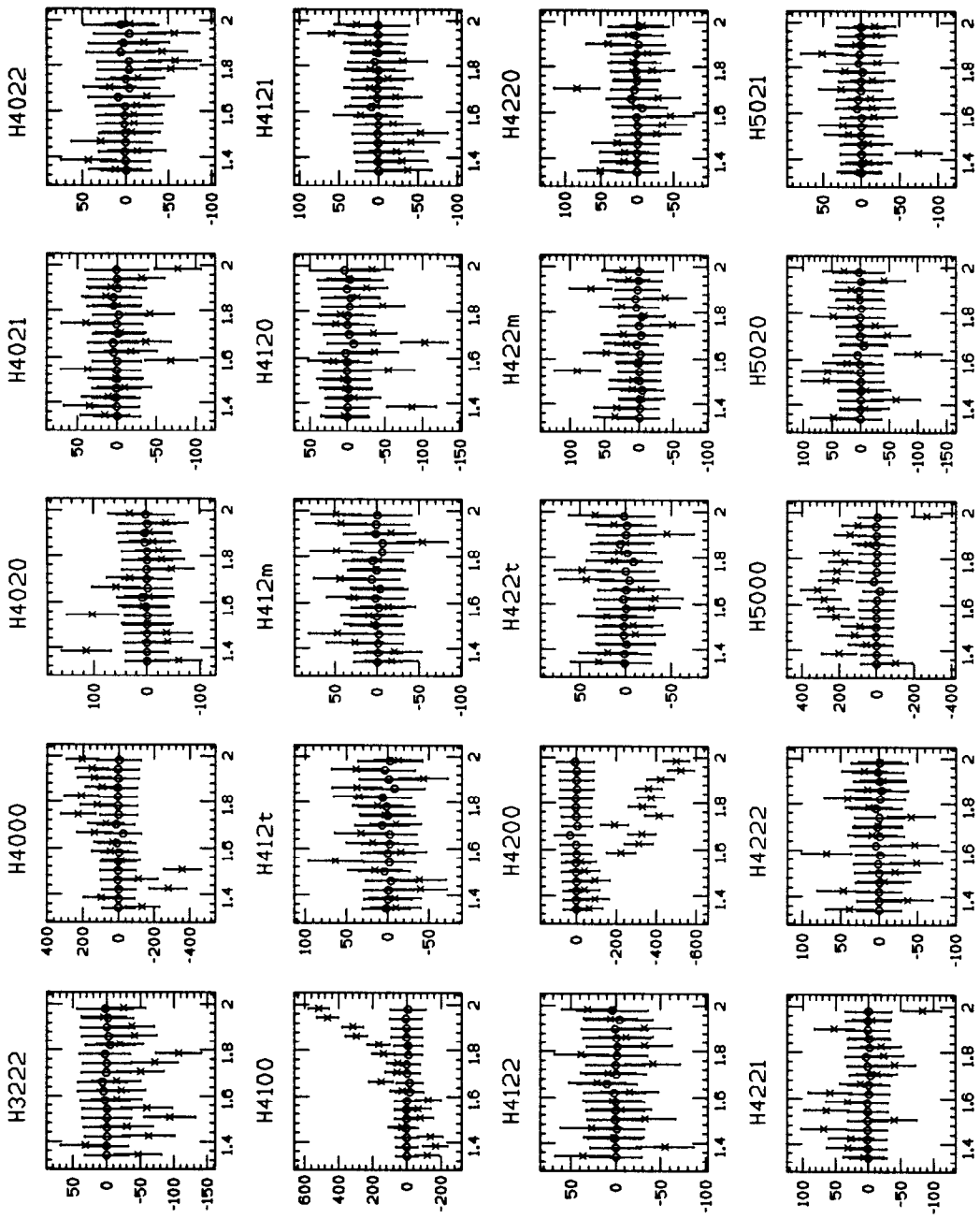

Figure 9.23 continued (3)

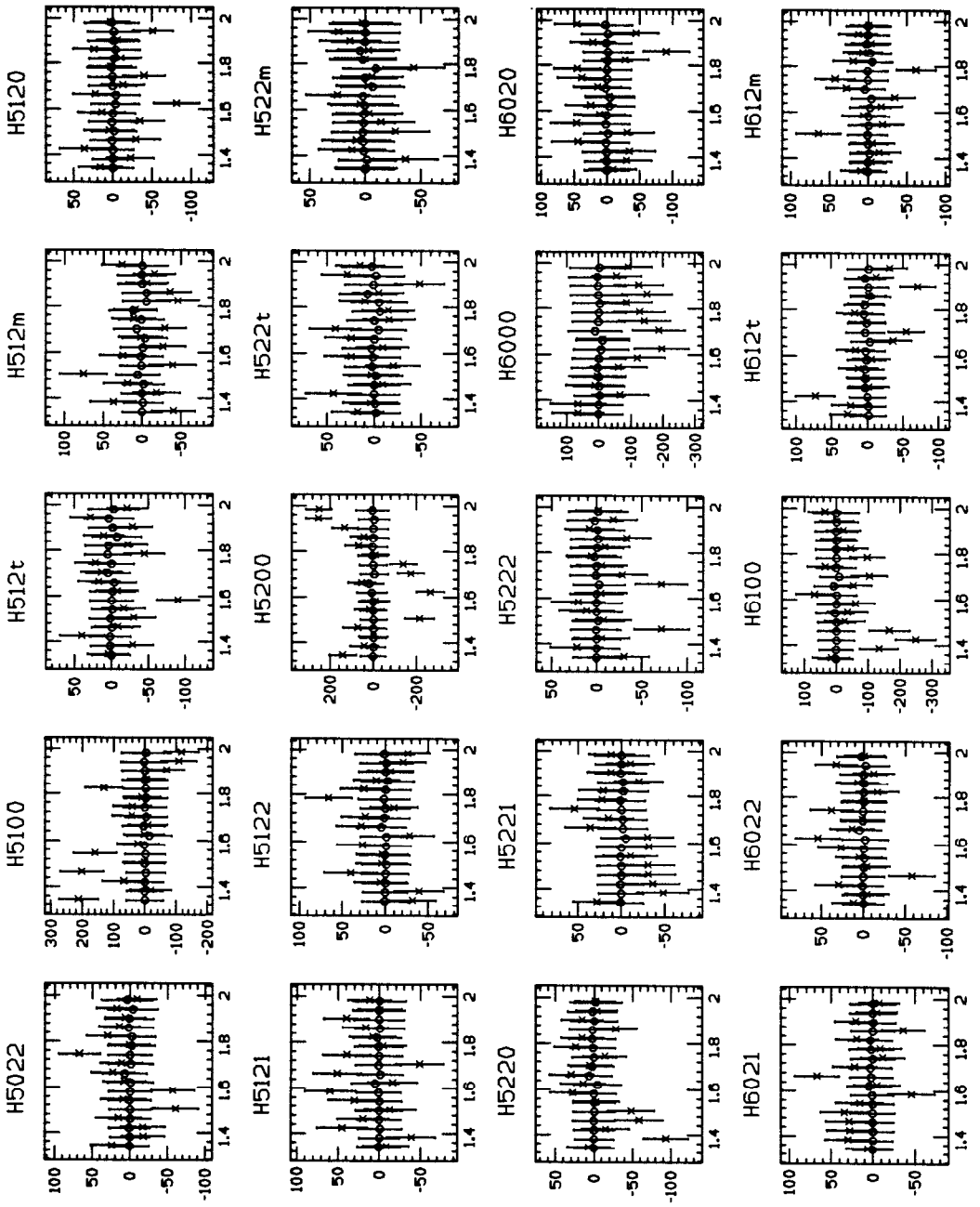

Figure 9.23 continued (4)

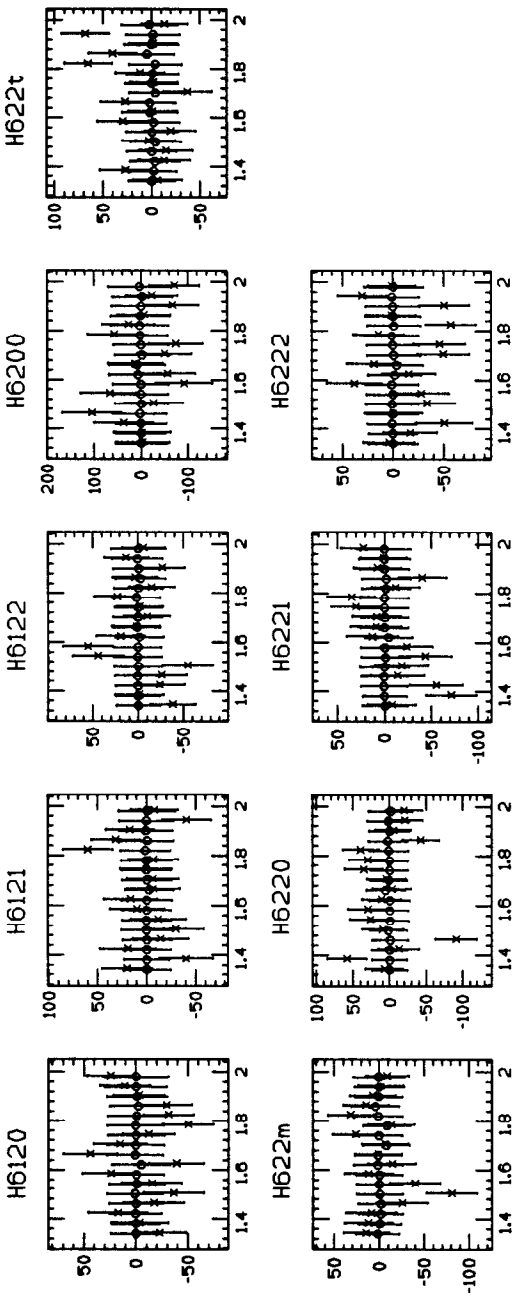

Figure 9.23 continued (5)

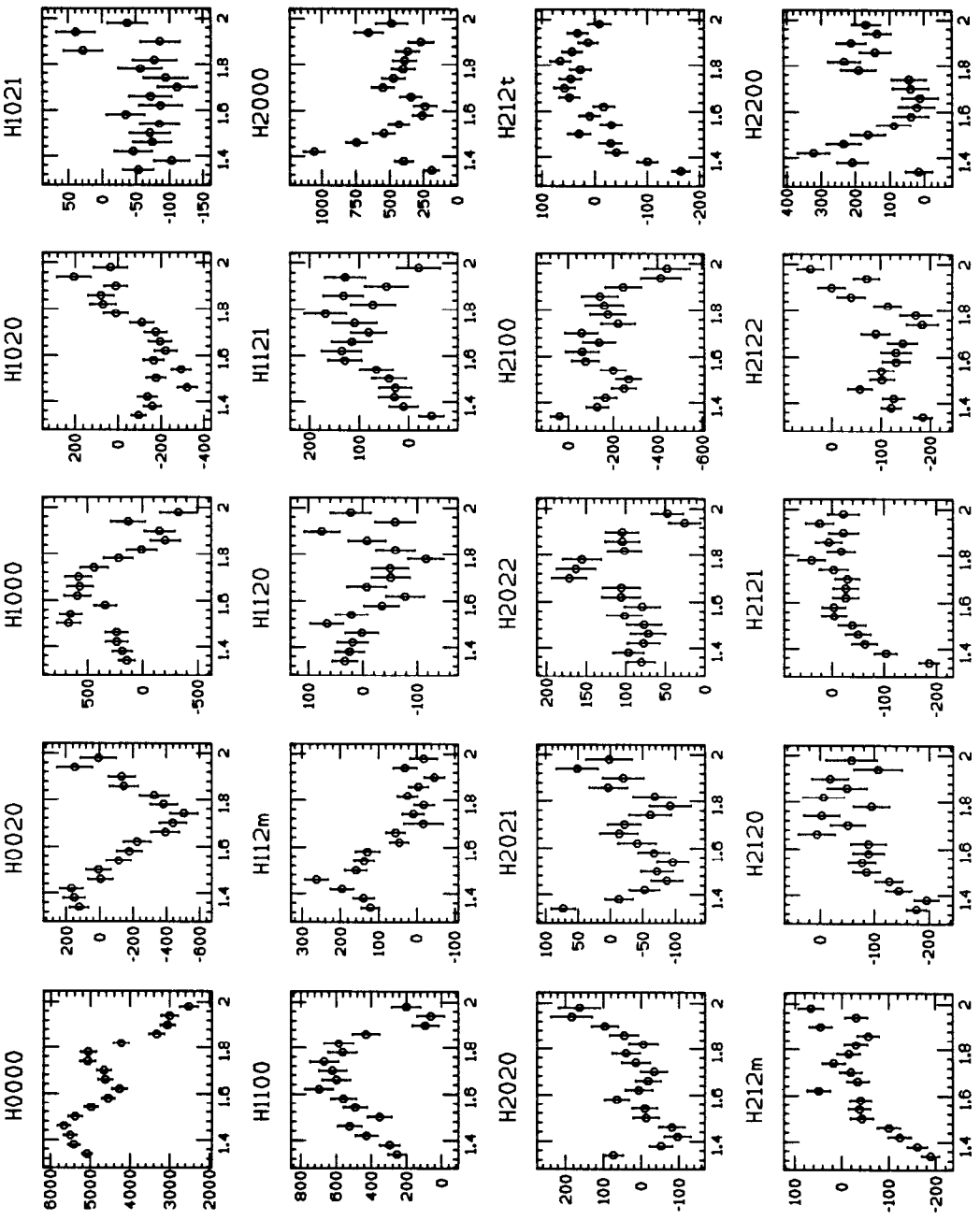

Figure 9.24: The acceptance-corrected moments

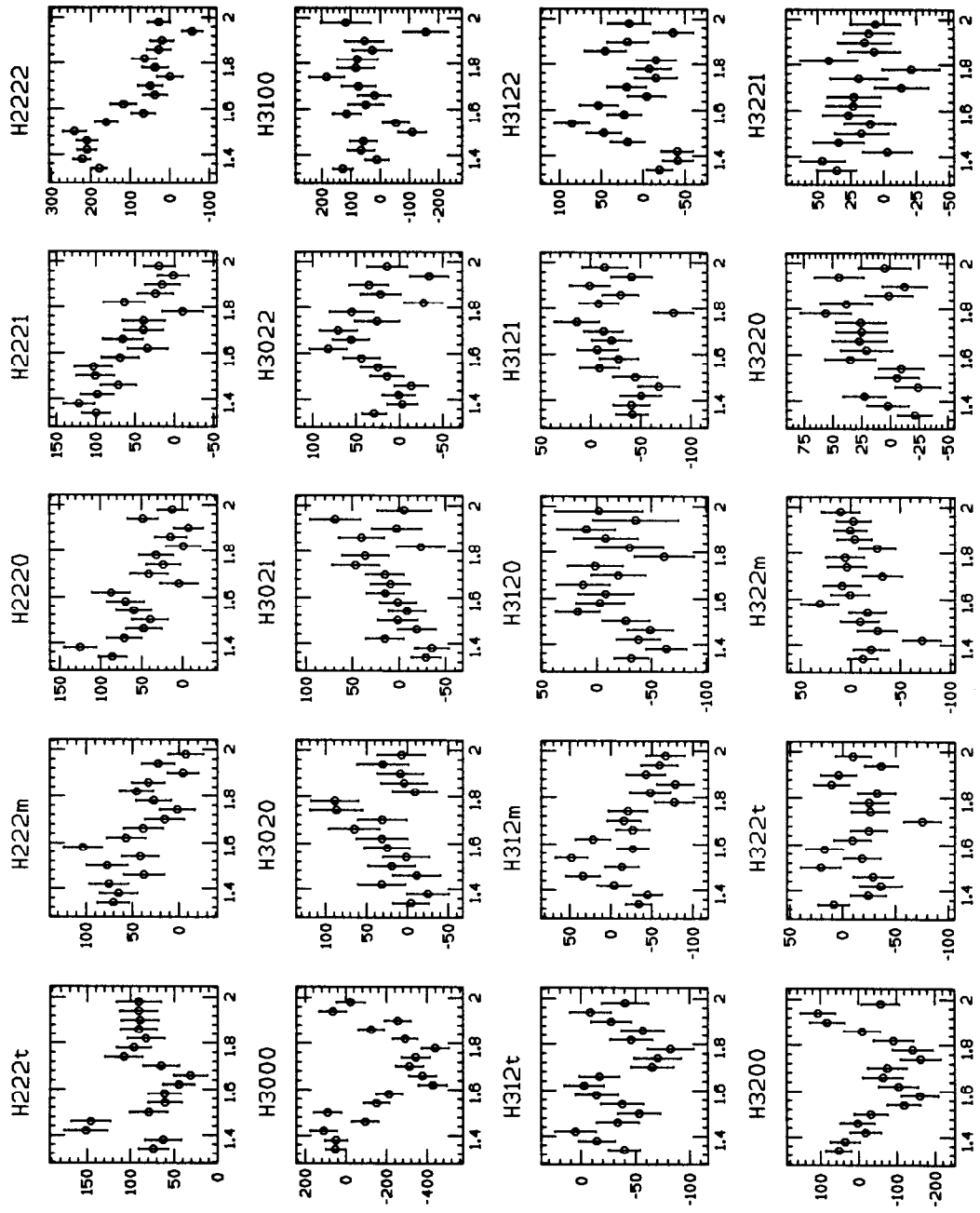

Figure 9.24 continued (2)

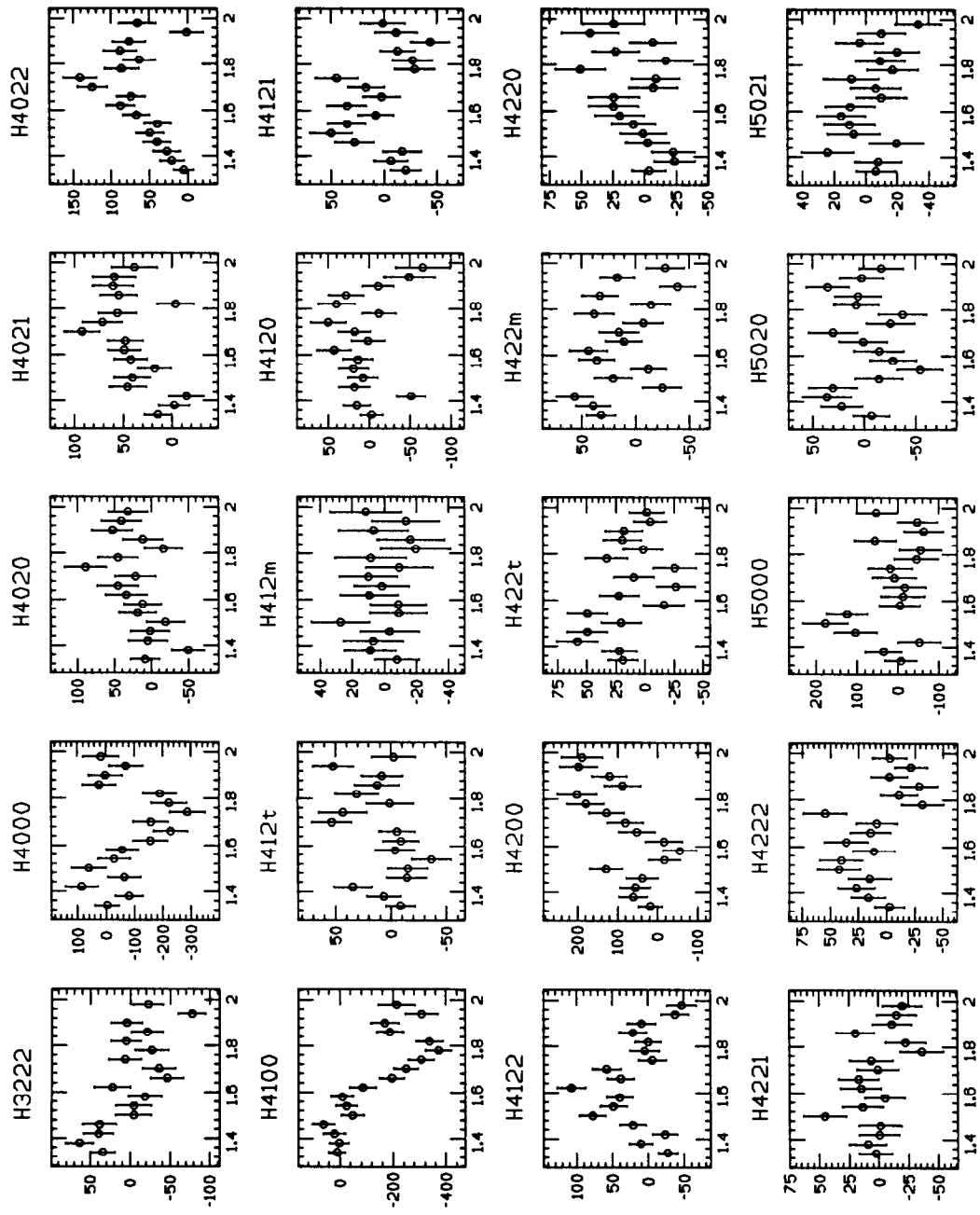

Figure 9.24 continued (3)

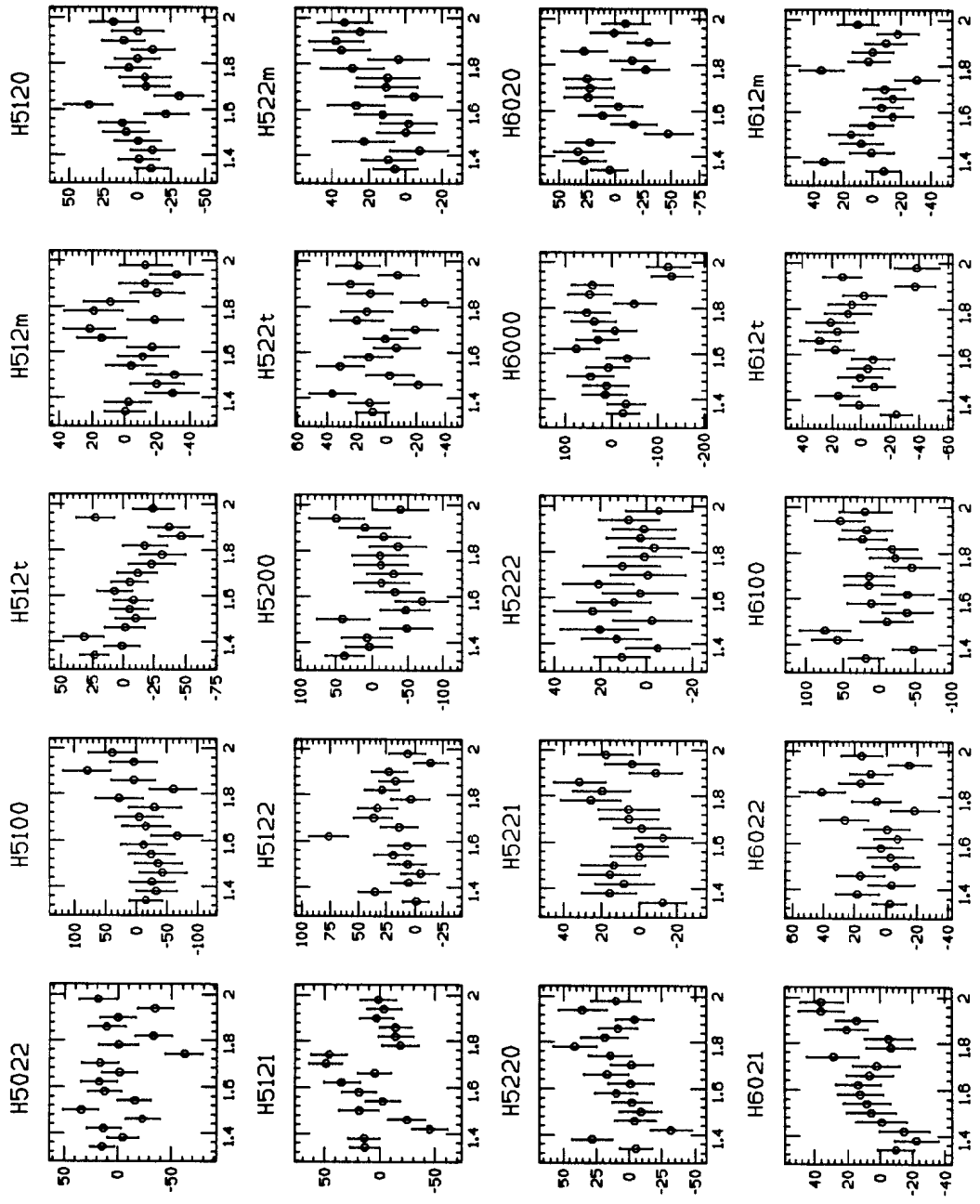

Figure 9.24 continued (4)

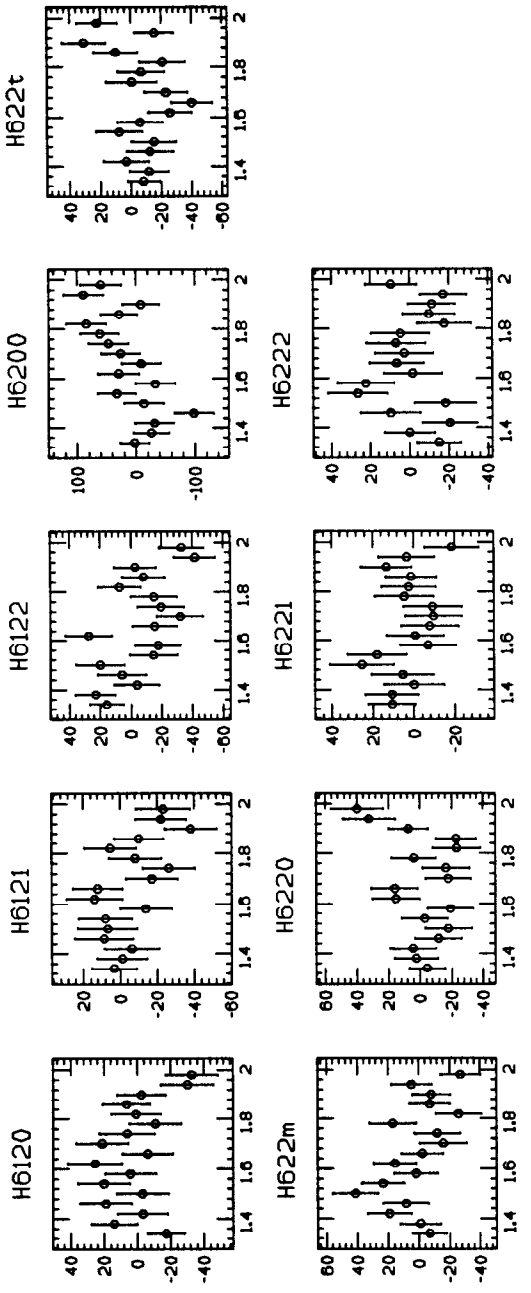

Figure 9.24 continued (5)

Chapter 10

$\overline{K}^{\circ}\phi$ system analysis

The flavor SU(3) octet of the light quark vector mesons ($J^P = 1^-$) consist of ρ, ω, ϕ, and K^*. Because of the SU(3) structure, the branching fractions of strange meson decays into $K\rho$, $K^*\pi$, $K\omega$, and $K\phi$ channels can be predicted. In E-135, the channels $K\rho$ and $K^*\pi$ were already studied by analyzing the reaction $K^-p \to \overline{K}^{\circ}\pi^+\pi^-n$[42]. The $K\omega$ channel analysis is described in the Chapters 7 and 9 of this thesis. This leaves the $K\phi$ channel. Analysis of this channel, in $\overline{K}^{\circ}\phi$, will be described in this chapter and the next. The event selection procedure is presented in section 10.1. The same formalism of partial wave decomposition based on the joint decay moments as in the $K\omega$ study is also used in the $\overline{K}^{\circ}\phi$ analysis. The general features of the data and the double moments are presented in section 10.2. The result of the partial wave analysis is presented in Chapter 9 along with the result from the $K\omega$ channel.

10.1 $\overline{K}^{\circ}\phi$ event selection

The $\overline{K}^{\circ}\phi$ data sample is obtained from the reaction

$$K^-p \to \overline{K}^{\circ}K^+K^-n \tag{10.1}$$

by selecting the events where the invariant mass of K^+K^- lies in the ϕ mass range in.

The selection of the $\overline{K}^{\circ}K^{+}K^{-}n$ sample consists of several "strips" performed to reduce the sample to a more manageable size and to isolate the desired events subsequently. The sequence of the strips is:

- the "meson" strip that isolates all the low-multiplicity events produced with a small missing momentum;
- the "topology" strip that requires the events to be topologically consistent with a 'V^0 + 2-prong' hypothesis;
- the "MVFit" strip that takes all events with $m_{K^+K^-}$ in a wide neighborhood around the ϕ mass and fits them geometrically and kinematically with the program **MVFit**.
- the "V^0" strip that places tighter cuts on the topological definitions of the V^0 candidate.

The above strips were originally performed by P. Sinervo[46] to select events from the reaction $K^{-}p \rightarrow \overline{K}^{\circ}\pi^{-}\pi^{+}n$. Since the final states $\overline{K}^{\circ}\pi^{-}\pi^{+}n$ and $\overline{K}^{\circ}K^{-}K^{+}n$ are topologically consistent with each other, it was possible to use his strip up to a point where the two channels diverge from each other. In the Monte Carlo analysis the "meson" strip was not performed explicitly because Monte Carlo events are generated according to the reaction $K^{-}p \rightarrow \overline{K}^{\circ}K^{-}K^{+}n$ so that essentially all of the reconstructed events would satisfy the strip.

10.1.1 Meson and Topology strips

The "meson" strip reduced the sample size to 1/3. The events selected are characterized by a forward produced multiparticle system accompanied by seen or unseen recoil particle(s). Events with between 2 and 9 charged tracks are selected with the requirement that

$$p_{\text{beam}} - \sum p_z < 2.0 \text{ GeV/c}^2. \tag{10.2}$$

The latter requirement is to choose the events where the charged particles carry most of the momentum. Such final states as $K^-\pi^+n$, $\overline{K}^{\circ}\pi^+\pi^-n$, $\overline{K}^{\circ}\pi^-p$, $K^-\pi^+\pi^-p$, $\overline{K}^{\circ}K^-K^+n$, $K^-K^-K^+p$ etc. all survive this strip.

The next stage is to select events that are topologically consistent with the 'V^0 + 2-prong' hypothesis. Events with at least four charged tracks where two of them with opposite charges are coming from the primary vertex ('2-prong') and two other tracks are from the secondary vertex forming a 'V^0' are selected. The secondary vertex ('V') is interpreted as due to the decay of a neutral ('0') particle produced at the primary vertex. The invariant mass of the V^0 is required to be consistent with the $\overline{K}^{\circ}$.

10.1.2 MVFit strip (1)

The next stage in the selection process involves the geometrical and kinematical fitting of the 'V^0+ 2-prong' events. Since the fitting requires a lot of computer processing time, some cuts are applied prior to fitting for further reduction of the sample size. First, it is required that the equation 10.2 be satisfied with the four charged tracks comprising the 'V^0 + 2-prong' topology. After that, events with $m_{\overline{K}^{\circ}\pi^+\pi^-} > 2.3$ GeV/c^2 are removed since the low-mass region of the $K\pi\pi$ system was of our main interest. Although this mass cut was for the $\overline{K}^{\circ}\pi^+\pi^-$ isobar analysis, it performs a similar function for the $\overline{K}^{\circ}\phi$ analysis, too.

Events satisfying these requirements are geometrically and kinematically fit using the fitting program MVFit, a multi-vertex least-squares track fitting program. MVFit fits a set of tracks to a particular topology hypothesis. The details of MVFit are described in the appendix of ref [46]. The first MVFit performed on each event is with "geometrical" constraints requiring two charged tracks from the primary vertex and two other charged tracks forming a V^0 which points to the primary vertex. This fit is called the 'GEOFIT'. Once the GEOFIT converges in an event, more MVFits, this time with kinematical constraints, are applied. The first of such kinematical constraints is that the mass of the V^0 be constrained to $m_{\overline{K}^{\circ}}$. If this $m_{\overline{K}^{\circ}}$-constrained fit is successful, the next one is to require energy

conservation at the primary vertex with a missing neutron. This is called the "1-C fit" because energy conservation gives one constraint equation, although the actual number of kinematic constraints is four: two more from forcing the V^0 to point to the primary vertex; and one more fixing V^0 mass to $m_{\overline{K}^{\circ}}$. Another fit imposing 4-momentum conservation at the primary vertex with no neutral track (4-C fit) is also performed on about 10 % of the events which are consistent with the $\overline{K}^{\circ}\pi^{-}p$ interpretation on the basis of the missing mass squared assuming a $\overline{K}^{\circ}\pi^{-}p$ final state ($mm^2(\overline{K}^{\circ}\pi^{-}p)$).

After the MVFit, further kinematical cuts are performed to improve the signal to background ratio of the sample. These are based on the V^0 decay length and the missing mass squared against $\overline{K}^{\circ}\pi^{+}\pi^{-}$. Events with the V^0 decay length smaller than 0.5 cm or $mm^2(\overline{K}^{\circ}\pi^{+}\pi^{-}) > 2.0(\mathrm{GeV/c^2})^2$ are removed. The latter cut removes events which are inconsistent with a missing neutron or are very poorly measured.

The resulting data set consists of approximately 900,000 events on 13 tapes. At this point of P. Sinervo's event selection process, the two channels $\overline{K}^{\circ}K^{-}K^{+}n$ and $\overline{K}^{\circ}\pi^{+}\pi^{-}n$ diverge in event selection. Figure 10.1 shows the plots for $m_{\pi^+\pi^-}$, $m_{K^+K^-}$ and missing mass squared against the recoiling neutral state.

10.1.3 MVFit strip (2)

In contrast to the $\overline{K}^{\circ}\pi^{+}\pi^{-}n$ MVFits where the two prongs from the primary vertex are assumed to be pions, the two prongs in the $\overline{K}^{\circ}\phi n$ final state are kaons. Therefore, the 1-C fit had to be done again this time using the kaon hypothesis for the 2-prong tracks. Not all events have to be fitted again. Since we are only interested in $K^{-}K^{+}$ system that is coming from a ϕ decay, only those events with the invariant mass of $K^{-}K^{+}$ consistent with m_{ϕ} need new MVFits and the other events can be removed. Assuming that the two prongs from the primary vertex are K^{-} and K^{+}, it is required that $|m_{KK} - m_{\phi}| \leq 0.051$ GeV/c^2. This alone removes a substantial fraction of data ($\sim$ 94 %). In addition, the following cuts are applied prior to the new MVFits:

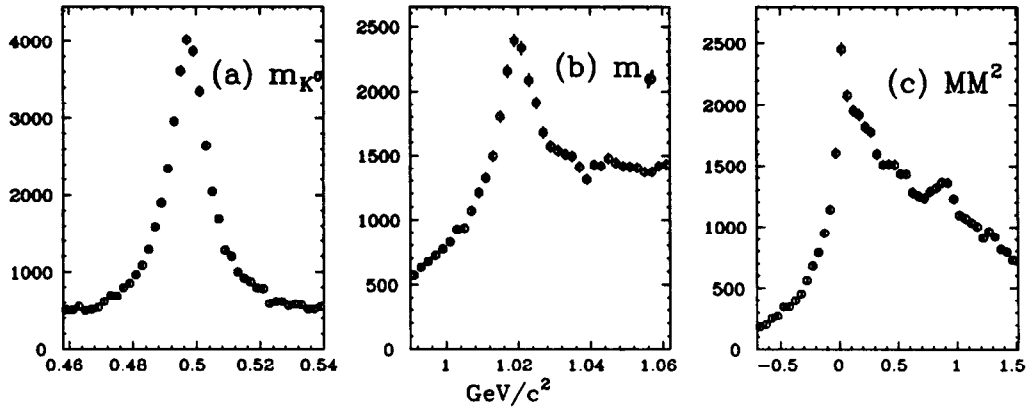

Figure 10.1: Mass distributions before PID cut and MVFit

Particle ID Requirements : Before new MVFits are performed the particle identification (PID) information from dE/dx, time-of-flight (TOF) and Cherenkov counters are used to remove events with unambiguously identified pions in the 2-prongs or with unambiguously identified kaons in the V^0, although the latter is unusual. Approximately 39 % of the events are removed by the PID requirements. The various mass distributions of the events removed by the particle identification requirements using Time-of-flight and dE/dx are shown in Fig. 10.2. The K^+K^- mass distribution shows there is a slight loss of the ϕ signal events. But the distribution of the missing-mass-squared (MM^2) against the $\overline{K}^{\circ}\phi$ system indicates almost no signal of recoiling neutrons. The events removed by the Cherenkov requirements are shown in Fig. 10.3. The $m_{K^+K^-}$ distribution shows that there is only a very little loss of the ϕ signal events.

Requirements on V^0 : More stringent requirements on the definition of the V^0 are applied to remove the events in which the secondary vertex is not consistent with a $\overline{K}^{\circ}$. For this purpose, the track parameters from the GEOFIT are utilized. First, the mass of V^0 is restricted to the range $0.48 - 0.52 \mathrm{GeV/c^2}$ to be consistent

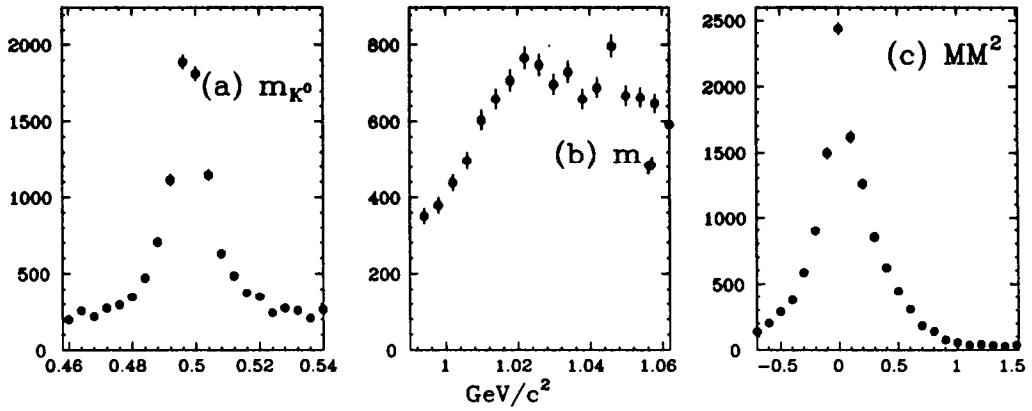

Figure 10.2: The mass distributions of the events removed by the particle identification requirements using Time-of-flight and dE/dx: (a)$m_{\overline{K}^{\circ}}$; (b)m_ϕ; and (c) MM^2 against $\overline{K}^{\circ}\phi$.

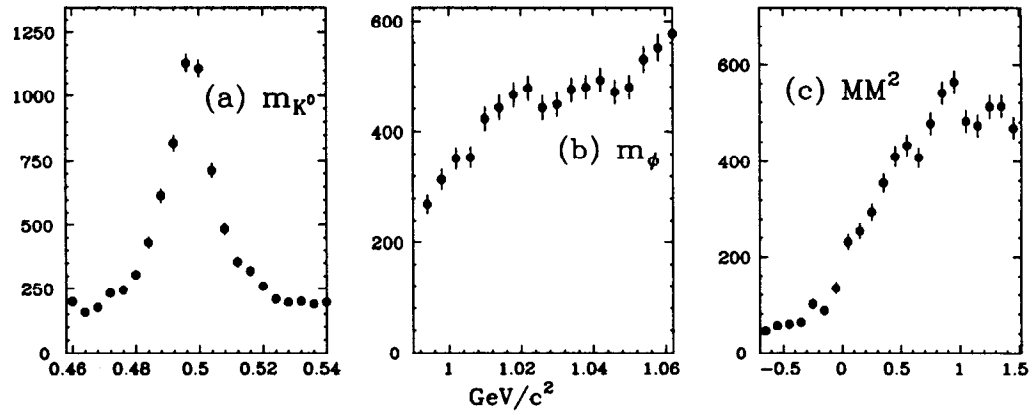

Figure 10.3: The mass distributions of the events removed by the particle identification requirements using Cherenkov informations: (a)$m_{\overline{K}^{\circ}}$; (b)m_ϕ; and (c) missing-mass-squared against $\overline{K}^{\circ}\phi$.

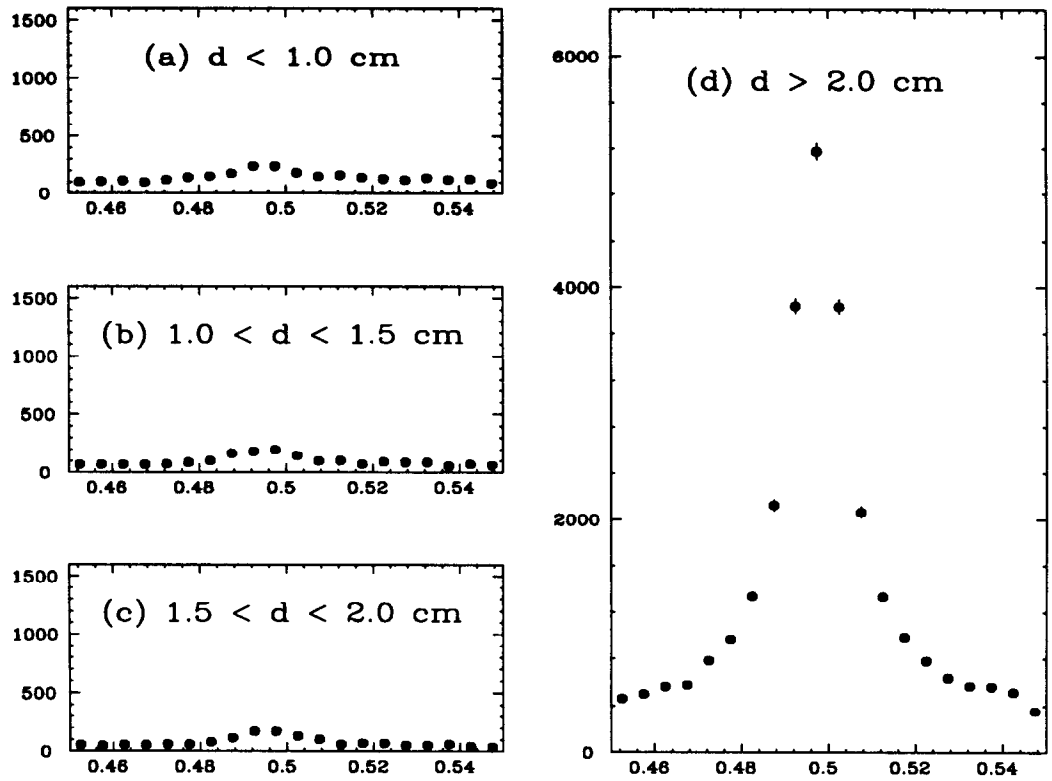

Figure 10.4: Invariant mass distributions of $\pi^+\pi^-$ for various $\overline{K}^{\circ}$ decay length

with $m_{\overline{K}^{\circ}}$, then cuts based on V^0 decay length and helicity angle are made as described below. The V^0 requirements removed $\sim$ 39 % of the remaining events.

Figures 10.4(a)-(d) show the $m_{\pi^+\pi^-}$ distribution for different $\overline{K}^{\circ}$ decay lengths from the primary vertex. The $\overline{K}^{\circ}$ signal-to-background ratio for events with decay length less than 2.0 cm is very low compared to the other events and removed from the sample.

Figure 10.5 shows the scatterplot of $m_{\pi^+\pi^-}$ vs. $\cos\theta_h$, where θ_h is defined to be the helicity angle of the $\pi^+\pi^-$ system. In addition to the vertical band representing the $\overline{K}^{\circ}$ decay into $\pi^+\pi^-$'s, a sharp horizontal band in the forward θ_h is observed. This horizontal band is found to be Λ contamination of the $\overline{K}^{\circ}$ signal. This is

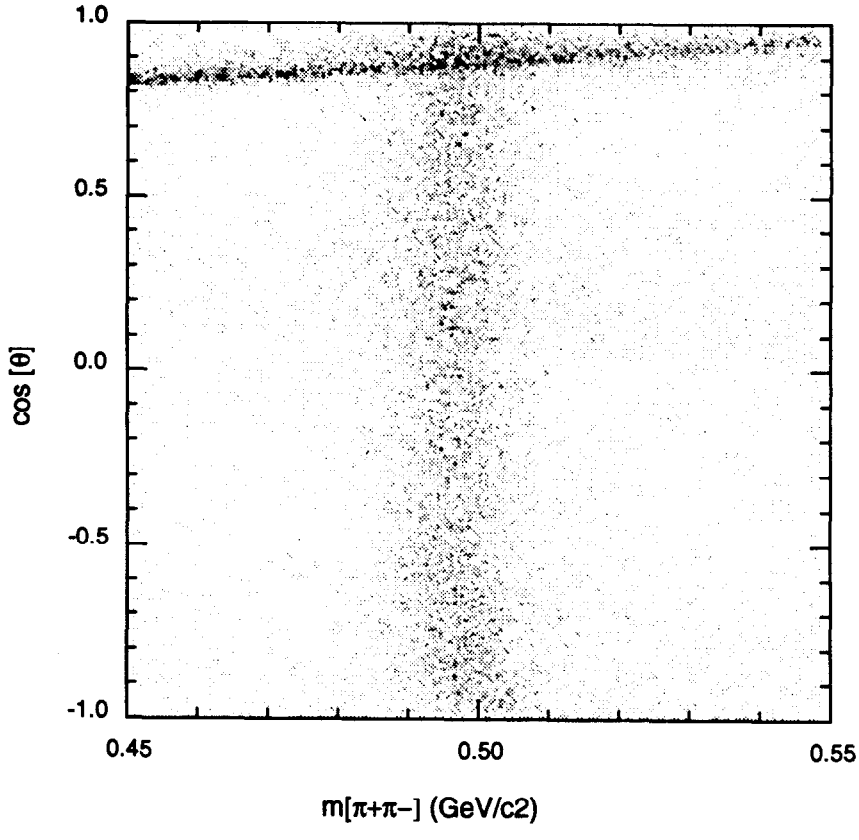

Figure 10.5: scatter plot: $\mathrm{m}(\pi\pi)$ vs. $\cos\theta_h$

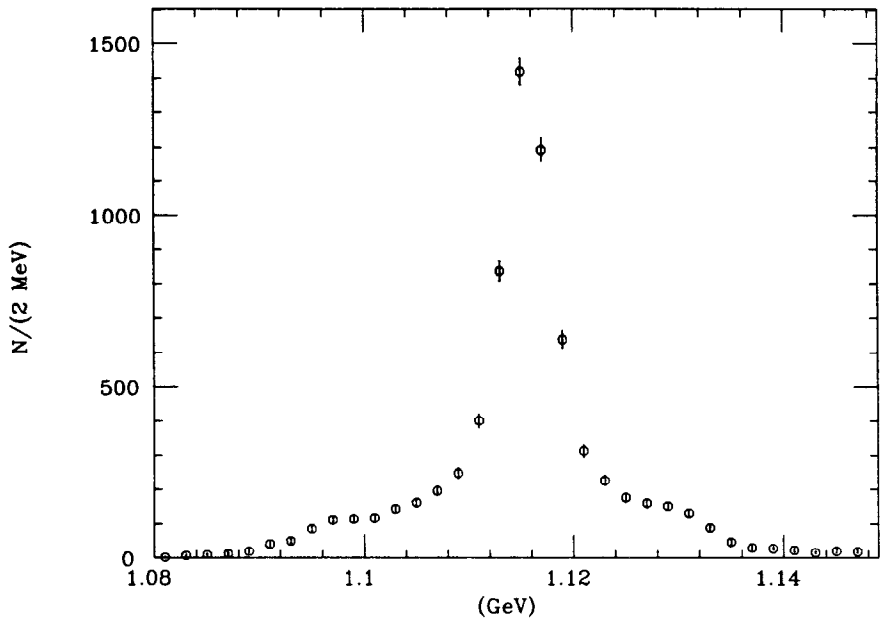

Figure 10.6: Invariant mass distribution of V^0 in the forward θ_h region under the hypothesis of $p\pi^-$. A clear peak at $\sim$ 1.15 GeV/c^2 is seen corresponding to Λ misidentified as $\overline{K}^{\circ}$.

easily seen if we select events in the forward θ_h region ($\cos\theta_h > 0.8$) and plot the invariant mass distribution of the V^0 under the $p\pi^-$ mass hypothesis instead of $\pi^+\pi^-$. Fig 10.6 shows the $p\pi^-$ mass plot. A clear peak at m_Λ is observed confirming that the horizontal band in Fig 10.5 is due to the Λ production misidentified as $\overline{K}^{\circ}$.

Events with $\cos\theta_h > 0.8$ are removed. This cut removes approximately 20 % of the events. While most of the Λ contamination is removed by this cut, $\sim$ 10 % of the true $\overline{K}^{\circ}\phi$ events are also removed. If we use the confidence level difference between the 1-C fits with $\overline{K}^{\circ}$ hypothesis and Λ hypothesis to remove the Λ contamination, more of the $\overline{K}^{\circ}\phi$ events could be retained, but it is also more difficult to simulate correctly in the Monte Carlo. For this reason the more straightforward $\cos\theta_h$ cut is employed.

Figure 10.7 shows various mass plots after the selection processes preceding kinematical MVFits. Compared with the mass distributions in Fig 10.1, a much

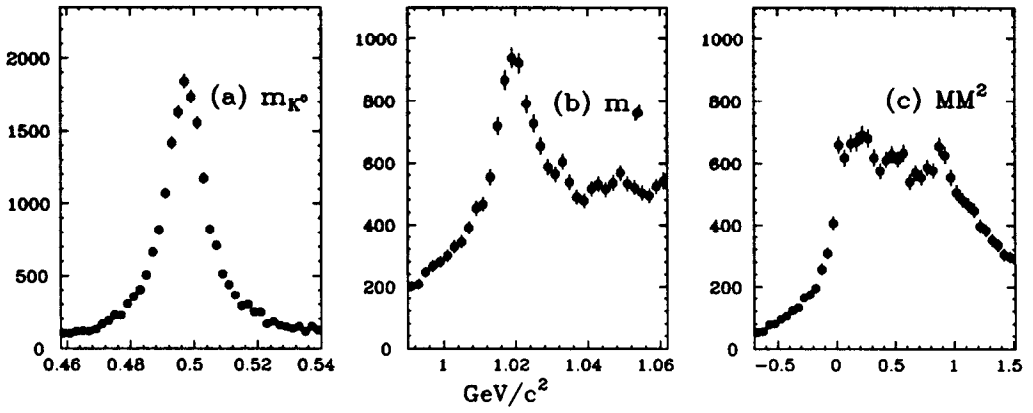

Figure 10.7: Mass distributions after PID and GEOFIT cuts and before MVFit

improved ϕ signal-to-background ratio is obtained. Further clean-up of the sample is achieved by kinematical MVFits, which, unlike GEOFIT, impose constraints on particle 4-momenta.

As in the $\overline{K}^{\circ}\pi^{+}\pi^{-}$ analysis, two kinds of MVFit with different hypotheses for final state configuration are used. First, a 4-C fit is performed in order to anti-select events consistent with the $\overline{K}^{\circ}\pi^{-}p$ interpretation. This fit requires 4-momentum conservation – hence it is called the '4-C Fit' – at the primary vertex assuming a $\overline{K}^{\circ}\pi^{-}p$ final state and no missing particles. Events yielding a 4-C fit confidence level (CL) bigger than 10^{-9} are interpreted to be inconsistent with $\overline{K}^{\circ}\phi n$ final state and are removed. Then, a 1-C fit is performed to the events surviving the 4-C fit anti-selection. This fit imposes a 'correct' mass hypothesis $\pi^{+}\pi^{-}K^{+}K^{-}$ where the two pions form a V^0 and the invariant mass of the V^0 is constrained to be equal to the $\overline{K}^{\circ}$ mass. The energy conservation at the primary vertex with a missing neutron is required. Only those events with a good 1-C fit (CL $\leq 10^{-9}$) are selected. Approximately 2 % of the events are removed by the 4-C fit anti-selection and $\sim$ 35 % of the remaining events are removed by the 1-C requirement.

The distributions of the invariant masses $m_{\pi^-\pi^+}$, $m_{K^+K^-}$, and the missing-mass-squared (mm^2) against $\overline{K}^{\circ}K^+K^-$ after the 4-C and 1-C MVFit selection are displayed in Fig. 10.8. The signal-to-background ratios for both $\overline{K}^{\circ}$ and ϕ are greatly improved showing the effectiveness of MVFit to select the desired events and clean up the background.

for those

10.1.4 Resolution cut and final selection

Figure 10.9 shows the $mm^2(\overline{K}^{\circ}K^-K^+)$ distribution as a function of the number of dipole-joined tracks in the event. For events with no dipole-joined tracks, it is very hard to evaluate the neutron signal while in the events with one or more dipole-joined tracks a clear neutron signal is seen in the missing mass plot. This is because the dipole-joined tracks have inherently better resolution.

To use partial wave analysis which needs well-measured angular distributions, a clean measurement of the track momenta is essential. For this reason, the momentum uncertainties are estimated for fast tracks that are not dipole-joined which in general are most poorly measured tracks in an event. It is shown by P. Sinervo [46] that such uncertainties can be estimated by the formula

$$\sigma_p^{\rm est} = 36\frac{pp_l}{(\Delta z)^2\tan\theta},$$

where p and p_l are the momentum and longitudinal momentum of the track, Δz is the separation in z between the first and last recorded coordinate on the track, and θ is the polar angle of the track. The factor 36 is determined from a direct comparison of $\sigma_p^{\rm est}$ and the momentum uncertainty from the geometry-constrained MVFit ($\sigma_p^{\rm MV}$). Since $\sigma_p^{\rm est}$ is a purely geometric quantity while $\sigma_p^{\rm MV}$ is determined by a sophisticated fit, it is easier to model cuts on $\sigma_p^{\rm est}$. Therefore, $\sigma_p^{\rm est}$ is chosen over $\sigma_p^{\rm MV}$. To remove the events with poorly measured track momenta, it is required that every fast track ($p > 3.0$GeV/c) be linked to a dipole track or to have $\sigma_p^{\rm est} < 0.36$GeV/c. The $mm^2(\overline{K}^{\circ}K^-K^+)$ distribution of the events removed by this requirement is displayed as the underlying histogram in Fig. 10.9(a).

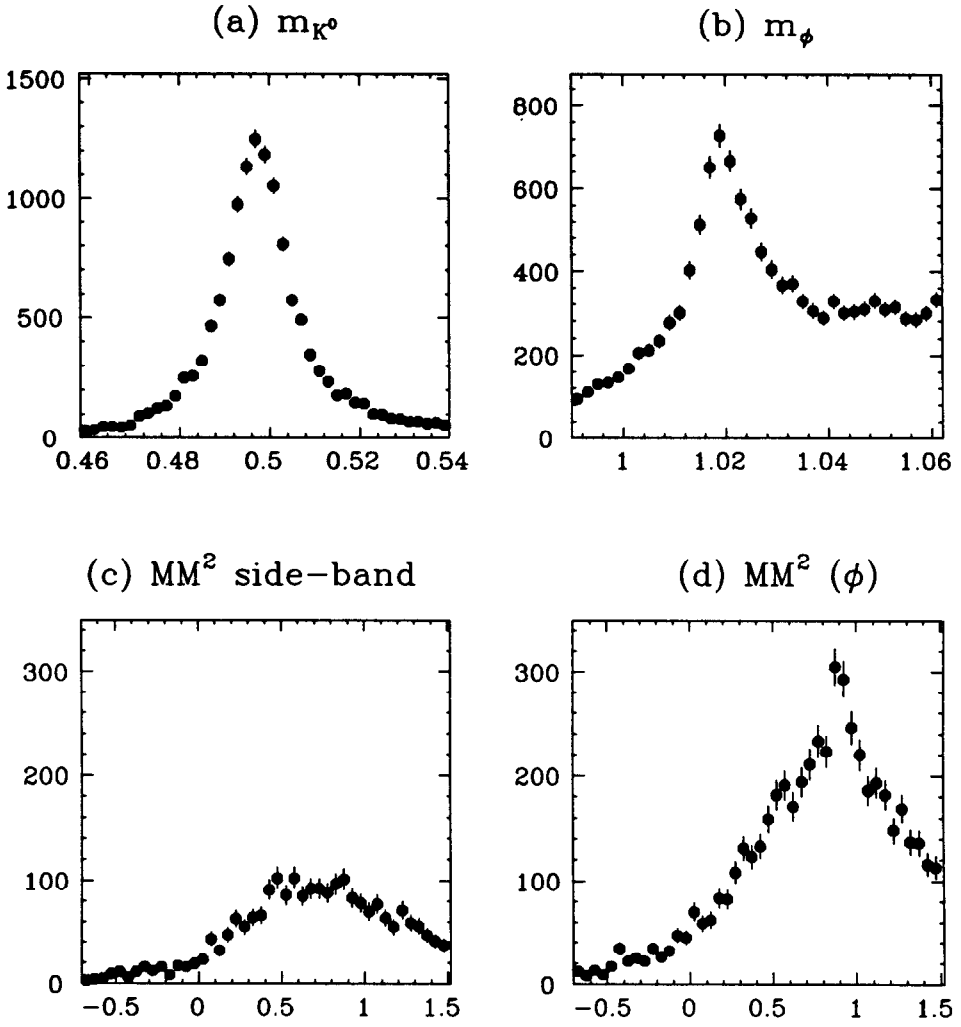

Figure 10.8: mass plots after MVFit: (a) $m_{\pi^-\pi^+}$; (b) $m_{K^+K^-}$; (c) missing-mass-squared (mm^2) against $\overline{K}^{\circ}K^+K^-$ for the events with $m_{K^+K^-}$ in the ϕ side-band control region; (d) mm^2 against $\overline{K}^{\circ}K^+K^-$ for the events with $m_{K^+K^-}$ in the ϕ signal region. The signal region and the side-band control region are defined in section 10.1.4.

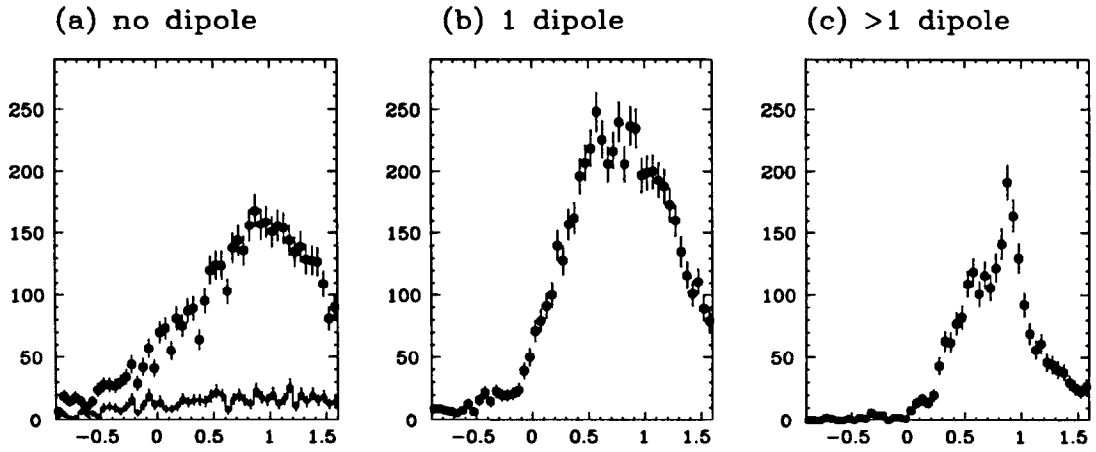

Figure 10.9: $mm^2(\overline{K}^{\circ}K^{-}K^{+})$ distribution as a function of the number of dipole-joined tracks in the event: (a) events with no dipole-joined tracks. The underlying histogram represents the events removed by the momentum resolution requirement; (b) events with only one dipole-joined track; and (c) with more than one dipole-joined tracks

The squared 4-momentum transfer from the beam to the $\overline{K}^{\circ}\phi$ system is limited to $10^{-3} \leq t' \leq 1.0$ $(\mathrm{GeV/c^2})^2$. The upper limit is made because we are interested in the forward produced $\overline{K}^{\circ}\phi$ system. In the low $m_{\overline{K}^{\circ}\phi}$ region from threshold to about 1.7 $\mathrm{GeV/c^2}$, there are many events with $t' < 10^{-3}(\mathrm{GeV/c})^2$ which survive the selection processes but do not show any $\overline{K}^{\circ}$ signal. These events are believed to be the three pion decays of beam kaon. Therefore the lower limit in t' is made to remove such events.

To complete the selection of $\overline{K}^{\circ}\phi n$ events, the invariant mass $m_{K^-K^+}$ is restricted to $m_{\phi} \pm 0.03$ $\mathrm{GeV/c^2}$ to be consistent with m_{ϕ}. Figure 10.10 shows the invariant mass distribution of the K^-K^+ system that satisfied all selection criteria. There still remains a substantial amount of continuum background under the ϕ peak. A linear background subtraction is used to evaluate the ϕ signal content in the K^+K^- system. The signal region and the side-band control regions are defined as:

- Signal Region: $|m_{K^+K^-} - m_{\phi}| \leq 0.012$ $\mathrm{GeV/c^2}$;
- Control Region: $m_{\phi} - 0.03 \leq m_{K^+K^-} \leq m_{\phi} - 0.018$ $\mathrm{GeV/c^2}$ and $m_{\phi} + 0.018 \leq m_{K^+K^-} \leq m_{\phi} + 0.03$ $\mathrm{GeV/c^2}$.

The positions of the signal and control regions are indicated in the Fig 10.10.

10.2 The general features of the $\overline{K}^{\circ}\phi$ data

The invariant mass distribution of $\overline{K}^{\circ}\phi$ system is obtained from $m_{\overline{K}^{\circ}K^-K^+}$ with a background subtraction (Fig 10.11). The only prominent structure observed is a big bump around $m_{\overline{K}^{\circ}\phi} \approx 1.9$ $\mathrm{GeV/c^2}$. The main goal of the analysis is to understand the spin-parity content of this bump.

The Dalitz plot of $m^2_{\overline{K}^{\circ}\phi}$ vs. $m^2_{\overline{K}^{\circ}n}$ (Fig 10.12) shows a narrow band in $m_{\overline{K}^{\circ}n} \simeq 1.8$ $\mathrm{GeV/c^2}$ indicating production of Y^*. The Y^* contamination becomes significant for $m_{\overline{K}^{\circ}\phi} > 2.0$ $\mathrm{GeV/c^2}$. To remove the contamination, events with $m_{\overline{K}^{\circ}n} < 1.9$ $\mathrm{GeV/c^2}$ are discarded. The events removed by this cut is shown

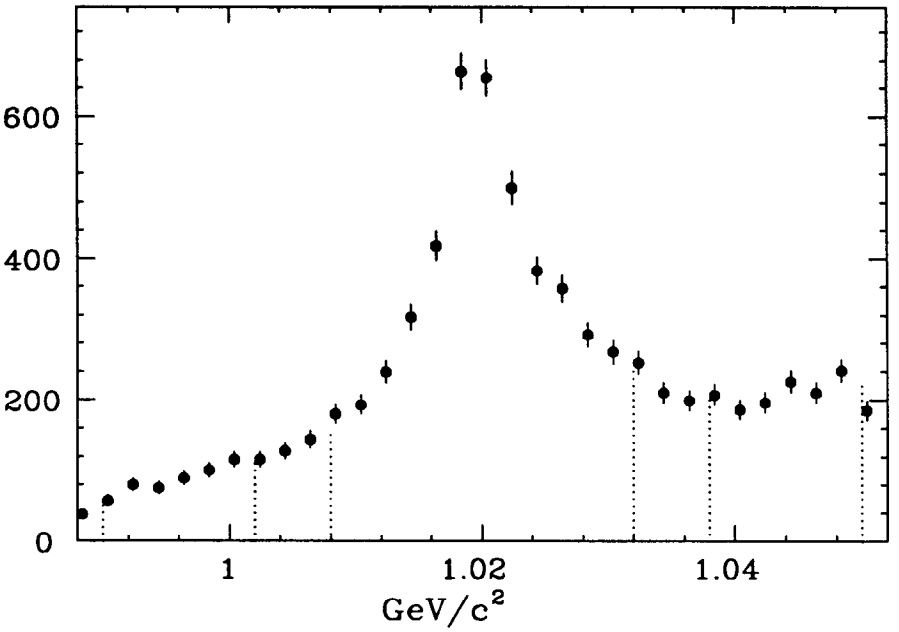

Figure 10.10: $K^{-}K^{+}$ mass distribution

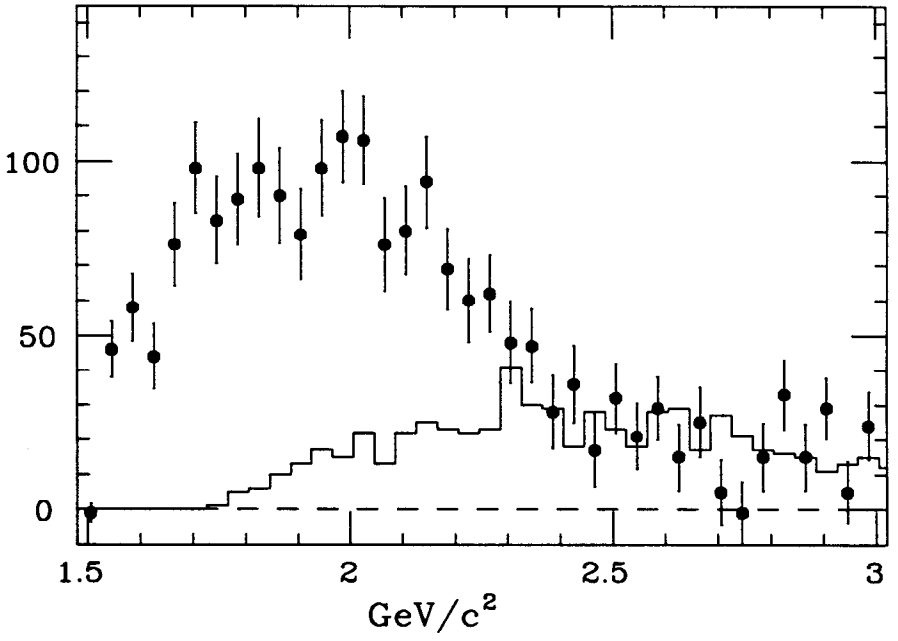

Figure 10.11: $\overline{K}^{\circ}\phi$ mass spectrum from background subtraction.

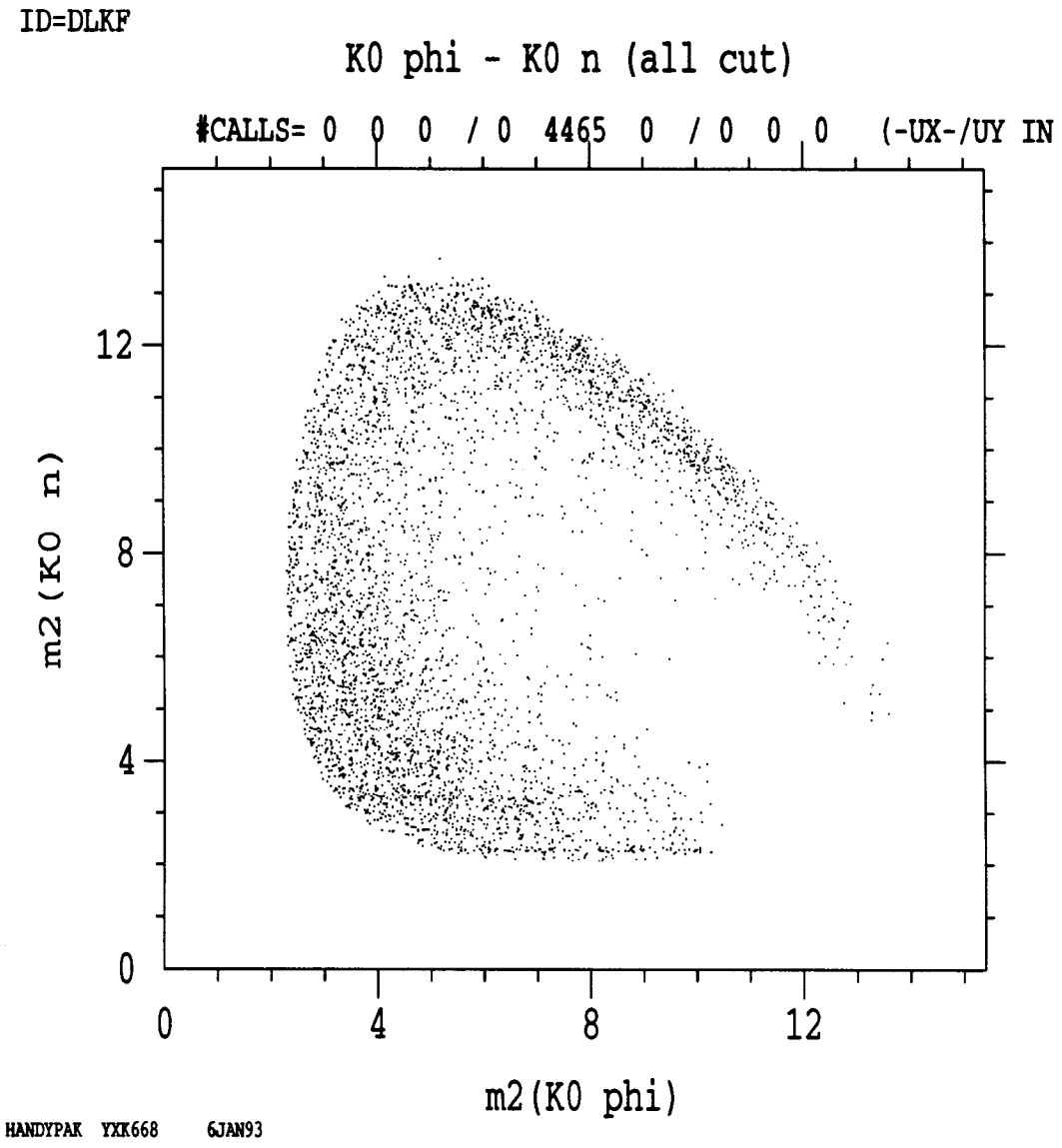

Figure 10.12: Dalitz plot $m^2_{\overline{K}^{\circ}\phi}$ vs. $m^2_{\overline{K}^{\circ}n}$

by the inner histogram in Fig. 10.11. A substantial number of events with $m_{\overline{K}^{\circ}\phi}$ over 2.0 GeV/c^2 is removed.

Figure 10.13 shows the distribution of momentum transfer t' between beam and $\overline{K}^{\circ}\phi$. The distribution is fitted to the exponential function of t' and compared with the reaction $K^-p \rightarrow K^-\pi^+n$. The production of the latter is dominated by one-pion exchange mechanism and mesons with natural spin-parity only can be produced in the reaction. The solid curve shows the fit with a free exponential slope parameter while the dotted curve shows the result with the slope parameter fixed to the value obtained from the $K^-\pi^+n$ production. Since it is observed that the t' distribution varies more slowly in $\overline{K}^{\circ}\phi$ than in $K^-\pi^+$ system, we speculate that the reaction $K^-p \rightarrow \overline{K}^{\circ}\phi n$ is not dominated by one-pion exchange and unnatural spin-parity mesons can be produced as well.

Figure 10.14 shows the momentum distributions of the final state particles for events with $m_{\overline{K}^{\circ}\phi} < 2.0$ GeV/c^2. The charged kaons from ϕ have higher momenta than the $\overline{K}^{\circ}$ and both K^- and K^+ display similar momentum spectra. This is consistent with the production of ϕ resonance from the incoming kaon beam.

10.3 The $\overline{K}^{\circ}\phi$ double moments

10.3.1 Angular distribution

It is not possible to understand the spin-parity structure of the $\overline{K}^{\circ}\phi$ system by looking at the mass distribution alone. A detailed study of the angular distributions of the $\overline{K}^{\circ}\phi$ decay and the subsequent $\phi \rightarrow K^-K^+$ is needed. For this purpose, the angular moments ($H(LMlm)$) of the $\overline{K}^{\circ}\phi$ system are measured. As in the $K\omega$ system, $\overline{K}^{\circ}\phi$ system is composed of pseudoscalar and vector mesons so a similar formalism of double moments can be used. The only difference is that $\phi \rightarrow K^-K^+$ is a two-body decay while $\omega \rightarrow \pi^+\pi^-\pi^0$ is a three-body decay. Therefore the angles are defined in a slightly different way. The first set of angles (θ_1, ϕ_1), which describes the decay of a particle in question into $\overline{K}^{\circ}\phi$, are defined

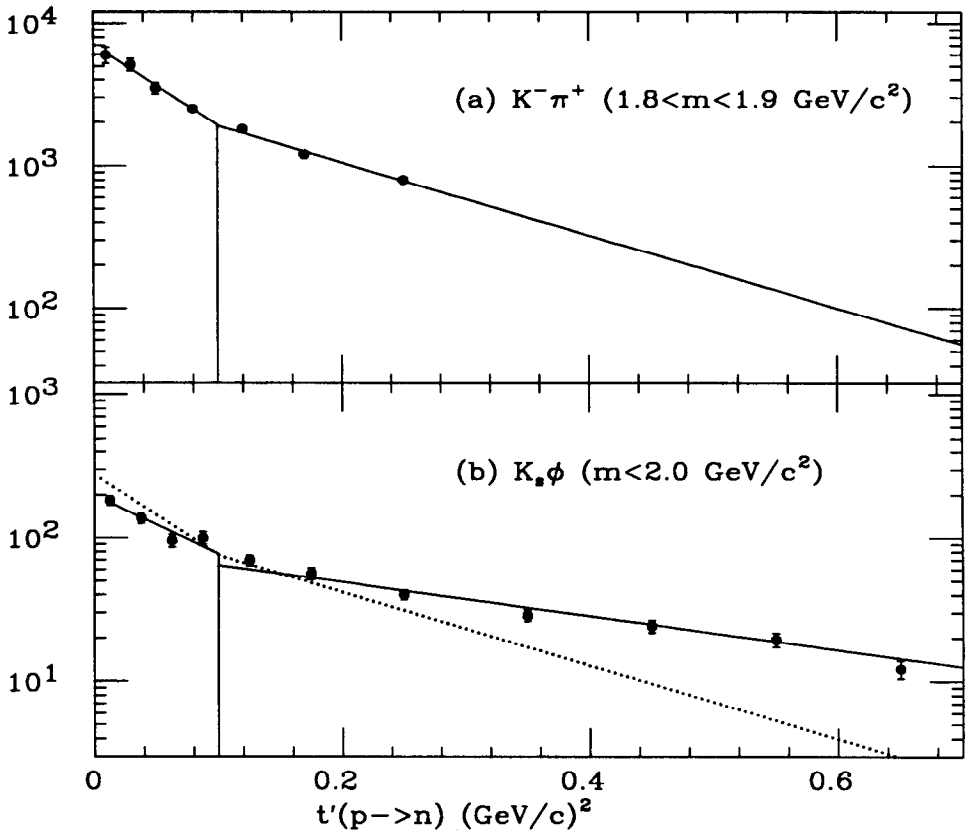

Figure 10.13: t' distribution of $\overline{K}^{\circ}\phi$

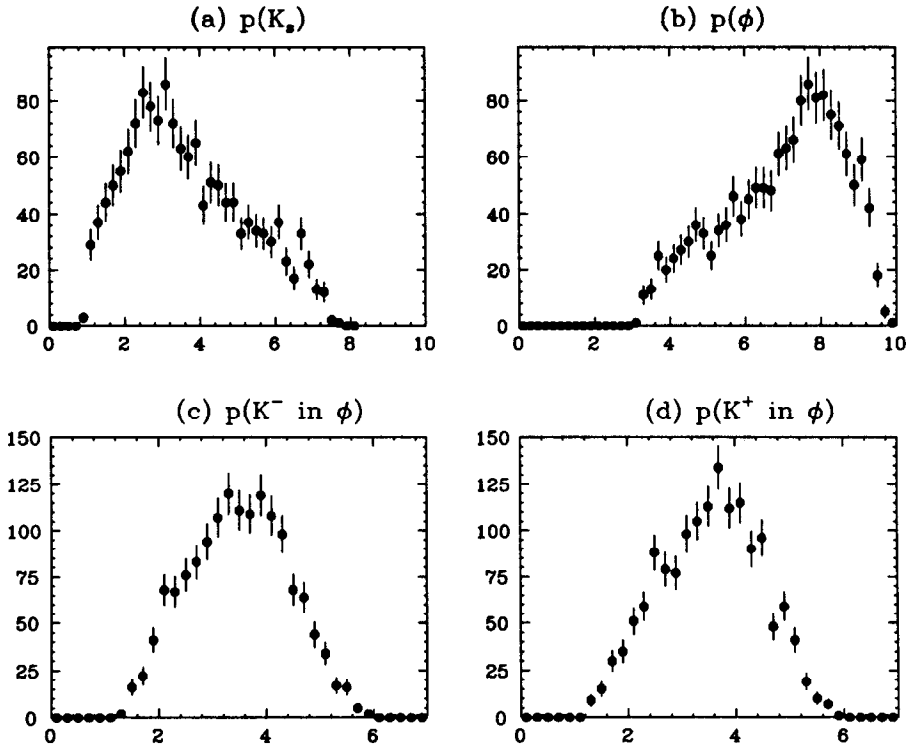

Figure 10.14: The momentum distributions of $\overline{K}^{\circ}\phi$ final state particles: (a) $\overline{K}^{\circ}$; (b) ϕ reconstructed from K^+K^-; (c) K^-; and (d) K^+.

in the same way as in $K\omega$ except that K^- and ω are replaced by $\overline{K}^{\circ}$ and ϕ respectively. The internal decay angles (θ_2, ϕ_2) are defined to describe the K^+ direction in the rest frame of ϕ. The axes of reference are defined such that $\mathbf{z_2}$ is along the momentum of the ϕ and $\mathbf{y_2}$ is along $\mathbf{z_1} \times \mathbf{z_2}$ in the $\overline{K}^{\circ}\phi$ rest frame.

Figure 10.15 shows the $\cos\theta_1$ distribution of $\overline{K}^{\circ}\phi$ within mass range of 1.6 – 2.0 GeV/c^2 obtained by background-subtraction. The curves marked by C_2, C_3, C_4, and C_6 superimposed on the data are the angular distributions predicted from the measured moments truncated at L = 2, 3, 4, and 6, respectively. Although the data are better represented by adding more terms, the improvement from C_4 to C_6 is marginal compared to the improvement from C_2 to C_3 or C_3 to C_4. Since the event sample is not statistically large enough to use higher angular moments, L is restricted to be less than or equal to 4. This implies that meson states with spin higher than 2 cannot be studied, in particular, the $K_3^*(1780)$ state, which is seen to decay into $K\rho$, $K^*\pi$, and $K\omega^*$.

Figure 10.16 shows the $\cos\theta_2$ distribution of the events with $1.6 \leq m_{\overline{K}^{\circ}\phi} <$ 2.0 GeV/c^2. The data are shown separately for events in the ϕ signal region (Fig. 10.16(a)) and in the background control region (Fig. 10.16(b)). The data in the ϕ signal region tend to follow a $\sin^2\theta_2$ plus uniform background; from this result, it can be inferred that the total $\overline{K}^{\circ}\phi$ cross section is not dominated by $J^P = 0^-$ wave. If the spin-parity of $\overline{K}^{\circ}\phi$ system were 0^-, its projected spin quantum number should be also 0. Since $\overline{K}^{\circ}$ is spin 0, ϕ should be in $(j, m) = (1, 0)$ state. Therefore, ϕ should have a distribution proportional to $|Y_{10}|^2$ which, in turn, is proportional to $\cos^2\theta_2$. Compared with the control region data, the background level to $\sin^2\theta_2$ in the signal region is a little higher, but the difference is much smaller than the $\sin^2\theta_2$ content. Since the θ_2 distribution in the signal region follows $\sin^2\theta_2$ rather than $\cos^2\theta_2$ and there is little margin left for the contribution from $\cos^2\theta_2$ signal, we conclude that there is little 0^-.

*See Chapter 9 for the first evidence for $K_3^*(1780) \to K\omega$ decay.

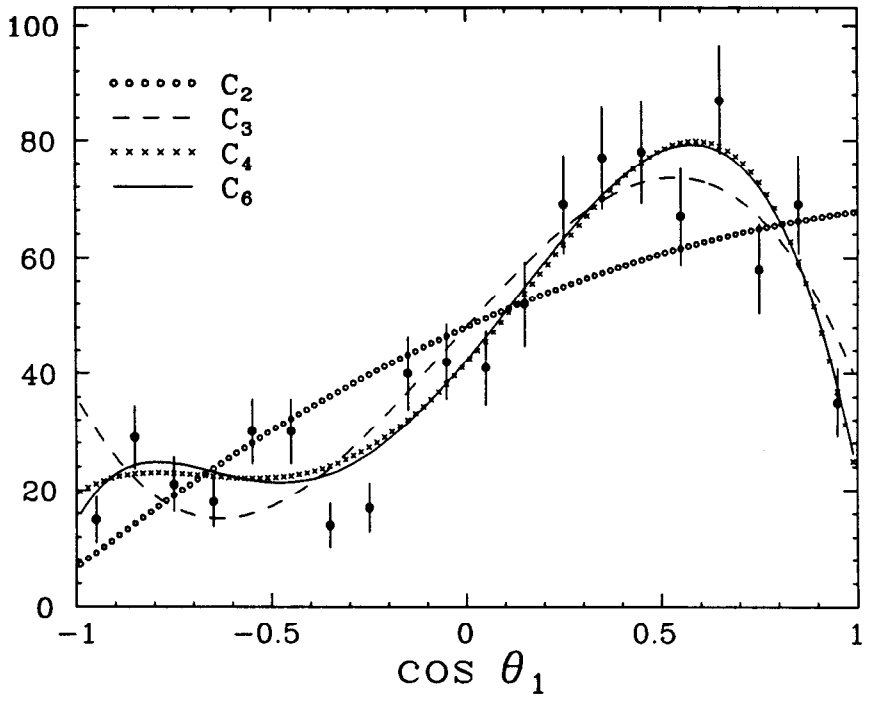

Figure 10.15: The θ_1 distributions of $\overline{K}^{\circ}\phi$ within mass range of 1.6 − 2.0 GeV/c^2. Curves superimposed on the data represent the predicted angular distributions from the measured moments truncated at: L = 2, 3, 4, and 6 for C_2, C_3, C_4, and C_6, respectively.

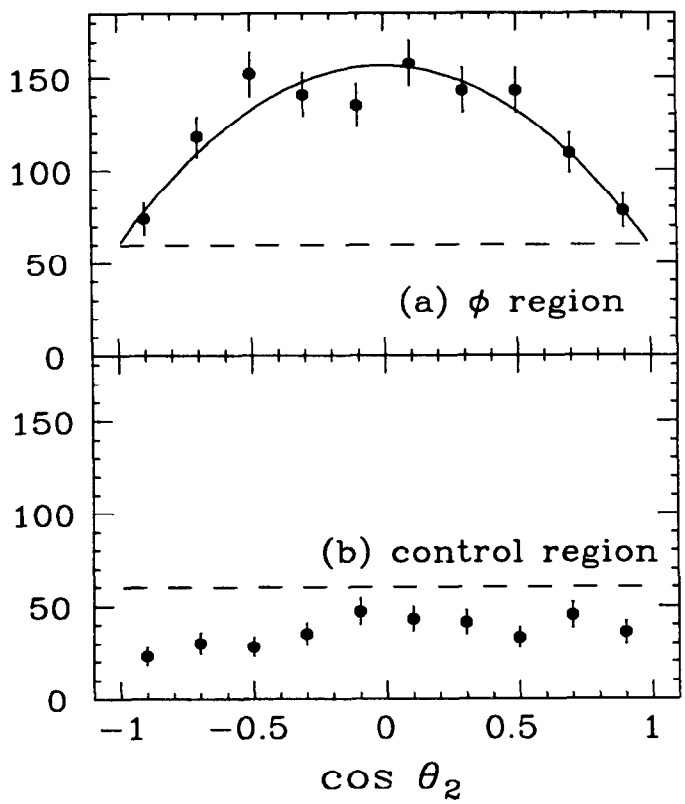

Figure 10.16: The θ_2 distribution: (a) events in the ϕ signal region; and (b) events in the background control region

10.3.2 Acceptance Correction

In the event selection process, a fraction of the correct $\overline{K}^{\circ}\phi n$ events have been removed resulting in a distortion of the angular distribution. This has to be corrected to obtain the true angular distribution and moments. The acceptance correction procedure using a Monte Carlo is the same as in the case of the $K\omega$ analysis (see section 9.3). Monte Carlo events are generated according to flat distributions in $m_{\overline{K}^{\circ}\phi}$ and the four angles, with an exponential distribution in $t'(K^{-} \rightarrow \overline{K}^{\circ}\phi)$. Figure 10.17 shows the acceptance corrected double moments of the $\overline{K}^{\circ}\phi$ system. In Fig. 10.17, the data are accumulated in 100 MeV/c^2 bin size, although displayed in every 50 MeV/c^2 ("overlapping" bins).

The acceptance of the $\overline{K}^{\circ}\phi n$ final state cannot be easily characterized as it depends on the way the events are produced. However, the overall acceptance is quantified by using Monte Carlo events which are distributed uniformly in phase space. Table 10.1 shows the effects of the various data selection requirements on the acceptance for two different $\overline{K}^{\circ}\phi$ mass regions; $1.6 \leq m_{\overline{K}^{\circ}\phi} < 1.7$ GeV/c^2 and $1.9 \leq m_{\overline{K}^{\circ}\phi} < 2.0$ GeV/c^2. The most significant factor in the acceptance loss is the topology requirement which removed $\sim$ 40 % of correct events.

10.3.3 Mass resolution

The ϕ signal of real and Monte Carlo data are compared in Fig 10.18. To account for the different background shapes, both real and MC data are background-subtracted assuming linear background functions. The resolutions of $m_{K^-K^+}$ in real and MC data agree very well each other.

The resolution of the invariant mass $m_{\overline{K}^{\circ}\phi}$ varies from 15 to 20 MeV/c^2 as shown in Fig 10.19. Although the $m_{\overline{K}^{\circ}\phi}$ resolution is less than that of $m_{K\omega}$ (section 9.4), the bin size of $m_{\overline{K}^{\circ}\phi}$ for PWA is determined mainly from the statistics of the sample rather than the mass resolution alone. Considering the size of the final $\overline{K}^{\circ}\phi n$ sample, it is determined that the minimum size of mass bins for PWA should be 100 MeV/c^2.

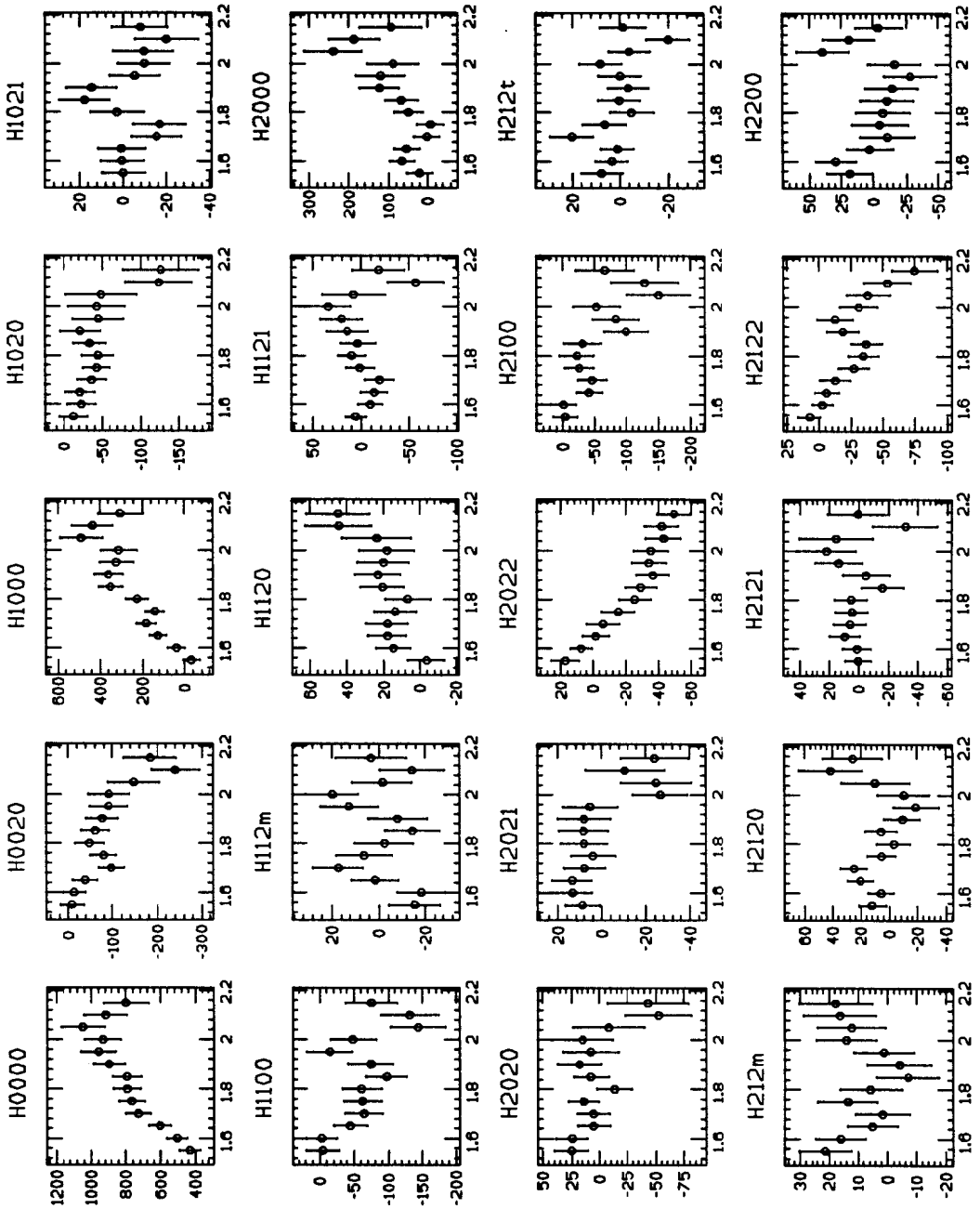

Figure 10.17: Acceptance-corrected moments of $\overline{K}^{\circ}\phi$

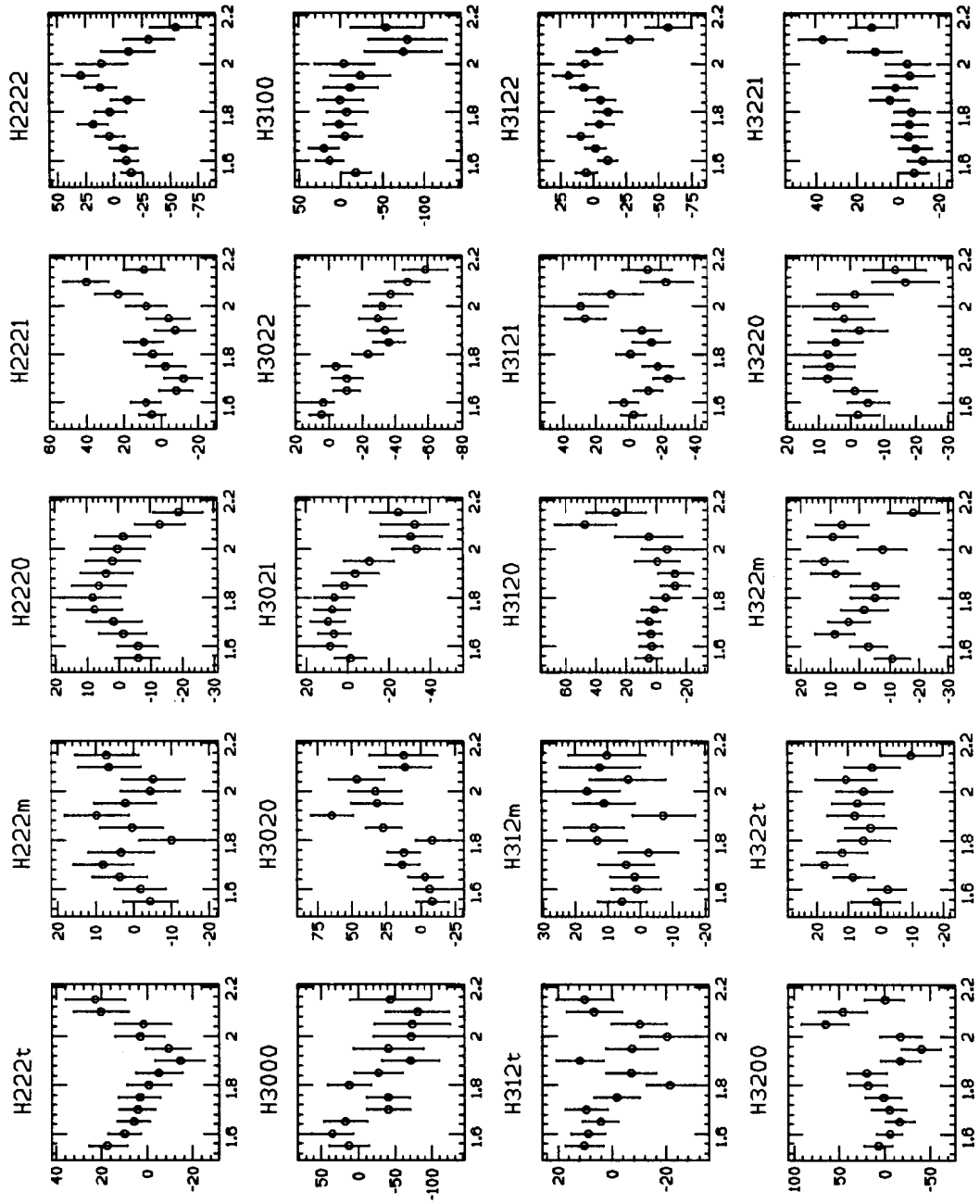

Figure 10.17 continued (2)

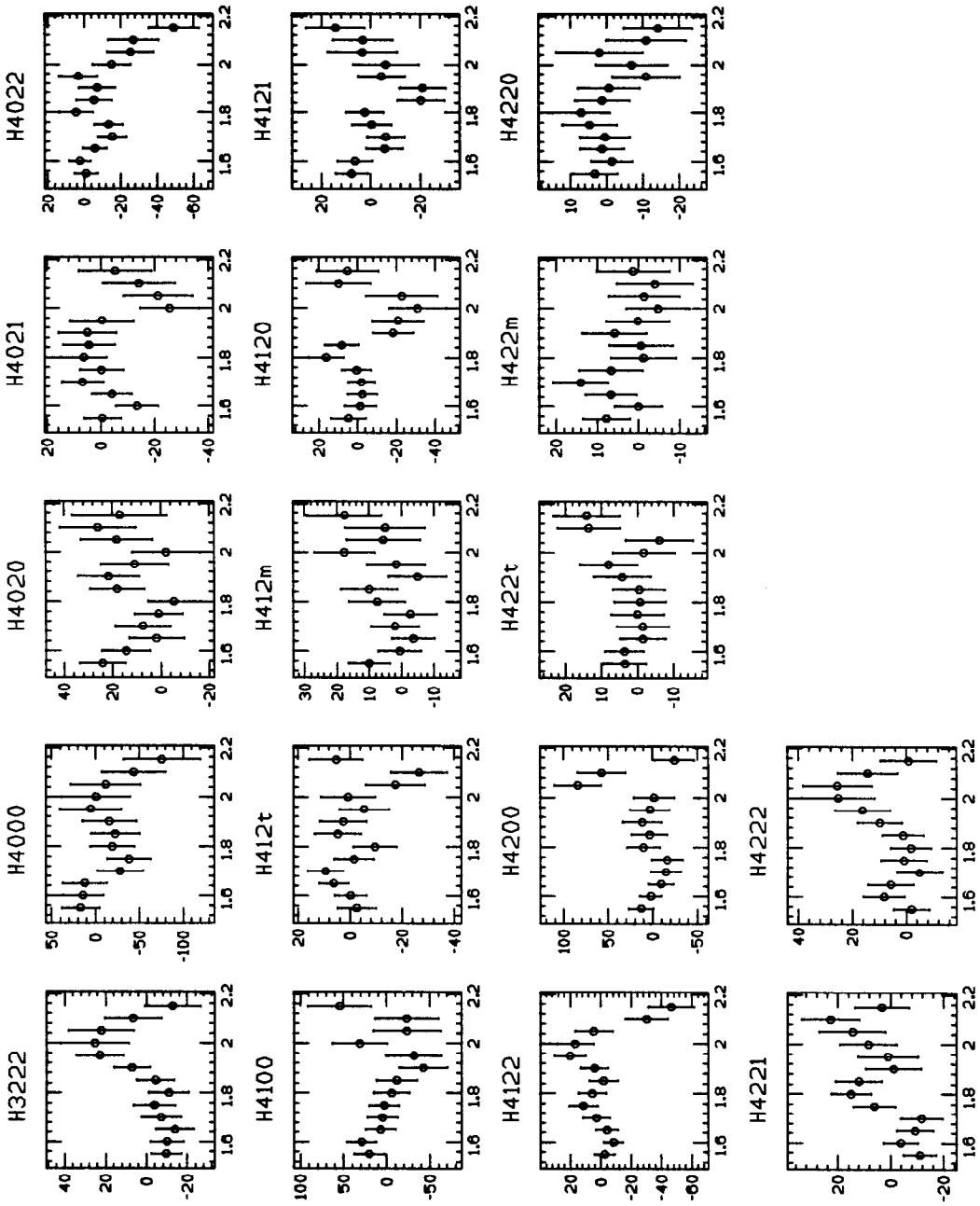

Figure 10.17 continued (3)

Table 10.1: The effect of the event selection on the acceptance.

	$1.6 \leq m_{\overline{K}^{\circ}\phi} < 1.7$ GeV/c^2		$1.9 \leq m_{\overline{K}^{\circ}\phi} < 2.0$ GeV/c^2	
Selection Criteria	Fraction cut	Accumulative Acceptance	Fraction cut	Accumulative Acceptance
1. Event Trigger	0.090	0.911	0.047	0.953
2. Topology	0.414	0.534	0.410	0.562
3. Loose Kinematical Cut	0.130	0.464	0.098	0.507
4. Particle Identification	0.056	0.438	0.034	0.490
5. Geometry MVFit	0.003	0.437	0.003	0.488
6. $\overline{K}^{\circ}$ Decay Length	0.039	0.420	0.037	0.470
7. Λ Removal	0.091	0.382	0.094	0.426
8. 4-C MVFit	0.0	0.382	0.0	0.426
9. 1-C MVFit	0.010	0.379	0.013	0.420
10. Resolution Cut	0.090	0.345	0.062	0.395
11. Baryon Cut $m_{\overline{K}^{\circ}n} \geq 1.9$ GeV/c^2	0.0	0.345	0.052	0.374
12. $\phi \rightarrow K^+K^-$ Background Subtraction	0.134	0.298	0.138	0.323

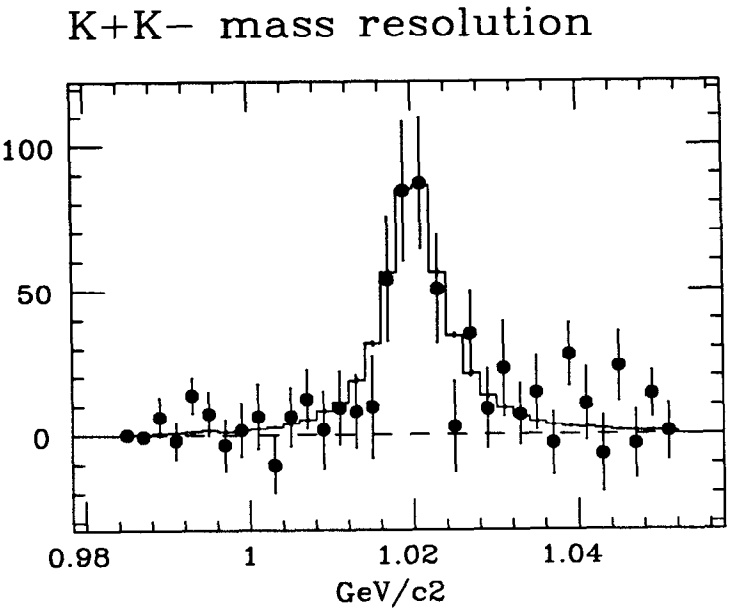

Figure 10.18: Background-subtracted K^-K^+ mass spectrum for real and MC data superposed to compare resolution

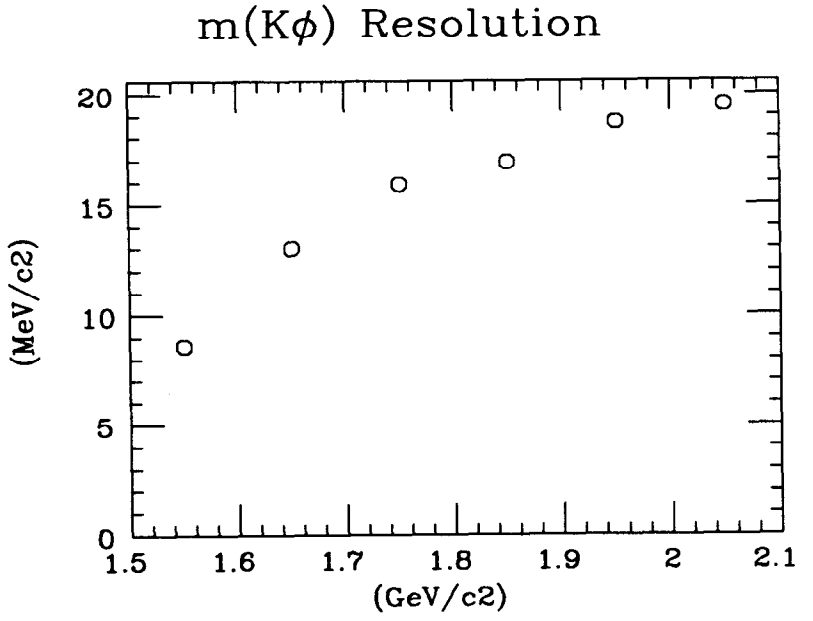

Figure 10.19: The resolution of $m_{\overline{K}^{\circ}\phi}$ as a function of $m_{\overline{K}^{\circ}\phi}$

Chapter 11

Partial Wave Analysis of $K^-\omega$ and $\overline{K}^\circ\phi$

To understand the physics underlying the $K^-\omega$ and $\overline{K}^\circ\phi$ systems, a partial wave analysis (PWA) is essential. The PWA establishes spin-parity (J^P) of the leading waves in a kinematic region and allows extraction of the underlying states, down to some noise level determined by statistics. The measured moments described in chapter 9 for $K^-\omega$ and in chapter 10 for $\overline{K}^\circ\phi$ systems reflect the underlying partial wave contents. This chapter will present the method of extracting partial wave amplitudes from the measured moments and the results in the $K^-\omega$ and the $\overline{K}^\circ\phi$ analysis.

11.1 The Formalism

The reactions we are considering are such that

$$a + b(\lambda_b) \rightarrow R(\Lambda) + c(\lambda_c)$$

where the resonance R decays into two bodies, $R \rightarrow R_1(\lambda) + R_2$, and the second-stage resonance R_1 subsequently decays into two ($\phi \rightarrow K^-K^+$ in $\overline{K}^\circ\phi$) or three ($\omega \rightarrow \pi^+\pi^-\pi^0$ in $K^-\omega$) spinless particles. The symbols in the parentheses represent

the helicities of corresponding particles. In both of our examples, the particle R_2 is a kaon which is a pseudoscalar. The formalism derived in this section is based on the work by Martin and Nef [44] and Chung [47].

To find the expressions of the moments in terms of the partial wave amplitudes, let us express the angular distributions $I(\Omega_1, \Omega_2)$ of the production and decay of the resonance R as sums of bilinear products of helicity amplitudes, T^A, where $A \equiv J^P$ is the spin-parity of R:

$$I(\Omega_1, \Omega_2) = \sum_{\lambda_b \lambda_c} \left| \sum_{A\Lambda\lambda} T^A \right|^2 . \tag{11.1}$$

The amplitude T^A can be factorized into production and decay parts as

$$T^A = \langle \Omega_2 | f | \lambda \rangle \langle \Omega_1, \lambda | F | A, \Lambda \rangle H^A_\Lambda(s, t, M_R), \tag{11.2}$$

where H is the helicity amplitude to produce a resonance R of mass M_R, spin-parity A and helicity Λ; s and t are the Mandelstam variables for the reaction. The matrix element $\langle\ |F|\ \rangle$ describes the decay $R \rightarrow R_1 + R_2$ and $\langle\ |f|\ \rangle$ describes the R_1 decay. In Eqn 11.2 it is assumed that the production amplitude H is independent of the helicities of particles b and c so that the density matrix

$$\rho^{AA'}_{\Lambda\Lambda'} = H^A_{\Lambda\lambda_b\lambda_c} H^{*A'}_{\Lambda'\lambda'_b\lambda'_c}$$

may be written as

$$\rho^{AA'}_{\Lambda\Lambda'} = H^A_\Lambda H^{*A'}_{\Lambda'} . \tag{11.3}$$

To derive an expression for the moments from Eqs 11.1 and 8.6, it is necessary to express the decay matrix elements in the angular momentum basis:

$$\langle \Omega_1, \lambda | F | A, \Lambda \rangle = \sqrt{\frac{2J+1}{4\pi}} D^{*J}_{\Lambda\lambda}(\Omega) F^A_\lambda , \tag{11.4}$$

and

$$\langle \Omega_2 | f | \lambda \rangle = \sqrt{\frac{2j+1}{4\pi}} D^{*j}_{\lambda 0}(\Omega), \tag{11.5}$$

where F^A_λ is the helicity coupling of the decay $R \rightarrow R_1 + R_2$; j is the spin of R_1 which is equal to 1 for both $K^-\omega$ and $\overline{K}^\circ\phi$. To obtain the moments, Eqs 11.2,

11.4, and 11.5 are substituted into Eqn 11.1, use is made of the Clebsch-Gordan coupling relation for the D matrices, and the result is compared with Eqn 7.6. We obtain

$$H(LMlm) = \frac{3\langle 1100|l0\rangle}{(2l+1)(2L+1)} \sum_{AA'\Lambda\Lambda'\lambda\lambda'} (-1)^{\Lambda'} \sqrt{(2J+1)(2J'+1)} H^A_\Lambda H^{*A'}_{\Lambda'} \times F^A_\lambda F^{*A'}_{\lambda'} \langle JJ'\Lambda\ -\Lambda'|LM\rangle \langle JJ'\lambda\ -\lambda'|Lm\rangle \langle 11\lambda\ -\lambda'|lm\rangle \quad (11.6)$$

It is, in general, convenient to convert the production amplitude H^A_Λ from the helicity basis $|J^P\Lambda\rangle$ to the reflectivity basis $|J^P\Lambda^\eta\rangle$ with $\eta = \pm 1$ defined by the relation;

$$H^{A\eta}_\Lambda = C_\Lambda (H^A_\Lambda - \eta\sigma(-1)^\Lambda H^A_{-\Lambda}), \quad (11.7)$$

where $\sigma = P(-1)^J$ is the 'naturality' of the resonance R, and where $C_0 = 1/2$ or $C_\Lambda = 1/\sqrt{2}$ if $\Lambda \neq 0$. $\sigma = +1$ describes a 'natural' series of spin-parity states such as $1^-, 2^+, 3^-$, etc., while $\sigma = -1$ describes an 'unnatural' series such as $0^-, 1^+, 2^-$, etc. Only reflectivity amplitudes with $\Lambda \geq 0$ are independent. The $|J^P\Lambda^\eta\rangle$ states with $\Lambda \geq 0$ and $\eta = \pm 1$ completely span the $|J^P\Lambda\rangle$ space where $-J \leq \Lambda \leq J$. Note for example

$$H^{A+}_{-\Lambda} = -\sigma(-1)^\Lambda H^{A+}_\Lambda \quad (11.8)$$

The advantages of using the reflectivity amplitudes are:

- it follows from Eqs 11.3 and 11.7 that there exist no interference terms between $\eta = +1$ and $\eta = -1$ amplitudes in the density matrix

$$\rho^{AA'}_{\Lambda\Lambda'} = \frac{1}{4C_\Lambda C_{\Lambda'}} (H^{A+}_\Lambda H^{*A'+}_{\Lambda'} + H^{A-}_\Lambda H^{*A'-}_{\Lambda'}). \quad (11.9)$$

- In a model where the resonance R is being produced via exchange mechanism, η represents the naturality of the exchanged particle. This interpretation is exact for $\Lambda = 0$ final states; for $\Lambda \neq 0$ this holds true to leading order of $1/s$. * (*I need a reference here!*)

*This combined with eq 11.8 tells us that for $\Lambda = 0$ the natural spin-parity resonance is only produced via unnatural parity exchange and vice versa.

Conventionally, to describe the joint decay process $R \to R_1 + R_2$ where R_1 has spin $j \neq 0$ with its decay subsequently measured and R_2 has spin zero – for example, reactions such as $R \to \rho K$, $K^*\pi$, ϕK, ωK, etc. – the relative orbital angular momentum L_o between R_1 and R_2 is used. The relation between the helicity coupling F^A_λ and the L_oS coupling $g^A_{L_o}$ [48] is

$$F^A_\lambda = \sum_{L_o}(-1)^{\lambda+1}\langle J1\ -\lambda\lambda|L_o0\rangle g^A_{L_o}, \tag{11.10}$$

where S is fixed to one as both ϕ and ω have spin 1 (i.e. $j = 1$ in our notation).

Inserting Eqs 11.8, 11.9, and 11.10 into Eqn 11.6, we obtain the equation for partial wave analysis:

$$H(LMlm) = \sum_{AA'\Lambda\Lambda'L_oL'_o\eta} C^{LMlm}(A, A', \Lambda, \Lambda', L_o, L'_o, \eta)H^{A\eta}_\Lambda g^A_{L_o} H^{*A'\eta'}_{\Lambda'} g^{*A'}_{L'_o}, \tag{11.11}$$

where $\Lambda, \Lambda' \geq 0$, $\eta = \pm 1$, and

$$\begin{aligned}
C^{LMlm}(...) \;=\; & \frac{3\langle 1100|l0\rangle}{(2l+1)(2L+1)}(-1)^{\Lambda'}\sqrt{(2J+1)(2J'+1)} \\
\times\; & \frac{1}{4C_\Lambda C_{\Lambda'}}(\langle JJ'\Lambda\ -\Lambda'|LM\rangle - \eta\sigma'(-1)^{\Lambda'}(1-\delta_{\Lambda'0})\langle JJ'\Lambda\Lambda'|LM\rangle \\
+\; & \eta\sigma(-1)^{\Lambda}(1-\delta_{\Lambda 0})\langle JJ'\ -\Lambda\ -\Lambda'|LM\rangle \\
+\; & \sigma\sigma'(-1)^{\Lambda+\Lambda'}(1-\delta_{\Lambda 0})(1-\delta_{\Lambda'0})\langle JJ'\ -\Lambda\Lambda'|LM\rangle) \\
\times\; & \sum_{\lambda\lambda'}\{(-1)^{\lambda+\lambda'}\langle J1\ -\lambda\lambda|L_o0\rangle\langle J'1\ -\lambda'\ -\lambda'|L'_o0\rangle\langle JJ'\lambda\ -\lambda'|Lm\rangle\langle 11\lambda\ -\lambda'|lm\rangle\}
\end{aligned}$$

Note that only the products

$$f^{A\eta}_{\Lambda L_o} = H^{A\eta}_\Lambda g^A_{L_o}$$

of the production and decay amplitudes can be extracted from the measured moments, not each amplitude separately. We take the products as 'waves' describing the $K^-\omega$ or $\overline{K}^\circ\phi$ system by a set of quantum numbers wave $= |J^P\Lambda^\eta L_o\rangle$. By choosing the same set of quantum numbers as in the 3-body isobar model analysis of the $\overline{K}^\circ\pi^+\pi^-$ system from the same experiment[42], it is easy to compare the results and compute the branching fractions. Another feature of this wave set is

that the sum of the squared amplitudes of all waves becomes simply the $H(0000)$ moment which represents the production cross-section:

$$H(0000) = \sum_{J^P\Lambda^\eta L_o} \left|\langle J^P\Lambda^\eta L_o\rangle\right|^2. \tag{11.12}$$

In other words, no interference terms contribute to the cross-section and the contribution a wave makes to the total cross-section is simply the absolute square of its amplitude.

The possible waves in the $K^-\omega$ and $\overline{K}^\circ\phi$ systems for $J \leq 3, \Lambda \leq 1$ are tabulated in appendix A. In appendix B, the expressions for the double moments $H(LMlm)$ in terms of the partial waves are listed.

The solutions to the equations in appendix B are obtained by minimizing the χ^2 function which is defined using the vectors of the predicted and measured double moments:

$$\chi^2 = \sum_{i,i'}(H^i_m - H^i_p)E^{-1}_{i,i'}(H^{i'}_m - \bar{H}^{i'}_p)$$

where $i \equiv (LMlm)$, H_m = measured moments, H_p = computed moments and E = covariance matrix of the moments. A CERN Library program MINUIT[49] is used to minimize the χ^2 function and hence to find the solutions.

11.2 Resonance Fitting with Breit-Wigner Model

After the PWA fitting described in the last section (11.1), it is necessary to extract the contents of resonant states from the resulting partial wave amplitudes. In order to do this, the amplitudes are fitted to the resonance model based on a standard relativistic Breit-Wigner (B-W) function containing a Blatt-Weisskopf barrier factor[50]. The B-W resonance model used in this analysis is described in this section.

Consider the case where we have the processes

$$K^-p \rightarrow RN \rightarrow (AB)N \tag{11.13}$$

Table 11.1: Blatt-Weisskopf barrier factors. $x = qr$, and the radius parameter r is given in GeV^{-1}.

l	$D_l(x)$
0	1
1	$1+x^2$
2	$9+3x^2+x^4$
3	$225+45x^2+6x^4+x^6$
4	$11025+1575x^2+135x^4+10x^6+x^8$

where R is a resonance state that has a two-body decay mode into A and B, and N is a recoiling nucleon – p or n depending on particular reaction. Denoting the mass and total width of R by m_0 and Γ_T, the differential cross section for process 11.13 can be written as[51]

$$d\sigma = F\left|\frac{\sqrt{\mathrm{m}_0\Gamma(m)}}{(\mathrm{m}_0^2-m^2)-i\mathrm{m}_0\Gamma_\mathrm{T}(m)}\right|^2 m\ dm. \tag{11.14}$$

The variable $\Gamma(m)$ describes the width at mass m defined by the relation:

$$\Gamma(m) = \left(\frac{q}{q_0}\right)^{2l+1}\left(\frac{\mathrm{m}_0}{m}\right)\frac{D_l(q_0r)}{D_l(qr)}\Gamma(\mathrm{m}_0),$$

where q describes the 3-momentum of the constituents (A, B) in the rest frame of the resonant state given by

$$q = \frac{1}{2m}\sqrt{\{m^2-(\mathrm{m}_A+\mathrm{m}_B)^2\}\{m^2-(\mathrm{m}_A-\mathrm{m}_B)^2\}},$$

D_l is a polynomial describing the Blatt-Weisskopf barrier factor as defined in Table 11.1, and r is the associated radius parameter.

Since, in this analysis, the PWA fitting determines the real and imaginary parts of the partial waves separately, the B-W resonance function is decomposed into real and imaginary parts and is used to fit all components of the partial wave amplitudes simultaneously.

Table 11.2: The wave set for the $K\omega$ partial wave analysis. In the low-mass region ($m_{K\omega} < 1.54$ GeV/c^2), two PWA's were tried; with and without the waves marked by '*'.

J^P	L_o	Waves	note
0^-	1	0^-0^+P	
1^+	0	1^+0^+S, 1^+1^+S, 1^+1^-S	
	2	1^+0^+D, 1^+1^+D, 1^+1^-D	
1^-	1	1^-0^-P, 1^-1^+P, 1^-1^-P	
2^+	2	2^+0^-D, 2^+1^+D, 2^+1^-D	
2^-	1	2^-0^+P, 2^-1^+P, 2^-1^-P	*
	3	2^-0^+F, 2^-1^+F, 2^-1^-F	*
3^-	3	3^-0^-F, 3^-1^+F, 3^-1^-F	*

11.3 $K^-\omega$ Partial Wave Amplitudes

Since the scattering reactions depend on both the mass of the $K\omega$ system and the momentum transfer t', the binning of the events, in principle, must be in two dimensions ($m_{K\omega}, t'$). In this analysis, however, the measurements are integrated over t' when the mass dependences are analyzed and vice versa: the selected t' range for mass-dependent PWA is

$$0.1 \leq t' \leq 2.0(\text{GeV/c})^2$$

as explained in Chapter 9.

The waves set used in fitting the $K\omega$ double moments is listed in Table 11.2. In the low-mass region ($m_{K\omega} \leq 1.54$ GeV/c^2), two PWA's were tried: first, including all the waves in Table 11.2, and later, without the 2^- and 3^- waves. As a matter of fact, it is not expected to observe $J^P = 2^-$ or 3^- states in this mass region. Although including the 2^- and 3^- waves gave a slightly better fit in terms of

χ^2 per degree of freedom, the difference is not significant and the fitted 2^- and 3^- waves did not show any resonant behavior but only the low-mass tails of the resonances at ~ 1.75 GeV/c^2. Moreover, including these waves caused ambiguities in determining other resonant amplitudes in the low mass region.

11.3.1 The Spin-parity Decomposition of the $K\omega$ Spectrum

Figure 11.1 shows the spin-parity decomposition of the acceptance-corrected $K\omega$ cross section. The intensities of the same spin-parity (J^P) waves are added and the resulting sum is plotted as a function of the invariant mass of $K\omega$.

It should be noted that due to the nonlinearity and complexity of the fitting equations, the PWA solutions are not unique. For each interval of $K^-\omega$ mass, therefore, the PWA fit is tried many times with random parameter initializations; any PWA solution which has a χ^2 exceeding by more than ~ 10 units the minimum value obtained in the interval in question is rejected. In most cases the accepted solutions overlap with one another within one standard deviation. The one standard deviation intervals from all surviving solutions are combined, and the span of the combined intervals is taken as the solution interval. The center of this solution interval is taken as the estimated value of the fitted amplitude, and the half-length of the interval is conservatively assigned as the one standard deviation uncertainty.

The points marked by '•' and 'o' describe the results from using the full wave set; they are displayed separately as they differ from each other by more than one standard deviation. The multiple solution ambiguity is most serious for $J^P = 1^+$ waves in the low mass region. The solutions marked by '•' have a slightly better χ^2 value on average, but without making enough difference to resolve the ambiguity on the basis of the χ^2. The results of PWA without $J^P = 2^-$ and 3^- waves are marked by '×'. They follow the '•' solutions in the 1^+ waves.

The $J^P = 1^+$ wave sum is dominant in the $K\omega$ threshold region with the production of $K_1(1270)$ and possibly $K_1(1400)$. In the same region, the $J^P = 2^+$

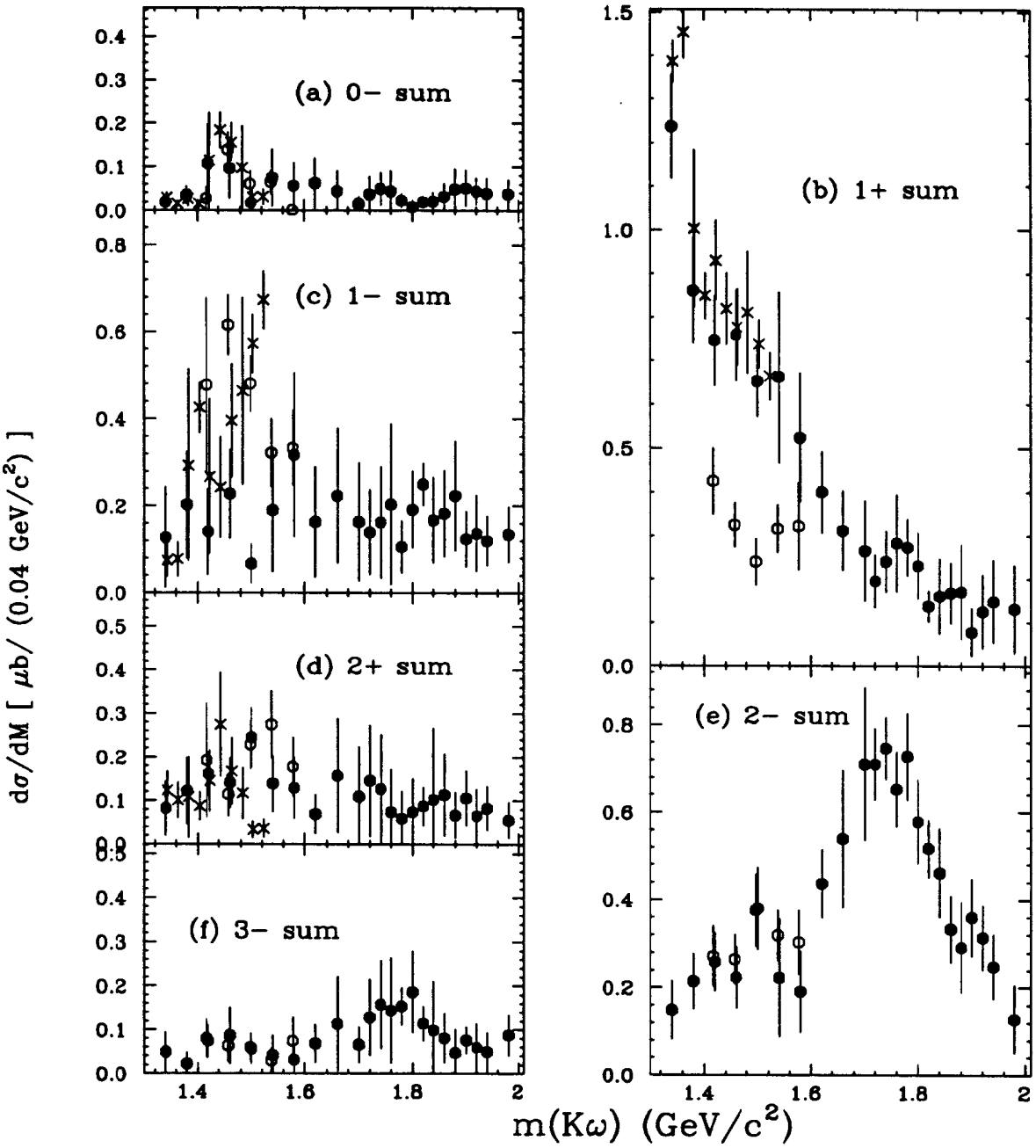

Figure 11.1: The J^P sum of the $K\omega$ partial waves. Symbols for data points are explained in the text.

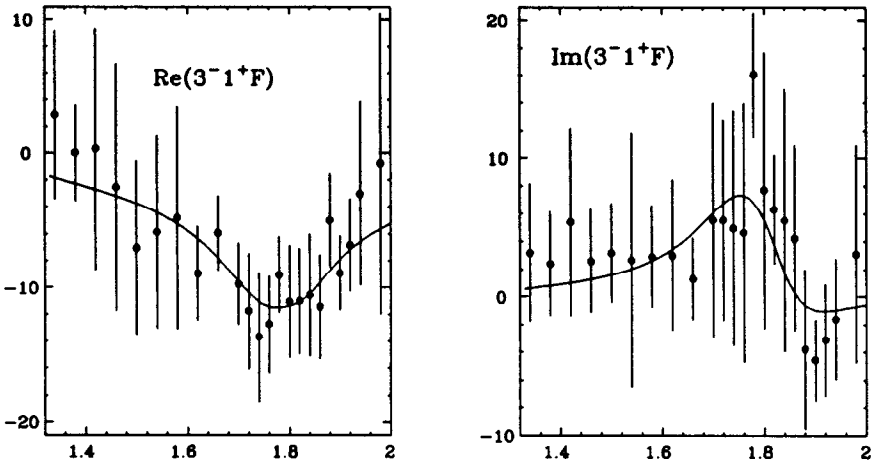

Figure 11.2: The 3^- partial wave; real and imaginary amplitudes

wave sum also shows a bump structure suggesting $K_2^*(1430)$ production. The 1^- waves are seen to make more contribution to the total cross section than 2^+ waves do but it is very difficult to understand the structure and extract any information from the 1^- states, due to the multiple solution ambiguities in the low-mass region.

The 2^- wave sum is dominant in the region $1.7 - 1.9$ GeV/c^2. This is clearly the production of $K_2(1770)$. The 3^- wave sum also shows a peak centered around 1.75 GeV/c^2 that can be interpreted as a $K_3^*(1780)$ production.

The J^P decompositions indicate that the structure of strange meson states seen in the $K\omega$ system is quite complicated, despite the rather uncomplicated appearance of the $K\omega$ mass spectrum. In particular, the two peaks in the $K\omega$ mass distribution (Fig.9.11) at ~ 1.4 and ~ 1.75 GeV/c^2 result not only from the leading unnatural J^P states but from the superposition of several states of different J^P. These results are in contrast with the naive expectation that the lower-lying structure is only from 1^+ and the upper one is only from 2^-.

11.3.2 3^- Amplitude

The $K_3^*(1780)$ is well-established from previous studies (refs. [46], [52]), and from the standard quark model there is no physical reason to assume multiple resonance structure for the $J^P = 3^-$ state around the $K_3^*(1780)$ region. Therefore, the 3^- wave is fitted to a single B-W resonance and provides the phase reference in this mass region, especially when we study the $J^P = 2^-$ waves (section 11.3.3).

Out of the three $J^P = 3^-$ partial waves that are used in the PWA fit, only the $|3^-1^+F\rangle$ wave shows a significant peak structure. The other waves that do not show resonant structures have the quantum number $\eta = -1$, implying that most of the resonant contents of $J^P = 3^-$ in the reaction $K^-p \to K^-\omega p$ is produced by natural spin-parity exchange. In other words, π-exchange does not contribute much in this reaction. Figure 11.2 shows the real and imaginary components of the $|3^-1^+F\rangle$ amplitude determined from the PWA fit. Other $J^P = 3^-$ amplitudes do not show clear resonance structures and will not be discussed. A clear structure is seen around 1.75 GeV/c^2. The curves in Fig. 11.2 represent the fit to the B-W resonance. The width of the resonance is fixed to the value 187 MeV/c^2, which was determined from analysis of the reaction $K^-p \to \overline{K}^\circ\pi^-p$ in the same experiment[52]. With the width fixed, the measured mass of the resonance is 1763 ± 14 MeV/c^2.

The B-W resonance function describes the 3^- amplitudes pretty well and the fitted mass value is consistent with the known 3^- mass. This is the first observation of the $K_3^*(1780)$ decaying into the $K\omega$ final state. The associated branching fraction could be measured and will be discussed in the next chapter (Chapter 12).

11.3.3 2^- Amplitude

Figs.11.3 shows the $J^P = 2^-$ wave amplitudes that exhibit significant signals in the $K_2(1770)$ region along with the 3^- waves. Only waves with $\eta = +1$ show significant structures as in the case of 3^- waves. The real and imaginary parts of the waves are displayed as they are directly obtained from PWA. Note that the imaginary part of the $|2^-0^+P\rangle$ wave is fixed to zero as we have the freedom

to arbitrarily choose the overall phase of the partial waves without altering the angular distribution and the double moments[†].

The 3^- amplitudes are first fitted to a single B-W resonance model to define a phase reference in the $K_2(1770)$ region (Sec 11.3.2). Then the 2^- and 3^- amplitudes are simultaneously fitted with the relative phases and strengths between the waves as free parameters. Two different hypotheses are tested:

(i) the 2^- waves observed in the $K_2(1770)$ region come from a single B-W resonance; or

(ii) they come from at least two B-W resonances.

The dotted curves in Fig. 11.3 show the fit results corresponding to the first hypothesis. The fitted mass and width of the 2^- resonance are 1728 ± 7 MeV/c^2 and 221 ± 22 MeV/c^2, respectively, and the χ^2 is 128.9 for 116 degrees of freedom. Although the χ^2 per degree of freedom is quite acceptable, the one-resonance fit does not reproduce the behavior of the 2^-1^+F wave at all well; also, the dip at ~ 1.84 GeV/c^2 in the Re(2^-0^+P) and the tail of Re(2^-0^+F) are not well represented by the fit. On the other hand, the fit results corresponding to the two-resonance hypothesis, represented by the solid curves in Fig. 11.3, reproduce all features of the amplitudes very well and provide a significantly better fit to the data, yielding a χ^2 of 70.6 for 110 degrees of freedom. The fitted masses of the two resonances are 1773 ± 8 MeV/c^2 and 1816 ± 13 MeV/c^2, and the corresponding widths are 186 ± 14 MeV/c^2 and 276 ± 35 MeV/c^2, respectively. The fit results are summarized in Table 11.3.

To further demonstrate the significance for the presence of two resonances in the 2^- waves, a set of least-square fits have been performed to the 2^- waves with a different parametrization. Three new parameters α_1, α_2 and α_3 are defined according to the relation:

$$W_i^{2^-} = N_0 \left[(\mathrm{BW}_1)_i^{2^-} + \alpha_i (\mathrm{BW}_2)_i^{2^-} \right] \ (i = 1, 3),$$

[†]In fact, we can fix two phases: corresponding to $\eta = +1$ or -1.

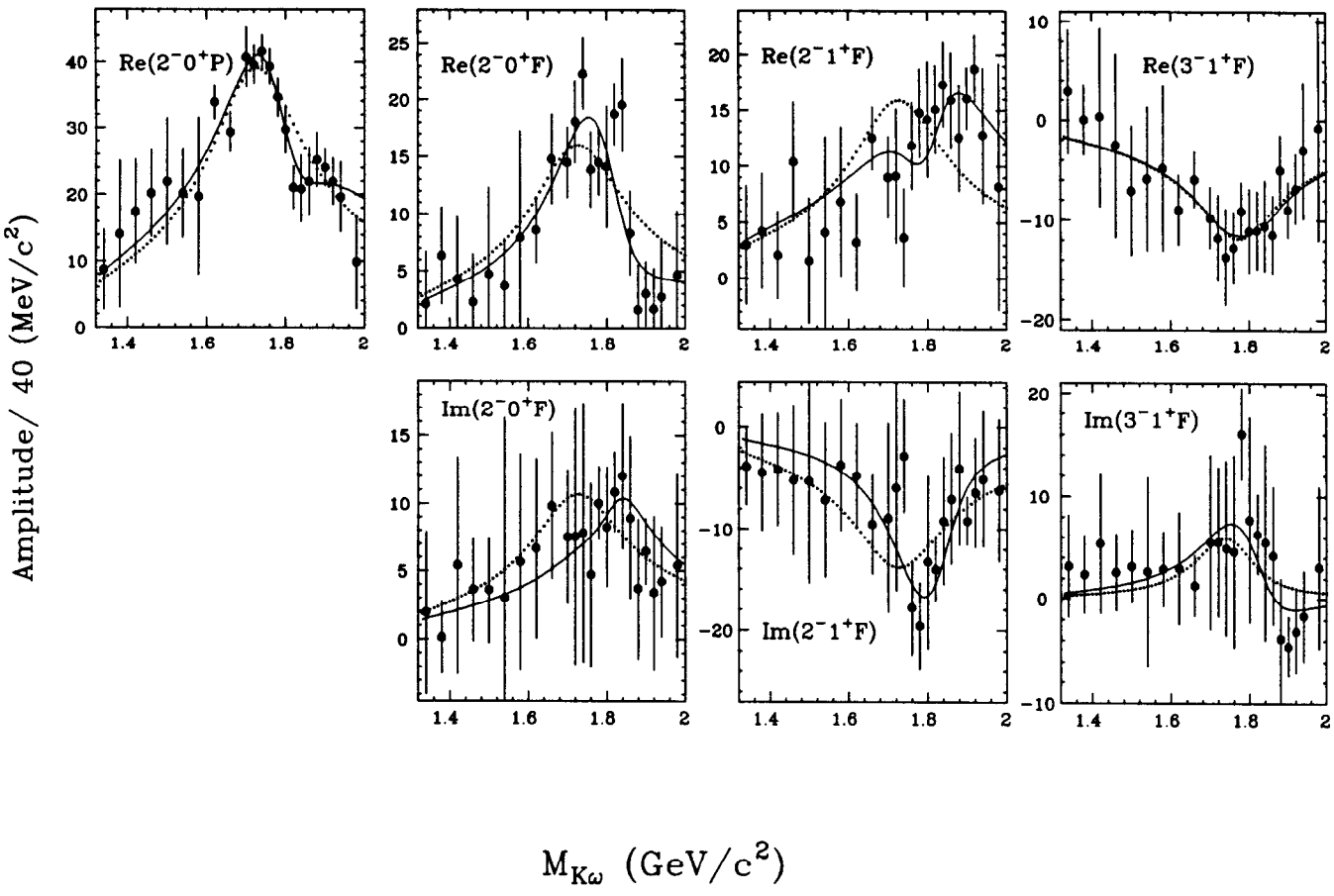

Figure 11.3: The real and imaginary amplitudes of 2^- and 3^- waves

Table 11.3: The results of the Breit-Wigner fits to the 2^- waves.

Fit Model	Mass (MeV/c^2)	Width (MeV/c^2)	χ^2/dof.
one 2^- resonance	1728 ± 7	221 ± 22	128.9/116
two 2^- resonances	1773 ± 8	186 ± 14	70.6/110
	1816 ± 13	276 ± 35	

where $W_i^{2^-}$ for $i = 1, 3$ are the three 2^- waves that are under consideration and $(\mathrm{BW}_1)_i^{2^-}$ and $(\mathrm{BW}_2)_i^{2^-}$ are the lower- and upper-mass Breit-Wigner resonances, respectively. In other words, each α_i illustrates the significance of the higher mass resonance in comparison to the one with lower mass in each 2^- wave. The α's are then combined to define a 'significance parameter', σ defined as the square-root of the summed squares of the α's with an arbitrary normalization:

$$\sigma = \sqrt{\frac{\sum_{i=1}^{3} \alpha_i^2}{3}}.$$

The 2^- waves are then fitted to the two resonance model with various combinations of α's defined as fixed parameters and the resulting χ^2 values of the various fits are plotted as a function of the significance parameter σ. A total of 152 combinations of α_i's are used. First, each α_i is independently chosen to be one of {0.0, 0.25, 0.5, 0.75, 1.0} independent of one another, resulting in $125(= 5^3)$ combinations. Then, to explore the region of small σ in more detail, new values of α_i's are selected from {0.0, 0.1, 0.2} which gave another 27 combinations. Four different random starting points were tried and the fit giving the best χ^2 is accepted for each combination. The result is shown in Fig. 11.4.

Although this grid-search is far from covering the complete α^3 space, it demonstrates that envelope of the best obtainable χ^2 is relatively smooth as a function of the significance parameters. The minimum χ^2 attainable for a given σ decreases

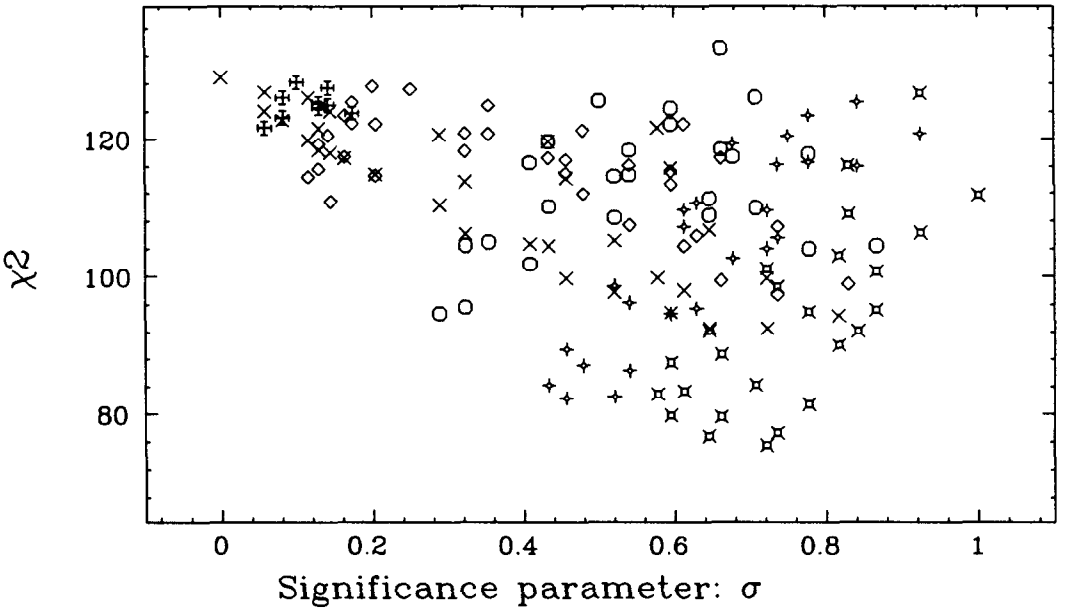

Figure 11.4: The distribution of χ^2 vs σ which shows the significance of the second resonance in the 2^- waves.

smoothly from $\sigma = 0$ to $\sigma \sim 0.8$. This suggests that the quality of a two resonance fit improves as the magnitude of the second resonance increases from zero to that comparable to the first one.

From all these tests, we found that the model with two 2^- resonances describes the relevant data very well and provides a significantly better fit than does a model containing only a single resonant 2^- amplitude. This is an evidence for the doublet structure of the $J^P = 2^-$ strange meson states in the $K_2(1770)$ region.

11.3.4 2^+ Amplitude

There is a bump in the $J^P = 2^+$ wave sum in the mass region $1.4 \sim 1.5$ GeV/c^2 (see Fig. 11.1) corresponding to the $K_2^*(1430)$ production. The bump is most clear in the '×' solutions which were obtained without using 2^- and 3^- waves in the low-mass region. Similar to the case of 3^- waves, only the $|2^+1^+D\rangle$ wave shows a significant peak structure in the $K_2^*(1430)$ region (Fig. 11.5). The other two 2^+ waves have the quantum number $\eta = -1$, therefore most of the resonant contents of $J^P = 2^+$ in the reaction $K^-p \to K^-\omega p$ is not produced by π-exchange.

To fit the real and imaginary components of the wave to a resonance function, we need a phase reference in this mass region. The 1^+ wave is dominant in this region as displayed in Fig. 11.1, but its structure is not well understood at this point so that it cannot provide a phase reference. On the other hand, though it is only a tail of a resonance (or two), the intensity of the $|2^-0^+P\rangle$ amplitude in the low-mass region is still large enough to provide the phase reference to the partial waves in the low mass region around $1.4 \sim 1.5$ GeV/c^2 (Fig 11.3). Therefore, to fit the 2^+ wave to a B-W resonance, $|2^-0^+P\rangle$ amplitude is used to give the phase reference.

With the low-mass tail of $|2^-0^+P\rangle$ wave defining the reference phase, which is almost constant over the $K_2^*(1430)$ region, the real and imaginary parts of the $|2^+1^+D\rangle$ wave is fitted to a B-W resonance function. The width is fixed to 98 MeV/c^2, which was obtained in the E-135 analysis of the reaction $K^-p \to \overline{K}^\circ \pm p$[52]. The fitted mass is 1.432 ± 0.006 GeV/c^2, which is consistent with

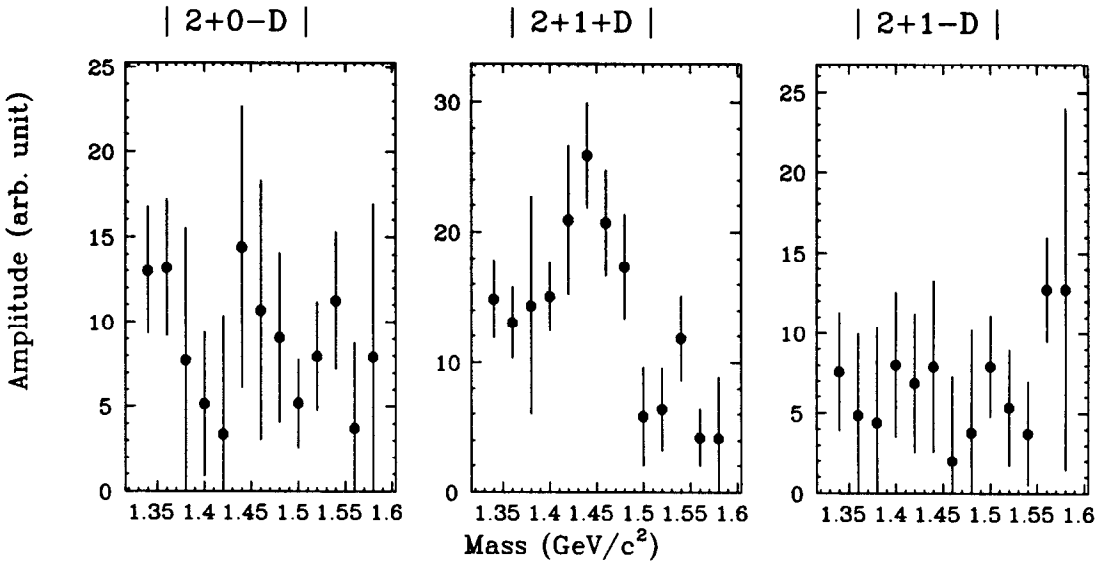

Figure 11.5: The amplitudes of $J^P = 2^+$ waves.

$K_2^*(1430)$ mass. The result is shown in Fig 11.6. The branching fraction of the decay $K_2^*(1430) \rightarrow K\omega$ is measured and will be discussed in the next chapter (Chapter 12).

11.3.5 1^+ Amplitude

Figure 11.1 shows a large 1^+ peak in the $K\omega$ threshold region. This peak is from the production and decay of $K_1(1270)$. However, it is very difficult to measure the resonance parameters because the mass of $K_1(1270)$ is below the $K\omega$ threshold (~ 1.276 GeV/c^2). No clear structure is seen around 1.4 GeV/c^2, where $K_1(1400)$ could be produced. There is a slight hint of a possible structure around 1.8 GeV/c^2 but the signal, if real, is too small to analyze. Although, following the 'o' solutions, there seems to be a broad bump around 1.6 GeV/c^2 in the 1^+ wave sum, no clear structure is observed when individual 1^+ wave amplitudes are examined.

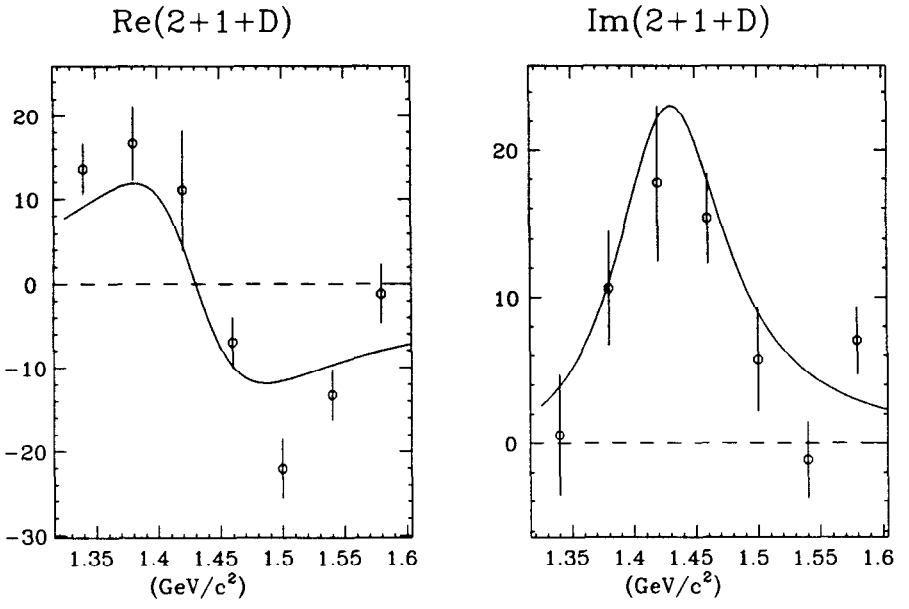

Figure 11.6: The real and imaginary components of the $|2^+1^+D\rangle$ wave. The curves corresponds to the fitted B-W resonance function.

11.3.6 t'-dependent PWA of $K^-\omega$

The t' dependence of the partial waves are studied mainly because: (1) the underlying production mechanism could be better understood by comparing the t' dependence with other reactions in which the production mechanism is fairly well known; and (2) by summing the intensity of a wave of interest over the t' bins and comparing with the similar result from the mass-dependent analysis, a consistency check can be made for production of the corresponding meson state. To analyze the t' dependence of the $K\omega$ partial waves, the events are integrated over selected mass windows, which are defined according to Table 11.4, and PWA is performed to the set of double moments computed in t' bins. The resulting amplitude is then fitted to a function of the form:

$$a(t') \propto (t')^{\frac{n}{2}} e^{-bt'} \tag{11.15}$$

This form is the consequence of angular momentum conservation in the forward direction ($t' \to 0$) and n is the number of units of net helicity flip in the reac-

Table 11.4: The t' analysis of the $K\omega$ partial waves. The t' slopes determined from least-squares fits are marked by ($\star$). Those marked by (1) and (2) are the slopes determined from the reaction $K^-p \to \overline{K}^\circ\pi^-p$ and shown for comparison: (1) for $|D^+|$ amplitude with $1.3 \leq m_{K\pi} \leq 1.54$; and (2) for $|F^-|$ amplitude with $1.6 \leq m_{K\pi} \leq 1.95$.

Mass (GeV/c^2)	Amplitude	t' slope	χ^2/dof
$1.32 \leq m_{K\omega} \leq 1.56$	2^+1^+D	$3.24 \pm 0.63^\star$	9.3/5
		$4.34 \pm 0.08^{(1)}$	11.1/6
$1.60 \leq m_{K\omega} \leq 1.80$	3^-1^+F	$2.95 \pm 0.45^\star$	5.0/5
		$3.58 \pm 0.26^{(2)}$	6.4/6
$1.80 \leq m_{K\omega} \leq 1.95$	3^-1^+F	$5.86 \pm 0.98^\star$	4.9/5
		$3.58 \pm 0.26^{(2)}$	11.9/6

tion. Since the predominant production mechanism involves isoscalar t-channel exchange (*i.e.*, ω, f exchange), n is expected to be 1, *i.e.*, the natural parity exchange amplitudes would be expected to behave like $\sim \sqrt{t'}$ at small t'.

The set of partial waves used in the t' analysis of the $|2^+1^+D\rangle$ wave is the same as that used in the mass-dependent PWA in the low-mass region (Table 11.2). The resulting $|2^+1^+D\rangle$ amplitude vs. t' is plotted in Fig. 11.7. The amplitude is fitted in two ways: first, the parameter b, which represents the t' slope in the logarithmic plot, is fixed to the value obtained from the analysis of the reaction $K^-p \to \overline{K}^\circ\pi^-p$[52]; second, the variable b is taken as a free parameter. The solid curve in Fig 11.7 corresponds to the former and the dashed one to the latter. The χ^2 of the fits and the resulting t' slopes are listed in Table 11.4.

The fit with a fixed slope parameter resulted in a good fit except for the last point of the highest t', which was responsible for most of the χ^2. The variable slope fit did not improve χ^2 per degrees of freedom significantly, either. What caused

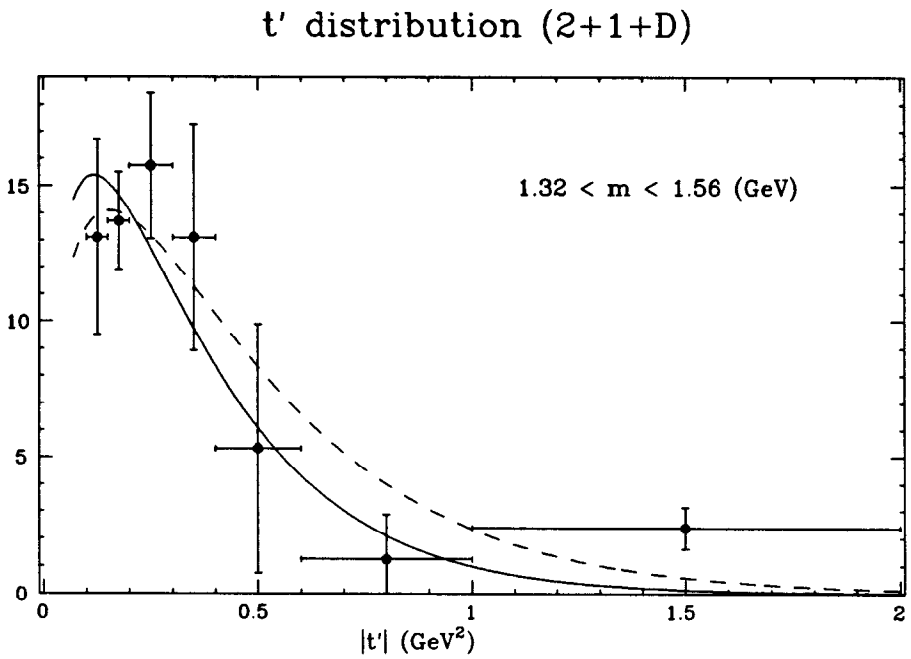

Figure 11.7: The t' dependence of the $|2^+1^+D\rangle$ amplitude. The fit function is described in the text. The solid curve represents the least-squares fit to a model where the t' slope is fixed to the value obtained from the $\overline{K}^\circ\pi^-$ analysis, while the dashed curve corresponds to the case where the slope is taken as a free parameter to be fitted.

Table 11.5: Estimated number of the $|2^+1^+D\rangle$ events as determined from mass-dependent and t'-dependent PWA's.

$m_{K\omega}$ (GeV/c^2)	PWA	N(2^+1^+D)
1.32 – 1.56	mass	1510 ± 185
	t'	1440 ± 520

the deviation of the last point is not clearly understood: it could be a background to 2^+ resonance production. Other than the last bin, both fits described the data reasonably well.

Since, in our formalism, the absolute square of an amplitude gives the number of produced events of a partial wave, the number of $|2^+1^+D\rangle$ events can be computed by squaring the amplitude and integrating over the selected range. Within the $(t', m_{K\omega})$ window of $0.1 < t' < 2.0$ (GeV/c)^2 and $1.32 < m_{K\omega} < 1.56$ GeV/c^2, the number of $|2^+1^+D\rangle$ events from mass-dependent and t'-dependent PWA are 1510 ± 185 and 1440 ± 520, respectively (Table 11.5. The latter is obtained from the fit where the slope variable b was taken as a free parameter. The two numbers agree quite well considering the large error in the value from t'-dependent PWA. Therefore, we decided that the $|2^+1^+D\rangle$ wave intensity produced in the mass-dependent PWA is consistent with the t'-dependent PWA.

The full wave set used in the mass-dependent PWA in the high-mass region (Table 11.2) is used in the t' analysis of the $|3^-1^+F\rangle$ wave as well. The mass window is split into two regions: $1.6 < m_{K\omega} \leq 1.8$ GeV/c^2 and $1.8 < m_{K\omega} \leq 1.95$ GeV/c^2. The split in the mass range made it easier to find the PWA solutions. The resulting $|3^-1^+F\rangle$ amplitudes vs. t' are plotted in Fig 11.8. The same fit function as in the 2^+ analysis is used. Moreover, fits are performed on both models, where the slope variable b is either fixed or free, for both mass regions. The fit result is shown in Table 11.4.

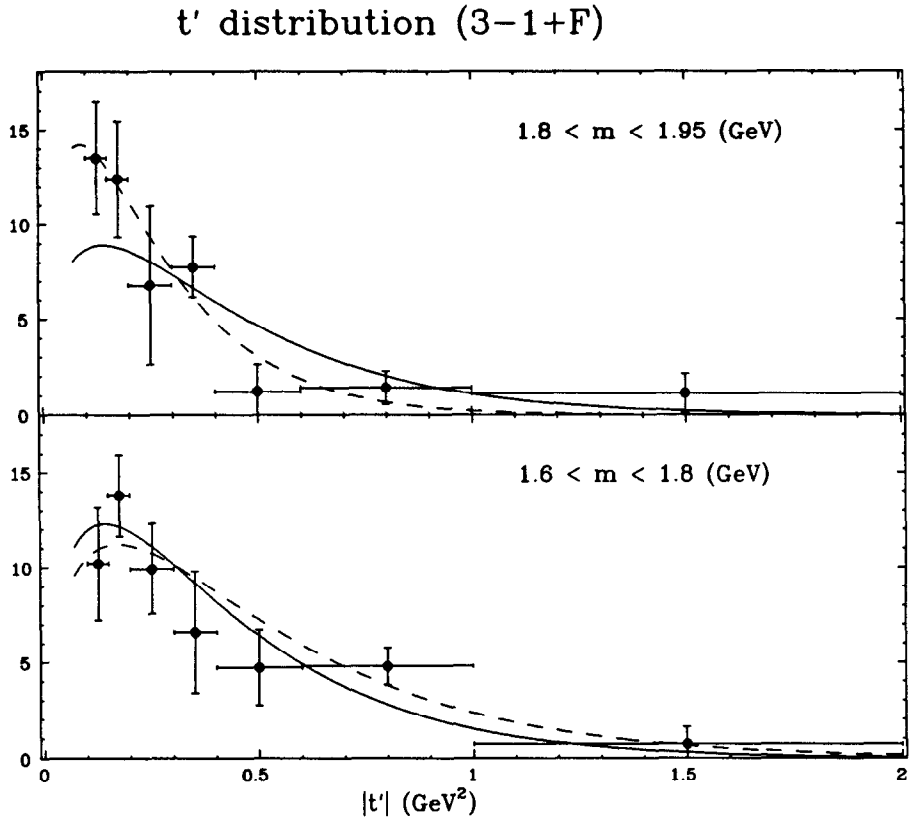

Figure 11.8: The t' dependence of the $|3^-1^+F\rangle$ amplitude. The fit function, the solid curves and the dashed curves have similar meanings to the ones used in the 2^+ analysis. The top figure shows the t' dependence in the upper-mass region $1.8 < m_{K\omega} \leq 1.95$ GeV/c^2 and the bottom one is for the lower-mass region $1.6 < m_{K\omega} \leq 1.8$ GeV/c^2.

Table 11.6: Estimated number of the $|3^-1^+F\rangle$ events.

$m_{K\omega}$ GeV/c^2	PWA	$N(3^-1^+F)$
1.6 – 1.8	t'	985 ± 360
1.8 – 1.95	t'	630 ± 340
1.6 – 1.95	mass	1375 ± 210

For the lower mass region, both models produced reasonable fits. The χ^2 per degree of freedom is about the same in both fits (~ 1) and the slope parameter difference is less than 1.5 standard deviations. The higher mass region shows, however, a substantial difference between the two models. The free slope-parameter fit made a substantial improvement in χ^2 per degrees of freedom (4.9/5 vs. 11.9/6) and the two slope values differ by more than 2 standard deviations. The deviation in the upper-mass region may be due to background to 3^- resonance productions, or since the underlying spectroscopic structures tend to become more complicated as $m_{K\omega}$ increases, it may be due to contaminations from the waves that were not included in the PWA. On the other hand, if the two mass regions are combined, the resulting t' slope is close to the fixed value in the other model, *i.e.*, the $\overline{K}^\circ\pi^-$ system result.

The mass-dependent and t'-dependent PWA's are compared to check the number of $|3^-1^+F\rangle$ events. The result is summarized in Table 11.6. If the values from the two mass ranges are combined with the errors added in quadratures, the number from t'-dependent PWA is 1615 ± 495. This agrees well with the number from mass-dependent PWA up to the associated errors, which implies that the $|3^-1^+F\rangle$ wave intensities obtained by two different ways are consistent.

11.4 $\overline{K}^\circ\phi$ Partial Wave Amplitudes

Since the size of the $\overline{K}^\circ\phi$ sample is small, partial wave analysis may not give a significant result by itself. Therefore it is worth trying to extract as much information as possible about the underlying structures prior to applying the PWA so that it could be later compared with the PWA results for consistency. Section 11.4.1 will discuss methods of combining $H(LMlm)$ moments to find out the spin-parity structure before PWA. The results of the mass-dependent PWA will be discussed in sec 11.4.2 and the t'-dependent PWA results will be discussed in sec 11.4.3

11.4.1 Moment Combinations

From the moment-amplitude table in Appendix B, we have

$$\begin{aligned} H(0000) &= \left|\left|0^-0^+P\right\rangle\right|^2 \\ &+ \sum_{\Lambda,\eta}\left|\left|1^-\Lambda^\eta P\right\rangle\right|^2 + \sum_{\Lambda,\eta}\left|\left|2^+\Lambda^\eta D\right\rangle\right|^2 + \sum_{\Lambda,\eta}\left|\left|3^-\Lambda^\eta F\right\rangle\right|^2 \\ &+ (\text{terms with } J^P = 1^+, 2^-) \end{aligned}$$

and

$$\begin{aligned} H(0020) &= \frac{2}{5}\times\left|\left|0^-0^+P\right\rangle\right|^2 \\ &- \frac{1}{5}\times\left(\sum_{\Lambda,\eta}\left|\left|1^-\Lambda^\eta P\right\rangle\right|^2 + \sum_{\Lambda,\eta}\left|\left|2^+\Lambda^\eta D\right\rangle\right|^2 + \sum_{\Lambda,\eta}\left|\left|3^-\Lambda^\eta F\right\rangle\right|^2\right) \\ &+ (\text{terms with } J^P = 1^+, 2^-). \end{aligned}$$

From these two moments, we note that the combination

$$|H_0|^2 \equiv H(0000) + 5H(0020)$$

does not contain any natural J^P terms. Therefore if $|H_0|^2$ is very small compared to $H(0000)$ in a given kinematic region, we can say that the system is dominated by natural spin-parity states in that region. Similarly, the following combination

$$\Delta_{0^-} \equiv H(0000) - \frac{5}{2}H(0020)$$

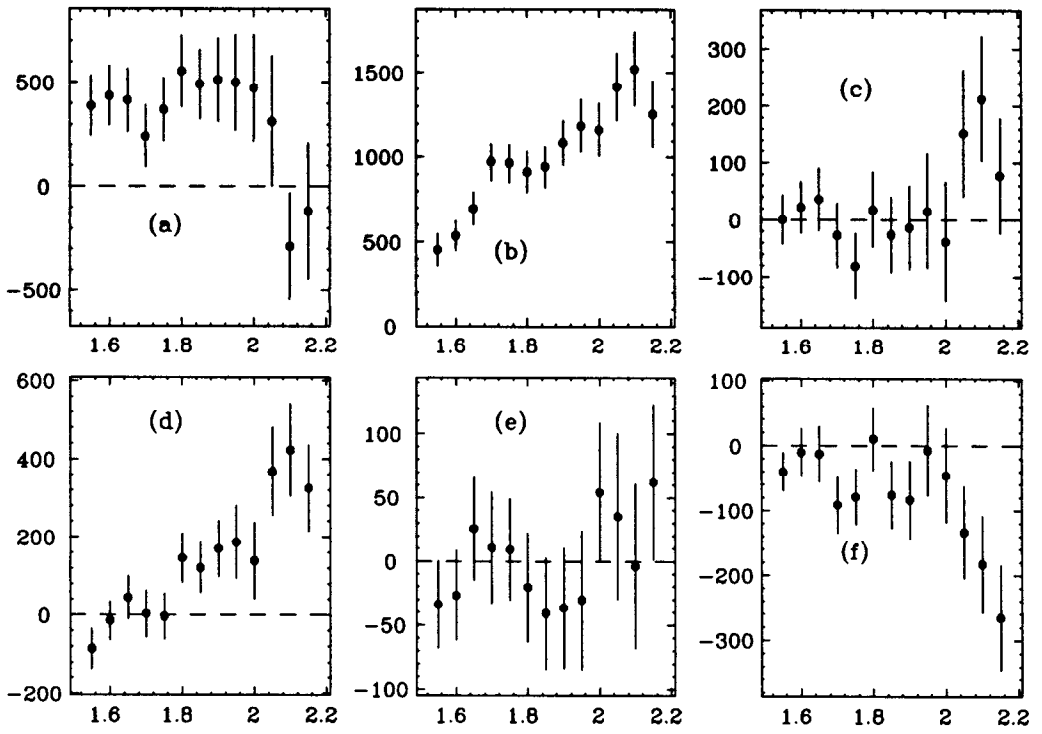

Figure 11.9: Combinations of moments as functions of $m_{K\phi}$: (a) $|H_0|^2 \equiv H(0000) + 5H(0020)$; (b) $\Delta_{0^-} \equiv H(0000) - \frac{5}{2}H(0020)$; (c) $\Delta_{1^+,2^+}(20)$: Both 1^+ and 2^+ give identical results; (d) $\Delta_{1^-,2^-}(20)$: Both 1^- and 2^- give identical results; (e) $\Delta_{2^+}(40)$; (f) $\Delta_{2^-}(40)$.

eliminates any contribution from $J^P = 0^-$ wave. Therefore if a system is dominated by this wave in a certain kinematic region, we must have $\Delta_{0^-} \approx 0$.

Moreover, if a system is in a pure J^P state with even $L \geq 2$, the following combination should be identically zero[47]:

$$\begin{aligned}\Delta_{J^P}(LM) \equiv & \sqrt{\frac{2L(L+1)}{3(L-1)(L+2)}}\left\{H(LM00) - \frac{5}{2}H(0020)\right\} \\ & + P(-1)^J\left\{1 - \frac{L(L+1)}{2J(J+1)}\right\}5H(LM22). \qquad (11.16)\end{aligned}$$

We display in Fig. 11.9 the combinations of acceptance-corrected moments that are relevant in looking into the $\overline{K}^\circ\phi$ spin-parity structure. From Fig. 11.9(a) and (b), we see that in the mass region 2.0 $\sim$ 2.2 GeV/c^2, where $|H_0|^2$ is fluctuating around zero well within twice the statistical errors, the natural spin-parity states such as 1^- or 2^+ could be dominant. From Fig 11.9(b) we see that since Δ_{0-} is far from zero everywhere, $J^P = 0^-$ state can not be prevailing. In fact it is consistent with the observation in Chapter 10 where the 0^- is almost ruled out because of the azimuthal angular distribution of $\phi \rightarrow K^+K^-$ decay. Due to the statistical limitations, the other plots ((c)-(f)) are harder to interpret as they are using higher L moments. The only conclusion that is consistent with all six plots is that 2^+ wave could be dominant at $\sim$ 2 GeV/c^2.

This method of combining moments to determine the spin-parity structure of a system is useful only when the system is in a pure J^P state. Since it is hard to make a clear interpretation in this case, we infer that this $\overline{K}^\circ\phi$ system may not be in the state of a pure spin-parity. Therefore we have to use partial wave analysis to analyze the spin-parity structure of the $\overline{K}^\circ\phi$ system as we did in the $K\omega$ analysis.

11.4.2 Mass-dependent PWA of $\overline{K}^\circ\phi$

As in the $K^-\omega$ analysis, the $\overline{K}^\circ\phi$ system is analyzed with both a mass-dependent and t'-dependent PWA. The waves of $J^P = 0^-, 1^-, 1^+, 2^+$ and 2^- are used in both analyses. As mentioned in Sec 10.3, double moments with $L \geq 5$ are truncated, and therefore partial waves with $J \geq 3$ can not be studied. Orbital angular momentum of the $\overline{K}^\circ\phi$ system is limited to $L_o \leq 2$, again due to low-statistics of the sample, and hence $2^-\Lambda^\eta F$ waves are not used in the PWA.

The binning of $\overline{K}^\circ\phi$ data is determined by considering the conflicting criteria of:

- having enough data within each bin to ensure that the PWA fitting process is stable; and
- choosing narrow bins to detect rapid variations in the partial wave

amplitudes.

An overlapping binning of width 0.1 GeV/c^2 is chosen as a compromise between the two criteria.

Figures 11.10 and 11.11 exhibit decompositions of the $\overline{K}^\circ\phi$ mass spectrum into natural and unnatural spin-parity components determined from the mass-dependent PWA. Figure 11.10(a) shows the acceptance-corrected $\overline{K}^\circ\phi$ mass spectrum. Data points marked with o are obtained by background-subtraction as explained in Chapter 10, while the ones marked with • are reconstructed from the PWA. There is a notable discrepancy between the two for $m_{\overline{K}^\circ\phi} > 2.0$ GeV/c^2. One explanation for this disagreement is that the contributions from partial waves which were not included in the PWA ($J \geq 3$ or $L_o \geq 3$), may not be negligible for this high-mass region. Figure 11.10(b) displays the summed intensities of the natural spin-parity waves and Figure 11.11(a) displays the unnatural J^P wave sum. These two figures confirm what we have deduced from Fig. 11.9(a) in section 11.4.1; natural spin-parity states are prevailing in the region 2.0 $\sim$ 2.2 GeV/c^2. In this region, the natural J^P sum contributes more than 2/3 of the total cross section. In the region around 1.8 GeV/c^2, where the unnatural wave sum shows peaking, the contributions of unnatural and natural J^P waves are about equal. In the threshold region, the unnatural J^P sum is larger than the natural J^P mostly due to the 1^+ waves.

The natural J^P sum shows a broad enhancement around 2.0 GeV/c^2 (Fig 11.10(b)). This feature is seen in both 1^- and 2^+ wave sums(Figs. 11.10(c) and (d)). The total intensities of 1^- and 2^+ waves are about equal. Since moments with $L \geq 5$ are truncated because of low-statistics, we cannot study the $K_3^*(1780)$ state in this analysis.

Figure 11.10(d) shows that there is a bump around 2.0 GeV/c^2 in the $J^P = 2^+$ wave. This structure may be interpreted as $K_2^*(1980)$, which has been previously observed from the reactions $K^-p \rightarrow \overline{K}^\circ\pi^-p$[52] and $K^-p \rightarrow \overline{K}^\circ\pi^+\pi^-n$[46] in the E-135‡ experiment. Assuming that this is from a resonance production, it is fitted

‡According to the 'Review of Particle Properties'[37], these are the only two places where

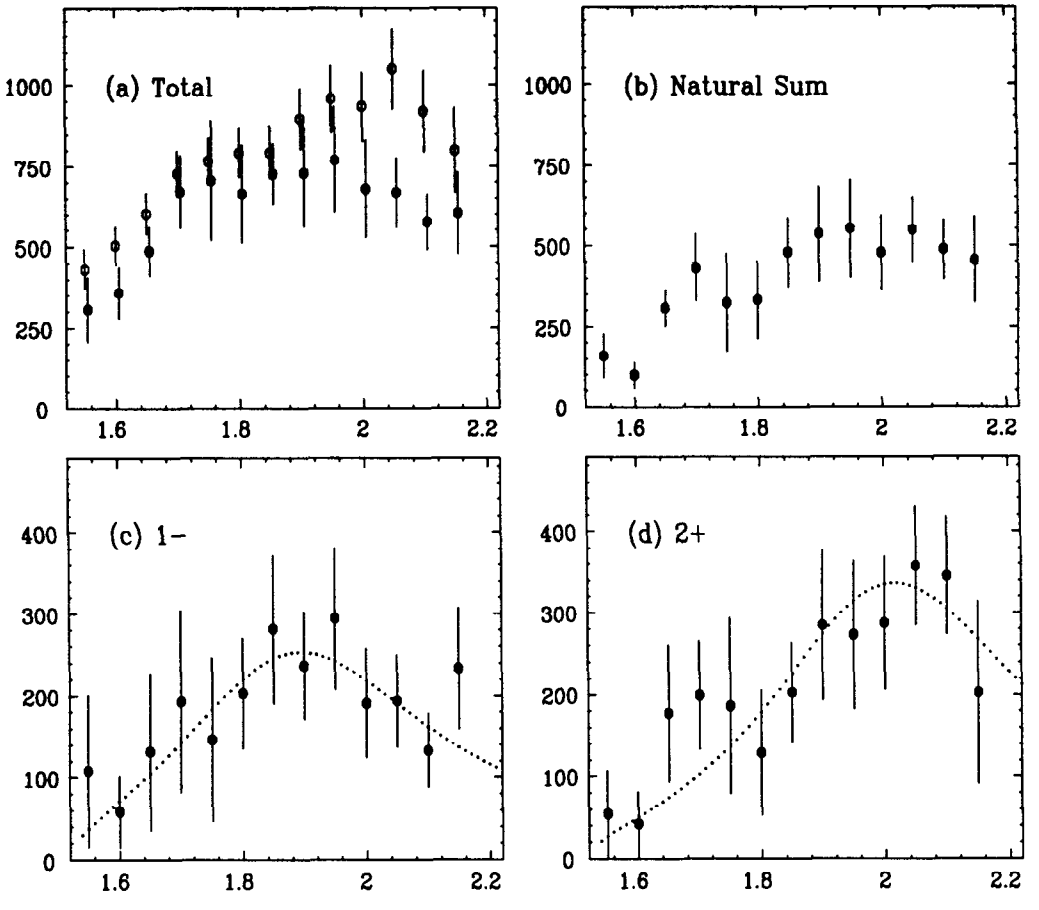

Figure 11.10: Decomposition of the $\overline{K}^\circ\phi$ mass spectrum into natural spin-parity (J^P) components: (a) the acceptance-corrected $\overline{K}^\circ\phi$ mass spectrum (o – mass spectrum from background subtraction; • – mass spectrum reconstructed from PWA); (b) sum of intensities of the natural J^P waves; (c) sum of intensities of the $J^P = 1^-$ waves; and (d) sum of intensities of the $J^P = 2^+$ waves.

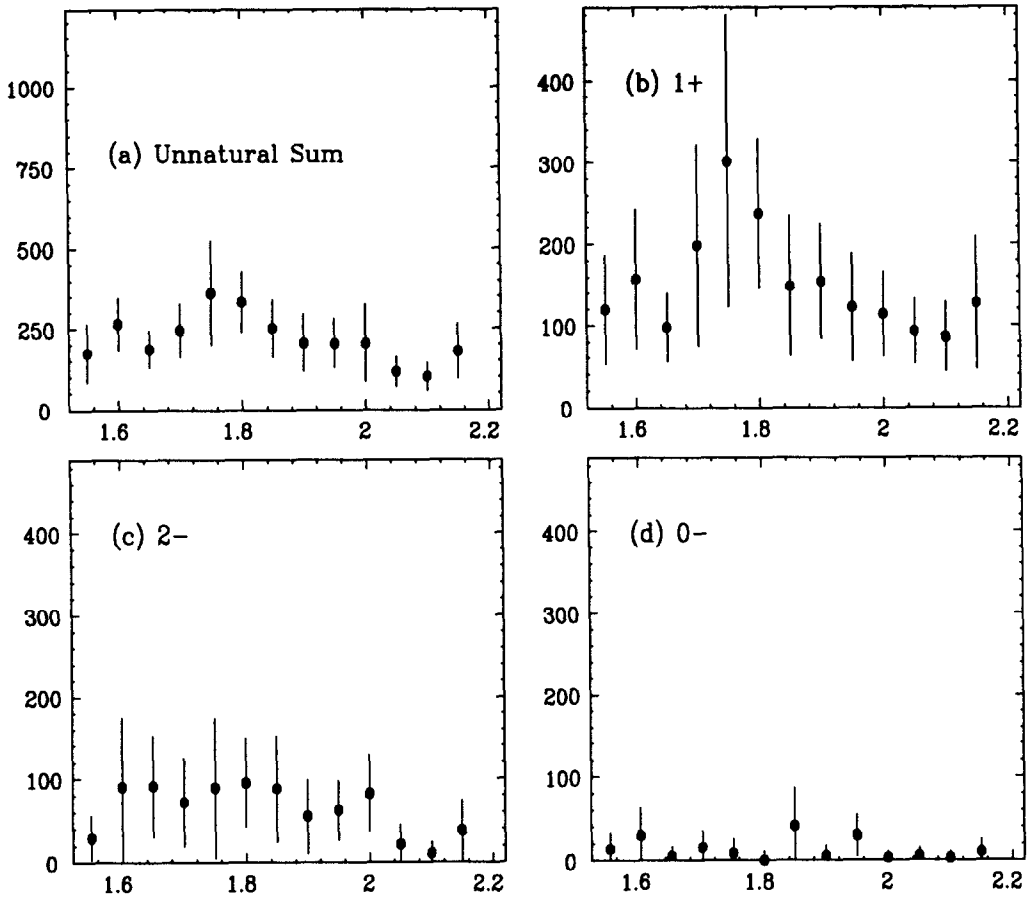

Figure 11.11: Decomposition of the $\overline{K}^\circ\phi$ mass spectrum into unnatural spin-parity (J^P) components: (a) sum of intensities of the unnatural J^P waves; (b) sum of intensities of the $J^P = 1^+$ waves; (c) sum of intensities of the $J^P = 2^-$ waves; and (d) sum of intensities of the $J^P = 0^-$ wave.

to a B-W resonance. The width is fixed to 0.39 GeV/c^2, which is an average (by Particle Data Group (PDG)[37]) of the previously measured values of $K_2^*(1980)$ width, while the mass is varied as a free parameter. The fitted value of mass is 2.01 ± 0.03 GeV/c^2. The error is only a MINUIT estimate and does not include any systematic sources, such as mass binning effects, moment truncations, etc. If these effects are considered, the fitted value is consistent with the $K_2^*(1980)$ mass, 1.975 ± 0.022 GeV/c^2. The dotted curve in the Fig. 11.10(d) represents the fitted resonance function.

The 1^- wave sum shows a bump around 1.9 GeV/c^2 (Fig. 11.10(c)). This is seen especially in the $|1^-0^+P\rangle$ wave which is the most prominent of the 1^- waves in the $\overline{K}^\circ\phi$ system. Assuming a resonance production, a Breit-Wigner fit to the 1^+ wave sum results in a mass of $\sim 1.91 \pm 0.04$ GeV/c^2 and width 0.5 ± 0.2 GeV/c^2 (MINUIT-estimated errors). The fit result is shown in Fig. 11.10(c) as a dotted curve. Although the 1^- wave is, along with 2^+, one of the two main contributions to the $\overline{K}^\circ\phi$ final states in the reaction $K^-p \to \overline{K}^\circ K^+K^-n$, we did not succeed in clearly understanding its resonance structure. Previous E-135 analyses of several reactions [42],[53],[52] have revealed that there is a $J^P = 1^-$ strange meson state at $\sim$ 1.7 GeV/c^2 ($K_1^*(1680)$). Compared with the mass of $K_1^*(1680)$, (1.714 ± 0.020 GeV/c^2 for PDG average; and 1.735 ± 0.022 GeV/c^2 from the E-135 $\overline{K}^\circ\pi^+\pi^-$ analysis[42]) the fitted mass is too high even considering the 100 MeV/c^2 mass binning. After all, it may not be $K_1^*(1680)$, but a $J^P = 1^-$ state of higher mass. In fact, there is an indication of the possible second radial excitation of the $K^*(892)$ at a mass around 2.05 GeV/c^2 in the reaction $K^-p \to K^-\pi^+n$.[53],[54]

In the unnatural J^P sum, there is a small enhancement around 1.8 GeV/c^2, especially in the $J^P = 1^+$ wave (Figs. 11.11(a) and (b)), but the signal is so small compared to the statistical uncertainty that it is difficult to make any conclusion from this data. It is interesting, however, to note that there are a few experiments that have observed a $J^P = 1^+$ strange meson state at $\sim$ 1.8 GeV/c^2[40],[55] or at $\sim$ 1.65 GeV/c^{2}Ref.[56]; all of these are classified as $K_1(1650)$ by the Particle Data

$K_2^*(1980)$ is observed.

Group[37].

Although the contribution of the 2^- waves to the total cross section is comparable to that of the 1^+ waves, the 2^- wave sum (Fig 11.11(c)) does not show any interesting structure. The 0^- wave sum is almost negligible in the entire region, which is consistent with what we have inferred in sec 11.4.1.

11.4.3 t'-dependent PWA of $\overline{K}^\circ\phi$

The purpose of studying the t'-dependence of $\overline{K}^\circ\phi$ system is similar to the $K\omega$ analysis discussed in sec 11.3.6. The difference, however, is in the production mechanism. The $\overline{K}^\circ\phi n$ state is likely to be produced by π exchange, while the $K^-\omega p$ state is produced mostly in diffractive scattering. Therefore, the t'-dependence of the $\overline{K}^\circ\phi$ system is expected to be different from that of the $K^-\omega$ system. In general, to a good approximation, the t'-distributions of $\overline{K}^\circ\phi$ partial waves can be characterized by an exponential function:

$$a(t') \propto e^{-bt'}. \tag{11.17}$$

The slope values of the exponents are then compared to other π-exchange reaction in the same experiment: e.g. the reaction $K^-p \to \overline{K}^\circ\pi^+\pi^-n$.

The t'-dependent PWA is performed over two broad, overlapping regions of $m_{K\phi}$: $1.6 \sim 2.0$ GeV/c^2 ('low $m_{K\phi}$ region') and $1.8 \sim 2.2$ GeV/c^2 ('high $m_{K\phi}$ region'). The low $m_{K\phi}$ region is concentrating on the 2^- production while the high $m_{K\phi}$ region is focusing on the 2^+. The 1^- state(s), which might well be considered in the low $m_{K\phi}$ region if it is from $K_1^*(1680)$ production, is analyzed in both regions since the 1^- enhancement in the mass spectrum was significant over both regions.

Figure 11.12 shows the t' distribution of 2^+, 1^-, and 2^- wave sums and the least-squares fit results to exponential functions. The fit result is summarized in Table 11.4. Figure 11.12(a) shows the t' dependence of the 2^- wave sum in the low $m_{K\phi}$ region. The fitted t' slope is 3.48 ± 0.8 (GeV/c)$^{-2}$. The t' dependence of the 2^+ wave sum is shown in Fig 11.12(b). The fitted t' slope is 8.55 ± 1.74 (GeV/c)$^{-2}$. The 1^- t' dependence is measured in both regions. The result of low $m_{\overline{K}^\circ\phi}$ region

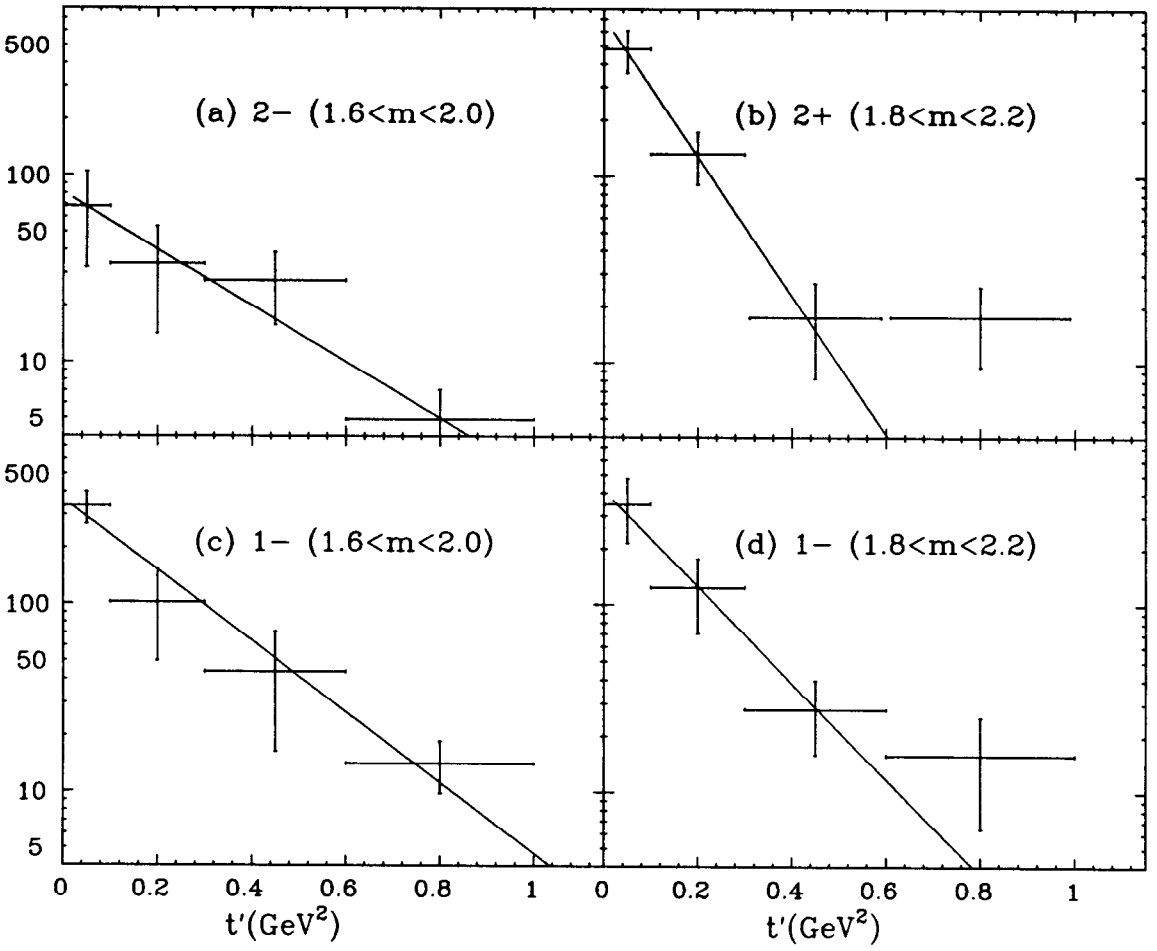

Figure 11.12: The t' dependence of the $\overline{K}^\circ\phi$ partial wave sums: (a) 2^- wave for $1.6 \leq m_{\overline{K}^\circ\phi} \leq 2.0$ GeV/c^2; (b) 2^+ wave for $1.8 \leq m_{\overline{K}^\circ\phi} \leq 2.2$ GeV/c^2; (c) 1^- wave for $1.6 \leq m_{\overline{K}^\circ\phi} \leq 2.0$ GeV/c^2; and (d) 1^- wave for $1.8 \leq m_{\overline{K}^\circ\phi} \leq 2.2$ GeV/c^2. The liens are the results of the fits described in the text.

Table 11.7: The t' slope parameters of the partial wave sums present in the $\overline{K}^\circ\phi$ system. The χ^2 values per degree of freedom of the least-squares fits are also listed.

J^P	$m_{K\phi}$ (GeV/c^2)	t' Slope (GeV/c^{-2})	χ^2/dof.
1^-	1.6 – 2.0	4.35 ± 0.62	1.8/2
1^-	1.8 – 2.2	5.91 ± 1.71	1.7/2
2^-	1.6 – 2.0	3.48 ± 0.81	0.9/2
2^+	1.8 – 2.2	8.55 ± 1.74	4.3/2

analysis is shown in Fig 11.12(c). The fitted t' slope is 4.35 ± 0.62 (GeV/c)$^{-2}$. On the other hand, Fig 11.12(d) shows the t' dependence of 1^- in the high $m_{\overline{K}^\circ\phi}$ region. The fitted t' slope is 5.91 ± 1.71 (GeV/c)$^{-2}$.

The t' slope of the 2^- wave sum is the shallowest of all. This shallow t' slope indicates that the 2^- wave is not dominantly produced by π-exchange, indeed, parity conservation forbids it. No such selection rule applies to 1^- or 2^+ waves. The t' slope of the 2^+ wave sum is the steepest, which indicates that 2^+ is produced mostly by π-exchange. The t' slopes of the 1^- wave sum take intermediate values.

Chapter 12

Spectroscopy and Conclusion

In this chapter, the results obtained in chapters 10 and 11 are interpreted in terms of their impact on the spectroscopy of the strange meson system. Section 12.1 describes new measurements of decay branching fractions. By comparing the results on 2^+ and 3^- waves with other E-135 analyses of different channels, branching fractions are measured and compared with predictions based on flavor SU(3). In section 12.2, the new result on the possible doublet structure of 2^- is discussed in comparison with phenomenological models that predict the mass splitting, the decay branching ratios, etc. Section 12.3 concludes the second part of the thesis by summarizing the results and suggesting future studies of a similar kind.

12.1 Branching Fractions and SU(3)

12.1.1 $K_2^*(1430) \rightarrow K\omega$

The decay of $K_2^*(1430) \rightarrow K\omega$ has been observed in a few previous experiments[57],[58],[59]. In estimating the $K_2^*(1430)$ content of the $K\omega$ final state, they all simply counted the number of events in the relevant kinematic regions without considering any possibility of contamination from underlying non-2^+ states. However, as shown in the analyses of high-statistics data using PWA, there usually is substantial contamination from other states: for example, in the E-135 analysis of the $\overline{K}^\circ\pi^+\pi^-n$

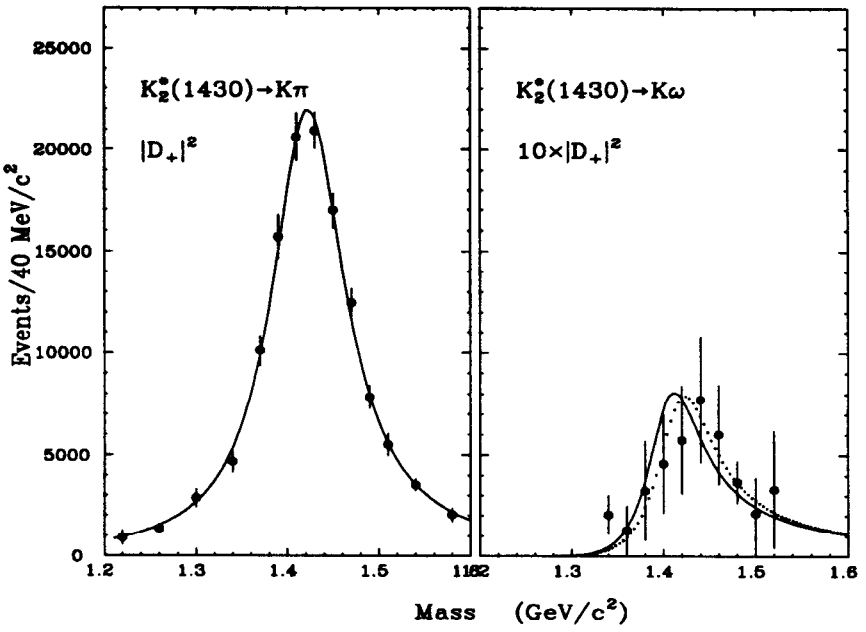

Figure 12.1: $K_2^*(1430)$ in $K\pi$, $K\omega$ channels. The $K\omega$ signal is multiplied by 10 to make a comparison easier. The Breit-Wigner fits with a fixed $K_2^*(1430)$ mass are shown in solid curves while the dotted curve represent the free-mass fit for $K\omega$.

channel[42], a substantial $K^*(1410)$ signal is seen in the kinematical region of $K_2^*(1430)$ in addition to the $K_2^*(1430)$ itself. This thesis describes for the first time a significant measurement of the branching fraction of $K_2^*(1430) \to K\omega$ decay, by observation of a statistically significant $K_2^*(1430)$ signal in the $J^P = 2^+$ $K\omega$ partial wave.

The $K\omega$ result is compared with the previous E-135 analyses of two diffractive reactions: $K^-p \to \overline{K}^0\pi^0 p$[52] and $K^-p \to K^-\eta p$[43]. In E-135, these reactions have been analyzed with the largest data sets ever achieved thus giving the most accurate measurements of the differential cross sections. In addition, their precise meaning, normalization, systematic uncertainties, etc. are well-understood as they come from the same experiment and have the same diffractive production mecha-

nism. In the case of $K\eta p$, however, no $K_2^*(1430)$ signal is observed after PWA. It is essentially forbidden in SU(3)[43]. Therefore only the $\overline{K}^\circ\pi^- p$ result is used for $K_2^*(1430)$ branching fraction calculation.

The Particle Data Group defines the branching fraction of a resonance as the ratio of the partial widths for the two final states at the peak of the resonance[37], which is equivalent to the ratio of the corresponding differential cross sections at the peak in a production experiment. These peak values are determined from the resonance fits to the differential cross sections which remove any background contributions and binning effects.

The $K^-\omega$ data is corrected for the unseen decays of ω, as the partial width of $\omega \to \pi^+\pi^-\pi^0$ decay is 89% of the total. Similarly, the $\overline{K}^\circ\pi^-$ data is corrected for the branching fraction of $\overline{K}^\circ \to \pi^+\pi^-$ and the K_S°-K_L° ratio. The $\overline{K}^\circ\pi^-$ data is further corrected for the isospin of $K\pi$ – $\frac{2}{3}$ of the negatively charged $K\pi$ is seen in $\overline{K}^\circ\pi^-$. Moreover, a correction for the t'-dependence is made by integrating the signals over $0.0 \leq t' \leq 10.0$ (GeV/c)^2.

Figure 12.1 shows the intensities of the 2^+ wave produced by a natural spin-parity exchange, which corresponds to 2^+1^+D in $K\omega$ PWA and is denoted as D_+. Both channels are corrected as described above. The peak cross sections are compared to give the following ratio of branching ratios:

$$\frac{\Gamma(K_2^*(1430) \to K\omega)}{\Gamma(K_2^*(1430) \to K\pi)} = 3.6 \pm 0.6\ \%. \tag{12.1}$$

Table 12.1 shows the relative decay amplitudes of $K_2^*(1430)$ into (pseudoscalar) + (vector) final states predicted by flavor SU(3). An ideal mixing between the singlet ϕ_1 and the octet ϕ_8 is assumed such that

$$\begin{aligned} \phi_1 &= \frac{1}{\sqrt{3}}(u\bar{u} + d\bar{d} + s\bar{s}) = \sqrt{\frac{2}{3}}\omega + \frac{1}{\sqrt{3}}\phi \\ \phi_8 &= \frac{1}{\sqrt{6}}(u\bar{u} + d\bar{d} - 2s\bar{s}) = \frac{1}{\sqrt{3}}\omega - \sqrt{\frac{2}{3}}\phi \end{aligned}$$

Including the phase-space factor, we obtain the SU(3) prediction of the $K_2^*(1430)$

Table 12.1: The SU(3) prediction of relative decay amplitudes of $K_2^*(1430)$ and $K_3^*(1780)$ into (pseudoscalar)+(vector) final states. An ideal mixing between ϕ_1 and ϕ_8 is assumed.

Initial State	Final State	Relative Amplitude	Initial State	Final State	Relative Amplitude
$K_2^*(1430)$	$K\rho$	$-\sqrt{3/2}$	$K_3^*(1780)$	$K\rho$	$\sqrt{3/2}$
	$K^*\pi$	$-\sqrt{3/2}$		$K^*\pi$	$-\sqrt{3/2}$
	$K\omega$	$\sqrt{1/2}$		$K\omega$	$\sqrt{1/2}$
	$K\phi$	no phase space		$K\phi$	1/3

decay branching ratios as

$$\frac{\Gamma(K_2^*(1430) \to K\omega)}{\Gamma(K_2^*(1430) \to K\rho)} = \frac{1}{3}\left(\frac{q_{K\omega}}{q_{K\rho}}\right)^5 = 0.27$$

$$\frac{\Gamma(K_2^*(1430) \to K\omega)}{\Gamma(K_2^*(1430) \to K^*\pi)} = \frac{1}{3}\left(\frac{q_{K\omega}}{q_{K^*\pi}}\right)^5 = 0.08$$

The branching ratios of $K\rho$ and $K^*\pi$ final states with respect to $K\pi$ were measured in the previous E-135 analysis of the reaction $K^-p \to \overline{K}^0\pi^+\pi^-n$[46]. However, those measurements were based on the old E-132 analysis of the reaction $K^-p \to K^-\pi^+n$[60]. Since then, the $K^-\pi^+n$ channel from E-135 has been analyzed[53] and the $K\pi$ elasticity values were updated as listed in Table 12.2. Both the original and the updated branching ratios are listed in the table as well.

The relative branching ratios between the $K\omega, K\rho$ and $K^*\pi$ final states are then computed and compared with the SU(3) prediction. The result for $K_2^*(1430)$ is summarized in Table 12.3

Table 12.2: The updated branching ratios ($K\rho/K\pi$) from E-135 charge-exchange reactions

$K\rho, K^*\pi$ from E-135 / $K\pi$ from E-132			$K\rho, K^*\pi$ from E-135 / $K\pi$ from E-135		
$\epsilon(K\pi)$	BR($K\rho/K\pi$)	BR($K^*\pi/K\pi$)	$\epsilon(K\pi)$	BR($K\rho/K\pi$)	BR($K^*\pi/K\pi$)
2^+ $K_2^*(1430)$					
0.43 ± 0.01	0.09 ± 0.02	0.33 ± 0.07	0.485 ± 0.006	0.08 ± 0.02	0.29 ± 0.07
3^- $K_3^*(1780)$					
0.16 ± 0.01	0.69 ± 0.22	0.46 ± 0.12	0.187 ± 0.008	0.59 ± 0.19	0.39 ± 0.10

Table 12.3: The $K_2^*(1430)$ branching ratios of $K\omega$ final state with respect to $K\rho$ and $K^*\pi$ final states: both measured and SU(3) predicted values are listed.

2^+ $K_2^*(1430)$		
	Measured	SU(3) Predicted
BR($K\omega/K\rho$)	$0.45^{+0.25}_{-0.15}$	0.27
BR($K\omega/K^*\pi$)	$0.12^{+0.07}_{-0.04}$	0.08
BR($K\rho/K^*\pi$)	$0.28^{+0.17}_{-0.11}$	0.30

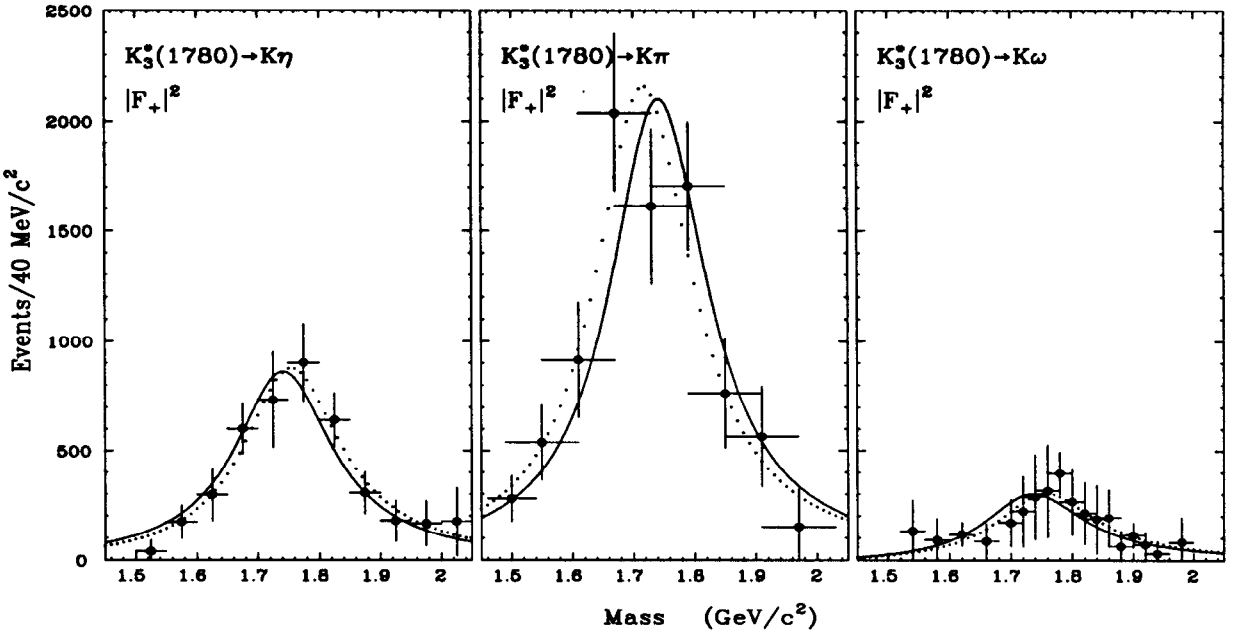

Figure 12.2: $K_3^*(1780)$ in $K\eta, K\pi$ and $K\omega$ channels. The Breit-Wigner fits with a fixed $K_3^*(1780)$ mass are shown in solid curves while the dotted curves represent the free-mass fit for each state.

12.1.2 $K_3^*(1780) \to K\omega$

The decay of $K_3^*(1780)$ into the $K\omega$ final state is observed for the first time and the branching fraction of this decay is measured. The procedure is very similar to the $K_2^*(1430)$ case. Figure 12.2 shows the intensities of the 3^- wave produced by natural spin-parity exchange, which is 3^-1^+F wave in $K\omega$ PWA and the F_+ in the $K\pi$ and $K\eta$ analyses. The following branching ratio is obtained by comparing the peak cross sections.

$$\frac{\Gamma(K_3^*(1780) \to K\omega)}{\Gamma(K_3^*(1780) \to K\pi)} = 15 \pm 3\ \%. \tag{12.2}$$

The flavor SU(3) predicts the following relative branching ratios of $K_3^*(1780)$

Table 12.4: The $K_3^*(1780)$ branching ratios of $K\omega$ final state with respect to $K\rho$ and $K^*\pi$ final states: both measured and SU(3) predicted values are listed.

3^- $K_3^*(1780)$		
	Measured	SU(3) Predicted
BR($K\omega/K\rho$)	$0.25^{+0.2}_{-0.1}$	0.33
BR($K\omega/K^*\pi$)	$0.38^{+0.2}_{-0.1}$	0.22
BR($K\rho/K^*\pi$)	$1.51^{+1.2}_{-0.7}$	0.66

decays:

$$\frac{\Gamma(K_3^*(1780) \to K\omega)}{\Gamma(K_3^*(1780) \to K\rho)} = \frac{1}{3}\left(\frac{q_{K\omega}}{q_{K\rho}}\right)^7 = 0.30$$
$$\frac{\Gamma(K_3^*(1780) \to K\omega)}{\Gamma(K_3^*(1780) \to K^*\pi)} = \frac{1}{3}\left(\frac{q_{K\omega}}{q_{K^*\pi}}\right)^7 = 0.20\ .$$

Using the values from Table 12.2 and Eq. 12.2, the relative branching ratios between the $K\omega, K\rho$ and $K^*\pi$ final states are computed and compared with the SU(3) prediction. The results are summarized in Table 12.4

12.2 $J^P = 2^-$ state

As described in Section 11.3.3, the partial wave analysis of the $K\omega$ system has provided very good evidence for two $J^P = 2^-$ strange meson states with masses around $\sim$ 1773 and $\sim$ 1816 MeV/c^2. These states are most naturally interpreted in the context of the quark model as the $^1D_2$ and $^3D_2$ ground states. The singlet/triplet assignment of these states cannot be determined, since the strange mesons are not eigenstates of charge conjugation. It follows from this that the observed states may even be mixtures of the singlet and triplet states, as is the case for the $K_1(1270)$ and $K_1(1400)$. Nevertheless, the observation of two 2^- states

means that the $q\bar{q}$ ground state D-wave level structure is complete in the strange meson sector, the only such sector for which this is the case.

It is interesting to note that Godfrey and Isgur[41] predict masses of 1780 and 1810 MeV/c^2 for the unmixed $^1D_2$ and $^3D_2$ states respectively, values which are remarkably close to those obtained in the present analysis. Kokowski and Isgur[61] also predicts that the pure states are essentially decoupled, with the lower mass state decaying mostly to P-wave and the higher-mass state to F-wave. Table 12.5 shows the coupling strengths obtained from the fit. For the helicity-1 states produced by a natural spin-parity exchange, the $K_2(1816)$ couples most strongly to F-wave (2^-1^+F), which is at least consistent with the Kokowski and Isgur model. Production of $K_2(1773)$ with helicity-1 is so small that little can be said regarding this state. On the other hand, the 2^- states of helicity-0, produced by natural spin-parity exchange, couple preferentially to P-wave $K\omega$ for both the higher ($K_2(1816)$) and the lower ($K_2(1773)$) mass state. It should be noted, however, that the interpretation of the data of Table 12.5 is complicated by the fact that the quoted cross section value for each state includes the effect of the corresponding production amplitude, which may well differ significantly from state to state.

12.3 Conclusion

The partial wave analysis of a high-statistics sample of $K^-\omega p$ events provided several new results in the $q\bar{q}$ spectroscopy of strange meson sector.

For the first time, very good evidence is found for the existence of two $J^P = 2^-$ strange meson resonances in the old $K_2(1770)$ region. With this observation, the Grotrian plot of the strange meson sector is updated as shown in Fig 12.3.

In addition, the signals of 2^+ and 3^- states are observed in $K\omega$ system. The relevant branching ratios are calculated and compared with the flavor SU(3) predictions. The results are, in general, agree with SU(3) with appropriate phase-space factors considered, although the experimental uncertainties are quite large.

There are other waves that are seen in PWA but didn't show clear resonance

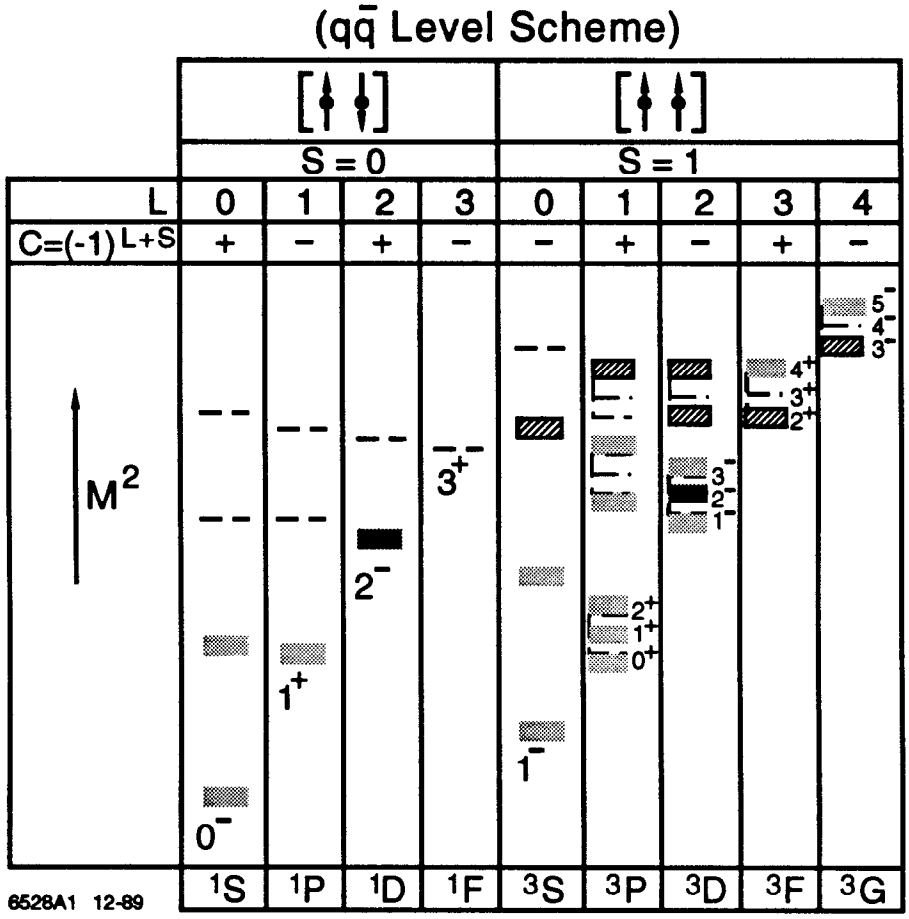

Figure 12.3: The $q\bar{q}$ level scheme of strange mesons. The states indicated by shading are clearly observed, and have generally been confirmed; in a few cases there are possible classification ambiguities. The states indicated by diagonal lines are more speculative and require confirmation. The two 2^- states are shown as dark rectangles.

Table 12.5: The strengths of the two $J^P = 2^-$ strange states, $K_2(1773)$ and $K_2(1816)$, in the partial wave amplitudes. The numbers represent the effective cross section (in μb) of each state contributing to the corresponding partial wave.

wave	$K_2(1773)$ (μb)	$K_2(1816)$ (μb)
2^-0^+P	7.6 ± 1.2	6.4 ± 1.4
2^-0^+F	1.1 ± 0.5	0.2 ± 0.2
2^-1^+P	small, no B-W fit	
2^-1^+F	0 ± 0.02	0.8 ± 0.4

structures. The most controversial state in $K\omega$ is $J^P = 1^+$. The 1^+ partial waves are dominant in the threshold region and show substantial contributions near 1.7 GeV/c^2 region, but their structures are difficult to explain.

From the PWA of the $\overline{K}^\circ\phi$ system, it is found that the two largest contributions to the $\overline{K}^\circ\phi$ cross-section in the reaction $K^-p \to \overline{K}^\circ\phi n$ are from $J^P = 1^-$ and 2^+ waves. Each wave appeared as a broad bump around 1.9 GeV/c^2 region but neither showed a clear evidence for a resonance. The 2^+ signal is consistent with $K_2^*(1980)$ if the large mass binning (100 MeV/c^2) is considered but the 1^- wave is not fitted well with the resonance parameters of $K_1^*(1680)$.

Although a partial wave analysis is a very powerful tool for uncovering the spin-parity contents of the underlying states, it demands a very large data sample. This is especially true for a PWA based on joint-decay moments, as used in both $K\omega$ and $\overline{K}^\circ\phi$ analyses, which involves far more parameters than the 2-body PWA. Note that in the PWA of the $K\omega$ system, 89 constraints were fitted using 44 free parameters. It turned out that the size of E-135 $K\omega$ sample, although at least 25 times larger than that of any other experiment, was barely enough to extract some

information from PWA. It is not surprising that no clear resonance structures were extracted from PWA of $\overline{K}^{\circ}\phi$ system which had far less than 10^4 total events.

In the future, two orders of magnitude increase in data size from E-135 is needed to clarify the many questions left unanswered in this thesis. It should also be noted that LASS was not equipped with a photon detector which could have greatly improved the measurement of neutral particles, such as n or π^0. With these improvements, if realized, future research of a similar kind could further extend our knowledge of meson spectroscopy and may lead to better understanding of the fundamental principles governing the dynamics of the strong interaction applied to mesons.

Appendix A

The Partial waves

In the Table A.1, the partial waves that might be realized in the $K^-\omega$ or $\overline{K}^\circ\phi$ systems are listed up to $J \leq 3$ and $\Lambda \leq 1$. The experimentally observed meson states with $m \leq 2.0$ GeV/c^2 are also indicated next to the corresponding waves. Those which are cited in the Particle Data Book to have decay modes into $K\omega$ or $K\phi$ are also indicated.

Table A.1: The possible waves in $K\omega$, $K\phi$ systems.

$J^P\Lambda^\eta L_o$	PDG listed	PDG $K\omega$	PDG $K\phi$
0^-0^+P	$K(1460), K(1830)$		$K(1830)$
1^+0^+S, 1^+0^+D 1^+1^-S, 1^+1^-D 1^+1^+S, 1^+1^+D	$K_1(1270), K_1(1400), K_1(1650)$	$K_1(1270), K_1(1400)$	$K_1(1650)$
2^-0^+P, 2^-0^+F 2^-1^-P, 2^-1^-F 2^-1^+P, 2^-1^+F	$K_2(1580), K_2(1770)$	$K_2(1770)$	$K_2(1770)$
3^+0^+D, 3^+0^+G 3^+1^-D, 3^+1^-G 3^+1^+D, 3^+1^+G			
1^-0^-P 1^-1^-P 1^-1^+P	$K^*(1370), K^*(1680)$		
2^+0^-D 2^+1^+D 2^+1^-D	$K_2^*(1430), K_2^*(1980)$	$K_2^*(1430)$	
3^-0^-F 3^-1^+F 3^-1^-F	$K_3^*(1780)$		

Appendix B

The moment-amplitude relations

The explicit forms of the measured double moments $H(LMlm)$ in terms of the waves are listed. Since $J^P = 3^+$ waves are not used in the analysis, their contributions to the moments are not included. Given the partial wave amplitudes, the moments are computed by summing the listed terms composed of three parts; the coefficient, the amplitude of a wave, and the complex-conjugated amplitude of the coupled wave.

```
H( 0 0 0 0)=
 1.00000 (0-0+P) (0-0+P)*
 1.00000 (1+0+S) (1+0+S)*
 1.00000 (1+1+S) (1+1+S)*
 1.00000 (1+1-S) (1+1-S)*
 1.00000 (1-0-P) (1-0-P)*
 1.00000 (1-1+P) (1-1+P)*
 1.00000 (1-1-P) (1-1-P)*
 1.00000 (1+0+D) (1+0+D)*
 1.00000 (1+1+D) (1+1+D)*
 1.00000 (1+1-D) (1+1-D)*
 1.00000 (2+0-D) (2+0-D)*
 1.00000 (2+1+D) (2+1+D)*
 1.00000 (2+1-D) (2+1-D)*
 1.00000 (2-0+P) (2-0+P)*
 1.00000 (2-1+P) (2-1+P)*
 1.00000 (2-1-P) (2-1-P)*
 1.00000 (3-0-F) (3-0-F)*
 1.00000 (3-1+F) (3-1+F)*
 1.00000 (3-1-F) (3-1-F)*
 1.00000 (2-0+F) (2-0+F)*
 1.00000 (2-1+F) (2-1+F)*
 1.00000 (2-1-F) (2-1-F)*


H( 0 0 2 0)=
 0.40000 (0-0+P) (0-0+P)*
-0.28284 (1+0+S) (1+0+D)*
-0.28284 (1+1+S) (1+1+D)*
-0.28284 (1+1-S) (1+1-D)*
-0.20000 (1-0-P) (1-0-P)*
-0.20000 (1-1+P) (1-1+P)*
-0.20000 (1-1-P) (1-1-P)*
-0.28284 (1+0+D) (1+0+S)*
 0.20000 (1+0+D) (1+0+D)*
-0.28284 (1+1+D) (1+1+S)*
 0.20000 (1+1+D) (1+1+D)*
-0.28284 (1+1-D) (1+1-S)*
 0.20000 (1+1-D) (1+1-D)*
-0.20000 (2+0-D) (2+0-D)*
-0.20000 (2+1+D) (2+1+D)*
-0.20000 (2+1-D) (2+1-D)*
 0.04000 (2-0+P) (2-0+P)*
-0.29394 (2-0+P) (2-0+F)*
 0.04000 (2-1+P) (2-1+P)*
-0.29394 (2-1+P) (2-1+F)*
 0.04000 (2-1-P) (2-1-P)*
-0.29394 (2-1-P) (2-1-F)*
-0.20000 (3-0-F) (3-0-F)*
-0.20000 (3-1+F) (3-1+F)*
-0.20000 (3-1-F) (3-1-F)*
-0.29394 (2-0+F) (2-0+P)*
 0.16000 (2-0+F) (2-0+F)*
-0.29394 (2-1+F) (2-1+P)*
 0.16000 (2-1+F) (2-1+F)*
-0.29394 (2-1-F) (2-1-P)*
 0.16000 (2-1-F) (2-1-F)*


H( 1 0 0 0)=
-0.33333 (0-0+P) (1+0+S)*
 0.47140 (0-0+P) (1+0+D)*
-0.33333 (1+0+S) (0-0+P)*
 0.47140 (1+0+S) (2-0+P)*
-0.40825 (1+1+S) (1-1+P)*
 0.40825 (1+1+S) (2-1+P)*
-0.40825 (1+1-S) (1-1-P)*
 0.40825 (1+1-S) (2-1-P)*
 0.44721 (1-0-P) (2+0-D)*
-0.40825 (1-1+P) (1+1+S)*
-0.28868 (1-1+P) (1+1+D)*
 0.38730 (1-1+P) (2+1+D)*
-0.40825 (1-1-P) (1+1-S)*
-0.28868 (1-1-P) (1+1-D)*
 0.38730 (1-1-P) (2+1-D)*
 0.47140 (1+0+D) (0-0+P)*
-0.06667 (1+0+D) (2-0+P)*
 0.48990 (1+0+D) (2-0+F)*
-0.28868 (1+1+D) (1-1+P)*
-0.05774 (1+1+D) (2-1+P)*
 0.42426 (1+1+D) (2-1+F)*
-0.28868 (1+1-D) (1-1-P)*
-0.05774 (1+1-D) (2-1-P)*
 0.42426 (1+1-D) (2-1-F)*
 0.44721 (2+0-D) (1-0-P)*
 0.47809 (2+0-D) (3-0-F)*
 0.38730 (2+1+D) (1-1+P)*
-0.12910 (2+1+D) (2-1+P)*
 0.45075 (2+1+D) (3-1+F)*
-0.10541 (2+1+D) (2-1+F)*
 0.38730 (2+1-D) (1-1-P)*
-0.12910 (2+1-D) (2-1-P)*
 0.45075 (2+1-D) (3-1-F)*
-0.10541 (2+1-D) (2-1-F)*
 0.47140 (2-0+P) (1+0+S)*
-0.06667 (2-0+P) (1+0+D)*
 0.40825 (2-1+P) (1+1+S)*
-0.05774 (2-1+P) (1+1+D)*
-0.12910 (2-1+P) (2+1+D)*
 0.40825 (2-1-P) (1+1-S)*
-0.05774 (2-1-P) (1+1-D)*
-0.12910 (2-1-P) (2+1-D)*
 0.47809 (3-0-F) (2+0-D)*
 0.45075 (3-1+F) (2+1+D)*
 0.45075 (3-1-F) (2+1-D)*
 0.48990 (2-0+F) (1+0+D)*
 0.42426 (2-1+F) (1+1+D)*
-0.10541 (2-1+F) (2+1+D)*
 0.42426 (2-1-F) (1+1-D)*
-0.10541 (2-1-F) (2+1-D)*


H( 1 0 2 0)=
-0.13333 (0-0+P) (1+0+S)*
 0.18856 (0-0+P) (1+0+D)*
-0.13333 (1+0+S) (0-0+P)*
 0.01886 (1+0+S) (2-0+P)*
-0.13856 (1+0+S) (2-0+F)*
 0.08165 (1+1+S) (1-1+P)*
 0.01633 (1+1+S) (2-1+P)*
-0.12000 (1+1+S) (2-1+F)*
 0.08165 (1+1-S) (1-1-P)*
 0.01633 (1+1-S) (2-1-P)*
-0.12000 (1+1-S) (2-1-F)*
-0.08944 (1-0-P) (2+0-D)*
 0.08165 (1-1+P) (1+1+S)*
 0.05774 (1-1+P) (1+1+D)*
-0.07746 (1-1+P) (2+1+D)*
 0.08165 (1-1-P) (1+1-S)*
 0.05774 (1-1-P) (1+1-D)*
-0.07746 (1-1-P) (2+1-D)*
 0.18856 (1+0+D) (0-0+P)*
-0.14667 (1+0+D) (2-0+P)*
 0.09798 (1+0+D) (2-0+F)*
 0.05774 (1+1+D) (1-1+P)*
-0.12702 (1+1+D) (2-1+P)*
 0.08485 (1+1+D) (2-1+F)*
 0.05774 (1+1-D) (1-1-P)*
-0.12702 (1+1-D) (2-1-P)*
 0.08485 (1+1-D) (2-1-F)*
-0.08944 (2+0-D) (1-0-P)*
-0.09562 (2+0-D) (3-0-F)*
-0.07746 (2+1+D) (1-1+P)*
 0.02582 (2+1+D) (2-1+P)*
-0.09015 (2+1+D) (3-1+F)*
 0.02108 (2+1+D) (2-1+F)*
-0.07746 (2+1-D) (1-1-P)*
 0.02582 (2+1-D) (2-1-P)*
-0.09015 (2+1-D) (3-1-F)*
 0.02108 (2+1-D) (2-1-F)*
 0.01886 (2-0+P) (1+0+S)*
-0.14667 (2-0+P) (1+0+D)*
 0.01633 (2-1+P) (1+1+S)*
-0.12702 (2-1+P) (1+1+D)*
 0.02582 (2-1+P) (2+1+D)*
 0.01633 (2-1-P) (1+1-S)*
-0.12702 (2-1-P) (1+1-D)*
 0.02582 (2-1-P) (2+1-D)*
-0.09562 (3-0-F) (2+0-D)*
-0.09015 (3-1+F) (2+1+D)*
-0.09015 (3-1-F) (2+1-D)*
-0.13856 (2-0+F) (1+0+S)*
 0.09798 (2-0+F) (1+0+D)*
-0.12000 (2-1+F) (1+1+S)*
 0.08485 (2-1+F) (1+1+D)*
 0.02108 (2-1+F) (2+1+D)*
-0.12000 (2-1-F) (1+1-S)*
 0.08485 (2-1-F) (1+1-D)*
 0.02108 (2-1-F) (2+1-D)*


H( 1 0 2 1)=
-0.11547 (0-0+P) (1+0+S)*
-0.08165 (0-0+P) (1+0+D)*
-0.11547 (1+0+S) (0-0+P)*
 0.01633 (1+0+S) (2-0+P)*
 0.08000 (1+0+S) (2-0+F)*
 0.07071 (1+1+S) (1-1+P)*
 0.01414 (1+1+S) (2-1+P)*
 0.06928 (1+1+S) (2-1+F)*
 0.07071 (1+1-S) (1-1-P)*
 0.01414 (1+1-S) (2-1-P)*
 0.06928 (1+1-S) (2-1-F)*
 0.07071 (1-1+P) (1+1+S)*
-0.10000 (1-1+P) (1+1+D)*
 0.07071 (1-1-P) (1+1-S)*
-0.10000 (1-1-P) (1+1-D)*
-0.08165 (1+0+D) (0-0+P)*
-0.09238 (1+0+D) (2-0+P)*
-0.02828 (1+0+D) (2-0+F)*
-0.10000 (1+1+D) (1-1+P)*
-0.08000 (1+1+D) (2-1+P)*
-0.02449 (1+1+D) (2-1+F)*
-0.10000 (1+1-D) (1-1-P)*
-0.08000 (1+1-D) (2-1-P)*
-0.02449 (1+1-D) (2-1-F)*
 0.04472 (2+1+D) (2-1+P)*
-0.05477 (2+1+D) (2-1+F)*
 0.04472 (2+1-D) (2-1-P)*
-0.05477 (2+1-D) (2-1-F)*
 0.01633 (2-0+P) (1+0+S)*
-0.09238 (2-0+P) (1+0+D)*
 0.01414 (2-1+P) (1+1+S)*
-0.08000 (2-1+P) (1+1+D)*
 0.04472 (2-1+P) (2+1+D)*
 0.01414 (2-1-P) (1+1-S)*
-0.08000 (2-1-P) (1+1-D)*
 0.04472 (2-1-P) (2+1-D)*
 0.08000 (2-0+F) (1+0+S)*
-0.02828 (2-0+F) (1+0+D)*
 0.06928 (2-1+F) (1+1+S)*
-0.02449 (2-1+F) (1+1+D)*
-0.05477 (2-1+F) (2+1+D)*
 0.06928 (2-1-F) (1+1-S)*
-0.02449 (2-1-F) (1+1-D)*
-0.05477 (2-1-F) (2+1-D)*


H( 1 1 0 0)=
-0.23570 (0-0+P) (1+1+S)*
 0.33333 (0-0+P) (1+1+D)*
 0.28868 (1+0+S) (1-1+P)*
 0.28868 (1+0+S) (2-1+P)*
-0.23570 (1+1+S) (0-0+P)*
-0.16667 (1+1+S) (2-0+P)*
 0.28868 (1+1-S) (1-0-P)*
 0.28868 (1-0-P) (1+1-S)*
 0.20412 (1-0-P) (1+1-D)*
 0.27386 (1-0-P) (2+1-D)*
 0.28868 (1-1+P) (1+0+S)*
 0.20412 (1-1+P) (1+0+D)*
-0.15811 (1-1-P) (2+0-D)*
 0.20412 (1+0+D) (1-1+P)*
-0.04082 (1+0+D) (2-1+P)*
 0.30000 (1+0+D) (2-1+F)*
 0.33333 (1+1+D) (0-0+P)*
 0.02357 (1+1+D) (2-0+P)*
-0.17321 (1+1+D) (2-0+F)*
 0.20412 (1+1-D) (1-0-P)*
-0.15811 (2+0-D) (1-1-P)*
 0.15811 (2+0-D) (2-1-P)*
```

```
 0.27603 (2+0-D) (3-1-F)*
 0.12910 (2+0-D) (2-1-F)*
 0.15811 (2+1+D) (2-0+P)*
 0.12910 (2+1+D) (2-0+F)*
 0.27386 (2+1-D) (1-0-P)*
-0.19518 (2+1-D) (3-0-F)*
-0.16667 (2-0+P) (1+1+S)*
 0.02357 (2-0+P) (1+1+D)*
 0.15811 (2-0+P) (2+1+D)*
 0.28868 (2-1+P) (1+0+S)*
-0.04082 (2-1+P) (1+0+D)*
 0.15811 (2-1-P) (2+0-D)*
-0.19518 (3-0-F) (2+1-D)*
 0.27603 (3-1-F) (2+0-D)*
-0.17321 (2-0+F) (1+1+D)*
 0.12910 (2-0+F) (2+1+D)*
 0.30000 (2-1+F) (1+0+D)*
 0.12910 (2-1-F) (2+0-D)*


H( 1 1 2-1)=
-0.08165 (0-0+P) (1+1+S)*
-0.10000 (0-0+P) (1-1+P)*
-0.05774 (0-0+P) (1+1+D)*
-0.05000 (1+0+S) (1-1+P)*
-0.08660 (1+0+S) (1+1+D)*
 0.03873 (1+0+S) (2+1+D)*
 0.01000 (1+0+S) (2-1+P)*
 0.04899 (1+0+S) (2-1+F)*
-0.08165 (1+1+S) (0-0+P)*
 0.08660 (1+1+S) (1+0+D)*
-0.00577 (1+1+S) (2-0+P)*
-0.02828 (1+1+S) (2-0+F)*
-0.05000 (1+1-S) (1-0-P)*
 0.02236 (1+1-S) (2+0-D)*
-0.05000 (1-0-P) (1+1-S)*
 0.07071 (1-0-P) (1+1-D)*
 0.02449 (1-0-P) (2-1-P)*
-0.03000 (1-0-P) (2-1-F)*
-0.10000 (1-1+P) (0-0+P)*
-0.05000 (1-1+P) (1+0+S)*
 0.07071 (1-1+P) (1+0+D)*
 0.01414 (1-1+P) (2-0+P)*
-0.01732 (1-1+P) (2-0+F)*
 0.08660 (1+0+D) (1+1+S)*
 0.07071 (1+0+D) (1-1+P)*
-0.05477 (1+0+D) (2+1+D)*
-0.05657 (1+0+D) (2-1+P)*
-0.01732 (1+0+D) (2-1+F)*
-0.05774 (1+1+D) (0-0+P)*
-0.08660 (1+1+D) (1+0+S)*
 0.03266 (1+1+D) (2-0+P)*
 0.01000 (1+1+D) (2-0+F)*
 0.07071 (1+1-D) (1-0-P)*
 0.03162 (1+1-D) (2+0-D)*
-0.03162 (2+0-D) (2+1-D)*
-0.05477 (2+0-D) (2-1-P)*
 0.06708 (2+0-D) (2-1-F)*
 0.03873 (2+1+D) (1+0+S)*
-0.05477 (2+1+D) (1+0+D)*
-0.05477 (2+1+D) (2-0+P)*
 0.06708 (2+1+D) (2-0+F)*
-0.00577 (2-0+P) (1+1+S)*
 0.01414 (2-0+P) (1-1+P)*
 0.03266 (2-0+P) (1+1+D)*
-0.05477 (2-0+P) (2+1+D)*
-0.03703 (2-0+P) (3-1+F)*
 0.08660 (2-0+P) (2-1+F)*
 0.01000 (2-1+P) (1+0+S)*
-0.05657 (2-1+P) (1+0+D)*
-0.08660 (2-1+P) (2-0+F)*
-0.02449 (2-1+P) (1-0-P)*
-0.05477 (2-1-P) (2+0-D)*
-0.02619 (2-1-P) (3-0-F)*
-0.02619 (3-0-F) (2-1-P)*
 0.03207 (3-0-F) (2-1-F)*
-0.03703 (3-1+F) (2-0+P)*
 0.04536 (3-1+F) (2-0+F)*
-0.02828 (2-0+F) (1+1+S)*
 0.01732 (2-0+F) (1-1+P)*
 0.01000 (2-0+F) (1+1+D)*
 0.06708 (2-0+F) (2+1+D)*
-0.08660 (2-0+F) (2-1+P)*
 0.04536 (2-0+F) (3-1+F)*
 0.04899 (2-1+F) (1+0+S)*
-0.01732 (2-1+F) (1+0+D)*
 0.08660 (2-1+F) (2-0+P)*
 0.03000 (2-1-F) (1-0-P)*
 0.06708 (2-1-F) (2+0-D)*
 0.03207 (2-1-F) (3-0-F)*


H( 1 1 2 0)=
-0.09428 (0-0+P) (1+1+S)*
 0.13333 (0-0+P) (1+1+D)*
-0.05774 (1+0+S) (1-1+P)*
 0.01155 (1+0+S) (2-1+P)*
-0.08485 (1+0+S) (2-1+F)*
-0.09428 (1+1+S) (0-0+P)*
-0.00667 (1+1+S) (2-0+P)*
 0.04899 (1+1+S) (2-0+F)*
-0.05774 (1+1-S) (1-0-P)*
-0.05774 (1-0-P) (1+1-S)*
-0.04082 (1-0-P) (1+1-D)*
-0.05477 (1-0-P) (2+1-D)*
-0.05774 (1-1+P) (1+0+S)*
-0.04082 (1-1+P) (1+0+D)*
 0.03162 (1-1-P) (2+0-D)*
-0.04082 (1+0+D) (1-1+P)*
-0.08981 (1+0+D) (2-1+P)*
 0.06000 (1+0+D) (2-1+F)*
 0.13333 (1+1+D) (0-0+P)*
 0.05185 (1+1+D) (2-0+P)*
-0.03464 (1+1+D) (2-0+F)*
-0.04082 (1+1-D) (1-0-P)*
 0.03162 (2+0-D) (1-1+P)*
-0.03162 (2+0-D) (2-1-P)*
-0.05521 (2+0-D) (3-1-F)*
-0.02582 (2+0-D) (2-1-F)*
-0.03162 (2+1+D) (2-0+P)*
-0.02582 (2+1+D) (2-0+F)*
-0.05477 (2+1-D) (1-0-P)*
 0.03904 (2+1-D) (3-0-F)*
-0.00667 (2-0+P) (1+1+S)*
 0.05185 (2-0+P) (1+1+D)*
-0.03162 (2-0+P) (2+1+D)*
 0.01155 (2-1+P) (1+0+S)*
-0.08981 (2-1+P) (1+0+D)*
-0.03162 (2-1-P) (2+0-D)*
 0.03904 (3-0-F) (2+1-D)*
-0.05521 (3-1-F) (2+0-D)*
 0.04899 (2-0+F) (1+1+S)*
-0.03464 (2-0+F) (1+1+D)*
-0.02582 (2-0+F) (2+1+D)*
-0.08485 (2-1+F) (1+0+S)*
 0.06000 (2-1+F) (1+0+D)*
-0.02582 (2-1-F) (2+0-D)*


H( 1 1 2 1)=
-0.08165 (0-0+P) (1+1+S)*
 0.10000 (0-0+P) (1-1+P)*
-0.05774 (0-0+P) (1+1+D)*
-0.05000 (1+0+S) (1-1+P)*
 0.08660 (1+0+S) (1+1+D)*
-0.03873 (1+0+S) (2+1+D)*
 0.01000 (1+0+S) (2-1+P)*
 0.04899 (1+0+S) (2-1+F)*
-0.08165 (1+1+S) (0-0+P)*
-0.08660 (1+1+S) (1+0+D)*
-0.00577 (1+1+S) (2-0+P)*
-0.02828 (1+1+S) (2-0+F)*
-0.05000 (1+1-S) (1-0-P)*
-0.02236 (1+1-S) (2+0-D)*
-0.05000 (1-0-P) (1+1-S)*
 0.07071 (1-0-P) (1+1-D)*
-0.02449 (1-0-P) (2-1-P)*
 0.03000 (1-0-P) (2-1-F)*
 0.10000 (1-1+P) (0-0+P)*
-0.05000 (1-1+P) (1+0+S)*
 0.07071 (1-1+P) (1+0+D)*
-0.01414 (1-1+P) (2-0+P)*
 0.01732 (1-1+P) (2-0+F)*
-0.08660 (1+0+D) (1+1+S)*
 0.07071 (1+0+D) (1-1+P)*
 0.05477 (1+0+D) (2+1+D)*
-0.05657 (1+0+D) (2-1+P)*
-0.01732 (1+0+D) (2-1+F)*
-0.05774 (1+1+D) (0-0+P)*
 0.08660 (1+1+D) (1+0+S)*
 0.03266 (1+1+D) (2-0+P)*
 0.01000 (1+1+D) (2-0+F)*
 0.07071 (1+1-D) (1-0-P)*
 0.03162 (1+1-D) (2+0-D)*
-0.02236 (2+0-D) (1+1-S)*
 0.03162 (2+0-D) (1+1-D)*
-0.05477 (2+0-D) (2-1-P)*
 0.06708 (2+0-D) (2-1-F)*
-0.03873 (2+1+D) (1+0+S)*
 0.05477 (2+1+D) (1+0+D)*
-0.05477 (2+1+D) (2-0+P)*
 0.06708 (2+1+D) (2-0+F)*
-0.00577 (2-0+P) (1+1+S)*
-0.01414 (2-0+P) (1-1+P)*
 0.03266 (2-0+P) (1+1+D)*
-0.05477 (2-0+P) (2+1+D)*
-0.03703 (2-0+P) (3-1+F)*
 0.08660 (2-0+P) (2-1+F)*
 0.02449 (2-1+P) (1-0-P)*
-0.05477 (2-1-P) (2+0-D)*
-0.02619 (2-1-P) (3-0-F)*
-0.02619 (3-0-F) (2-1-P)*
 0.03207 (3-0-F) (2-1-F)*
-0.03703 (3-1+F) (2-0+P)*
 0.04536 (3-1+F) (2-0+F)*
-0.02828 (2-0+F) (1+1+S)*
 0.01732 (2-0+F) (1-1+P)*
 0.01000 (2-0+F) (1+1+D)*
 0.06708 (2-0+F) (2+1+D)*
-0.08660 (2-0+F) (2-1+P)*
 0.04536 (2-0+F) (3-1+F)*
 0.04899 (2-1+F) (1+0+S)*
-0.01732 (2-1+F) (1+0+D)*
 0.08660 (2-1+F) (2-0+P)*
 0.03000 (2-1-F) (1-0-P)*
 0.06708 (2-1-F) (2+0-D)*
 0.03207 (2-1-F) (3-0-F)*


H( 2 0 0 0)=
-0.28284 (0-0+P) (2-0+P)*
 0.34641 (0-0+P) (2-0+F)*
-0.28284 (1+0+S) (1+0+D)*
 0.14142 (1+1+S) (1+1+D)*
-0.31623 (1+1+S) (2+1+D)*
 0.14142 (1+1-S) (1+1-D)*
-0.31623 (1+1-S) (2+1-D)*
-0.20000 (1-0-P) (1-0-P)*
 0.32071 (1-0-P) (3-0-F)*
 0.10000 (1-1+P) (1-1+P)*
-0.30000 (1-1+P) (2-1+P)*
 0.26186 (1-1+P) (3-1+F)*
-0.24495 (1-1+P) (2-1+F)*
 0.10000 (1-1-P) (1-1-P)*
-0.30000 (1-1-P) (2-1-P)*
 0.26186 (1-1-P) (3-1-F)*
-0.24495 (1-1-P) (2-1-F)*
-0.28284 (1+0+D) (1+0+S)*
 0.20000 (1+0+D) (1+0+D)*
 0.14142 (1+1+D) (1+1+S)*
-0.10000 (1+1+D) (1+1+D)*
-0.22361 (1+1+D) (2+1+D)*
 0.14142 (1+1-D) (1+1-S)*
-0.10000 (1+1-D) (1+1-D)*
-0.22361 (1+1-D) (2+1-D)*
 0.14286 (2+0-D) (2+0-D)*
-0.31623 (2+1+D) (1+1+S)*
-0.22361 (2+1+D) (1+1+D)*
 0.07143 (2+1+D) (2+1+D)*
```

```
-0.31623 (2+1-D) (1+1-S)*
-0.22361 (2+1-D) (1+1-D)*
 0.07143 (2+1-D) (2+1-D)*
-0.28284 (2-0+P) (0-0+P)*
 0.20000 (2-0+P) (2-0+P)*
-0.06999 (2-0+P) (2-0+F)*
-0.30000 (2-1+P) (1-1+P)*
 0.10000 (2-1+P) (2-1+P)*
-0.13093 (2-1+P) (3-1+F)*
-0.03499 (2-1+P) (2-1+F)*
-0.30000 (2-1-P) (1-1-P)*
 0.10000 (2-1-P) (2-1-P)*
-0.13093 (2-1-P) (3-1-F)*
-0.03499 (2-1-P) (2-1-F)*
 0.32071 (3-0-F) (1-0-P)*
 0.20000 (3-0-F) (3-0-F)*
 0.26186 (3-1+F) (1-1+P)*
-0.13093 (3-1+F) (2-1+P)*
 0.15000 (3-1+F) (3-1+F)*
-0.10690 (3-1+F) (2-1+F)*
 0.26186 (3-1-F) (1-1-P)*
-0.13093 (3-1-F) (2-1-P)*
 0.15000 (3-1-F) (3-1-F)*
-0.10690 (3-1-F) (2-1-F)*
 0.34641 (2-0+F) (0-0+P)*
-0.06999 (2-0+F) (2-0+P)*
 0.22857 (2-0+F) (2-0+F)*
-0.24495 (2-1+F) (1-1+P)*
-0.03499 (2-1+F) (2-1+P)*
-0.10690 (2-1+F) (3-1+F)*
 0.11429 (2-1+F) (2-1+F)*
-0.24495 (2-1-F) (1-1-P)*
-0.03499 (2-1-F) (2-1-P)*
-0.10690 (2-1-F) (3-1-F)*
 0.11429 (2-1-F) (2-1-F)*


H( 2 0 2 0)=
-0.11314 (0-0+P) (2-0+P)*
 0.13856 (0-0+P) (2-0+F)*
 0.08000 (1+0+S) (1+0+S)*
-0.05657 (1+0+S) (1+0+D)*
-0.04000 (1+1+S) (1+1+S)*
 0.02828 (1+1+S) (1+1+D)*
 0.06325 (1+1+S) (2+1+D)*
-0.04000 (1+1-S) (1+1-S)*
 0.02828 (1+1-S) (1+1-D)*
 0.06325 (1+1-S) (2+1-D)*
 0.04000 (1-0-P) (1-0-P)*
-0.06414 (1-0-P) (3-0-F)*
-0.02000 (1-1+P) (1-1+P)*
 0.06000 (1-1+P) (2-1+P)*
-0.05237 (1-1+P) (3-1+F)*
 0.04899 (1-1+P) (2-1+F)*
-0.02000 (1-1-P) (1-1-P)*
 0.06000 (1-1-P) (2-1-P)*
-0.05237 (1-1-P) (3-1-F)*
 0.04899 (1-1-P) (2-1-F)*
-0.05657 (1+0+D) (1+0+S)*
 0.12000 (1+0+D) (1+0+D)*
 0.02828 (1+1+D) (1+1+S)*
-0.06000 (1+1+D) (1+1+D)*
 0.04472 (1+1+D) (2+1+D)*
 0.02828 (1+1-D) (1+1-S)*
-0.06000 (1+1-D) (1+1-D)*
 0.04472 (1+1-D) (2+1-D)*
-0.02857 (2+0-D) (2+0-D)*
 0.06325 (2+1+D) (1+1+S)*
 0.04472 (2+1+D) (1+1+D)*
-0.01429 (2+1+D) (2+1+D)*
 0.06325 (2+1-D) (1+1-S)*
 0.04472 (2+1-D) (1+1-D)*
-0.01429 (2+1-D) (2+1-D)*
-0.11314 (2-0+P) (0-0+P)*
 0.02857 (2-0+P) (2-0+P)*
-0.06999 (2-0+P) (2-0+F)*
 0.06000 (2-1+P) (1-1+P)*
 0.01429 (2-1+P) (2-1+P)*
 0.02619 (2-1+P) (3-1+F)*
-0.03499 (2-1+P) (2-1+F)*
 0.06000 (2-1-P) (1-1-P)*
 0.01429 (2-1-P) (2-1-P)*
 0.02619 (2-1-P) (3-1-F)*
-0.03499 (2-1-P) (2-1-F)*
-0.06414 (3-0-F) (1-0-P)*
-0.04000 (3-0-F) (3-0-F)*
-0.05237 (3-1+F) (1-1+P)*
 0.02619 (3-1+F) (2-1+P)*
-0.03000 (3-1+F) (3-1+F)*
 0.02138 (3-1+F) (2-1+F)*
-0.05237 (3-1-F) (1-1-P)*
 0.02619 (3-1-F) (2-1-P)*
-0.03000 (3-1-F) (3-1-F)*
 0.02138 (3-1-F) (2-1-F)*
 0.13856 (2-0+F) (0-0+P)*
-0.06999 (2-0+F) (2-0+P)*
 0.05714 (2-0+F) (2-0+F)*
 0.04899 (2-1+F) (1-1+P)*
-0.03499 (2-1+F) (2-1+P)*
 0.02138 (2-1+F) (3-1+F)*
 0.02857 (2-1+F) (2-1+F)*
 0.04899 (2-1-F) (1-1-P)*
-0.03499 (2-1-F) (2-1-P)*
 0.02138 (2-1-F) (3-1-F)*
 0.02857 (2-1-F) (2-1-F)*


H( 2 0 2 1)=
-0.08485 (0-0+P) (2-0+P)*
-0.06928 (0-0+P) (2-0+F)*
 0.08000 (1+0+S) (1+0+S)*
-0.02828 (1+0+S) (1+0+D)*
-0.04000 (1+1+S) (1+1+S)*
 0.01414 (1+1+S) (1+1+D)*
 0.03162 (1+1+S) (2+1+D)*
-0.04000 (1+1-S) (1+1-S)*
 0.01414 (1+1-S) (1+1-D)*
 0.03162 (1+1-S) (2+1-D)*
 0.06000 (1-1+P) (2-1+P)*
-0.07348 (1-1+P) (2-1+F)*
 0.06000 (1-1-P) (2-1-P)*
-0.07348 (1-1-P) (2-1-F)*
-0.02828 (1+0+D) (1+0+S)*
-0.08000 (1+0+D) (1+0+D)*
 0.01414 (1+1+D) (1+1+S)*
 0.04000 (1+1+D) (1+1+D)*
-0.04472 (1+1+D) (2+1+D)*
 0.01414 (1+1-D) (1+1-S)*
 0.04000 (1+1-D) (1+1-D)*
-0.04472 (1+1-D) (2+1-D)*
 0.03162 (2+1+D) (1+1+S)*
-0.04472 (2+1+D) (1+1+D)*
 0.03162 (2+1-D) (1+1-S)*
-0.04472 (2+1-D) (1+1-D)*
-0.08485 (2-0+P) (0-0+P)*
 0.03429 (2-0+P) (2-0+P)*
-0.00700 (2-0+P) (2-0+F)*
 0.06000 (2-1+P) (1-1+P)*
 0.01714 (2-1+P) (2-1+F)*
 0.02619 (2-1+P) (3-1+F)*
-0.00350 (2-1+P) (2-1+F)*
 0.06000 (2-1-P) (1-1-P)*
 0.01714 (2-1-P) (2-1-F)*
 0.02619 (2-1-P) (3-1-F)*
-0.00350 (2-1-P) (2-1-F)*
 0.02619 (3-1+F) (2-1+P)*
-0.03207 (3-1+F) (2-1+F)*
 0.02619 (3-1-F) (2-1-P)*
-0.03207 (3-1-F) (2-1-F)*
-0.06928 (2-0+F) (0-0+P)*
-0.00700 (2-0+F) (2-0+P)*
-0.03429 (2-0+F) (2-0+F)*
-0.07348 (2-1+F) (1-1+P)*
-0.00350 (2-1+F) (2-1+P)*
-0.03207 (2-1+F) (3-1+F)*
-0.01714 (2-1+F) (2-1+F)*
-0.07348 (2-1-F) (1-1-P)*
-0.00350 (2-1-F) (2-1-P)*
-0.03207 (2-1-F) (3-1-F)*
-0.01714 (2-1-F) (2-1-F)*


H( 2 0 2 2)=
 0.08000 (1+0+S) (1+0+S)*
 0.05657 (1+0+S) (1+0+D)*
-0.04000 (1+1+S) (1+1+S)*
-0.02828 (1+1+S) (1+1+D)*
-0.06325 (1+1+S) (2+1+D)*
-0.04000 (1+1-S) (1+1-S)*
-0.02828 (1+1-S) (1+1-D)*
-0.06325 (1+1-S) (2+1-D)*
-0.12000 (1-0-P) (1-0-P)*
 0.03207 (1-0-P) (3-0-F)*
 0.06000 (1-1+P) (1-1+P)*
 0.06000 (1-1+P) (2-1+P)*
 0.02619 (1-1+P) (3-1+F)*
 0.04899 (1-1+P) (2-1+F)*
 0.06000 (1-1-P) (1-1-P)*
 0.06000 (1-1-P) (2-1-P)*
 0.02619 (1-1-P) (3-1-F)*
 0.04899 (1-1-P) (2-1-F)*
 0.05657 (1+0+D) (1+0+S)*
 0.04000 (1+0+D) (1+0+D)*
-0.02828 (1+1+D) (1+1+S)*
-0.02000 (1+1+D) (1+1+D)*
-0.04472 (1+1+D) (2+1+D)*
-0.02828 (1+1-D) (1+1-S)*
-0.02000 (1+1-D) (1+1-D)*
-0.04472 (1+1-D) (2+1-D)*
-0.08571 (2+0-D) (2+0-D)*
-0.06325 (2+1+D) (1+1+S)*
-0.04472 (2+1+D) (1+1+D)*
-0.04286 (2+1+D) (2+1+D)*
-0.06325 (2+1-D) (1+1-S)*
-0.04472 (2+1-D) (1+1-D)*
-0.04286 (2+1-D) (2+1-D)*
 0.05143 (2-0+P) (2-0+P)*
 0.04199 (2-0+P) (2-0+F)*
 0.06000 (2-1+P) (1-1+P)*
 0.02571 (2-1+P) (2-1+P)*
-0.03928 (2-1+P) (3-1+F)*
 0.02100 (2-1+P) (2-1+F)*
 0.06000 (2-1-P) (1-1-P)*
 0.02571 (2-1-P) (2-1-P)*
-0.03928 (2-1-P) (3-1-F)*
 0.02100 (2-1-P) (2-1-F)*
 0.03207 (3-0-F) (1-0-P)*
-0.08000 (3-0-F) (3-0-F)*
 0.02619 (3-1+F) (1-1+P)*
-0.03928 (3-1+F) (2-1+P)*
-0.06000 (3-1+F) (3-1+F)*
-0.03207 (3-1+F) (2-1+F)*
 0.02619 (3-1-F) (1-1-P)*
-0.03928 (3-1-F) (2-1-P)*
-0.06000 (3-1-F) (3-1-F)*
-0.03207 (3-1-F) (2-1-F)*
 0.04199 (2-0+F) (2-0+P)*
 0.03429 (2-0+F) (2-0+F)*
 0.04899 (2-1+F) (1-1+P)*
 0.02100 (2-1+F) (2-1+P)*
-0.03207 (2-1+F) (3-1+F)*
 0.01714 (2-1+F) (2-1+F)*
 0.04899 (2-1-F) (1-1-P)*
 0.02100 (2-1-F) (2-1-P)*
-0.03207 (2-1-F) (3-1-F)*
 0.01714 (2-1-F) (2-1-F)*


H( 2 1 0 0)=
-0.20000 (0-0+P) (2-1+P)*
 0.24495 (0-0+P) (2-1+F)*
-0.17321 (1+0+S) (1+1+D)*
 0.12910 (1+0+S) (2+1+D)*
-0.17321 (1+1+S) (1+0+D)*
 0.22361 (1+1-S) (2+0-D)*
-0.12247 (1-0-P) (1-1-P)*
 0.12247 (1-0-P) (2-1-P)*
 0.21381 (1-0-P) (3-1-F)*
 0.10000 (1-0-P) (2-1-F)*
 0.21213 (1-1+P) (2-0+P)*
 0.17321 (1-1+P) (2-0+F)*
-0.12247 (1-1-P) (1-0-P)*
```

```
-0.13093 (1-1-P) (3-0-F)*
-0.17321 (1+0+D) (1+1+S)*
 0.12247 (1+0+D) (1+1+D)*
 0.09129 (1+0+D) (2+1+D)*
-0.17321 (1+1+D) (1+0+S)*
 0.12247 (1+1+D) (1+0+D)*
 0.15811 (1+1-D) (2+0-D)*
 0.22361 (2+0-D) (1+1-S)*
 0.15811 (2+0-D) (1+1-D)*
 0.05051 (2+0-D) (2+1-D)*
 0.12910 (2+1+D) (1+0+S)*
 0.09129 (2+1+D) (1+0+D)*
 0.05051 (2+1-D) (2+0-D)*
 0.21213 (2-0+P) (1-1+P)*
 0.07071 (2-0+P) (2-1+P)*
 0.09258 (2-0+P) (3-1+F)*
-0.02474 (2-0+P) (2-1+F)*
-0.20000 (2-1+P) (0-0+P)*
 0.07071 (2-1+P) (2-0+P)*
-0.02474 (2-1+P) (2-0+F)*
 0.12247 (2-1-P) (1-0-P)*
 0.13093 (2-1-P) (3-0-F)*
-0.13093 (3-0-F) (1-1-P)*
 0.13093 (3-0-F) (2-1-P)*
 0.05000 (3-0-F) (3-1-F)*
 0.10690 (3-0-F) (2-1-F)*
 0.09258 (3-1+F) (2-0+P)*
 0.07559 (3-1+F) (2-0+F)*
 0.21381 (3-1-F) (1-0-P)*
 0.05000 (3-1-F) (3-0-F)*
 0.17321 (2-0+F) (1-1+P)*
-0.02474 (2-0+F) (2-1+P)*
 0.07559 (2-0+F) (3-1+F)*
 0.08081 (2-0+F) (2-1+F)*
 0.24495 (2-1+F) (0-0+P)*
-0.02474 (2-1+F) (2-0+P)*
 0.08081 (2-1+F) (2-0+F)*
 0.10000 (2-1-F) (1-0-P)*
 0.10690 (2-1-F) (3-0-F)*


H( 2 1 2-2)=
 0.04899 (1+0+S) (1+1+S)*
 0.06000 (1+0+S) (1-1+P)*
 0.03464 (1+0+S) (1+1+D)*
 0.02582 (1+0+S) (2+1+D)*
 0.02000 (1+0+S) (2-1+P)*
-0.01746 (1+0+S) (3-1+F)*
 0.01633 (1+0+S) (2-1+F)*
 0.04899 (1+1+S) (1+0+S)*
 0.03464 (1+1+S) (1+0+D)*
-0.03464 (1+1+S) (2-0+P)*
-0.02828 (1+1+S) (2-0+F)*
-0.06000 (1+1-S) (1-0-P)*
 0.04472 (1+1-S) (2+0-D)*
-0.01069 (1+1-S) (3-0-F)*
-0.06000 (1-0-P) (1+1-S)*
-0.07348 (1-0-P) (1-1-P)*
-0.04243 (1-0-P) (1+1-D)*
-0.03162 (1-0-P) (2+1-D)*
-0.02449 (1-0-P) (2-1-P)*
 0.02138 (1-0-P) (3-1-F)*
-0.02000 (1-0-P) (2-1-F)*
 0.06000 (1-1+P) (1+0+S)*
 0.04243 (1-1+P) (1+0+D)*
-0.04243 (1-1+P) (2-0+P)*
-0.03464 (1-1+P) (2-0+F)*
-0.07348 (1-1-P) (1-0-P)*
 0.05477 (1-1-P) (2+0-D)*
-0.01309 (1-1-P) (3-0-F)*
 0.03464 (1+0+D) (1+1+S)*
 0.04243 (1+0+D) (1-1+P)*
 0.02449 (1+0+D) (1+1+D)*
 0.01826 (1+0+D) (2+1+D)*
 0.01414 (1+0+D) (2-1+P)*
-0.01234 (1+0+D) (3-1+F)*
 0.01155 (1+0+D) (2-1+F)*
 0.03464 (1+1+D) (1+0+S)*
 0.02449 (1+1+D) (1+0+D)*
-0.02449 (1+1+D) (2-0+P)*
-0.02000 (1+1+D) (2-0+F)*

-0.04243 (1+1-D) (1-0-P)*
 0.03162 (1+1-D) (2+0-D)*
-0.00756 (1+1-D) (3-0-F)*
 0.04472 (2+0-D) (1+1-S)*
 0.05477 (2+0-D) (1-1-P)*
 0.03162 (2+0-D) (1+1-D)*
-0.03030 (2+0-D) (2+1-D)*
-0.02347 (2+0-D) (2-1-P)*
-0.03586 (2+0-D) (3-1-F)*
-0.01917 (2+0-D) (2-1-F)*
 0.02582 (2+1+D) (1+0+S)*
 0.01826 (2+1+D) (1+0+D)*
 0.02347 (2+1+D) (2-0+P)*
 0.01917 (2+1+D) (2-0+F)*
-0.03162 (2+1-D) (1-0-P)*
-0.03030 (2+1-D) (2+0-D)*
 0.05071 (2+1-D) (3-0-F)*
-0.03464 (2-0+P) (1+1+S)*
-0.04243 (2-0+P) (1-1+P)*
-0.02449 (2-0+P) (1+1+D)*
 0.02347 (2-0+P) (2+1+D)*
 0.01818 (2-0+P) (2-1+P)*
 0.02777 (2-0+P) (3-1+F)*
 0.01485 (2-0+P) (2-1+F)*
 0.02000 (2-1+P) (1+0+S)*
 0.01414 (2-1+P) (1+0+D)*
 0.01818 (2-1+P) (2-0+P)*
 0.01485 (2-1+P) (2-0+F)*
-0.02449 (2-1-P) (1-0-P)*
-0.02347 (2-1-P) (2+0-D)*
 0.03928 (2-1-P) (3-0-F)*
-0.01069 (3-0-F) (1+1-S)*
-0.01309 (3-0-F) (1-1-P)*
-0.00756 (3-0-F) (1+1-D)*
 0.05071 (3-0-F) (2+1-D)*
 0.03928 (3-0-F) (2-1-P)*
-0.02000 (3-0-F) (3-1-F)*
 0.03207 (3-0-F) (2-1-F)*
-0.01746 (3-1+F) (1+0+S)*
-0.01234 (3-1+F) (1+0+D)*
 0.02777 (3-1+F) (2-0+P)*
 0.02268 (3-1+F) (2-0+F)*
 0.02138 (3-1-F) (1-0-P)*
-0.03586 (3-1-F) (2+0-D)*
-0.02000 (3-1-F) (3-0-F)*
-0.02828 (2-0+F) (1+1+S)*
-0.03464 (2-0+F) (1-1+P)*
-0.02000 (2-0+F) (1+1+D)*
 0.01917 (2-0+F) (2+1+D)*
 0.01485 (2-0+F) (2-1+P)*
 0.02268 (2-0+F) (3-1+F)*
 0.01212 (2-0+F) (2-1+F)*
 0.01633 (2-1+F) (1+0+S)*
 0.01155 (2-1+F) (1+0+D)*
 0.01485 (2-1+F) (2-0+P)*
 0.01212 (2-1+F) (2-0+F)*
-0.02000 (2-1-F) (1-0-P)*
-0.01917 (2-1-F) (2+0-D)*
 0.03207 (2-1-F) (3-0-F)*


H( 2 1 2-1)=
-0.07746 (0-0+P) (2+1+D)*
-0.06000 (0-0+P) (2-1+P)*
-0.04899 (0-0+P) (2-1+F)*
 0.04899 (1+0+S) (1+1+S)*
 0.03000 (1+0+S) (1-1+P)*
-0.01732 (1+0+S) (1+1+D)*
-0.01291 (1+0+S) (2+1+D)*
 0.01000 (1+0+S) (2-1+P)*
 0.03491 (1+0+S) (3-1+F)*
-0.03266 (1+0+S) (2-1+F)*
 0.04899 (1+1+S) (1+0+S)*
-0.01732 (1+1+S) (2-0+P)*
 0.05657 (1+1+S) (2-0+F)*
-0.03000 (1+1-S) (1-0-P)*
-0.02236 (1+1-S) (2+0-D)*
 0.02138 (1+1-S) (3-0-F)*
-0.03000 (1-0-P) (1+1-S)*
 0.04243 (1-0-P) (1+1-D)*

-0.02449 (1-0-P) (2-1-P)*
 0.03000 (1-0-P) (2-1-F)*
 0.03000 (1-1+P) (1+0+S)*
-0.04243 (1-1+P) (1+0+D)*
-0.04243 (1-1+P) (2-0+P)*
 0.05196 (1-1+P) (2-0+F)*
-0.01732 (1+0+D) (1+1+S)*
-0.04243 (1+0+D) (1-1+P)*
-0.04899 (1+0+D) (1+1+D)*
 0.01826 (1+0+D) (2+1+D)*
 0.02828 (1+0+D) (2-1+P)*
-0.04938 (1+0+D) (3-1+F)*
-0.00577 (1+0+D) (2-1+F)*
-0.01732 (1+1+D) (1+0+S)*
-0.04899 (1+1+D) (1+0+D)*
-0.04899 (1+1+D) (2-0+P)*
 0.01000 (1+1+D) (2-0+F)*
 0.04243 (1+1-D) (1-0-P)*
 0.03162 (1+1-D) (2+0-D)*
-0.03024 (1+1-D) (3-0-F)*
-0.02236 (2+0-D) (1+1-S)*
 0.03162 (2+0-D) (1+1-D)*
-0.00782 (2+0-D) (2-1-P)*
 0.00958 (2+0-D) (2-1-F)*
-0.07746 (2+1+D) (0-0+P)*
-0.01291 (2+1+D) (1+0+S)*
 0.01826 (2+1+D) (1+0+D)*
 0.00782 (2+1+D) (2-0+P)*
-0.00958 (2+1+D) (2-0+F)*
-0.01732 (2-0+P) (1+1+S)*
-0.04243 (2-0+P) (1-1+P)*
-0.04899 (2-0+P) (1+1+D)*
 0.00782 (2-0+P) (2+1+D)*
 0.01212 (2-0+P) (2-1+P)*
-0.01852 (2-0+P) (3-1+F)*
-0.00247 (2-0+P) (2-1+F)*
-0.06000 (2-1+P) (0-0+P)*
 0.01000 (2-1+P) (1+0+S)*
 0.02828 (2-1+P) (1+0+D)*
 0.01212 (2-1+P) (2-0+P)*
-0.00247 (2-1+P) (2-0+F)*
-0.02449 (2-1-P) (1-0-P)*
-0.00782 (2-1-P) (2+0-D)*
-0.02619 (2-1-P) (3-0-F)*
 0.02138 (3-0-F) (1+1-S)*
-0.03024 (3-0-F) (1+1-D)*
-0.02619 (3-0-F) (2-1-P)*
 0.03207 (3-0-F) (2-1-F)*
 0.03491 (3-1+F) (1+0+S)*
-0.04938 (3-1+F) (1+0+D)*
-0.01852 (3-1+F) (2-0+P)*
 0.02268 (3-1+F) (2-0+F)*
 0.05657 (2-0+F) (1+1+S)*
 0.05196 (2-0+F) (1-1+P)*
 0.01000 (2-0+F) (1+1+D)*
-0.00958 (2-0+F) (2+1+D)*
-0.00247 (2-0+F) (2-1+P)*
 0.02268 (2-0+F) (3-1+F)*
-0.01212 (2-0+F) (2-1+F)*
-0.04899 (2-1+F) (0-0+P)*
-0.03266 (2-1+F) (1+0+S)*
-0.00577 (2-1+F) (1+0+D)*
-0.00247 (2-1+F) (2-0+P)*
-0.01212 (2-1+F) (2-0+F)*
 0.03000 (2-1-F) (1-0-P)*
 0.00958 (2-1-F) (2+0-D)*
 0.03207 (2-1-F) (3-0-F)*


H( 2 1 2 0)=
-0.08000 (0-0+P) (2-1+P)*
 0.09798 (0-0+P) (2-1+F)*
 0.04899 (1+0+S) (1+1+S)*
-0.03464 (1+0+S) (1+1+D)*
-0.02582 (1+0+S) (2+1+D)*
 0.04899 (1+1+S) (1+0+S)*
-0.03464 (1+1+S) (1+0+D)*
-0.04472 (1+1-S) (2+0-D)*
 0.02449 (1-0-P) (1-1-P)*
-0.02449 (1-0-P) (2-1-P)*
-0.04276 (1-0-P) (3-1-F)*
```

```
-0.02000 (1-0-P) (2-1-F)*
-0.04243 (1-1+P) (2-0+P)*
-0.03464 (1-1+P) (2-0+F)*
 0.02449 (1-1-P) (1-0-P)*
 0.02619 (1-1-P) (3-0-F)*
-0.03464 (1+0+D) (1+1+S)*
 0.07348 (1+0+D) (1+1+D)*
-0.01826 (1+0+D) (2+1+D)*
-0.03464 (1+1+D) (1+0+S)*
 0.07348 (1+1+D) (1+0+D)*
-0.03162 (1+1-D) (2+0-D)*
-0.04472 (2+0-D) (1+1-S)*
-0.03162 (2+0-D) (1+1-D)*
-0.01010 (2+0-D) (2+1-D)*
-0.02582 (2+1+D) (1+0+S)*
-0.01826 (2+1+D) (1+0+D)*
-0.01010 (2+1-D) (2+0-D)*
-0.04243 (2-0+P) (1-1+P)*
 0.01010 (2-0+P) (2-1+P)*
-0.01852 (2-0+P) (3-1+F)*
-0.02474 (2-0+P) (2-1+F)*
-0.08000 (2-1+P) (0-0+P)*
 0.01010 (2-1+P) (2-0+P)*
-0.02474 (2-1+P) (2-0+F)*
-0.02449 (2-1-P) (1-0-P)*
-0.02619 (2-1-P) (3-0-F)*
 0.02619 (3-0-F) (1-1-P)*
-0.02619 (3-0-F) (2-1-P)*
-0.01000 (3-0-F) (3-1-F)*
-0.02138 (3-0-F) (2-1-F)*
-0.01852 (3-1+F) (2-0+P)*
-0.01512 (3-1+F) (2-0+F)*
-0.04276 (3-1-F) (1-0-P)*
-0.01000 (3-1-F) (3-0-F)*
-0.03464 (2-0+F) (1-1+P)*
-0.02474 (2-0+F) (2-1+P)*
-0.01512 (2-0+F) (3-1+F)*
 0.02020 (2-0+F) (2-1+F)*
 0.09798 (2-1+F) (0-0+P)*
-0.02474 (2-1+F) (2-0+P)*
 0.02020 (2-1+F) (2-0+F)*
-0.02000 (2-1-F) (1-0-P)*
-0.02138 (2-1-F) (3-0-F)*


H( 2 1 2 1)=
 0.07746 (0-0+P) (2+1+D)*
-0.06000 (0-0+P) (2-1+P)*
-0.04899 (0-0+P) (2-1+F)*
 0.04899 (1+0+S) (1+1+S)*
-0.03000 (1+0+S) (1-1+P)*
-0.01732 (1+0+S) (1+1+D)*
-0.01291 (1+0+S) (2+1+D)*
-0.01000 (1+0+S) (2-1+P)*
-0.03491 (1+0+S) (3-1+F)*
 0.03266 (1+0+S) (2-1+F)*
 0.04899 (1+1+S) (1+0+S)*
-0.01732 (1+1+S) (1+0+D)*
 0.01732 (1+1+S) (2-0+P)*
-0.05657 (1+1+S) (2-0+F)*
 0.03000 (1+1-S) (1-0-P)*
-0.02236 (1+1-S) (2+0-D)*
-0.02138 (1+1-S) (3-0-F)*
 0.03000 (1-0-P) (1+1-S)*
-0.04243 (1-0-P) (1+1-D)*
-0.02449 (1-0-P) (2-1-P)*
 0.03000 (1-0-P) (2-1-F)*
-0.03000 (1-1+P) (1+0+S)*
 0.04243 (1-1+P) (1+0+D)*
-0.04243 (1-1+P) (2-0+P)*
 0.05196 (1-1+P) (2-0+F)*
-0.01732 (1+0+D) (1+1+S)*
 0.04243 (1+0+D) (1-1+P)*
-0.04899 (1+0+D) (1+1+D)*
 0.01826 (1+0+D) (2+1+D)*
-0.02828 (1+0+D) (2-1+P)*
 0.04938 (1+0+D) (3-1+F)*
 0.00577 (1+0+D) (2-1+F)*
-0.01732 (1+1+D) (1+0+S)*
-0.04899 (1+1+D) (1+0+D)*
 0.04899 (1+1+D) (2-0+P)*

-0.01000 (1+1+D) (2-0+F)*
-0.04243 (1+1-D) (1-0-P)*
 0.03162 (1+1-D) (2+0-D)*
 0.03024 (1+1-D) (3-0-F)*
-0.02236 (2+0-D) (1+1-S)*
 0.03162 (2+0-D) (1+1-D)*
 0.00782 (2+0-D) (2-1-P)*
-0.00958 (2+0-D) (2-1-F)*
 0.07746 (2+1+D) (0-0+P)*
-0.01291 (2+1+D) (1+0+S)*
 0.01826 (2+1+D) (1+0+D)*
-0.00782 (2+1+D) (2-0+P)*
 0.00958 (2+1+D) (2-0+F)*
 0.01732 (2-0+P) (1+1+S)*
-0.04243 (2-0+P) (1-1+P)*
 0.04899 (2-0+P) (1+1+D)*
-0.00782 (2-0+P) (2+1+D)*
 0.01212 (2-0+P) (2-1+P)*
-0.01852 (2-0+P) (3-1+F)*
-0.00247 (2-0+P) (2-1+F)*
-0.06000 (2-1+P) (0-0+P)*
-0.01000 (2-1+P) (1+0+S)*
-0.02828 (2-1+P) (1+0+D)*
 0.01212 (2-1+P) (2-0+P)*
-0.00247 (2-1+P) (2-0+F)*
-0.02449 (2-1-P) (1-0-P)*
 0.00782 (2-1-P) (2+0-D)*
-0.02619 (2-1-P) (3-0-F)*
-0.02138 (3-0-F) (1+1-S)*
 0.03024 (3-0-F) (1+1-D)*
-0.02619 (3-0-F) (2-1-P)*
 0.03207 (3-0-F) (2-1-F)*
-0.03491 (3-1+F) (1+0+S)*
 0.04938 (3-1+F) (1+0+D)*
-0.01852 (3-1+F) (2-0+P)*
 0.02268 (3-1+F) (2-0+F)*
-0.05657 (2-0+F) (1+1+S)*
 0.05196 (2-0+F) (1-1+P)*
-0.01000 (2-0+F) (1+1+D)*
 0.00958 (2-0+F) (2+1+D)*
-0.00247 (2-0+F) (2-1+P)*
 0.02268 (2-0+F) (3-1+F)*
-0.01212 (2-0+F) (2-1+F)*
-0.04899 (2-1+F) (0-0+P)*
 0.03266 (2-1+F) (1+0+S)*
 0.00577 (2-1+F) (1+0+D)*
-0.00247 (2-1+F) (2-0+P)*
-0.01212 (2-1+F) (2-0+F)*
 0.03000 (2-1-F) (1-0-P)*
-0.00958 (2-1-F) (2+0-D)*
 0.03207 (2-1-F) (3-0-F)*


H( 2 1 2 2)=
 0.04899 (1+0+S) (1+1+S)*
-0.06000 (1+0+S) (1-1+P)*
 0.03464 (1+0+S) (1+1+D)*
 0.02582 (1+0+S) (2+1+D)*
-0.02000 (1+0+S) (2-1+P)*
 0.01746 (1+0+S) (3-1+F)*
-0.01633 (1+0+S) (2-1+F)*
 0.04899 (1+1+S) (1+0+S)*
 0.03464 (1+1+S) (1+0+D)*
 0.03464 (1+1+S) (2-0+P)*
 0.02828 (1+1+S) (2-0+F)*
 0.06000 (1+1-S) (1-0-P)*
 0.04472 (1+1-S) (2+0-D)*
 0.01069 (1+1-S) (3-0-F)*
 0.06000 (1-0-P) (1+1-S)*
-0.07348 (1-0-P) (1-1-P)*
 0.04243 (1-0-P) (1+1-D)*
 0.03162 (1-0-P) (2+1-D)*
-0.02449 (1-0-P) (2-1-P)*
 0.02138 (1-0-P) (3-1-F)*
-0.02000 (1-0-P) (2-1-F)*
-0.06000 (1-1+P) (1+0+S)*
-0.04243 (1-1+P) (1+0+D)*
-0.04243 (1-1+P) (2-0+P)*
-0.03464 (1-1+P) (2-0+F)*
-0.07348 (1-1-P) (1-0-P)*
-0.05477 (1-1-P) (2+0-D)*

-0.01309 (1-1-P) (3-0-F)*
 0.03464 (1+0+D) (1+1+S)*
-0.04243 (1+0+D) (1-1+P)*
 0.02449 (1+0+D) (1+1+D)*
 0.01826 (1+0+D) (2+1+D)*
-0.01414 (1+0+D) (2-1+P)*
 0.01234 (1+0+D) (3-1+F)*
-0.01155 (1+0+D) (2-1+F)*
 0.03464 (1+1+D) (1+0+S)*
 0.02449 (1+1+D) (1+0+D)*
 0.02449 (1+1+D) (2-0+P)*
 0.02000 (1+1+D) (2-0+F)*
 0.04243 (1+1-D) (1-0-P)*
 0.03162 (1+1-D) (2+0-D)*
 0.00756 (1+1-D) (3-0-F)*
 0.04472 (2+0-D) (1+1-S)*
-0.05477 (2+0-D) (1-1-P)*
 0.03162 (2+0-D) (1+1-D)*
-0.03030 (2+0-D) (2+1-D)*
 0.02347 (2+0-D) (2-1-P)*
 0.03586 (2+0-D) (3-1-F)*
 0.01917 (2+0-D) (2-1-F)*
 0.02582 (2+1+D) (1+0+S)*
 0.01826 (2+1+D) (1+0+D)*
-0.02347 (2+1+D) (2-0+P)*
-0.01917 (2+1+D) (2-0+F)*
 0.03162 (2+1-D) (1-0-P)*
-0.03030 (2+1-D) (2+0-D)*
-0.05071 (2+1-D) (3-0-F)*
 0.03464 (2-0+P) (1+1+S)*
-0.04243 (2-0+P) (1-1+P)*
 0.02449 (2-0+P) (1+1+D)*
-0.02347 (2-0+P) (2+1+D)*
 0.01818 (2-0+P) (2-1+P)*
 0.02777 (2-0+P) (3-1+F)*
 0.01485 (2-0+P) (2-1+F)*
-0.02000 (2-1+P) (1+0+S)*
-0.01414 (2-1+P) (1+0+D)*
 0.01818 (2-1+P) (2-0+P)*
 0.01485 (2-1+P) (2-0+F)*
-0.02449 (2-1-P) (1-0-P)*
 0.02347 (2-1-P) (2+0-D)*
 0.03928 (2-1-P) (3-0-F)*
 0.01069 (3-0-F) (1+1-S)*
-0.01309 (3-0-F) (1-1-P)*
 0.00756 (3-0-F) (1+1-D)*
-0.05071 (3-0-F) (2+1-D)*
 0.03928 (3-0-F) (2-1-P)*
-0.02000 (3-0-F) (3-1-F)*
 0.03207 (3-0-F) (2-1-F)*
 0.01746 (3-1+F) (1+0+S)*
 0.01234 (3-1+F) (1+0+D)*
 0.02777 (3-1+F) (2-0+P)*
 0.02268 (3-1+F) (2-0+F)*
 0.02138 (3-1-F) (1-0-P)*
 0.03586 (3-1-F) (2+0-D)*
-0.02000 (3-1-F) (3-0-F)*
 0.02828 (2-0+F) (1+1+S)*
-0.03464 (2-0+F) (1-1+P)*
 0.02000 (2-0+F) (1+1+D)*
-0.01917 (2-0+F) (2+1+D)*
 0.01485 (2-0+F) (2-1+P)*
 0.02268 (2-0+F) (3-1+F)*
 0.01212 (2-0+F) (2-1+F)*
-0.01633 (2-1+F) (1+0+S)*
-0.01155 (2-1+F) (1+0+D)*
 0.01485 (2-1+F) (2-0+P)*
 0.01212 (2-1+F) (2-0+F)*
-0.02000 (2-1-F) (1-0-P)*
 0.01917 (2-1-F) (2+0-D)*
 0.03207 (2-1-F) (3-0-F)*


H( 2 2 0 0)=
-0.17321 (1+1+S) (1+1+D)*
-0.12910 (1+1+S) (2+1+D)*
 0.17321 (1+1-S) (1+1-D)*
 0.12910 (1+1-S) (2+1-D)*
 0.12247 (1-1+P) (1-1+P)*
 0.12247 (1-1+P) (2-1+P)*
 0.05345 (1-1+P) (3-1+F)*
```

```
 0.10000 (1-1+P) (2-1+F)*
-0.12247 (1-1-P) (1-1-P)*
-0.12247 (1-1-P) (2-1-P)*
-0.05345 (1-1-P) (3-1-F)*
-0.10000 (1-1-P) (2-1-F)*
-0.17321 (1+1+D) (1+1+S)*
 0.12247 (1+1+D) (1+1+D)*
-0.09129 (1+1+D) (2+1+D)*
 0.17321 (1+1-D) (1+1-S)*
-0.12247 (1+1-D) (1+1-D)*
 0.09129 (1+1-D) (2+1-D)*
-0.12910 (2+1+D) (1+1+S)*
-0.09129 (2+1+D) (1+1+D)*
-0.08748 (2+1+D) (2+1+D)*
 0.12910 (2+1-D) (1+1-S)*
 0.09129 (2+1-D) (1+1-D)*
 0.08748 (2+1-D) (2+1-D)*
 0.12247 (2-1+P) (1-1+P)*
 0.12247 (2-1+P) (2-1+P)*
-0.08018 (2-1+P) (3-1+F)*
-0.04286 (2-1+P) (2-1+F)*
-0.12247 (2-1-P) (1-1-P)*
-0.12247 (2-1-P) (2-1-P)*
 0.08018 (2-1-P) (3-1-F)*
 0.04286 (2-1-P) (2-1-F)*
 0.05345 (3-1+F) (1-1+P)*
-0.08018 (3-1+F) (2-1+P)*
-0.12247 (3-1+F) (3-1+F)*
-0.06547 (3-1+F) (2-1+F)*
-0.05345 (3-1-F) (1-1-P)*
 0.08018 (3-1-F) (2-1-P)*
 0.12247 (3-1-F) (3-1-F)*
 0.06547 (3-1-F) (2-1-F)*
 0.10000 (2-1+F) (1-1+P)*
-0.04286 (2-1+F) (2-1+P)*
-0.06547 (2-1+F) (3-1+F)*
 0.13997 (2-1+F) (2-1+F)*
-0.10000 (2-1-F) (1-1-P)*
 0.04286 (2-1-F) (2-1-P)*
 0.06547 (2-1-F) (3-1-F)*
-0.13997 (2-1-F) (2-1-F)*


H( 2 2 2-2)=
 0.04899 (1+1+S) (1+1+S)*
 0.06000 (1+1+S) (1-1+P)*
 0.03464 (1+1+S) (1+1+D)*
-0.02582 (1+1+S) (2+1+D)*
-0.02000 (1+1+S) (2-1+P)*
 0.00436 (1+1+S) (3-1+F)*
-0.01633 (1+1+S) (2-1+F)*
-0.04899 (1+1-S) (1+1-S)*
-0.06000 (1+1-S) (1-1-P)*
-0.03464 (1+1-S) (1+1-D)*
 0.02582 (1+1-S) (2+1-D)*
 0.02000 (1+1-S) (2-1-P)*
-0.00436 (1+1-S) (3-1-F)*
 0.01633 (1+1-S) (2-1-F)*
 0.06000 (1-1+P) (1+1+S)*
 0.07348 (1-1+P) (1-1+P)*
 0.04243 (1-1+P) (1+1+D)*
-0.03162 (1-1+P) (2+1+D)*
-0.02449 (1-1+P) (2-1+P)*
 0.00535 (1-1+P) (3-1+F)*
-0.02000 (1-1+P) (2-1+F)*
-0.06000 (1-1-P) (1+1-S)*
-0.07348 (1-1-P) (1-1-P)*
-0.04243 (1-1-P) (1+1-D)*
 0.03162 (1-1-P) (2+1-D)*
 0.02449 (1-1-P) (2-1-P)*
-0.00535 (1-1-P) (3-1-F)*
 0.02000 (1-1-P) (2-1-F)*
 0.03464 (1+1+D) (1+1+S)*
 0.04243 (1+1+D) (1-1+P)*
 0.02449 (1+1+D) (1+1+D)*
-0.01826 (1+1+D) (2+1+D)*
-0.01414 (1+1+D) (2-1+P)*
 0.00309 (1+1+D) (3-1+F)*
-0.01155 (1+1+D) (2-1+F)*
-0.03464 (1+1-D) (1+1-S)*
-0.04243 (1+1-D) (1-1-P)*

-0.02449 (1+1-D) (1+1-D)*
 0.01826 (1+1-D) (2+1-D)*
 0.01414 (1+1-D) (2-1-P)*
-0.00309 (1+1-D) (3-1-F)*
 0.01155 (1+1-D) (2-1-F)*
-0.02582 (2+1+D) (1+1+S)*
-0.03162 (2+1+D) (1-1+P)*
-0.01826 (2+1+D) (1+1+D)*
 0.05249 (2+1+D) (2+1+D)*
 0.04066 (2+1+D) (2-1+P)*
-0.03105 (2+1+D) (3-1+F)*
 0.03320 (2+1+D) (2-1+F)*
 0.02582 (2+1-D) (1+1-S)*
 0.03162 (2+1-D) (1-1-P)*
 0.01826 (2+1-D) (1+1-D)*
-0.05249 (2+1-D) (2+1-D)*
-0.04066 (2+1-D) (2-1-P)*
 0.03105 (2+1-D) (3-1-F)*
-0.03320 (2+1-D) (2-1-F)*
-0.02000 (2-1+P) (1+1+S)*
-0.02449 (2-1+P) (1-1+P)*
-0.01414 (2-1+P) (1+1+D)*
 0.04066 (2-1+P) (2+1+D)*
 0.03149 (2-1+P) (2-1+P)*
-0.02405 (2-1+P) (3-1+F)*
 0.02571 (2-1+P) (2-1+F)*
 0.02000 (2-1-P) (1+1-S)*
 0.02449 (2-1-P) (1-1-P)*
 0.01414 (2-1-P) (1+1-D)*
-0.04066 (2-1-P) (2+1-D)*
-0.03149 (2-1-P) (2-1-P)*
 0.02405 (2-1-P) (3-1-F)*
-0.02571 (2-1-P) (2-1-F)*
 0.00436 (3-1+F) (1+1+S)*
 0.00535 (3-1+F) (1-1+P)*
 0.00309 (3-1+F) (1+1+D)*
-0.03105 (3-1+F) (2+1+D)*
-0.02405 (3-1+F) (2-1+P)*
 0.04899 (3-1+F) (3-1+F)*
-0.01964 (3-1+F) (2-1+F)*
-0.00436 (3-1-F) (1+1-S)*
-0.00535 (3-1-F) (1-1-P)*
-0.00309 (3-1-F) (1+1-D)*
 0.03105 (3-1-F) (2+1-D)*
 0.02405 (3-1-F) (2-1-P)*
-0.04899 (3-1-F) (3-1-F)*
 0.01964 (3-1-F) (2-1-F)*
-0.01633 (2-1+F) (1+1+S)*
-0.02000 (2-1+F) (1-1+P)*
-0.01155 (2-1+F) (1+1+D)*
 0.03320 (2-1+F) (2+1+D)*
 0.02571 (2-1+F) (2-1+P)*
-0.01964 (2-1+F) (3-1+F)*
 0.02100 (2-1+F) (2-1+F)*
 0.01633 (2-1-F) (1+1-S)*
 0.02000 (2-1-F) (1-1-P)*
 0.01155 (2-1-F) (1+1-D)*
-0.03320 (2-1-F) (2+1-D)*
-0.02571 (2-1-F) (2-1-P)*
 0.01964 (2-1-F) (3-1-F)*
-0.02100 (2-1-F) (2-1-F)*


H( 2 2 2-1)=
 0.04899 (1+1+S) (1+1+S)*
 0.03000 (1+1+S) (1-1+P)*
-0.01732 (1+1+S) (1+1+D)*
 0.01291 (1+1+S) (2+1+D)*
-0.01000 (1+1+S) (2-1+P)*
-0.00873 (1+1+S) (3-1+F)*
 0.03266 (1+1+S) (2-1+F)*
-0.04899 (1+1-S) (1+1-S)*
-0.03000 (1+1-S) (1-1-P)*
 0.01732 (1+1-S) (1+1-D)*
-0.01291 (1+1-S) (2+1-D)*
 0.01000 (1+1-S) (2-1-P)*
 0.00873 (1+1-S) (3-1-F)*
-0.03266 (1+1-S) (2-1-F)*
 0.03000 (1-1+P) (1+1+S)*
-0.04243 (1-1+P) (1+1+D)*

-0.02449 (1-1+P) (2-1+P)*
 0.03000 (1-1+P) (2-1+F)*
-0.03000 (1-1-P) (1+1-S)*
 0.04243 (1-1-P) (1+1-D)*
 0.02449 (1-1-P) (2-1-P)*
-0.03000 (1-1-P) (2-1-F)*
-0.01732 (1+1+D) (1+1+S)*
-0.04243 (1+1+D) (1-1+P)*
-0.04899 (1+1+D) (1+1+D)*
-0.01826 (1+1+D) (2+1+D)*
-0.02828 (1+1+D) (2+1+P)*
 0.01234 (1+1+D) (3-1+F)*
 0.00577 (1+1+D) (2-1+F)*
 0.01732 (1+1-D) (1+1-S)*
 0.04243 (1+1-D) (1-1-P)*
 0.04899 (1+1-D) (1+1-D)*
 0.01826 (1+1-D) (2+1-D)*
 0.02828 (1+1-D) (2-1-P)*
-0.01234 (1+1-D) (3-1-F)*
-0.00577 (1+1-D) (2-1-F)*
 0.01291 (2+1+D) (1+1+S)*
-0.01826 (2+1+D) (1+1+D)*
 0.01355 (2+1+D) (2+1+P)*
-0.01660 (2+1+D) (2+1+F)*
-0.01291 (2+1-D) (1+1-S)*
 0.01826 (2+1-D) (1+1-D)*
-0.01355 (2+1-D) (2-1-P)*
 0.01660 (2+1-D) (2-1-F)*
-0.01000 (2-1+P) (1+1+S)*
-0.02449 (2-1+P) (1-1+P)*
-0.02828 (2-1+P) (1+1+D)*
 0.01355 (2-1+P) (2+1+D)*
 0.02100 (2-1+P) (2+1+P)*
 0.01604 (2-1+P) (3-1+F)*
-0.00429 (2-1+P) (2-1+F)*
 0.01000 (2-1-P) (1+1-S)*
 0.02449 (2-1-P) (1-1-P)*
 0.02828 (2-1-P) (1+1-D)*
-0.01355 (2-1-P) (2+1-D)*
-0.02100 (2-1-P) (2-1-P)*
-0.01604 (2-1-P) (3-1-F)*
 0.00429 (2-1-P) (2-1-F)*
-0.00873 (3-1+F) (1+1+S)*
 0.01234 (3-1+F) (1+1+D)*
 0.01604 (3-1+F) (2-1+P)*
-0.01964 (3-1+F) (2-1+F)*
 0.00873 (3-1-F) (1+1-S)*
-0.01234 (3-1-F) (1+1-D)*
-0.01604 (3-1-F) (2-1-P)*
 0.01964 (3-1-F) (2-1-F)*
 0.03266 (2-1+F) (1+1+S)*
 0.03000 (2-1+F) (1-1+P)*
 0.00577 (2-1+F) (1+1+D)*
-0.01660 (2-1+F) (2+1+D)*
-0.00429 (2-1+F) (2-1+P)*
-0.01964 (2-1+F) (3-1+F)*
-0.02100 (2-1+F) (2-1+F)*
-0.03266 (2-1-F) (1+1-S)*
-0.03000 (2-1-F) (1-1-P)*
-0.00577 (2-1-F) (1+1-D)*
 0.01660 (2-1-F) (2+1-D)*
 0.00429 (2-1-F) (2-1-P)*
 0.01964 (2-1-F) (3-1-F)*
 0.02100 (2-1-F) (2-1-F)*


H( 2 2 2 0)=
 0.04899 (1+1+S) (1+1+S)*
-0.03464 (1+1+S) (1+1+D)*
 0.02582 (1+1+S) (2+1+D)*
-0.04899 (1+1-S) (1+1-S)*
 0.03464 (1+1-S) (1+1-D)*
-0.02582 (1+1-S) (2+1-D)*
-0.02449 (1-1+P) (1-1+P)*
-0.02449 (1-1+P) (2-1+P)*
-0.01069 (1-1+P) (3-1+F)*
-0.02000 (1-1+P) (2-1+F)*
 0.02449 (1-1-P) (1-1-P)*
 0.02449 (1-1-P) (2-1-P)*
 0.01069 (1-1-P) (3-1-F)*
 0.02000 (1-1-P) (2-1-F)*
```

```
-0.03464 (1+1+D) (1+1+S)*
 0.07348 (1+1+D) (1+1+D)*
 0.01826 (1+1+D) (2+1+D)*
 0.03464 (1+1-D) (1+1-S)*
-0.07348 (1+1-D) (1+1-D)*
-0.01826 (1+1-D) (2+1-D)*
 0.02582 (2+1+D) (1+1+S)*
 0.01826 (2+1+D) (1+1+D)*
 0.01750 (2+1+D) (2+1+D)*
-0.02582 (2+1-D) (1+1-S)*
-0.01826 (2+1-D) (1+1-D)*
-0.01750 (2+1-D) (2+1-D)*
-0.02449 (2-1+P) (1-1+P)*
 0.01750 (2-1+P) (2-1+P)*
 0.01604 (2-1+P) (3-1+F)*
-0.04286 (2-1+P) (2-1+F)*
 0.02449 (2-1-P) (1-1-P)*
-0.01750 (2-1-P) (2-1-P)*
-0.01604 (2-1-P) (3-1-F)*
 0.04286 (2-1-P) (2-1-F)*
-0.01069 (3-1+F) (1-1+P)*
 0.01604 (3-1+F) (2-1+P)*
 0.02449 (3-1+F) (3-1+F)*
 0.01309 (3-1+F) (2-1+F)*
 0.01069 (3-1-F) (1-1-P)*
-0.01604 (3-1-F) (2-1-P)*
-0.02449 (3-1-F) (3-1-F)*
-0.01309 (3-1-F) (2-1-F)*
-0.02000 (2-1+F) (1-1+P)*
-0.04286 (2-1+F) (2-1+P)*
 0.01309 (2-1+F) (3-1+F)*
 0.03499 (2-1+F) (2-1+F)*
 0.02000 (2-1-F) (1-1-P)*
 0.04286 (2-1-F) (2-1-P)*
-0.01309 (2-1-F) (3-1-F)*
-0.03499 (2-1-F) (2-1-F)*


H( 2 2 2 1)=
 0.04899 (1+1+S) (1+1+S)*
-0.03000 (1+1+S) (1-1+P)*
-0.01732 (1+1+S) (1+1+D)*
 0.01291 (1+1+S) (2+1+D)*
 0.01000 (1+1+S) (2-1+P)*
 0.00873 (1+1+S) (3-1+F)*
-0.03266 (1+1+S) (2-1+F)*
-0.04899 (1+1-S) (1+1-S)*
 0.03000 (1+1-S) (1-1-P)*
 0.01732 (1+1-S) (1+1-D)*
-0.01291 (1+1-S) (2+1-D)*
-0.01000 (1+1-S) (2-1-P)*
-0.00873 (1+1-S) (3-1-F)*
 0.03266 (1+1-S) (2-1-F)*
-0.03000 (1-1+P) (1+1+S)*
 0.04243 (1-1+P) (1+1+D)*
-0.02449 (1-1+P) (2-1+P)*
 0.03000 (1-1+P) (2-1+F)*
 0.03000 (1-1-P) (1+1-S)*
-0.04243 (1-1-P) (1+1-D)*
 0.02449 (1-1-P) (2-1-P)*
-0.03000 (1-1-P) (2-1-F)*
-0.01732 (1+1+D) (1+1+S)*
 0.04243 (1+1+D) (1-1+P)*
-0.04899 (1+1+D) (1+1+D)*
-0.01826 (1+1+D) (2+1+D)*
 0.02828 (1+1+D) (2-1+P)*
-0.01234 (1+1+D) (3-1+F)*
-0.00577 (1+1+D) (2-1+F)*
 0.01732 (1+1-D) (1+1-S)*
-0.04243 (1+1-D) (1-1-P)*
 0.04899 (1+1-D) (1+1-D)*
 0.01826 (1+1-D) (2+1-D)*
-0.02828 (1+1-D) (2-1-P)*
 0.01234 (1+1-D) (3-1-F)*
 0.00577 (1+1-D) (2-1-F)*
 0.01291 (2+1+D) (1+1+S)*
-0.01826 (2+1+D) (1+1+D)*
-0.01355 (2+1+D) (2-1+P)*
 0.01660 (2+1+D) (2-1+F)*
-0.01291 (2+1-D) (1+1-S)*
 0.01826 (2+1-D) (1+1-D)*
 0.01355 (2+1-D) (2-1-P)*
-0.01660 (2+1-D) (2-1-F)*
 0.01000 (2-1+P) (1+1+S)*
-0.02449 (2-1+P) (1-1+P)*
 0.02828 (2-1+P) (1+1+D)*
-0.01355 (2-1+P) (2+1+D)*
 0.02100 (2-1+P) (2-1+P)*
 0.01604 (2-1+P) (3-1+F)*
-0.00429 (2-1+P) (2-1+F)*
-0.01000 (2-1-P) (1+1-S)*
 0.02449 (2-1-P) (1-1-P)*
-0.02828 (2-1-P) (1+1-D)*
 0.01355 (2-1-P) (2+1-D)*
-0.02100 (2-1-P) (2-1-P)*
-0.01604 (2-1-P) (3-1-F)*
 0.00429 (2-1-P) (2-1-F)*
 0.00873 (3-1+F) (1+1+S)*
-0.01234 (3-1+F) (1+1+D)*
 0.01604 (3-1+F) (2-1+P)*
-0.01964 (3-1+F) (2-1+F)*
-0.00873 (3-1-F) (1+1-S)*
 0.01234 (3-1-F) (1+1-D)*
-0.01604 (3-1-F) (2-1-P)*
 0.01964 (3-1-F) (2-1-F)*
-0.03266 (2-1+F) (1+1+S)*
 0.03000 (2-1+F) (1-1+P)*
-0.00577 (2-1+F) (1+1+D)*
 0.01660 (2-1+F) (2+1+D)*
-0.00429 (2-1+F) (2-1+P)*
-0.01964 (2-1+F) (3-1+F)*
-0.02100 (2-1+F) (2-1+F)*
 0.03266 (2-1-F) (1+1-S)*
-0.03000 (2-1-F) (1-1-P)*
 0.00577 (2-1-F) (1+1-D)*
-0.01660 (2-1-F) (2+1-D)*
 0.00429 (2-1-F) (2-1-P)*
 0.01964 (2-1-F) (3-1-F)*
 0.02100 (2-1-F) (2-1-F)*


H( 2 2 2 2)=
 0.04899 (1+1+S) (1+1+S)*
-0.06000 (1+1+S) (1-1+P)*
 0.03464 (1+1+S) (1+1+D)*
-0.02582 (1+1+S) (2+1+D)*
 0.02000 (1+1+S) (2-1+P)*
-0.00436 (1+1+S) (3-1+F)*
 0.01633 (1+1+S) (2-1+F)*
-0.04899 (1+1-S) (1+1-S)*
 0.06000 (1+1-S) (1-1-P)*
-0.03464 (1+1-S) (1+1-D)*
 0.02582 (1+1-S) (2+1-D)*
-0.02000 (1+1-S) (2-1-P)*
 0.00436 (1+1-S) (3-1-F)*
-0.01633 (1+1-S) (2-1-F)*
-0.06000 (1-1+P) (1+1+S)*
 0.07348 (1-1+P) (1-1+P)*
-0.04243 (1-1+P) (1+1+D)*
 0.03162 (1-1+P) (2+1+D)*
-0.02449 (1-1+P) (2-1+P)*
 0.00535 (1-1+P) (3-1+F)*
-0.02000 (1-1+P) (2-1+F)*
 0.06000 (1-1-P) (1+1-S)*
-0.07348 (1-1-P) (1-1-P)*
 0.04243 (1-1-P) (1+1-D)*
-0.03162 (1-1-P) (2+1-D)*
 0.02449 (1-1-P) (2-1-P)*
-0.00535 (1-1-P) (3-1-F)*
 0.02000 (1-1-P) (2-1-F)*
 0.03464 (1+1+D) (1+1+S)*
-0.04243 (1+1+D) (1-1+P)*
 0.02449 (1+1+D) (1+1+D)*
-0.01826 (1+1+D) (2+1+D)*
 0.01414 (1+1+D) (2-1+P)*
-0.00309 (1+1+D) (3-1+F)*
 0.01155 (1+1+D) (2-1+F)*
-0.03464 (1+1-S) (1+1-S)*
 0.04243 (1+1-D) (1-1-P)*
-0.02449 (1+1-D) (2-1-P)*
 0.01414 (1+1-D) (2-1-F)*
 0.00429 (2-1+P) (1+1+S)*
-0.01234 (2-1+P) (1+1+D)*
 0.01604 (2-1+P) (2-1+P)*
-0.01964 (2-1+P) (2-1+F)*
-0.00873 (2-1-P) (1+1-S)*
 0.01234 (2-1-P) (1+1-D)*
-0.01604 (2-1-P) (2-1-P)*
 0.01964 (2-1-P) (2-1-F)*
-0.03266 (2-1+F) (1+1+S)*
 0.03000 (2-1+F) (1-1+P)*
-0.00577 (2-1+F) (1+1+D)*
 0.01660 (2-1+F) (2+1+D)*
-0.00429 (2-1+F) (2-1+P)*
-0.01964 (2-1+F) (3-1+F)*
-0.02100 (2-1+F) (2-1+F)*
 0.03266 (2-1-F) (1+1-S)*
-0.03000 (2-1-F) (1-1-P)*
 0.00577 (2-1-F) (1+1-D)*
-0.01660 (2-1-F) (2+1-D)*
 0.00429 (2-1-F) (2-1-P)*
 0.01964 (2-1-F) (3-1-F)*
 0.02100 (2-1-F) (2-1-F)*


 0.00309 (1+1-D) (3-1-F)*
-0.01155 (1+1-D) (2-1-F)*
-0.02582 (2+1+D) (1+1+S)*
 0.03162 (2+1+D) (1-1+P)*
-0.01826 (2+1+D) (1+1+D)*
 0.05249 (2+1+D) (2+1+D)*
-0.04066 (2+1+D) (2-1+P)*
 0.03105 (2+1+D) (3-1+F)*
-0.03320 (2+1+D) (2-1+F)*
 0.02582 (2+1-D) (1+1-S)*
-0.03162 (2+1-D) (1-1-P)*
 0.01826 (2+1-D) (1+1-D)*
-0.05249 (2+1-D) (2+1-D)*
 0.04066 (2+1-D) (2-1-P)*
-0.03105 (2+1-D) (3-1-F)*
 0.03320 (2+1-D) (2-1-F)*
 0.02000 (2-1+P) (1+1+S)*
-0.02449 (2-1+P) (1-1+P)*
 0.01414 (2-1+P) (1+1+D)*
-0.04066 (2-1+P) (2+1+D)*
 0.03149 (2-1+P) (2-1+P)*
-0.02405 (2-1+P) (3-1+F)*
 0.02571 (2-1+P) (2-1+F)*
-0.02000 (2-1-P) (1+1-S)*
 0.02449 (2-1-P) (1-1-P)*
-0.01414 (2-1-P) (1+1-D)*
 0.04066 (2-1-P) (2+1-D)*
-0.03149 (2-1-P) (2-1-P)*
 0.02405 (2-1-P) (3-1-F)*
-0.02571 (2-1-P) (2-1-F)*
-0.00436 (3-1+F) (1+1+S)*
 0.00535 (3-1+F) (1-1+P)*
-0.00309 (3-1+F) (1+1+D)*
 0.03105 (3-1+F) (2+1+D)*
-0.02405 (3-1+F) (2-1+P)*
 0.04899 (3-1+F) (3-1+F)*
-0.01964 (3-1+F) (2-1+F)*
 0.00436 (3-1-F) (1+1-S)*
-0.00535 (3-1-F) (1-1-P)*
 0.00309 (3-1-F) (1+1-D)*
-0.03105 (3-1-F) (2+1-D)*
 0.02405 (3-1-F) (2-1-P)*
-0.04899 (3-1-F) (3-1-F)*
 0.01964 (3-1-F) (2-1-F)*
-0.02000 (2-1+F) (1-1+P)*
 0.01155 (2-1+F) (1+1+D)*
-0.03320 (2-1+F) (2+1+D)*
 0.02571 (2-1+F) (2-1+P)*
-0.01964 (2-1+F) (3-1+F)*
 0.02100 (2-1+F) (2-1+F)*
-0.01633 (2-1-F) (1+1-S)*
 0.02000 (2-1-F) (1-1-P)*
-0.01155 (2-1-F) (1+1-D)*
 0.03320 (2-1-F) (2+1-D)*
-0.02571 (2-1-F) (2-1-P)*
 0.01964 (2-1-F) (3-1-F)*
-0.02100 (2-1-F) (2-1-F)*


H( 3 0 0 0)=
-0.24744 (1+0+S) (2-0+F)*
-0.26726 (1+1+S) (3-1+F)*
 0.14286 (1+1+S) (2-1+F)*
-0.26726 (1+1-S) (3-1-F)*
 0.14286 (1+1-S) (2-1-F)*
-0.19166 (1-0-P) (2+0-D)*
 0.11066 (1-1+P) (2+1+D)*
 0.11066 (1-1-P) (2+1-D)*
-0.25714 (1+0+D) (2-0+P)*
 0.13997 (1+0+D) (2-0+F)*
 0.14846 (1+1+D) (2-1+P)*
-0.18898 (1+1+D) (3-1+F)*
-0.08081 (1+1+D) (2-1+F)*
 0.14846 (1+1-D) (2-1-P)*
-0.18898 (1+1-D) (3-1-F)*
-0.08081 (1+1-D) (2-1-F)*
-0.19166 (2+0-D) (1-0-P)*
 0.07968 (2+0-D) (3-0-F)*
 0.11066 (2+1+D) (1-1+P)*
-0.22131 (2+1+D) (2-1+P)*
```

```
 0.02817 (2+1+D) (3-1+F)*
-0.18070 (2+1+D) (2-1+F)*
 0.11066 (2+1-D) (1-1-P)*
-0.22131 (2+1-D) (2-1-P)*
 0.02817 (2+1-D) (3-1-F)*
-0.18070 (2+1-D) (2-1-F)*
-0.25714 (2-0+P) (1+0+D)*
 0.14846 (2-1+P) (1+1+D)*
-0.22131 (2-1+P) (2+1+D)*
 0.14846 (2-1-P) (1+1-D)*
-0.22131 (2-1-P) (2+1-D)*
 0.07968 (3-0-F) (2+0-D)*
-0.26726 (3-1+F) (1+1+S)*
-0.18898 (3-1+F) (1+1+D)*
 0.02817 (3-1+F) (2+1+D)*
-0.26726 (3-1-F) (1+1-S)*
-0.18898 (3-1-F) (1+1-D)*
 0.02817 (3-1-F) (2+1-D)*
-0.24744 (2-0+F) (1+0+S)*
 0.13997 (2-0+F) (1+0+D)*
 0.14286 (2-1+F) (1+1+S)*
-0.08081 (2-1+F) (1+1+D)*
-0.18070 (2-1+F) (2+1+D)*
 0.14286 (2-1-F) (1+1-S)*
-0.08081 (2-1-F) (1+1-D)*
-0.18070 (2-1-F) (2+1-D)*


H( 3 0 2 0)=
 0.07273 (1+0+S) (2-0+P)*
-0.03959 (1+0+S) (2-0+F)*
-0.04199 (1+1+S) (2-1+P)*
 0.05345 (1+1+S) (3-1+F)*
 0.02286 (1+1+S) (2-1+F)*
-0.04199 (1+1-S) (2-1-P)*
 0.05345 (1+1-S) (3-1-F)*
 0.02286 (1+1-S) (2-1-F)*
 0.03833 (1-0-P) (2+0-D)*
-0.02213 (1-1+P) (2+1+D)*
-0.02213 (1-1-P) (2+1-D)*
-0.05143 (1+0+D) (2-0+P)*
 0.09798 (1+0+D) (2-0+F)*
 0.02969 (1+1+D) (2-1+P)*
 0.03780 (1+1+D) (3-1+F)*
-0.05657 (1+1+D) (2-1+F)*
 0.02969 (1+1-D) (2-1-P)*
 0.03780 (1+1-D) (3-1-F)*
-0.05657 (1+1-D) (2-1-F)*
 0.03833 (2+0-D) (1-0-P)*
-0.01594 (2+0-D) (3-0-F)*
-0.02213 (2+1+D) (1-1+P)*
 0.04426 (2+1+D) (2-1+P)*
-0.00563 (2+1+D) (3-1+F)*
 0.03614 (2+1+D) (2-1+F)*
-0.02213 (2+1-D) (1-1-P)*
 0.04426 (2+1-D) (2-1-P)*
-0.00563 (2+1-D) (3-1-F)*
 0.03614 (2+1-D) (2-1-F)*
 0.07273 (2-0+P) (1+0+S)*
-0.05143 (2-0+P) (1+0+D)*
-0.04199 (2-1+P) (1+1+S)*
 0.02969 (2-1+P) (1+1+D)*
 0.04426 (2-1+P) (2+1+D)*
-0.04199 (2-1-P) (1+1-S)*
 0.02969 (2-1-P) (1+1-D)*
 0.04426 (2-1-P) (2+1-D)*
-0.01594 (3-0-F) (2+0-D)*
 0.05345 (3-1+F) (1+1+S)*
 0.03780 (3-1+F) (1+1+D)*
-0.00563 (3-1+F) (2+1+D)*
 0.05345 (3-1-F) (1+1-S)*
 0.03780 (3-1-F) (1+1-D)*
-0.00563 (3-1-F) (2+1-D)*
-0.03959 (2-0+F) (1+0+S)*
 0.09798 (2-0+F) (1+0+D)*
 0.02286 (2-1+F) (1+1+S)*
-0.05657 (2-1+F) (1+1+D)*
 0.03614 (2-1+F) (2+1+D)*
 0.02286 (2-1-F) (1+1-S)*
-0.05657 (2-1-F) (1+1-D)*
 0.03614 (2-1-F) (2+1-D)*


H( 3 0 2 1)=
 0.06857 (1+0+S) (2-0+P)*
-0.01400 (1+0+S) (2-0+F)*
-0.03959 (1+1+S) (2-1+P)*
 0.01890 (1+1+S) (3-1+F)*
 0.00808 (1+1+S) (2-1+F)*
-0.03959 (1+1-S) (2-1-P)*
 0.01890 (1+1-S) (3-1-F)*
 0.00808 (1+1-S) (2-1-F)*
-0.02424 (1+0+D) (2-0+P)*
-0.06928 (1+0+D) (2-0+F)*
 0.01400 (1+1+D) (2-1+P)*
-0.02673 (1+1+D) (3-1+F)*
 0.04000 (1+1+D) (2-1+F)*
 0.01400 (1+1-D) (2-1-P)*
-0.02673 (1+1-D) (3-1-F)*
 0.04000 (1+1-D) (2-1-F)*
 0.03130 (2+1+D) (2-1+P)*
-0.03833 (2+1+D) (2-1+F)*
 0.03130 (2+1-D) (2-1-P)*
-0.03833 (2+1-D) (2-1-F)*
 0.06857 (2-0+P) (1+0+S)*
-0.02424 (2-0+P) (1+0+D)*
-0.03959 (2-1+P) (1+1+S)*
 0.01400 (2-1+P) (1+1+D)*
 0.03130 (2-1+P) (2+1+D)*
-0.03959 (2-1-P) (1+1-S)*
 0.01400 (2-1-P) (1+1-D)*
 0.03130 (2-1-P) (2+1-D)*
 0.01890 (3-1+F) (1+1+S)*
-0.02673 (3-1+F) (1+1+D)*
 0.01890 (3-1-F) (1+1-S)*
-0.02673 (3-1-F) (1+1-D)*
-0.01400 (2-0+F) (1+0+S)*
-0.06928 (2-0+F) (1+0+D)*
 0.00808 (2-1+F) (1+1+S)*
 0.04000 (2-1+F) (1+1+D)*
-0.03833 (2-1+F) (2+1+D)*
 0.00808 (2-1-F) (1+1-S)*
 0.04000 (2-1-F) (1+1-D)*
-0.03833 (2-1-F) (2+1-D)*


H( 3 0 2 2)=
 0.05421 (1+0+S) (2-0+P)*
 0.04426 (1+0+S) (2-0+F)*
-0.03130 (1+1+S) (2-1+P)*
-0.05976 (1+1+S) (3-1+F)*
-0.02556 (1+1+S) (2-1+F)*
-0.03130 (1+1-S) (2-1-P)*
-0.05976 (1+1-S) (3-1-F)*
-0.02556 (1+1-S) (2-1-F)*
-0.08571 (1-0-P) (2+0-D)*
 0.04949 (1-1+P) (2+1+D)*
 0.04949 (1-1-P) (2+1-D)*
 0.03833 (1+0+D) (2-0+P)*
 0.03130 (1+0+D) (2-0+F)*
-0.02213 (1+1+D) (2-1+P)*
-0.04226 (1+1+D) (3-1+F)*
-0.01807 (1+1+D) (2-1+F)*
-0.02213 (1+1-D) (2-1-P)*
-0.04226 (1+1-D) (3-1-F)*
-0.01807 (1+1-D) (2-1-F)*
-0.08571 (2+0-D) (1-0-P)*
-0.05345 (2+0-D) (3-0-F)*
 0.04949 (2+1+D) (1-1+P)*
-0.01890 (2+1+D) (3-1+F)*
 0.04949 (2+1-D) (1-1-P)*
-0.01890 (2+1-D) (3-1-F)*
 0.05421 (2-0+P) (1+0+S)*
 0.03833 (2-0+P) (1+0+D)*
-0.03130 (2-1+P) (1+1+S)*
-0.02213 (2-1+P) (1+1+D)*
-0.03130 (2-1-P) (1+1-S)*
-0.02213 (2-1-P) (1+1-D)*
-0.05345 (3-0-F) (2+0-D)*
-0.05976 (3-1+F) (1+1+S)*
-0.04226 (3-1+F) (1+1+D)*
-0.01890 (3-1+F) (2+1+D)*
-0.05976 (3-1-F) (1+1-S)*
-0.04226 (3-1-F) (1+1-D)*
-0.01890 (3-1-F) (2+1-D)*
 0.04426 (2-0+F) (1+0+S)*
 0.03130 (2-0+F) (1+0+D)*
-0.02556 (2-1+F) (1+1+S)*
-0.01807 (2-1+F) (1+1+D)*
-0.02556 (2-1-F) (1+1-S)*
-0.01807 (2-1-F) (1+1-D)*


H( 3 1 0 0)=
 0.07715 (1+0+S) (3-1+F)*
-0.16496 (1+0+S) (2-1+F)*
-0.14286 (1+1+S) (2-0+F)*
 0.18898 (1+1-S) (3-0-F)*
-0.12778 (1-0-P) (2+1-D)*
-0.11066 (1-1-P) (2+0-D)*
-0.17143 (1+0+D) (2-1+P)*
 0.05455 (1+0+D) (3-1+F)*
 0.09331 (1+0+D) (2-1+F)*
-0.14846 (1+1+D) (2-0+P)*
 0.08081 (1+1+D) (2-0+F)*
 0.13363 (1+1-D) (3-0-F)*
-0.11066 (2+0-D) (1-1-P)*
 0.11066 (2+0-D) (2-1-P)*
 0.04226 (2+0-D) (3-1-F)*
 0.09035 (2+0-D) (2-1-F)*
 0.11066 (2+1+D) (2-0+P)*
 0.09035 (2+1+D) (2-0+F)*
-0.12778 (2+1-D) (1-0-P)*
 0.01992 (2+1-D) (3-0-F)*
-0.14846 (2-0+P) (1+1+D)*
 0.11066 (2-0+P) (2+1+D)*
-0.17143 (2-1+P) (1+0+D)*
 0.11066 (2-1-P) (2+0-D)*
 0.18898 (3-0-F) (1+1-S)*
 0.13363 (3-0-F) (1+1-D)*
 0.01992 (3-0-F) (2+1-D)*
 0.07715 (3-1+F) (1+0+S)*
 0.05455 (3-1+F) (1+0+D)*
 0.04226 (3-1-F) (2+0-D)*
-0.14286 (2-0+F) (1+1+S)*
 0.08081 (2-0+F) (1+1+D)*
 0.09035 (2-0+F) (2+1+D)*
-0.16496 (2-1+F) (1+0+S)*
 0.09331 (2-1+F) (1+0+D)*
 0.09035 (2-1-F) (2+0-D)*


H( 3 1 2-2)=
 0.04666 (1+0+S) (2+1+D)*
 0.03614 (1+0+S) (2-1+P)*
 0.01725 (1+0+S) (3-1+F)*
 0.02951 (1+0+S) (2-1+F)*
 0.03130 (1+1+S) (2-0+P)*
 0.02556 (1+1+S) (2-0+F)*
-0.04041 (1+1-S) (2+0-D)*
 0.04226 (1+1-S) (3-0-F)*
-0.05714 (1-0-P) (2+1-D)*
-0.04426 (1-0-P) (2-1-P)*
-0.02113 (1-0-P) (3-1-F)*
-0.03614 (1-0-P) (2-1-F)*
 0.03833 (1-1+P) (2-0+P)*
 0.03130 (1-1+P) (2-0+F)*
-0.04949 (1-1-P) (2+0-D)*
 0.05175 (1-1-P) (3-0-F)*
 0.03299 (1+0+D) (2+1+D)*
 0.02556 (1+0+D) (2-1+P)*
 0.01220 (1+0+D) (3-1+F)*
 0.02087 (1+0+D) (2-1+F)*
 0.02213 (1+1+D) (2-0+P)*
 0.01807 (1+1+D) (2-0+F)*
-0.02857 (1+1-D) (2+0-D)*
 0.02988 (1+1-D) (3-0-F)*
-0.04041 (2+0-D) (1+1-S)*
-0.04949 (2+0-D) (1-1-P)*
-0.02857 (2+0-D) (1+1-D)*
-0.02835 (2+0-D) (3-1-F)*
 0.04666 (2+1+D) (1+0+S)*
 0.03299 (2+1+D) (1+0+D)*
```

```
-0.05714 (2+1-D) (1-0-P)*
-0.01336 (2+1-D) (3-0-F)*
 0.03130 (2-0+P) (1+1+S)*
 0.03833 (2-0+P) (1-1+P)*
 0.02213 (2-0+P) (1+1+D)*
 0.02196 (2-0+P) (3-1+F)*
 0.03614 (2-1+P) (1+0+S)*
 0.02556 (2-1+P) (1+0+D)*
-0.04426 (2-1-P) (1-0-P)*
-0.01035 (2-1-P) (3-0-F)*
 0.04226 (3-0-F) (1+1-S)*
 0.05175 (3-0-F) (1-1-P)*
 0.02988 (3-0-F) (1+1-D)*
-0.01336 (3-0-F) (2+1-D)*
-0.01035 (3-0-F) (2-1-P)*
-0.00845 (3-0-F) (2-1-F)*
 0.01725 (3-1+F) (1+0+S)*
 0.01220 (3-1+F) (1+0+D)*
 0.02196 (3-1+F) (2-0+P)*
 0.01793 (3-1+F) (2-0+F)*
-0.02113 (3-1-F) (1-0-P)*
-0.02835 (3-1-F) (2+0-D)*
 0.02556 (2-0+F) (1+1+S)*
 0.03130 (2-0+F) (1-1+P)*
 0.01807 (2-0+F) (1+1+D)*
 0.01793 (2-0+F) (3-1+F)*
 0.02951 (2-1+F) (1+0+S)*
 0.02087 (2-1+F) (1+0+D)*
-0.03614 (2-1-F) (1-0-P)*
-0.00845 (2-1-F) (3-0-F)*


H( 3 1 2-1)=
-0.06547 (0-0+P) (3-1+F)*
 0.02951 (1+0+S) (2+1+D)*
 0.04571 (1+0+S) (2-1+P)*
-0.00546 (1+0+S) (3-1+F)*
-0.00933 (1+0+S) (2-1+F)*
 0.03959 (1+1+S) (2-0+P)*
-0.00808 (1+1+S) (2-0+F)*
-0.02556 (1+1-S) (2+0-D)*
-0.01336 (1+1-S) (3-0-F)*
-0.02799 (1-0-P) (2-1-P)*
 0.03429 (1-0-P) (2-1-F)*
 0.02424 (1-1+P) (2-0+P)*
-0.02969 (1-1+P) (2-0+F)*
-0.04173 (1+0+D) (2+1+D)*
-0.01616 (1+0+D) (2-1+P)*
 0.00772 (1+0+D) (3-1+F)*
-0.04619 (1+0+D) (2-1+F)*
-0.01400 (1+1+D) (2-0+P)*
-0.04000 (1+1+D) (2-0+F)*
 0.03614 (1+1-D) (2+0-D)*
 0.01890 (1+1-D) (3-0-F)*
-0.02556 (2+0-D) (1+1-S)*
 0.03614 (2+0-D) (1+1-D)*
-0.01565 (2+0-D) (2-1-P)*
 0.01917 (2+0-D) (2-1-F)*
 0.02951 (2+1+D) (1+0+S)*
-0.04173 (2+1+D) (1+0+D)*
-0.01565 (2+1+D) (2-0+P)*
 0.01917 (2+1+D) (2-0+F)*
 0.03959 (2-0+P) (1+1+S)*
 0.02424 (2-0+P) (1-1+P)*
-0.01400 (2-0+P) (1+1+D)*
-0.01565 (2-0+P) (2+1+D)*
 0.01389 (2-0+P) (3-1+F)*
-0.02474 (2-0+P) (2-1+F)*
 0.04571 (2-1+P) (1+0+S)*
-0.01616 (2-1+P) (1+0+D)*
 0.02474 (2-1+P) (2-0+F)*
-0.02799 (2-1-P) (1-0-P)*
-0.01565 (2-1-P) (2+0-D)*
-0.00655 (2-1-P) (3-0-F)*
-0.01336 (3-0-F) (1+1-S)*
 0.01890 (3-0-F) (1+1-D)*
-0.00655 (3-0-F) (2-1-P)*
 0.00802 (3-0-F) (2-1-F)*
-0.06547 (3-1+F) (0-0+P)*
-0.00546 (3-1+F) (1+0+S)*

 0.00772 (3-1+F) (1+0+D)*
 0.01389 (3-1+F) (2-0+P)*
-0.01701 (3-1+F) (2-0+F)*
-0.00808 (2-0+F) (1+1+S)*
-0.02969 (2-0+F) (1-1+P)*
-0.04000 (2-0+F) (1+1+D)*
 0.01917 (2-0+F) (2+1+D)*
 0.02474 (2-0+F) (2-1+P)*
-0.01701 (2-0+F) (3-1+F)*
-0.00933 (2-1+F) (1+0+S)*
-0.04619 (2-1+F) (1+0+D)*
-0.02474 (2-1+F) (2-0+P)*
 0.03429 (2-1-F) (1-0-P)*
 0.01917 (2-1-F) (2+0-D)*
 0.00802 (2-1-F) (3-0-F)*


H( 3 1 2 0)=
 0.04849 (1+0+S) (2-1+P)*
-0.01543 (1+0+S) (3-1+F)*
-0.02639 (1+0+S) (2-1+F)*
 0.04199 (1+1+S) (2-0+P)*
-0.02286 (1+1+S) (2-0+F)*
-0.03780 (1+1-S) (3-0-F)*
 0.02556 (1-0-P) (2+1-D)*
 0.02213 (1-1-P) (2+0-D)*
-0.03429 (1+0+D) (2-1+P)*
-0.01091 (1+0+D) (3-1+F)*
 0.06532 (1+0+D) (2-1+F)*
-0.02969 (1+1+D) (2-0+P)*
 0.05657 (1+1+D) (2-0+F)*
-0.02673 (1+1-D) (3-0-F)*
 0.02213 (2+0-D) (1-1-P)*
-0.02213 (2+0-D) (2-1-P)*
-0.00845 (2+0-D) (3-1-F)*
-0.01807 (2+0-D) (2-1-F)*
-0.02213 (2+1+D) (2-0+P)*
-0.01807 (2+1+D) (2-0+F)*
 0.02556 (2+1-D) (1-0-P)*
-0.00398 (2+1-D) (3-0-F)*
 0.04199 (2-0+P) (1+1+S)*
-0.02969 (2-0+P) (1+1+D)*
-0.02213 (2-0+P) (2+1+D)*
 0.04849 (2-1+P) (1+0+S)*
-0.03429 (2-1+P) (1+0+D)*
-0.02213 (2-1-P) (2+0-D)*
-0.03780 (3-0-F) (1+1-S)*
-0.02673 (3-0-F) (1+1-D)*
-0.00398 (3-0-F) (2+1-D)*
-0.01543 (3-1+F) (1+0+S)*
-0.01091 (3-1+F) (1+0+D)*
-0.00845 (3-1-F) (2+0-D)*
-0.02286 (2-0+F) (1+1+S)*
 0.05657 (2-0+F) (1+1+D)*
-0.01807 (2-0+F) (2+1+D)*
-0.02639 (2-1+F) (1+0+S)*
 0.06532 (2-1+F) (1+0+D)*
-0.01807 (2-1-F) (2+0-D)*


H( 3 1 2 1)=
 0.06547 (0-0+P) (3-1+F)*
-0.02951 (1+0+S) (2+1+D)*
 0.04571 (1+0+S) (2-1+P)*
-0.00546 (1+0+S) (3-1+F)*
-0.00933 (1+0+S) (2-1+F)*
 0.03959 (1+1+S) (2-0+P)*
-0.00808 (1+1+S) (2-0+F)*
 0.02556 (1+1-S) (2+0-D)*
-0.01336 (1+1-S) (3-0-F)*
 0.02799 (1-0-P) (2-1-P)*
-0.03429 (1-0-P) (2-1-F)*
-0.02424 (1-1+P) (2-0+P)*
 0.02969 (1-1+P) (2-0+F)*
 0.04173 (1+0+D) (2+1+D)*
-0.01616 (1+0+D) (2-1+P)*
 0.00772 (1+0+D) (3-1+F)*
-0.04619 (1+0+D) (2-1+F)*
-0.01400 (1+1+D) (2-0+P)*
-0.04000 (1+1+D) (2-0+F)*
-0.03614 (1+1-D) (2+0-D)*

 0.01890 (1+1-D) (3-0-F)*
 0.02556 (2+0-D) (1+1-S)*
-0.03614 (2+0-D) (1+1-D)*
-0.01565 (2+0-D) (2-1-P)*
 0.01917 (2+0-D) (2-1-F)*
-0.02951 (2+1+D) (1+0+S)*
 0.04173 (2+1+D) (1+0+D)*
-0.01565 (2+1+D) (2-0+P)*
 0.01917 (2+1+D) (2-0+F)*
 0.03959 (2-0+P) (1+1+S)*
-0.02424 (2-0+P) (1-1+P)*
-0.01400 (2-0+P) (1+1+D)*
-0.01565 (2-0+P) (2+1+D)*
-0.01389 (2-0+P) (3-1+F)*
 0.02474 (2-0+P) (2-1+F)*
 0.04571 (2-1+P) (1+0+S)*
-0.01616 (2-1+P) (1+0+D)*
-0.02474 (2-1+P) (2-0+F)*
 0.02799 (2-1-P) (1-0-P)*
-0.01565 (2-1-P) (2+0-D)*
 0.00655 (2-1-P) (3-0-F)*
-0.01336 (3-0-F) (1+1-S)*
 0.01890 (3-0-F) (1+1-D)*
 0.00655 (3-0-F) (2-1-P)*
-0.00802 (3-0-F) (2-1-F)*
 0.06547 (3-1+F) (0-0+P)*
-0.00546 (3-1+F) (1+0+S)*
 0.00772 (3-1+F) (1+0+D)*
-0.01389 (3-1+F) (2-0+P)*
 0.01701 (3-1+F) (2-0+F)*
-0.00808 (2-0+F) (1+1+S)*
 0.02969 (2-0+F) (1-1+P)*
-0.04000 (2-0+F) (1+1+D)*
 0.01917 (2-0+F) (2+1+D)*
-0.02474 (2-0+F) (2-1+P)*
 0.01701 (2-0+F) (3-1+F)*
-0.00933 (2-1+F) (1+0+S)*
-0.04619 (2-1+F) (1+0+D)*
 0.02474 (2-1+F) (2-0+P)*
-0.03429 (2-1-F) (1-0-P)*
 0.01917 (2-1-F) (2+0-D)*
-0.00802 (2-1-F) (3-0-F)*


H( 3 1 2 2)=
-0.04666 (1+0+S) (2+1+D)*
 0.03614 (1+0+S) (2-1+P)*
 0.01725 (1+0+S) (3-1+F)*
 0.02951 (1+0+S) (2-1+F)*
 0.03130 (1+1+S) (2-0+P)*
 0.02556 (1+1+S) (2-0+F)*
 0.04041 (1+1-S) (2+0-D)*
 0.04226 (1+1-S) (3-0-F)*
-0.05714 (1-0-P) (2+1-D)*
 0.04426 (1-0-P) (2-1-P)*
 0.02113 (1-0-P) (3-1-F)*
 0.03614 (1-0-P) (2-1-F)*
-0.03833 (1-1+P) (2-0+P)*
-0.03130 (1-1+P) (2-0+F)*
-0.04949 (1-1-P) (2+0-D)*
-0.05175 (1-1-P) (3-0-F)*
-0.03299 (1+0+D) (2+1+D)*
 0.02556 (1+0+D) (2-1+P)*
 0.01220 (1+0+D) (3-1+F)*
 0.02087 (1+0+D) (2-1+F)*
 0.02213 (1+1+D) (2-0+P)*
 0.01807 (1+1+D) (2-0+F)*
 0.02857 (1+1-D) (2+0-D)*
 0.02988 (1+1-D) (3-0-F)*
 0.04041 (2+0-D) (1+1-S)*
-0.04949 (2+0-D) (1-1-P)*
 0.02857 (2+0-D) (1+1-D)*
-0.02835 (2+0-D) (3-1-F)*
-0.04666 (2+1+D) (1+0+S)*
-0.03299 (2+1+D) (1+0+D)*
-0.05714 (2+1-D) (1-0-P)*
-0.01336 (2+1-D) (3-0-F)*
 0.03130 (2-0+P) (1+1+S)*
-0.03833 (2-0+P) (1-1+P)*
 0.02213 (2-0+P) (1+1+D)*
-0.02196 (2-0+P) (3-1+F)*
```

```
 0.03614 (2-1+P) (1+0+S)*
 0.02556 (2-1+P) (1+0+D)*
 0.04426 (2-1-P) (1-0-P)*
 0.01035 (2-1-P) (3-0-F)*
 0.04226 (3-0-F) (1+1-S)*
-0.05175 (3-0-F) (1-1-P)*
 0.02988 (3-0-F) (1+1-D)*
-0.01336 (3-0-F) (2+1-D)*
 0.01035 (3-0-F) (2-1-P)*
 0.00845 (3-0-F) (2-1-F)*
 0.01725 (3-1+F) (1+0+S)*
 0.01220 (3-1+F) (1+0+D)*
-0.02196 (3-1+F) (2-0+P)*
-0.01793 (3-1+F) (2-0+F)*
 0.02113 (3-1-F) (1-0-P)*
-0.02835 (3-1-F) (2+0-D)*
 0.02556 (2-0+F) (1+1+S)*
-0.03130 (2-0+F) (1-1+P)*
 0.01807 (2-0+F) (1+1+D)*
-0.01793 (2-0+F) (3-1+F)*
 0.02951 (2-1+F) (1+0+S)*
 0.02087 (2-1+F) (1+0+D)*
 0.03614 (2-1-F) (1-0-P)*
 0.00845 (2-1-F) (3-0-F)*


H( 3 2 0 0)=
-0.12199 (1+1+S) (3-1+F)*
-0.13041 (1+1+S) (2-1+F)*
 0.12199 (1+1-S) (3-1-F)*
 0.13041 (1+1-S) (2-1-F)*
 0.10102 (1-1+P) (2+1+D)*
-0.10102 (1-1-P) (2+1-D)*
-0.13553 (1+1+D) (2-1+P)*
-0.08626 (1+1+D) (3-1+F)*
 0.07377 (1+1+D) (2-1+F)*
 0.13553 (1+1-D) (2-1-P)*
 0.08626 (1+1-D) (3-1-F)*
-0.07377 (1+1-D) (2-1-F)*
 0.10102 (2+1+D) (1-1+P)*
-0.03858 (2+1+D) (3-1+F)*
-0.10102 (2+1-D) (1-1-P)*
 0.03858 (2+1-D) (3-1-F)*
-0.13553 (2-1+P) (1+1+D)*
 0.13553 (2-1-P) (1+1-D)*
-0.12199 (3-1+F) (1+1+S)*
-0.08626 (3-1+F) (1+1+D)*
-0.03858 (3-1+F) (2+1+D)*
 0.12199 (3-1-F) (1+1-S)*
 0.08626 (3-1-F) (1+1-D)*
 0.03858 (3-1-F) (2+1-D)*
-0.13041 (2-1+F) (1+1+S)*
 0.07377 (2-1+F) (1+1+D)*
 0.13041 (2-1-F) (1+1-S)*
-0.07377 (2-1-F) (1+1-D)*


H( 3 2 2-2)=
 0.03689 (1+1+S) (2+1+D)*
 0.02857 (1+1+S) (2-1+P)*
-0.02728 (1+1+S) (3-1+F)*
 0.02333 (1+1+S) (2-1+F)*
-0.03689 (1+1-S) (2+1-D)*
-0.02857 (1+1-S) (2-1-P)*
 0.02728 (1+1-S) (3-1-F)*
-0.02333 (1+1-S) (2-1-F)*
 0.04518 (1-1+P) (2+1+D)*
 0.03499 (1-1+P) (2-1+P)*
-0.03341 (1-1+P) (3-1+F)*
 0.02857 (1-1+P) (2-1+F)*
-0.04518 (1-1-P) (2+1-D)*
-0.03499 (1-1-P) (2-1-P)*
 0.03341 (1-1-P) (3-1-F)*
-0.02857 (1-1-P) (2-1-F)*
 0.02608 (1+1+D) (2+1+D)*
 0.02020 (1+1+D) (2-1+P)*
-0.01929 (1+1+D) (3-1+F)*
 0.01650 (1+1+D) (2-1+F)*
-0.02608 (1+1-D) (2+1-D)*
-0.02020 (1+1-D) (2-1-P)*
 0.01929 (1+1-D) (3-1-F)*

-0.01650 (1+1-D) (2-1-F)*
 0.03689 (2+1+D) (1+1+S)*
 0.04518 (2+1+D) (1-1+P)*
 0.02608 (2+1+D) (1+1+D)*
 0.02588 (2+1+D) (3-1+F)*
-0.03689 (2+1-D) (1+1-S)*
-0.04518 (2+1-D) (1-1-P)*
-0.02608 (2+1-D) (1+1-D)*
-0.02588 (2+1-D) (3-1-F)*
 0.02857 (2-1+P) (1+1+S)*
 0.03499 (2-1+P) (1-1+P)*
 0.02020 (2-1+P) (1+1+D)*
 0.02004 (2-1+P) (3-1+F)*
-0.02857 (2-1-P) (1+1-S)*
-0.03499 (2-1-P) (1-1-P)*
-0.02020 (2-1-P) (1+1-D)*
-0.02004 (2-1-P) (3-1-F)*
-0.02728 (3-1+F) (1+1+S)*
-0.03341 (3-1+F) (1-1+P)*
-0.01929 (3-1+F) (1+1+D)*
 0.02588 (3-1+F) (2+1+D)*
 0.02004 (3-1+F) (2-1+P)*
 0.01637 (3-1+F) (2-1+F)*
 0.02728 (3-1-F) (1+1-S)*
 0.03341 (3-1-F) (1-1-P)*
 0.01929 (3-1-F) (1+1-D)*
-0.02588 (3-1-F) (2+1-D)*
-0.02004 (3-1-F) (2-1-P)*
-0.01637 (3-1-F) (2-1-F)*
 0.02333 (2-1+F) (1+1+S)*
 0.02857 (2-1+F) (1-1+P)*
 0.01650 (2-1+F) (1+1+D)*
 0.01637 (2-1+F) (3-1+F)*
-0.02333 (2-1-F) (1+1-S)*
-0.02857 (2-1-F) (1-1-P)*
-0.01650 (2-1-F) (1+1-D)*
-0.01637 (2-1-F) (3-1-F)*


H( 3 2 2-1)=
 0.02333 (1+1+S) (2+1+D)*
 0.03614 (1+1+S) (2-1+P)*
 0.00863 (1+1+S) (3-1+F)*
-0.00738 (1+1+S) (2-1+F)*
-0.02333 (1+1-S) (2+1-D)*
-0.03614 (1+1-S) (2-1-P)*
-0.00863 (1+1-S) (3-1-F)*
 0.00738 (1+1-S) (2-1-F)*
 0.02213 (1-1+P) (2+1+D)*
-0.02711 (1-1+P) (2-1+P)*
-0.02213 (1-1-P) (2-1-P)*
 0.02711 (1-1-P) (2-1-F)*
-0.03299 (1+1+D) (2+1+D)*
-0.01278 (1+1+D) (2-1+P)*
-0.01220 (1+1+D) (3-1+F)*
-0.03651 (1+1+D) (2-1+F)*
 0.03299 (1+1-D) (2+1-D)*
 0.01278 (1+1-D) (2-1-P)*
 0.01220 (1+1-D) (3-1-F)*
 0.03651 (1+1-D) (2-1-F)*
 0.02333 (2+1+D) (1+1+S)*
-0.03299 (2+1+D) (1+1+D)*
-0.02333 (2+1-D) (1+1-S)*
 0.03299 (2+1-D) (1+1-D)*
 0.03614 (2-1+P) (1+1+S)*
 0.02213 (2-1+P) (1-1+P)*
-0.01278 (2-1+P) (1+1+D)*
 0.01268 (2-1+P) (3-1+F)*
-0.03614 (2-1-P) (1+1-S)*
-0.02213 (2-1-P) (1-1-P)*
 0.01278 (2-1-P) (1+1-D)*
-0.01268 (2-1-P) (3-1-F)*
 0.00863 (3-1+F) (1+1+S)*
-0.01220 (3-1+F) (1+1+D)*
 0.01268 (3-1+F) (2-1+P)*
-0.01553 (3-1+F) (2-1+F)*
-0.00863 (3-1-F) (1+1-S)*
 0.01220 (3-1-F) (1+1-D)*
-0.01268 (3-1-F) (2-1-P)*
 0.01553 (3-1-F) (2-1-F)*
-0.00738 (2-1+F) (1+1+S)*

-0.02711 (2-1+F) (1-1+P)*
-0.03651 (2-1+F) (1+1+D)*
-0.01553 (2-1+F) (3-1+F)*
 0.00738 (2-1+F) (1+1-S)*
 0.02711 (2-1-F) (1-1-P)*
 0.03651 (2-1-F) (1+1-D)*
 0.01553 (2-1-F) (3-1-F)*


H( 3 2 2 0)=
 0.03833 (1+1+S) (2-1+P)*
 0.02440 (1+1+S) (3-1+F)*
-0.02087 (1+1+S) (2-1+F)*
-0.03833 (1+1-S) (2-1-P)*
-0.02440 (1+1-S) (3-1-F)*
 0.02087 (1+1-S) (2-1-F)*
-0.02020 (1-1+P) (2+1+D)*
 0.02020 (1-1-P) (2+1-D)*
-0.02711 (1+1+D) (2-1+P)*
 0.01725 (1+1+D) (3-1+F)*
 0.05164 (1+1+D) (2-1+F)*
 0.02711 (1+1-D) (2-1-P)*
-0.01725 (1+1-D) (3-1-F)*
-0.05164 (1+1-D) (2-1-F)*
-0.02020 (2+1+D) (1-1+P)*
 0.00772 (2+1+D) (3-1+F)*
 0.02020 (2+1-D) (1-1-P)*
-0.00772 (2+1-D) (3-1-F)*
 0.03833 (2-1+P) (1+1+S)*
-0.02711 (2-1+P) (1+1+D)*
-0.03833 (2-1-P) (1+1-S)*
 0.02711 (2-1-P) (1+1-D)*
 0.02440 (3-1+F) (1+1+S)*
 0.01725 (3-1+F) (1+1+D)*
 0.00772 (3-1+F) (2+1+D)*
-0.02440 (3-1-F) (1+1-S)*
-0.01725 (3-1-F) (1+1-D)*
-0.00772 (3-1-F) (2+1-D)*
-0.02087 (2-1+F) (1+1+S)*
 0.05164 (2-1+F) (1+1+D)*
 0.02087 (2-1-F) (1+1-S)*
-0.05164 (2-1-F) (1+1-D)*


H( 3 2 2 1)=
-0.02333 (1+1+S) (2+1+D)*
 0.03614 (1+1+S) (2-1+P)*
 0.00863 (1+1+S) (3-1+F)*
-0.00738 (1+1+S) (2-1+F)*
 0.02333 (1+1-S) (2+1-D)*
-0.03614 (1+1-S) (2-1-P)*
-0.00863 (1+1-S) (3-1-F)*
 0.00738 (1+1-S) (2-1-F)*
-0.02213 (1-1+P) (2-1+P)*
 0.02711 (1-1+P) (2-1+F)*
 0.02213 (1-1-P) (2-1-P)*
-0.02711 (1-1-P) (2-1-F)*
 0.03299 (1+1+D) (2+1+D)*
-0.01278 (1+1+D) (2-1+P)*
-0.01220 (1+1+D) (3-1+F)*
-0.03651 (1+1+D) (2-1+F)*
-0.03299 (1+1-D) (2+1-D)*
 0.01278 (1+1-D) (2-1-P)*
 0.01220 (1+1-D) (3-1-F)*
 0.03651 (1+1-D) (2-1-F)*
-0.02333 (2+1+D) (1+1+S)*
 0.03299 (2+1+D) (1+1+D)*
 0.02333 (2+1-D) (1+1-S)*
-0.03299 (2+1-D) (1+1-D)*
 0.03614 (2-1+P) (1+1+S)*
-0.02213 (2-1+P) (1-1+P)*
-0.01278 (2-1+P) (1+1+D)*
-0.01268 (2-1+P) (3-1+F)*
-0.03614 (2-1-P) (1+1-S)*
 0.02213 (2-1-P) (1-1-P)*
 0.01278 (2-1-P) (1+1-D)*
 0.01268 (2-1-P) (3-1-F)*
 0.00863 (3-1+F) (1+1+S)*
-0.01220 (3-1+F) (1+1+D)*
-0.01268 (3-1+F) (2-1+P)*
 0.01553 (3-1+F) (2-1+F)*
```

```
-0.00863 (3-1-F) (1+1-S)*
 0.01220 (3-1-F) (1+1-D)*
 0.01268 (3-1-F) (2-1-P)*
-0.01553 (3-1-F) (2-1-F)*
-0.00738 (2-1+F) (1+1+S)*
 0.02711 (2-1+F) (1-1+P)*
-0.03651 (2-1+F) (1+1+D)*
 0.01553 (2-1+F) (3-1+F)*
 0.00738 (2-1-F) (1+1-S)*
-0.02711 (2-1-F) (1-1-P)*
 0.03651 (2-1-F) (1+1-D)*
-0.01553 (2-1-F) (3-1-F)*


H( 3 2 2 2)=
-0.03689 (1+1+S) (2+1+D)*
 0.02857 (1+1+S) (2-1+P)*
-0.02728 (1+1+S) (3-1+F)*
 0.02333 (1+1+S) (2-1+F)*
 0.03689 (1+1-S) (2+1-D)*
-0.02857 (1+1-S) (2-1-P)*
 0.02728 (1+1-S) (3-1-F)*
-0.02333 (1+1-S) (2-1-F)*
 0.04518 (1-1+P) (2+1+D)*
-0.03499 (1-1+P) (2-1+P)*
 0.03341 (1-1+P) (3-1+F)*
-0.02857 (1-1+P) (2-1+F)*
-0.04518 (1-1-P) (2+1-D)*
 0.03499 (1-1-P) (2-1-P)*
-0.03341 (1-1-P) (3-1-F)*
 0.02857 (1-1-P) (2-1-F)*
-0.02608 (1+1+D) (2+1+D)*
 0.02020 (1+1+D) (2-1+P)*
-0.01929 (1+1+D) (3-1+F)*
 0.01650 (1+1+D) (2-1+F)*
 0.02608 (1+1-D) (2+1-D)*
-0.02020 (1+1-D) (2-1-P)*
 0.01929 (1+1-D) (3-1-F)*
-0.01650 (1+1-D) (2-1-F)*
-0.03689 (2+1+D) (1+1+S)*
 0.04518 (2+1+D) (1-1+P)*
-0.02608 (2+1+D) (1+1+D)*
 0.02588 (2+1+D) (3-1+F)*
 0.03689 (2+1-D) (1+1-S)*
-0.04518 (2+1-D) (1-1-P)*
 0.02608 (2+1-D) (1+1-D)*
-0.02588 (2+1-D) (3-1-F)*
 0.02857 (2-1+P) (1+1+S)*
-0.03499 (2-1+P) (1-1+P)*
 0.02020 (2-1+P) (1+1+D)*
-0.02004 (2-1+P) (3-1+F)*
-0.02857 (2-1-P) (1+1-S)*
 0.03499 (2-1-P) (1-1-P)*
-0.02020 (2-1-P) (1+1-D)*
 0.02004 (2-1-P) (3-1-F)*
-0.02728 (3-1+F) (1+1+S)*
 0.03341 (3-1+F) (1-1+P)*
-0.01929 (3-1+F) (1+1+D)*
 0.02588 (3-1+F) (2+1+D)*
-0.02004 (3-1+F) (2-1+P)*
-0.01637 (3-1+F) (2-1+F)*
 0.02728 (3-1-F) (1+1-S)*
-0.03341 (3-1-F) (1-1-P)*
 0.01929 (3-1-F) (1+1-D)*
-0.02588 (3-1-F) (2+1-D)*
 0.02004 (3-1-F) (2-1-P)*
 0.01637 (3-1-F) (2-1-F)*
 0.02333 (2-1+F) (1+1+S)*
-0.02857 (2-1+F) (1-1+P)*
 0.01650 (2-1+F) (1+1+D)*
-0.01637 (2-1+F) (3-1+F)*
-0.02333 (2-1-F) (1+1-S)*
 0.02857 (2-1-F) (1-1-P)*
-0.01650 (2-1-F) (1+1-D)*
 0.01637 (2-1-F) (3-1-F)*


H( 4 0 0 0)=
-0.17817 (1-0-P) (3-0-F)*
 0.10911 (1-1+P) (3-1+F)*
 0.10911 (1-1-P) (3-1-F)*
-0.19048 (2+0-D) (2+0-D)*
 0.12698 (2+1+D) (2+1+D)*
 0.12698 (2+1-D) (2+1-D)*
-0.23328 (2-0+P) (2-0+F)*
-0.18185 (2-1+P) (3-1+F)*
 0.15552 (2-1+P) (2-1+F)*
-0.18185 (2-1-P) (3-1-F)*
 0.15552 (2-1-P) (2-1-F)*
-0.17817 (3-0-F) (1-0-P)*
 0.03030 (3-0-F) (3-0-F)*
 0.10911 (3-1+F) (1-1+P)*
-0.18185 (3-1+F) (2-1+P)*
 0.00505 (3-1+F) (3-1+F)*
-0.14848 (3-1+F) (2-1+F)*
 0.10911 (3-1-F) (1-1-P)*
-0.18185 (3-1-F) (2-1-P)*
 0.00505 (3-1-F) (3-1-F)*
-0.14848 (3-1-F) (2-1-F)*
-0.23328 (2-0+F) (2-0+P)*
 0.09524 (2-0+F) (2-0+F)*
 0.15552 (2-1+F) (2-1+P)*
-0.14848 (2-1+F) (3-1+F)*
-0.06349 (2-1+F) (2-1+F)*
 0.15552 (2-1-F) (2-1-P)*
-0.14848 (2-1-F) (3-1-F)*
-0.06349 (2-1-F) (2-1-F)*


H( 4 0 2 0)=
 0.03563 (1-0-P) (3-0-F)*
-0.02182 (1-1+P) (3-1+F)*
-0.02182 (1-1-P) (3-1-F)*
 0.03810 (2+0-D) (2+0-D)*
-0.02540 (2+1+D) (2+1+D)*
-0.02540 (2+1-D) (2+1-D)*
 0.06857 (2-0+P) (2-0+P)*
-0.03733 (2-0+P) (2-0+F)*
-0.04571 (2-1+P) (2-1+P)*
 0.03637 (2-1+P) (3-1+F)*
 0.02488 (2-1+P) (2-1+F)*
-0.04571 (2-1-P) (2-1-P)*
 0.03637 (2-1-P) (3-1-F)*
 0.02488 (2-1-P) (2-1-F)*
 0.03563 (3-0-F) (1-0-P)*
-0.00606 (3-0-F) (3-0-F)*
-0.02182 (3-1+F) (1-1+P)*
 0.03637 (3-1+F) (2-1+P)*
-0.00101 (3-1+F) (3-1+F)*
 0.02970 (3-1+F) (2-1+F)*
-0.02182 (3-1-F) (1-1-P)*
 0.03637 (3-1-F) (2-1-P)*
-0.00101 (3-1-F) (3-1-F)*
 0.02970 (3-1-F) (2-1-F)*
-0.03733 (2-0+F) (2-0+P)*
 0.08381 (2-0+F) (2-0+F)*
 0.02488 (2-1+F) (2-1+P)*
 0.02970 (2-1+F) (3-1+F)*
-0.05587 (2-1+F) (2-1+F)*
 0.02488 (2-1-F) (2-1-P)*
 0.02970 (2-1-F) (3-1-F)*
-0.05587 (2-1-F) (2-1-F)*


H( 4 0 2 1)=
 0.06260 (2-0+P) (2-0+P)*
-0.01278 (2-0+P) (2-0+F)*
-0.04173 (2-1+P) (2-1+P)*
 0.01992 (2-1+P) (3-1+F)*
 0.00852 (2-1+P) (2-1+F)*
-0.04173 (2-1-P) (2-1-P)*
 0.01992 (2-1-P) (3-1-F)*
 0.00852 (2-1-P) (2-1-F)*
 0.01992 (3-1+F) (2-1+P)*
-0.02440 (3-1+F) (2-1+F)*
 0.01992 (3-1-F) (2-1-P)*
-0.02440 (3-1-F) (2-1-F)*
-0.01278 (2-0+F) (2-0+P)*
-0.06260 (2-0+F) (2-0+F)*
 0.00852 (2-1+F) (2-1+P)*
-0.02440 (2-1+F) (3-1+F)*
 0.04173 (2-1+F) (2-1+F)*
 0.00852 (2-1-F) (2-1-P)*
-0.02440 (2-1-F) (3-1-F)*
 0.04173 (2-1-F) (2-1-F)*


H( 4 0 2 2)=
-0.06901 (1-0-P) (3-0-F)*
 0.04226 (1-1+P) (3-1+F)*
 0.04226 (1-1-P) (3-1-F)*
-0.07377 (2+0-D) (2+0-D)*
 0.04918 (2+1+D) (2+1+D)*
 0.04918 (2+1-D) (2+1-D)*
 0.04426 (2-0+P) (2-0+P)*
 0.03614 (2-0+P) (2-0+F)*
-0.02951 (2-1+P) (2-1+P)*
-0.01409 (2-1+P) (3-1+F)*
-0.02409 (2-1+P) (2-1+F)*
-0.02951 (2-1-P) (2-1-P)*
-0.01409 (2-1-P) (3-1-F)*
-0.02409 (2-1-P) (2-1-F)*
-0.06901 (3-0-F) (1-0-P)*
-0.04695 (3-0-F) (3-0-F)*
 0.04226 (3-1+F) (1-1+P)*
-0.01409 (3-1+F) (2-1+P)*
-0.00782 (3-1+F) (3-1+F)*
-0.01150 (3-1+F) (2-1+F)*
 0.04226 (3-1-F) (1-1-P)*
-0.01409 (3-1-F) (2-1-P)*
-0.00782 (3-1-F) (3-1-F)*
-0.01150 (3-1-F) (2-1-F)*
 0.03614 (2-0+F) (2-0+P)*
 0.02951 (2-0+F) (2-0+F)*
-0.02409 (2-1+F) (2-1+P)*
-0.01150 (2-1+F) (3-1+F)*
-0.01967 (2-1+F) (2-1+F)*
-0.02409 (2-1-F) (2-1-P)*
-0.01150 (2-1-F) (3-1-F)*
-0.01967 (2-1-F) (2-1-F)*


H( 4 1 0 0)=
-0.12199 (1-0-P) (3-1-F)*
-0.09960 (1-1-P) (3-0-F)*
-0.12295 (2+0-D) (2+1-D)*
-0.12295 (2+1-D) (2+0-D)*
 0.07043 (2-0+P) (3-1+F)*
-0.15058 (2-0+P) (2-1+F)*
-0.15058 (2-1+P) (2-0+F)*
 0.09960 (2-1-P) (3-0-F)*
-0.09960 (3-0-F) (1-1-P)*
 0.09960 (3-0-F) (2-1-P)*
 0.01383 (3-0-F) (3-1-F)*
 0.08133 (3-0-F) (2-1-F)*
 0.07043 (3-1+F) (2-0+P)*
 0.05751 (3-1+F) (2-0+F)*
-0.12199 (3-1-F) (1-0-P)*
 0.01383 (3-1-F) (3-0-F)*
-0.15058 (2-0+F) (2-1+P)*
 0.05751 (2-0+F) (3-1+F)*
 0.06148 (2-0+F) (2-1+F)*
-0.15058 (2-1+F) (2-0+P)*
 0.06148 (2-1+F) (2-0+F)*
 0.08133 (2-1-F) (3-0-F)*


H( 4 1 2-2)=
 0.03858 (1+0+S) (3-1+F)*
-0.03150 (1+1-S) (3-0-F)*
-0.04725 (1-0-P) (3-1-F)*
-0.03858 (1-1-P) (3-0-F)*
 0.02728 (1+0+D) (3-1+F)*
-0.02227 (1+1-D) (3-0-F)*
-0.04762 (2+0-D) (2+1-D)*
-0.03689 (2+0-D) (2-1-P)*
-0.00704 (2+0-D) (3-1-F)*
-0.03012 (2+0-D) (2-1-F)*
 0.03689 (2+1+D) (2-0+P)*
 0.03012 (2+1+D) (2-0+F)*
-0.04762 (2+1-D) (2+0-D)*
 0.00996 (2+1-D) (3-0-F)*
```

```
 0.03689 (2-0+P) (2+1+D)*
 0.02857 (2-0+P) (2-1+P)*
 0.00546 (2-0+P) (3-1+F)*
 0.02333 (2-0+P) (2-1+F)*
 0.02857 (2-1+P) (2-0+P)*
 0.02333 (2-1+P) (2-0+F)*
-0.03689 (2-1-P) (2+0-D)*
 0.00772 (2-1-P) (3-0-F)*
-0.03150 (3-0-F) (1+1-S)*
-0.03858 (3-0-F) (1-1-P)*
-0.02227 (3-0-F) (1+1-D)*
 0.00996 (3-0-F) (2+1-D)*
 0.00772 (3-0-F) (2-1-P)*
-0.02143 (3-0-F) (3-1-F)*
 0.00630 (3-0-F) (2-1-F)*
 0.03858 (3-1+F) (1+0+S)*
 0.02728 (3-1+F) (1+0+D)*
 0.00546 (3-1+F) (2-0+P)*
 0.00445 (3-1+F) (2-0+F)*
-0.04725 (3-1-F) (1-0-P)*
-0.00704 (3-1-F) (2+0-D)*
-0.02143 (3-1-F) (3-0-F)*
 0.03012 (2-0+F) (2+1+D)*
 0.02333 (2-0+F) (2-1+P)*
 0.00445 (2-0+F) (3-1+F)*
 0.01905 (2-0+F) (2-1+F)*
 0.02333 (2-1+F) (2-0+P)*
 0.01905 (2-1+F) (2-0+F)*
 0.03012 (2-1-F) (2+0-D)*
 0.00630 (2-1-F) (3-0-F)*


H( 4 1 2-1)=
 0.02728 (1+0+S) (3-1+F)*
-0.02227 (1+1-S) (3-0-F)*
-0.03858 (1+0+D) (3-1+F)*
 0.03150 (1+1-D) (3-0-F)*
-0.02608 (2+0-D) (2-1-P)*
 0.03194 (2+0-D) (2-1-F)*
 0.02608 (2+1+D) (2-0+P)*
-0.03194 (2+1+D) (2-0+F)*
 0.02608 (2-0+P) (2+1+D)*
 0.04041 (2-0+P) (2-1+P)*
-0.00772 (2-0+P) (3-1+F)*
-0.00825 (2-0+P) (2-1+F)*
 0.04041 (2-1+P) (2-0+P)*
-0.00825 (2-1+P) (2-0+F)*
-0.02608 (2-1-P) (2+0-D)*
-0.01091 (2-1-P) (3-0-F)*
-0.02227 (3-0-F) (1+1-S)*
 0.03150 (3-0-F) (1+1-D)*
-0.01091 (3-0-F) (2-1-P)*
 0.01336 (3-0-F) (2-1-F)*
 0.02728 (3-1+F) (1+0+S)*
-0.03858 (3-1+F) (1+0+D)*
-0.00772 (3-1+F) (2-0+P)*
 0.00945 (3-1+F) (2-0+F)*
-0.03194 (2-0+F) (2+1+D)*
-0.00825 (2-0+F) (2-1+P)*
 0.00945 (2-0+F) (3-1+F)*
-0.04041 (2-0+F) (2-1+F)*
-0.00825 (2-1+F) (2-0+P)*
-0.04041 (2-1+F) (2-0+F)*
 0.03194 (2-1-F) (2+0-D)*
 0.01336 (2-1-F) (3-0-F)*


H( 4 1 2 0)=
 0.02440 (1-0-P) (3-1-F)*
 0.01992 (1-1-P) (3-0-F)*
 0.02459 (2+0-D) (2+1-D)*
 0.02459 (2+1-D) (2+0-D)*
 0.04426 (2-0+P) (2-1+P)*
-0.01409 (2-0+P) (3-1+F)*
-0.02409 (2-0+P) (2-1+F)*
 0.04426 (2-1+P) (2-0+P)*
-0.02409 (2-1+P) (2-0+F)*
-0.01992 (2-1-P) (3-0-F)*
 0.01992 (3-0-F) (1-1-P)*
-0.01992 (3-0-F) (2-1-P)*
-0.00277 (3-0-F) (3-1-F)*
-0.01627 (3-0-F) (2-1-F)*
-0.01409 (3-1+F) (2-0+P)*
-0.01150 (3-1+F) (2-0+F)*
 0.02440 (3-1-F) (1-0-P)*
-0.00277 (3-1-F) (3-0-F)*
-0.02409 (2-0+F) (2-1+P)*
-0.01150 (2-0+F) (3-1+F)*
 0.05410 (2-0+F) (2-1+F)*
-0.02409 (2-1+F) (2-0+P)*
 0.05410 (2-1+F) (2-0+F)*
-0.01627 (2-1-F) (3-0-F)*


H( 4 1 2 1)=
-0.02728 (1+0+S) (3-1+F)*
 0.02227 (1+1-S) (3-0-F)*
 0.03858 (1+0+D) (3-1+F)*
-0.03150 (1+1-D) (3-0-F)*
 0.02608 (2+0-D) (2-1-P)*
-0.03194 (2+0-D) (2-1-F)*
-0.02608 (2+1+D) (2-0+P)*
 0.03194 (2+1+D) (2-0+F)*
-0.02608 (2-0+P) (2+1+D)*
 0.04041 (2-0+P) (2-1+P)*
-0.00772 (2-0+P) (3-1+F)*
-0.00825 (2-0+P) (2-1+F)*
 0.04041 (2-1+P) (2-0+P)*
-0.00825 (2-1+P) (2-0+F)*
 0.02608 (2-1+P) (2+0-D)*
-0.01091 (2-1-P) (3-0-F)*
 0.02227 (3-0-F) (1+1-S)*
-0.03150 (3-0-F) (1+1-D)*
-0.01091 (3-0-F) (2-1-P)*
 0.01336 (3-0-F) (2-1-F)*
-0.02728 (3-1+F) (1+0+S)*
 0.03858 (3-1+F) (1+0+D)*
-0.00772 (3-1+F) (2-0+P)*
 0.00945 (3-1+F) (2-0+F)*
 0.03194 (2-0+F) (2+1+D)*
-0.00825 (2-0+F) (2-1+P)*
 0.00945 (2-0+F) (3-1+F)*
-0.04041 (2-0+F) (2-1+F)*
-0.00825 (2-1+F) (2-0+P)*
-0.04041 (2-1+F) (2-0+F)*
-0.03194 (2-1-F) (2+0-D)*
 0.01336 (2-1-F) (3-0-F)*


H( 4 1 2 2)=
-0.03858 (1+0+S) (3-1+F)*
 0.03150 (1+1-S) (3-0-F)*
-0.04725 (1-0-P) (3-1-F)*
-0.03858 (1-1-P) (3-0-F)*
-0.02728 (1+0+D) (3-1+F)*
 0.02227 (1+1-D) (3-0-F)*
-0.04762 (2+0-D) (2+1-D)*
 0.03689 (2+0-D) (2-1-P)*
 0.00704 (2+0-D) (3-1-F)*
 0.03012 (2+0-D) (2-1-F)*
-0.03689 (2+1+D) (2-0+P)*
-0.03012 (2+1+D) (2-0+F)*
-0.04762 (2+1-D) (2+0-D)*
-0.00996 (2+1-D) (3-0-F)*
-0.03689 (2-0+P) (2+1+D)*
 0.02857 (2-0+P) (2-1+P)*
 0.00546 (2-0+P) (3-1+F)*
 0.02333 (2-0+P) (2-1+F)*
 0.02857 (2-1+P) (2-0+P)*
 0.02333 (2-1+P) (2-0+F)*
 0.03689 (2-1-P) (2+0-D)*
 0.00772 (2-1-P) (3-0-F)*
 0.03150 (3-0-F) (1+1-S)*
-0.03858 (3-0-F) (1-1-P)*
 0.02227 (3-0-F) (1+1-D)*
-0.00996 (3-0-F) (2+1-D)*
 0.00772 (3-0-F) (2-1-P)*
-0.02143 (3-0-F) (3-1-F)*
 0.00630 (3-0-F) (2-1-F)*
-0.03858 (3-1+F) (1+0+S)*
-0.02728 (3-1+F) (1+0+D)*
 0.00546 (3-1+F) (2-0+P)*
 0.00445 (3-1+F) (2-0+F)*
-0.04725 (3-1-F) (1-0-P)*
-0.00704 (3-1-F) (2+0-D)*
-0.02143 (3-1-F) (3-0-F)*
-0.03012 (2-0+F) (2+1+D)*
 0.02333 (2-0+F) (2-1+P)*
 0.00445 (2-0+F) (3-1+F)*
 0.01905 (2-0+F) (2-1+F)*
 0.02333 (2-1+F) (2-0+P)*
 0.01905 (2-1+F) (2-0+F)*
 0.03012 (2-1-F) (2+0-D)*
 0.00630 (2-1-F) (3-0-F)*


H( 4 2 0 0)=
 0.08626 (1-1+P) (3-1+F)*
-0.08626 (1-1-P) (3-1-F)*
 0.10039 (2+1+D) (2+1+D)*
-0.10039 (2+1-D) (2+1-D)*
-0.02875 (2-1+P) (3-1+F)*
-0.12295 (2-1+P) (2-1+F)*
 0.02875 (2-1-P) (3-1-F)*
 0.12295 (2-1-P) (2-1-F)*
 0.08626 (3-1+F) (1-1+P)*
-0.02875 (3-1+F) (2-1+P)*
-0.01597 (3-1+F) (3-1+F)*
-0.02348 (3-1+F) (2-1+F)*
-0.08626 (3-1-F) (1-1-P)*
 0.02875 (3-1-F) (2-1-P)*
 0.01597 (3-1-F) (3-1-F)*
 0.02348 (3-1-F) (2-1-F)*
-0.12295 (2-1+F) (2-1+P)*
-0.02348 (2-1+F) (3-1+F)*
 0.05019 (2-1+F) (2-1+F)*
 0.12295 (2-1-F) (2-1-P)*
 0.02348 (2-1-F) (3-1-F)*
-0.05019 (2-1-F) (2-1-F)*


H( 4 2 2-2)=
 0.02728 (1+1+S) (3-1+F)*
-0.02728 (1+1-S) (3-1-F)*
 0.03341 (1-1+P) (3-1+F)*
-0.03341 (1-1-P) (3-1-F)*
 0.01929 (1+1+D) (3-1+F)*
-0.01929 (1+1-D) (3-1-F)*
 0.03888 (2+1+D) (2+1+D)*
 0.03012 (2+1+D) (2-1+P)*
-0.00288 (2+1+D) (3-1+F)*
 0.02459 (2+1+D) (2-1+F)*
-0.03888 (2+1-D) (2+1-D)*
-0.03012 (2+1-D) (2-1-P)*
 0.00288 (2+1-D) (3-1-F)*
-0.02459 (2+1-D) (2-1-F)*
 0.03012 (2-1+P) (2+1+D)*
 0.02333 (2-1+P) (2-1+P)*
-0.00223 (2-1+P) (3-1+F)*
 0.01905 (2-1+P) (2-1+F)*
-0.03012 (2-1-P) (2+1-D)*
-0.02333 (2-1-P) (2-1-P)*
 0.00223 (2-1-P) (3-1-F)*
-0.01905 (2-1-P) (2-1-F)*
 0.02728 (3-1+F) (1+1+S)*
 0.03341 (3-1+F) (1-1+P)*
 0.01929 (3-1+F) (1+1+D)*
-0.00288 (3-1+F) (2+1+D)*
-0.00223 (3-1+F) (2-1+P)*
 0.02474 (3-1+F) (3-1+F)*
-0.00182 (3-1+F) (2-1+F)*
-0.02728 (3-1-F) (1+1-S)*
-0.03341 (3-1-F) (1-1-P)*
-0.01929 (3-1-F) (1+1-D)*
 0.00288 (3-1-F) (2+1-D)*
 0.00223 (3-1-F) (2-1-P)*
-0.02474 (3-1-F) (3-1-F)*
 0.00182 (3-1-F) (2-1-F)*
 0.02459 (2-1+F) (2+1+D)*
 0.01905 (2-1+F) (2-1+P)*
-0.00182 (2-1+F) (3-1+F)*
 0.01555 (2-1+F) (2-1+F)*
-0.02459 (2-1-F) (2+1-D)*
```

```
-0.01905 (2-1-F) (2-1-P)*
 0.00182 (2-1-F) (3-1-F)*
-0.01555 (2-1-F) (2-1-F)*


H( 4 2 2-1)=
 0.01929 (1+1+S) (3-1+F)*
-0.01929 (1+1-S) (3-1-F)*
-0.02728 (1+1+D) (3-1+F)*
 0.02728 (1+1-D) (3-1-F)*
 0.02130 (2+1+D) (2-1+P)*
-0.02608 (2+1+D) (2-1+F)*
-0.02130 (2+1-D) (2-1-P)*
 0.02608 (2+1-D) (2-1-F)*
 0.02130 (2-1+P) (2+1+D)*
 0.03299 (2-1+P) (2-1+P)*
 0.00315 (2-1+P) (3-1+F)*
-0.00673 (2-1+P) (2-1+F)*
-0.02130 (2-1-P) (2+1-D)*
-0.03299 (2-1-P) (2-1-P)*
-0.00315 (2-1-P) (3-1-F)*
 0.00673 (2-1-P) (2-1-F)*
 0.01929 (3-1+F) (1+1+S)*
-0.02728 (3-1+F) (1+1+D)*
 0.00315 (3-1+F) (2-1+P)*
-0.00386 (3-1+F) (2-1+F)*
-0.01929 (3-1-F) (1+1-S)*
 0.02728 (3-1-F) (1+1-D)*
 0.00386 (3-1-F) (2-1-F)*
 0.02608 (2-1+F) (2+1+D)*
 0.00673 (2-1+F) (2-1+P)*
 0.00386 (2-1+F) (3-1+F)*
 0.03299 (2-1+F) (2-1+F)*
-0.02608 (2-1-F) (2+1-D)*
-0.00673 (2-1-F) (2-1-P)*
-0.00386 (2-1-F) (3-1-F)*
-0.03299 (2-1-F) (2-1-F)*


H( 4 2 2 0)=
-0.01725 (1-1+P) (3-1+F)*
 0.01725 (1-1-P) (3-1-F)*
-0.02008 (2+1+D) (2+1+D)*
 0.02008 (2+1-D) (2+1-D)*
 0.03614 (2-1+P) (2-1+P)*
 0.00575 (2-1+P) (3-1+F)*
-0.01967 (2-1+P) (2-1+F)*
-0.03614 (2-1-P) (2-1-P)*
-0.00575 (2-1-P) (3-1-F)*
 0.01967 (2-1-P) (2-1-F)*
-0.01725 (3-1+F) (1-1+P)*
 0.00575 (3-1+F) (2-1+P)*
 0.00319 (3-1+F) (3-1+F)*
 0.00470 (3-1+F) (2-1+F)*
 0.01725 (3-1-F) (1-1-P)*
-0.00575 (3-1-F) (2-1-P)*
-0.00319 (3-1-F) (3-1-F)*
-0.00470 (3-1-F) (2-1-F)*
-0.01967 (2-1+F) (2-1+P)*
 0.00470 (2-1+F) (3-1+F)*
 0.04417 (2-1+F) (2-1+F)*
 0.01967 (2-1-F) (2-1-P)*
-0.00470 (2-1-F) (3-1-F)*
-0.04417 (2-1-F) (2-1-F)*


H( 4 2 2 1)=
-0.01929 (1+1+S) (3-1+F)*
 0.01929 (1+1-S) (3-1-F)*
 0.02728 (1+1+D) (3-1+F)*
-0.02728 (1+1-D) (3-1-F)*
-0.02130 (2+1+D) (2-1+P)*
 0.02608 (2+1+D) (2-1+F)*
 0.02130 (2+1-D) (2-1-P)*
-0.02608 (2+1-D) (2-1-F)*
-0.02130 (2-1+P) (2+1+D)*
 0.03299 (2-1+P) (2-1+P)*
 0.00315 (2-1+P) (3-1+F)*
-0.00673 (2-1+P) (2-1+F)*
 0.02130 (2-1-P) (2+1-D)*
-0.03299 (2-1-P) (2-1-P)*
-0.00315 (2-1-P) (3-1-F)*
 0.00673 (2-1-P) (2-1-F)*
 0.01929 (3-1+F) (1+1+S)*
-0.02728 (3-1+F) (1+1+D)*
 0.00315 (3-1+F) (2-1+P)*
-0.00386 (3-1+F) (2-1+F)*
-0.01929 (3-1-F) (1+1-S)*
 0.02728 (3-1-F) (1+1-D)*
 0.00386 (3-1-F) (2-1-F)*
 0.02608 (2-1+F) (2+1+D)*
 0.00673 (2-1+F) (2-1+P)*
 0.00386 (2-1+F) (3-1+F)*
 0.03299 (2-1+F) (2-1+F)*
-0.02608 (2-1-F) (2+1-D)*
-0.00673 (2-1-F) (2-1-P)*
-0.00386 (2-1-F) (3-1-F)*
-0.03299 (2-1-F) (2-1-F)*


H( 4 2 2 2)=
-0.02728 (1+1+S) (3-1+F)*
 0.02728 (1+1-S) (3-1-F)*
 0.03341 (1-1+P) (3-1+F)*
-0.03341 (1-1-P) (3-1-F)*
-0.01929 (1+1+D) (3-1+F)*
 0.01929 (1+1-D) (3-1-F)*
 0.03888 (2+1+D) (2+1+D)*
-0.03012 (2+1+D) (2-1+P)*
 0.00288 (2+1+D) (3-1+F)*
-0.02459 (2+1+D) (2-1+F)*
-0.03888 (2+1-D) (2+1-D)*
 0.03012 (2+1-D) (2-1-P)*
-0.00288 (2+1-D) (3-1-F)*
 0.02459 (2+1-D) (2-1-F)*
-0.03012 (2-1+P) (2+1+D)*
 0.02333 (2-1+P) (2-1+P)*
-0.00223 (2-1+P) (3-1+F)*
 0.01905 (2-1+P) (2-1+F)*
 0.03012 (2-1-P) (2+1-D)*
-0.02333 (2-1-P) (2-1-P)*
 0.00223 (2-1-P) (3-1-F)*
-0.01905 (2-1-P) (2-1-F)*
-0.02728 (3-1+F) (1+1-S)*
 0.03341 (3-1+F) (1-1+P)*
-0.01929 (3-1+F) (1+1+D)*
 0.00288 (3-1+F) (2+1+D)*
-0.00223 (3-1+F) (2-1+P)*
 0.02474 (3-1+F) (3-1+F)*
-0.00182 (3-1+F) (2-1+F)*
 0.02728 (3-1-F) (1+1-S)*
-0.03341 (3-1-F) (1-1-P)*
 0.01929 (3-1-F) (1+1-D)*
-0.00288 (3-1-F) (2+1-D)*
 0.00223 (3-1-F) (2-1-P)*
-0.02474 (3-1-F) (3-1-F)*
 0.00182 (3-1-F) (2-1-F)*
-0.02459 (2-1+F) (2+1+D)*
 0.01905 (2-1+F) (2-1+P)*
-0.00182 (2-1+F) (3-1+F)*
 0.01555 (2-1+F) (2-1+F)*
 0.02459 (2-1-F) (2+1-D)*
-0.01905 (2-1-F) (2-1-P)*
 0.00182 (2-1-F) (3-1-F)*
-0.01555 (2-1-F) (2-1-F)*


H( 5 0 0 0)=
-0.18110 (2+0-D) (3-0-F)*
 0.12805 (2+1+D) (3-1+F)*
 0.12805 (2+1-D) (3-1-F)*
-0.18110 (3-0-F) (2+0-D)*
 0.12805 (3-1+F) (2+1+D)*
 0.12805 (3-1-F) (2+1-D)*


H( 5 0 2 0)=
 0.03622 (2+0-D) (3-0-F)*
-0.02561 (2+1+D) (3-1+F)*
-0.02561 (2+1-D) (3-1-F)*


H( 5 0 2 1)= 0.0


H( 5 0 2 2)=
-0.06428 (2+0-D) (3-0-F)*
 0.04545 (2+1+D) (3-1+F)*
 0.04545 (2+1-D) (3-1-F)*
-0.06428 (3-0-F) (2+0-D)*
 0.04545 (3-1+F) (2+1+D)*
 0.04545 (3-1-F) (2+1-D)*


H( 5 1 0 0)=
-0.12148 (2+0-D) (3-1-F)*
-0.11453 (2+1-D) (3-0-F)*
-0.11453 (3-0-F) (2+1-D)*
-0.12148 (3-1-F) (2+0-D)*


H( 5 1 2-2)=
-0.04312 (2+0-D) (3-1-F)*
-0.04066 (2+1-D) (3-0-F)*
 0.03340 (2-0+P) (3-1+F)*
-0.03149 (2-1-P) (3-0-F)*
-0.04066 (3-0-F) (2+1-D)*
-0.03149 (3-0-F) (2-1-P)*
-0.02571 (3-0-F) (2-1-F)*
 0.03340 (3-1+F) (2-0+P)*
 0.02727 (3-1+F) (2-0+F)*
-0.04312 (3-1-F) (2+0-D)*
 0.02727 (2-0+F) (3-1+F)*
-0.02571 (2-1-F) (3-0-F)*


H( 5 1 2-1)=
 0.02525 (2-0+P) (3-1+F)*
-0.02381 (2-1-P) (3-0-F)*
-0.02381 (3-0-F) (2-1-P)*
 0.02916 (3-0-F) (2-1-F)*
 0.02525 (3-1+F) (2-0+P)*
-0.03092 (3-1+F) (2-0+F)*
-0.03092 (2-0+F) (3-1+F)*
 0.02916 (2-1-F) (3-0-F)*


H( 5 1 2 0)=
 0.02430 (2+0-D) (3-1-F)*
 0.02291 (2+1-D) (3-0-F)*
 0.02291 (3-0-F) (2+1-D)*
 0.02430 (3-1-F) (2+0-D)*


H( 5 1 2 1)=
-0.02525 (2-0+P) (3-1+F)*
 0.02381 (2-1-P) (3-0-F)*
 0.02381 (3-0-F) (2-1-P)*
-0.02916 (3-0-F) (2-1-F)*
-0.02525 (3-1+F) (2-0+P)*
 0.03092 (3-1+F) (2-0+F)*
 0.03092 (2-0+F) (3-1+F)*
-0.02916 (2-1-F) (3-0-F)*


H( 5 1 2 2)=
-0.04312 (2+0-D) (3-1-F)*
-0.04066 (2+1-D) (3-0-F)*
-0.03340 (2-0+P) (3-1+F)*
 0.03149 (2-1-P) (3-0-F)*
-0.04066 (3-0-F) (2+1-D)*
 0.03149 (3-0-F) (2-1-P)*
 0.02571 (3-0-F) (2-1-F)*
-0.03340 (3-1+F) (2-0+P)*
-0.02727 (3-1+F) (2-0+F)*
-0.04312 (3-1-F) (2+0-D)*
-0.02727 (2-0+F) (3-1+F)*
 0.02571 (2-1-F) (3-0-F)*
```

```
H( 5 2 0 0)=
 0.09278 (2+1+D) (3-1+F)*
-0.09278 (2+1-D) (3-1-F)*
 0.09278 (3-1+F) (2+1+D)*
-0.09278 (3-1-F) (2+1-D)*

H( 5 2 2-2)=
 0.03293 (2+1+D) (3-1+F)*
-0.03293 (2+1-D) (3-1-F)*
 0.02551 (2-1+P) (3-1+F)*
-0.02551 (2-1-P) (3-1-F)*
 0.03293 (3-1+F) (2+1+D)*
 0.02551 (3-1+F) (2-1+P)*
 0.02083 (3-1+F) (2-1+F)*
-0.03293 (3-1-F) (2+1-D)*
-0.02551 (3-1-F) (2-1-P)*
-0.02083 (3-1-F) (2-1-F)*
 0.02083 (2-1+F) (3-1+F)*
-0.02083 (2-1-F) (3-1-F)*

H( 5 2 2-1)=
 0.01928 (2-1+P) (3-1+F)*
-0.01928 (2-1-P) (3-1-F)*
 0.01928 (3-1+F) (2-1+P)*
-0.02362 (3-1+F) (2-1+F)*
-0.01928 (3-1-F) (2-1-P)*
 0.02362 (3-1-F) (2-1-F)*
-0.02362 (2-1+F) (3-1+F)*
 0.02362 (2-1-F) (3-1-F)*

H( 5 2 2 0)=
-0.01856 (2+1+D) (3-1+F)*
 0.01856 (2+1-D) (3-1-F)*
-0.01856 (3-1+F) (2+1+D)*
 0.01856 (3-1-F) (2+1-D)*

H( 5 2 2 1)=
-0.01928 (2-1+P) (3-1+F)*
 0.01928 (2-1-P) (3-1-F)*
-0.01928 (3-1+F) (2-1+P)*
 0.02362 (3-1+F) (2-1+F)*
 0.01928 (3-1-F) (2-1-P)*
-0.02362 (3-1-F) (2-1-F)*
 0.02362 (2-1+F) (3-1+F)*
-0.02362 (2-1-F) (3-1-F)*

H( 5 2 2 2)=
 0.03293 (2+1+D) (3-1+F)*
-0.03293 (2+1-D) (3-1-F)*
-0.02551 (2-1+P) (3-1+F)*
 0.02551 (2-1-P) (3-1-F)*
 0.03293 (3-1+F) (2+1+D)*
-0.02551 (3-1+F) (2-1+P)*
-0.02083 (3-1+F) (2-1+F)*
-0.03293 (3-1-F) (2+1-D)*
 0.02551 (3-1-F) (2-1-P)*
 0.02083 (3-1-F) (2-1-F)*
-0.02083 (2-1+F) (3-1+F)*
 0.02083 (2-1-F) (3-1-F)*

H( 6 0 0 0)=
-0.17483 (3-0-F) (3-0-F)*
 0.13112 (3-1+F) (3-1+F)*
 0.13112 (3-1-F) (3-1-F)*

H( 6 0 2 0)=
 0.03497 (3-0-F) (3-0-F)*
-0.02622 (3-1+F) (3-1+F)*
-0.02622 (3-1-F) (3-1-F)*

H( 6 0 2 1)= 0.0

H( 6 0 2 2)=
-0.05851 (3-0-F) (3-0-F)*
 0.04388 (3-1+F) (3-1+F)*
 0.04388 (3-1-F) (3-1-F)*

H( 6 1 0 0)=
-0.11564 (3-0-F) (3-1-F)*
-0.11564 (3-1-F) (3-0-F)*

H( 6 1 2-2)=
-0.03870 (3-0-F) (3-1-F)*
-0.03870 (3-1-F) (3-0-F)*

H( 6 1 2-1)= 0.0

H( 6 1 2 0)=
 0.02313 (3-0-F) (3-1-F)*
 0.02313 (3-1-F) (3-0-F)*

H( 6 1 2 1)= 0.0

H( 6 1 2 2)=
-0.03870 (3-0-F) (3-1-F)*
-0.03870 (3-1-F) (3-0-F)*

H( 6 2 0 0)=
 0.08957 (3-1+F) (3-1+F)*
-0.08957 (3-1-F) (3-1-F)*

H( 6 2 2-2)=
 0.02998 (3-1+F) (3-1+F)*
-0.02998 (3-1-F) (3-1-F)*

H( 6 2 2-1)= 0.0

H( 6 2 2 0)=
-0.01791 (3-1+F) (3-1+F)*
 0.01791 (3-1-F) (3-1-F)*

H( 6 2 2 1)= 0.0

H( 6 2 2 2)=
 0.02998 (3-1+F) (3-1+F)*
-0.02998 (3-1-F) (3-1-F)*
```

Bibliography

[1] D. Leith, Nucl. Inst. and Meth. A265 (1987) 120.

[2] P. A. Cherenkov , Izvestiya AN, SSSR, Seriya Fiz., OMEN (1937).

[3] I. M. Frank and Ig. Tamm, Doklady Akad. Nauk, SSSR, 14(3) (1937) 109.

[4] J. Seguinot and T. Ypsilantis, Ncul. Inst. and Meth. 142 (1977) 377.

[5] A. Roberts, Ncul. Inst. and Meth. 9 (1960) 55.

[6] H. Glass *et al.*, IEEE Trans. Nucl. Sci. NS-32 (1985) 692.

[7] R. J. Apsimon *et al.*, IEEE Trans. Nucl. Sci. NS-32 (1985) 674.

[8] DELPHI Proposal, LEPC 83-3 and LEPC 84-16.

[9] SLD Design Report, SLAC-Report-273 (1984).

[10] J. D. Jackson, *Classical Electrodynamics*, 2nd ed., Wiley, New York (1975) p.638.

[11] H. Jansen, Univ. of Leiden (The Netherlands), Ph.D Thesis (1988).

[12] G. Charpak and F. Sauli, Ncul. Inst. and Meth. 225 (1984) 627.

[13] K. Abe *et al.*, Ncul. Inst. and Meth. A300 (1991) 501.

[14] J. Va'vra *et al.*, SLAC-PUB-5214.

[15] J. Hoefflich *et al.*, IEEE Trans. Nucl. Sci. NS-38 (1991) 348.

[16] P. Antilogus *et al.*, SLAC-PUB-5365 (1991).

[17] P. Antilogus *et al.*, SLAC-PUB-5105 (1989).

[18] C. Delaney, ***Electronics for the physicist***, Ellis Horwood, Chichester, England (1980) Chapter 11.

[19] H. Nyquist, Phys. Rev. 32 (1928) 110.

[20] P. Antilogus *et al.*, IEEE Trans. Nucl. Sci. NS-38 (1991) 408.

[21] Tim Bienz, Ph.D. Thesis, SLAC-REP-369 (1990).

[22] AD590: Analog Devics, Norwood, MA 02062, USA.

[23] D. Nelson, SLAC-ELD-DOC 39 (1983).

[24] J. Keifer, SLAC Tech. Note 83-03.

[25] 70 OAC5: Grayhill Inc., LaGrange, IL 60525, USA.

[26] J. Keifer, SLAC Tech. Note 83-01.

[27] G. Hallewell *et al.*, SLD CRID Internal Note 53 (1988).

[28] S. Haderle *et al.*,, SLD CRID Internal Note 64 (1990).

[29] R. Watt, SLAC Memorandum 11/24/89 to CRID Gas Group.

[30] G. Hallewell *et al.*, Ncul. Inst. and Meth. A264 (1988) 219.

[31] Polaroid Corp. instrument grade transducer, part no. 604142: Ultrasonic Ranging System User's Manual and Application Notes. Polaroid Corporation, Cambridge, MA 02139.

[32] J. Va'vra, *The first results from CRID*, SLD CRID Internal Note 68 (1991).

[33] K. Abe et al., SLAC-Pub 5680 (1991), *presented at the IEEE Nuclear Science Symposium and Medical Imaging Conference, Nov. 5-9, 1991*; J. Va'vra et al., SLAC-Pub 5945 (1992), *presented at the 26th International Conference on High Energy Physics, Aug.12-16, 1992, Dallas, TX*; K. Abe et al., SLAC-Pub 5986 (1992), *presented at the IEEE Nuclear Science Symposium, Oct. 27-31, 1992.*

[34] 13X Molecular Sieve made by Union Carbide Co., Danburg, CT 06817-0001, U.S.A.

[35] Oxysorb made by Messer Griesheim GmbH, 4000 Dusseldorf, Germany.

[36] M. Cavalli-Sforza, *Electron Lifetime Measurements in the Disaster Monitor*, CRID MEMO 15 (1986).

[37] K. Hikasa *et al.*, *Review of Particle Properties*, Phys. Rev. D45 (1992).

[38] D. Aston *et al.*, *The LASS Spectrometer*, SLAC-Report 298 (1986).

[39] See, for example, D. Aston *et al.*, SLAC-Pub 5236 (1990) and *Proceedings of the 15th DPF meeting*, Houston, TX (1990) 651.

[40] C. Daum *et al.*, Nucl. Phys. B187 (1981) 1.

[41] S. Godfrey and N. Isgur, Phys. Rev. D32 (1985) 189.

[42] D. Aston *et al.*, Nucl. Phys. B292 (1987) 693.

[43] D. Aston *et al.*, Phys. Lett. B201 (1988) 169.

[44] A.D. Martin and C. Nef, Nucl. Phys. B181 (1981) 61.

[45] D. Aston, T.A. Lasinski and P. K. Sinervo, *SLAC 3-body Partial Wave Analysis*, SLAC-Report 287 (1986).

[46] P. K. Sinervo, Ph.D. thesis, Stanford University, SLAC-Report 299 (1986).

[47] S.U. Chung, *Spin Formalisms*, CERN 71-8 (1970).

[48] A.D. Martin and T.D. Spearman, *Elementary Particle Theory*, North-Holland, Amsterdam (1970).

[49] Computer program MINUIT, CERN Library; F. James and M. Roos, Computer Phys. Commun. 10 (1975) 343.

[50] J.M. Blatt and V.F. Weisskopf, *Theoretical Nuclear Physics*, Wiley, New York (1957) p. 52.

[51] J.D. Jackson, Nuovo Cimento 34 (1964) 1144.

[52] P. F. Bird, Ph.D. thesis, Stanford University, SLAC-Report 332 (1988).

[53] D. Aston *et al.*, Phys. Lett. B296 (1988) 493.

[54] D. Aston *et al.*, invited talk by D.W.G.S. Leith in the 3rd International Conference on Hadron Spectroscopy, SLAC-PUB 5151 (1989).

[55] T. Armstrong *et al.*, Nucl. Phys. B221 (1983) 1.

[56] D. Frame *et al.*, Nucl. Phys. B276 (1986) 667.

[57] Aguilar-Benitez *et al.*, Phys. Rev. D4 (1971) 2583.

[58] Bassompierre *et al.*, Nucl. Phys. B13 (1969) 189.

[59] Field *et al.*, Phys. Lett. 24B (1967) 638.

[60] D. Aston *et al.*, Phys. Lett. 106B (1981) 235.

[61] R. Kokowski and N. Isgur, Phys. Rev. D35 (1987) 907.